LUND UNIVERSITY

Probing Proton Translocation in Influenza A/M2 Proteoliposomes - A systematic Approach to Membrane-Protein Reconstitutions

Leiding, Thom

2010

Total number of authors:
1

Probing Proton Translocation in Influenza A/M2 Proteoliposomes

A Systematic Approach to Membrane-Protein Reconstitution

Thom Leiding

Doctoral thesis

Department of Biochemistry and Structural Biology

Lund University, 2010

Title and subtitle   Probing Proton Translocation in Influenza A/M2 Proteoliposomes
A Systematic Approach to Membrane-Protein Reconstitution

Abstract

An improved method for reconstituting membrane proteins into artificial liposomes for quantitative functional analysis is presented. A number of key parameters for reconstitution by detergent removal are assessed in this thesis: The lipid-to-protein ratio, the detergent-to-lipid ratio and the lipid and cholesterol composition. New porphyrin-based pH-probes are evaluated. Based on this systematic, comprehensive approach to protein reconstitution, we present a robust system for quantitative proton-flux analysis, as demonstrated by influenza virus A M2 reconstitution into large unilamellar vesicles.

The M2 protein is a small, single-span transmembrane protein, which plays an important role in the life cycle of influenza A virus and is the target of the adamantane series of anti-influenza drugs. This virus enters cells via the endosomes; as the endosomes acidify M2 facilitates proton transport into the viral interior, thereby disrupting matrix protein/RNA interactions required for infectivity. A mystery has been how protons can accumulate in the viral interior without developing a large electrical potential that impedes further inward proton translocation, which is required to effect a significant change in the internal effective pH. Here, we show that M2 has essential antiporter-like activity. This should lead to future investigations of the biophysical mechanism of transport, which will have implications for the design of new generations of M2-targeting drugs as well as furthering our understanding of cotransport.

Key words:
Proteoliposome; reconstitution; proton translocation; pH; antiporter; porphyrine pH-probe

Classification system and/or index termes (if any):

Populärvetenskaplig sammanfattning

Allt levande består av celler. Cellen är livets allra minsta byggsten. Cellen har ett hölje som kallas cellmembran. Detta membran skiljer cellens inre som kallas cytosol från omvärlden. I detta cellmembran sitter olika protein inbäddade. Genom dessa protein kommunicerar och utbyter cellen ämnen med sin omgivning. Många av dessa protein är mål för läkemedel och är därför viktiga att studera. Det är inte alltid så lätt att studera dessa membranproteiner när de sitter i cellmembranet eftersom andra intilliggande protein kan påverka mätningarna. Jag har utvecklat en ny metod för att sätta in membranprotein och då speciellt membranprotein som transporterar protoner eller vätejoner över cellmembran. Dessa protontransportörer är ofta med i olika sjukdomsbilder var av en är cancer. Vi har systematiskt och noga utrett förutsättningarna för att lyckas med dessa mätningar och har bland annat utvärderat nya färger som man kan använda för att mäta pH inuti dessa konstgjorda cellskal eller liposomer.

Vi har använt allt detta till att sätta in en protonkanal från ett influensavirus (från samma typ av virus som svininfluensaviruset) i liposomer och undersökt hur de fungerar. Detta protein är nödvändigt för att viruset ska kunna infektera sin värd och om man kan stoppa proteinets funktion kan virusets smitta förhindras. Om man kan hitta en medicin som gör just detta så skulle man inte längre enbart vare hänvisad till vaccination för att skydda sig mot influensan. Jag har mätt hur fort protoner flödar genom kanalen och mätt hur väl vissa droger bromsar eller helt stoppar transporten genom proteinet. Jag har upptäck att denna kanal inte bara transporterar protoner utan även andra joner som kaliumjoner och natriumjoner. Detta gör att man nu har en bättre förståelse för hur influensaviruset smittar.

List of Contents

List of Publications

I   Efficient and non-denaturing membrane solubilization combined with enrichment of membrane protein complexes by detergent/polymer aqueous two-phase partitioning for proteome analysis.
Henrik Everberg, Thom Leiding, Anna Schiöth, Folke Tjerneld and Niklas Gustavsson.
Journal of Chromatography A 1122 (2006) 35–46.

II   Precise detection of pH inside large unilamellar vesicles using membrane-impermeable dendritic porphyrin-based nanoprobes.
Thom Leiding, Kamil Górecki, Tomas Kjellman, Sergei A. Vinogradov, Cecilia Hägerhäll and Sindra Peterson Årsköld.
Analytical Biochemistry 388 (2009) 296–305.

III   Membrane-impermeable ratiometric pH nanosensor based on highly non-planar dendritic porphyrin.
Sujitha Thyagarajan, Thom Leiding, Jonas Martinsson, Sindra Peterson Årsköld and Sergei Vinogradov.
Manuscript.

IV   An improved detergent-mediated reconstitution method yields unidirectional influenza A/M2 proteoliposomes.
Thom Leiding, Jonas Martinsson, Katja Bernfur, Alexandra Franzén, Björn Borgström, Alexei L. Polishchuk, William DeGrado and Sindra Peterson Årsköld.
Submitted to *BBA Biomembranes*.

V   Functional antiporter activity of the M2 proton channel from influenza A virus.

Thom Leiding, Jonas Martinsson, Jun Wang, Sergei Vinogradov, William DeGrado and Sindra Peterson Årsköld.

Submitted to *Proc. Nat. Acad. Sci. USA*.

VI   A cytochrome *c-* fusion protein domain for convenient detection, quantification and enhanced production of membrane proteins in *Escherichia coli -* expression and characterization of cytochrome-tagged complex I subunits.

Tobias Gustavsson, Maria Trane, Vamsi K. Moparthi, Egle Miklovyte, Lavanya Moparthi, Kamil Górecki, Thom Leiding, Sindra Peterson Årsköld and Cecilia Hägerhäll.

Submitted to *Protein Science.*

My contributions to the articles above were as follows:

I   I did preparations of mithochondrial membranes and made solubilization studies on them with different detergents.

II   I performed or supervised all experiments except fluorescence measurements and I wrote the paper.

III   I took part in dye evaluation experiments and spectral analysis and wrote those parts of the paper.

IV   I performed, supervised or took part in all experiments and wrote the paper.

V   I performed, supervised or took part in all experiments and wrote parts of the paper.

VI   I performed redox-titrations on the cytochrome-tagged subunits.

1. Introduction

The cell is the basic functional unit of life. It was discovered by Robert Hooke, who presented it in his 1665 book Micrographia (1), where he among many other things depicted the structure of cork (Figure 1). He named the smallest units he could see cells, for their likeness to monk quarters. Modern cell theory is credited to Schwann, Schleiden and Virchow, who published it in the mid 19th century (2). It defines the cell as the smallest unit of life classified as a living thing, and states that all cells come from pre-existing cells. Some organisms, such as bacteria, consist of a single cell. Other organisms are multicellular, where different cells may specialize in performing different tasks. We know today that all cells consist of three main molecular components: nucleic acids, phospholipids, and amino acids.

Deoxyribonucleic acid (DNA) is a nucleic acid that contains the genetic instructions used for construction and progression in all known living organisms and some viruses. The main role of DNA is long-term storage of information. DNA is often compared to a set of blueprints, since it contains the instructions needed to construct other key components of the cell, such as proteins. The DNA molecules or
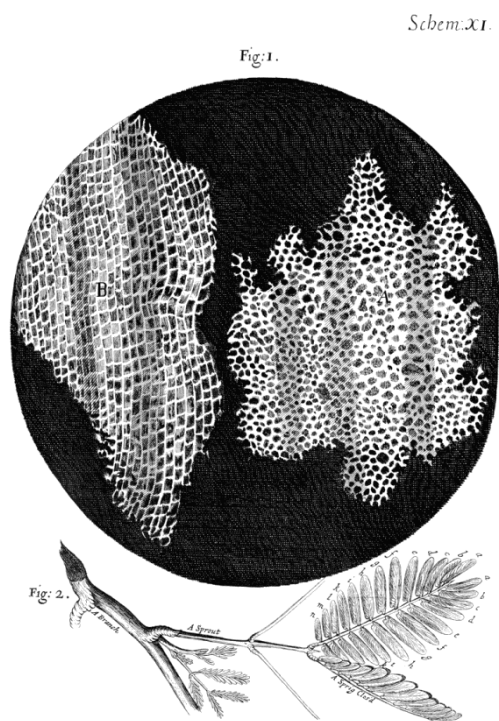
Figure 1. Cork slices by Hooke.

chromosomes are logically divided into functional segments called genes. Large parts of the chromosomes do not code for proteins, and we have limited knowledge about the purpose of these segments. Nucleic acids fall outside the scope of this book and will not be elucidated further.

Phospholipids are a class of lipids that serve to separate the compartments of the cell. Phospholipids are amphiphilic, with a hydrophilic head and two hydrophobic tails. The hydrophobic part is often constituted by a diglyceride, and the polar headgroup by a phosphate group and a simple organic molecule such as choline. When phospholipids are exposed to water, they arrange themselves into a two-layered sheet, called a bilayer, with their tails pointing toward the center of the sheet. The center of this bilayer contains virtually no water, and excludes water-soluble molecules. The hydrophobic effect drives this assembly process. This type of membrane is partially permeable and capable of elastic movement. It has fluid properties, such that embedded proteins and phospholipid molecules are able to move laterally in the bilayer. The fluid-mosaic model (3) describes the membrane as a mosaic of lipid molecules that act as a solvent for all the substances and proteins within it, allowing proteins and lipid molecules to diffuse laterally through the lipid matrix and migrate over the membrane. Cholesterol contributes to membrane fluidity by preventing the packing together of phospholipids. The fluid-mosaic model has now been superseded, as studies of lipid polymorphism indicate quite complicated behavior of lipids under physiological conditions. Evidence is also accumulating that apart from structural importance, phospholipids can have activating or regulating effects on membrane-associated proteins - effects that can be both specific and crucial.

A membrane transport protein (or transporter) is a protein involved in the movement of ions, small molecules, or macromolecules across a membrane. Transporters are integral membrane proteins, which span the membrane across which they transport substances. The proteins may assist in the movement of substances by facilitated diffusion or active transport. The mechanism of action of these proteins is known as carrier-mediated transport (see Figure 2). A good example of transporters performing facilitated diffusion is ion

channels. Ion channels can be highly selective and are capable of very high transport rates. A typical characteristic of a passive transporter is that it can assume an open or a closed state, determined either by ligand binding or by voltage. Active transporters can be divided into primary and secondary transporters. Primary transporters, or pumps, transport ions or molecules against a concentration gradient using chemical energy, for example by ATP hydrolysis.
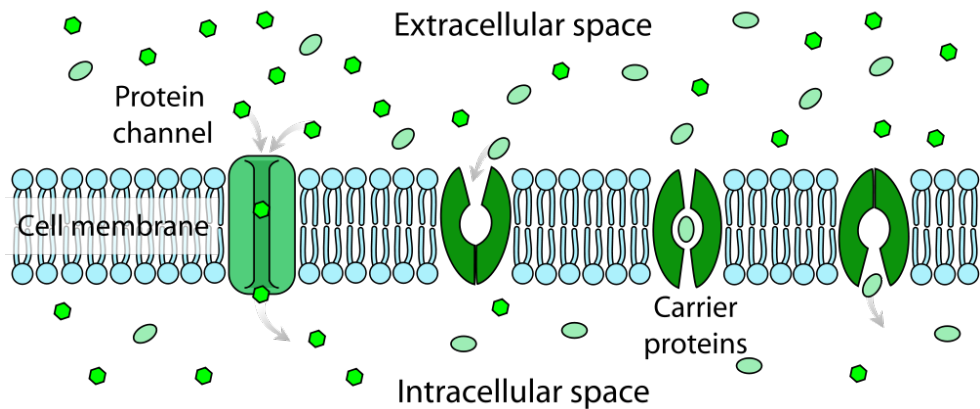
Figure 2. Cartoon of facilitated-diffusion transporters.

Secondary transporters are symporters or antiporters, which utilize a concentration gradient of one species to transport another species against its gradient. Secondary transporters typically depend on the concentration gradients created by primary transporters; for instance, the proton concentration gradient maintained by the pump ATPase can be utilized by secondary transporters to move nutrients and other solutes across the membrane. Both pumps and secondary transporters normally have much lower transport rates than ion channels. Proton translocators are an important group of transporters. There are examples of proton translocators in all categories of pumps and channels mentioned above.

The proton gradient – a difference in hydrogen ion concentration inside and outside a closed membrane compartment – plays a pivotal role in biology. In photosynthesis, light energy is trapped by a series of large membrane-protein complexes, which convert the energy to a proton gradient. In respiration, energy from metabolized carbohydrates is similarly captured in a proton gradient. Proton-translocating membrane proteins are also implicated in various diseases. Peptic diseases are treated with proton-pump inhibitors. Importantly, abnormal proton distribution between organelles, the cytoplasm and the extracellular matrix has emerged as a common feature of cancer tumor tissues (4, 5). An overly acidic extracellular pH prevents many drugs (weak bases at physiological pH) from entering the cells, and in drug-resistant cell lines, the drugs that do penetrate the cell wall accumulate in abnormally acidified organelles rather than entering the nucleus. Several antiviral drugs target the Influenza A virus M2 proton transporter, which is pivotal for viral propagation(6).

These proteins thus drive a number of fundamentally important biological processes, and unraveling their proton-translocating mechanisms is important for understanding the world we live in as well as developing therapeutic agents against a range of maladies.

An important step in investigating proton transporters is to establish the rate and stoichiometry of protein-mediated proton transport. In the native membrane, several proton-conducting mechanisms work in concert - some known and some putative - and it is difficult to monitor the activity of one specific type of protein. By removing a proton translocator from its native membrane, purifying it and reconstituting it into liposomes, it can be characterized in a well-defined environment without bias from other proteins. However, this procedure can be quite challenging. In this text and Paper IV, I address a number of determinant aspects in the protein reconstitution procedure, aiming to present a comprehensive picture of the proteoliposome assembly process.

In Paper V we use everything we have learned about lipids, liposomes and pH sensors to investigate A/M2 reconstituted into proteoliposomes. We determine proton flux at different pH and with different driving forces, with and without cation de-coupling. Based on these results we conclude that M2 has essential antiporter-like activity. This will have implications for the design of new generations of M2-targeting drugs as well as furthering our understanding of cotransport.

Proton transfer

Electron and proton transfer both involve movement of a point charge, and as such have certain fundamental similarities. However, they differ greatly at a phenomenological level - especially as they are encountered in the context of protein function. With few exceptions, biological electron transfer is highly insensitive to the structural details of the protein as a transmission medium. The protein plays a critical role in tuning the thermodynamic properties of redox-active cofactors, and positions them at distances that allow sufficiently fast electron-transfer rates, but there is no orderly electron path between the cofactors. Not to say that the intervening medium does not provide the mechanism of electron transfer - electrons are transmitted by virtue of the molecular-orbital wave functions that set the excited-state energies of the medium. However, the specific structure of the protein is not in any way critical for this. The reason for this is that electrons can tunnel. The distances observed for intramolecular electron transfer in physiological reactions are almost universally less than 15 Å, edge-to-edge. From Marcus' theory of non-adiabatic electron transfer or tunneling (7, 8), this distance limit ensures electron-transfer times faster than 100 μs for reactions that are energetically favorable or even slightly endergonic. At shorter distances, the rate increases by 10-fold for every 1.7 Å decrease in distance, allowing very rapid rates to be achieved without direct contact.

In contrast to electron transfer, proton transfer is exquisitely dependent on structure. Since tunneling is inversely proportional to the square root of the particle mass, the distance over which the relatively heavy proton can tunnel is

less than a covalent bond length. Therefore, the most important requirement for proton transfer is proximity, whether the mechanism is non-adiabatic or adiabatic.

Proton transfer in water

The electrostatic binding energy of the proton is so large that it has no independent existence in condensed phases. In water, it is generally considered to be present as hydronium, H_3O^+, which is similar to Na^+ in size and solvation characteristics. It can therefore be expected to exhibit diffusive properties similar to Na^+ or perhaps water. However, the rapid exchange of H^+ between H_3O^+ and H_2O allows for a unique transport process known as the Grotthuss mechanism, in which net protonic charge is transferred without diffusive movement of individual H^+ or oxygen atoms (see Figure 3).
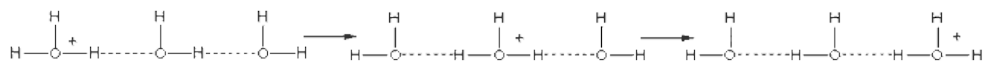
Figure 3. Schematic of the Grotthuss mechanism.

The current view of the Grotthuss mechanism in bulk water is that proton transfer occurs in a step-wise manner, via the interconversion of an Eigen cation, $H_9O_4^+ = (H_2O)_3H_3O^+$, and a Zundel cation, $H_5O_2^+ = H_2O–H^+–OH_2$. The activation energy of this conversion reflects the breakage of a hydrogen bond in the second solvation shell of the Eigen cation (between $H_9O_4^+$ and another H_2O; approximately 2.5 kcal/mol). This allows reorganization around the hydronium ion to produce the Zundel ion configuration, within which the excess proton is shared equally between two oxygen centers. Reformation of a hydrogen bond with another water molecule localizes the excess proton on a new Eigen ion. By repeating this step of shifting a covalent bond with a hydrogen bond, an effective proton charge can traverse a chain of water molecules very fast, circumventing the limitation of the related diffusion coefficients of Na^+ or H_2O. The resulting proton diffusion coefficient of 0.93

$Å^2$ ps^{-1} is seven times faster than that for Na^+ and four times faster than that for H_2O. The difference between proton and water diffusion is even more pronounced in single-file water channels, where the water diffusion is reduced by a factor of ten while the proton diffusion stays the same, resulting in 40 times difference in diffusion rates.

Proton transfer in protein channels

The interior of a protein is generally hydrophobic, and moving a proton through it would incur a large energetic penalty. To avoid this, proton-translocating proteins have evolved specific proton-transfer pathways. These pathways are essentially proton wires, consisting of hydrogen-bonded chains through the hydrophobic interior of the protein. Common pathways contain single-file water and stationary water molecules connecting the bulk water on each side of the membrane, enabling the Grotthuss mechanism described above to catalyze rapid proton transfer. Hydrophilic amino acids typically line such water-filled pores, and hydrogen-bonding amino-acid side chains are commonly a part of the proton-transfer pathway. These side chains can provide ion selectivity by size-specific dehydration, and active transport is often effectuated by conformational changes of the protein influencing the hydrogen-bonding network in the proton pathway. The poster child of the Grotthuss mechanism is gramicidin, which transfers alkali metals at the diffusion rate of water but transfers protons about 20 times faster through a single-file water pore (9-13). In aquaporins we see an example of the rate-limiting effect of hydrogen-bonding amino acids interfering with the water wire through the protein: A polarity shift in the chain of waters appears to obstruct Grotthus-type proton conduction. In combination with desolvation penalties and a positive charge in the center of the channel, this allows aquaporins to transfer water without releasing proton gradients (14-16).

The most common methods for monitoring proton translocation are single-current patch-clamp measurements *in vivo* or methods related to purified proton-translocators reconstituted into proteoliposomes.

Proteoliposomes

The complexity of most biological membranes makes it difficult to study individual membrane proteins *in situ*. Therefore, such proteins are usually purified from the native membrane for analysis, e.g. by solubilization. In order to monitor transport from one compartment to another and the build-up of concentration gradients, however, compartmentalization is necessary. This can be achieved away from the native system by reconstituting the purified membrane protein into an artificial lipid bilayer forming a closed vesicle, or liposome.

Methods for producing high-quality proteoliposomes have not advanced in step with other biochemical, biophysical, and molecular-biology techniques. A key obstacle is the lack of reproducible methods of protein reconstitution.

Four main strategies have been used for reconstitution of membrane proteins into liposomes: sonication, freeze-thawing, organic solvents, and detergents. Methods including organic solvents are rarely used as these solvents often have a denaturing effect on the proteins. Sonication and freeze-thawing are widely used in the literature, but have a major drawback in that they facilitate a very abrupt reformation of the lipid bilayers. This gives very limited influence over the morphology of the resulting vesicles, and heterogenous populations are likely to appear. Sonication produces heat that can damage protein close to the sonication horn, and freeze-thawing imposes strain on protruding protein domains and is prone to produce a quite large fraction of multilamellar vesicles (see Figure 1b, Paper IV).

The most promising strategy of proteoliposome formation is by detergent solubilization followed by gradual detergent removal. This method is very gentle to the protein, and the morphology and homogeneity of the proteoliposomes can be adjusted by using different detergents and by varying the degree of solubilization and the rate of detergent removal. There are several ways of lowering the detergent concentration to allow vesicle formation, but the only two of importance today are dialysis and hydrophobic beads. When

applicable, the hydrophobic-bead method (17) provides a much wider field of opportunities regarding control of vesicle morphology and choice of detergent. It is the method of choice for the work presented in this thesis.

2. Molecular pH Probes

Advanced molecular sensors is a rapidly developing area of research (18), and proton nanosensors attract special interest because of their applicability in monitoring proton concentration gradients across membranes. A good pH sensor provides the opportunity to monitor proton transfer across a lipid bilayer from the inside of the liposome. Compared to monitoring bulk pH with an electrode, this gives adequate time resolution, high precision, and a greater sensitivity to proton movement since the internal volume is much smaller than the bulk.

An ideal pH-probe would have the following characteristics.
1) It would display a spectroscopic signal with a significant spectral shift correlating to variations in pH, with high molar extinction coefficients in both protonated and non-protonated forms.
2) The emission quantum yields of both protonated and non-protonated forms would be high enough to allow ratiometric pH detection.
3) It would have a useful pK value: According the Henderson-Hasselbalch equation, the typical probe spans a pH-range of about two pH-units centered on the pK. For biological applications, a pK around 7 is the most useful.
4) It would report on a process without interfering with or influencing it in any way, including:
5) Complete membrane impermeability, ensuring reliable localization of the probe as well as avoiding all interactions with the membrane that may affect the measurement,
6) High water-solubility and no tendency to aggregate or form complexes with biological macrostructures, and
7) A robustness of probe behavior with respect to external factors: no pK drift due to varying ionic strength, no inhibition from assay compounds or incompatibilities with the proteoliposome production, such as interactions

with detergents or hydrophobic beads.

8) Lastly, the ideal probe would report on the encapsulated liposome volume, for reliable conversion of pH to amount of protons.

To overcome the divergence of the probe properties from ideality, a reliable calibration procedure of the final probe/proteoliposome system *in situ* is desirable. For a method with the ambition of producing quantitative proton-transfer data, such calibration is vital.

Commercially available pH-probes

Several commercially available colorimetric pH and membrane potential indicators are presented in Table 1 of Paper II. Many of these probes, can permeate lipid membranes. Membrane-permeable pH-sensitive dyes, such as Neutral red (19), have been used to monitor intravesicular pH changes by using a weak buffering solution on the inside of the vesicle and a strong buffer in the bulk (20). Although Neutral red diffuses freely in and out of the vesicle, the difference in buffering strength ensures that any detected spectral changes result from a pH change inside the vesicles. However, a probe that diffuses through the membrane is likely to alter the membrane properties. Indeed, Neutral red has been reported to show significant protonophore activity, facilitating proton transfer across the membrane (21). A permeable probe may also accumulate on one side of the membrane as the pH changes. In addition, the difference in buffer strength required for these experiments obstructs quantification of proton movements. Phenol red (22) is less likely to diffuse across the membrane, but displays a relatively weak spectroscopic signal, making it less suitable for intravesicular pH determination. A combination of experiments using membrane-permeable Neutral red and membrane-impermeable Phenol red has resulted in estimated pumping stoichiometries of $2H^+/e^-$ for respiratory Complex I in submitochondrial particles (23, 24) and $3.6H^+/2e^-$ for Complex I reconstituted in liposomes (20). The semi-naphthofluorescein chromophore SNARF (25) also monitors pH and does not diffuse significantly through lipid bilayers. It was, however, shown to bind to the membrane surface of large and small unilamellar vesicles (LUVs and

SUVs), resulting in a sensor sub-population with characteristics different than those of the dissolved probe (25). The ratiometric fluorescence probe Pyranine (also known as HPTS) (26) is more suitable for monitoring intravesicular pH, and has been combined with the membrane-potential probe Oxonol for mechanistic studies of H^+-ATPase (27). However, the modest brightness of Pyranine fluorescence limits the sensitivity of these measurements.

A significant improvement was made with the introduction of SNARF-dextrans, which have been used in several proton-pumping studies (28, 29). The ligation of a dextran polymer to the SNARF core effectively eliminates probe diffusion through membranes. However, the SNARF group in these conjugates is not shielded and can still attach to membrane lipids. Furthermore, the molecular compositions of SNARF-dextrans are not uniquely defined, and although they permit ratiometric measurements, the spectral changes accompanying their protonation are not large.

In order to encapsulate the pH probe inside liposomes, the probe has to be present in the lipid suspension through-out the bead-mediated detergent removal. We therefore assessed the interaction of a number of pH probes with hydrophobic beads. Table 1 in Paper II shows that for most of the tested dyes a substantial fraction, 30–100%, was adsorbed to hydrophobic beads during a 90-minute incubation. By starting with a high probe concentration, a signal might still be engendered from the resulting liposomes. This would exclude internal volume determination by probe absorbance.

Novel porphyrin-based pH sensors

Porphyrins are a ubiquitous group of organic compounds, best known as the iron-containing red haeme in hemoglobin and the magnesium-containing chlorophyll in green plants. A metal-free porphyrin is called a free base. Porphyrins are heterocyclic macrocycles characterized by the presence of four modified pyrrole subunits interconnected at their α-carbon atoms via methane bridges. Porphyrins obey Hückel's rule for aromaticity in that they possess 4n+2 π-electrons that are delocalized over the macrocycle. The macrocycles are

therefore highly conjugated systems, and as a consequence, they have very high extinction coefficients in the visible region and are deeply colored.

Two imine nitrogens of a free-base porphyrin (H_2P) are protonatable, forming porphyrin monocations (H_3P^+) and dications (H_4P^{2+}). The dication H_4P^{2+} can be viewed as a Brønsted acid, characterized by two ionization constants K_1 and K_2 (see Scheme 1, Paper II). Porphyrin protonation is accompanied by distinct changes in the optical spectrum: Figure 2A in Paper II shows a significant red shift of the Soret bands upon double protonation. The protonation state of a porphyrin can thus be followed spectroscopically (see Fig. 2B, Paper II). For the majority of porphyrins, constants K_1 and K_2 are indistinguishably close, and the monocation H_3P^+ is an elusive species whose concentration is extremely low at all proton concentrations [38]. In the normal case these molecules also emit fluorescence with a high quantum yield.

The high extinction coefficients and high quantum yields in combination with the distinct spectral change correlated to pH makes these molecules interesting candidates for colorimetric pH-probes. However, other aspects of porphyrin chemistry render them less suitable. In order to protonate the free base, two protons have to be attached to the two imine nitrogens in the inner ring of the molecule. To fit two extra positive charges in this confined area is not favorable, and the pK of the porphyrin is normally quite low, well out of physiologically interesting areas. Furthermore, porphyrins are highly hydrophobic and virtually insoluble in aqueous buffers.

Fortunately, these characteristics can be modified by attaching different substituents to the porphyrin molecule.

Porphyrin core tuning

A porphyrin can be modified in different ways to raise its pK into a regime that is useful for biological measurements, i.e. making the protonation of the free base more favorable.

The pK of water-soluble porphyrin species (30), are dependent on the electronic effects of substituents, macrocycle planarity, (31-33) and the peripheral charges surrounding the protonation site (34-36). Any one of these factors, or all of them together, can be used to tune the porphyrin pK, bringing it into the desired range.

Adding substituents that influence the conjugated π-system of the core may change the pK of the porphyrin. By adding electron-donating groups, the core electron density is elevated and the positively charged dication will be stabilized, thus raising the pK. The opposite will happen if the π-system is extended, as the conjugated electrons will be spread over a larger area (37).

By adding substituents it is possible to distort the planarity of the core porphyrin into a saddle-shaped form, making the protonation sites more accessible. By extending the pyrrols with extra cyclohexane or benzene rings we get tetracyclohexanoporphyrins (TCHP) or tetrabenzoporphyrins (TBP) (37, 38). Both these molecules are clearly saddle-shaped with higher pK than the undistorted porphyrin. TCHP has a lower pK than TBP, which corroborates the statement above that an extension of the conjugated π-system, in this case by aromatic benzene rings compared to non-aromatic cyclohexane rings, lowers the pK of the free base. A common side effect of inflicted non-planarity is loss of fluorescence.

The pK of the porphyrin can also be tuned by surrounding the core with the peripheral charges of poly-glutamic dendrites. For such porphyrin dendrimers, the porphyrin protonation constants were shown to change with the size of the attached dendritic ligands (39), suggesting that the negative charges on the outer layer of dendrimers stabilize the porphyrin dications, possibly via through-space electrostatic shielding.

Probe Glu^3

The pH-sensitive, fluorescent nanoprobe Glu^3, shown in Figure 1 of Paper II, consists of a tetraarylporphyrin core with generation 3, poly-glutamic dendrites attached to the aryl groups. The dendrites have multiple carboxylate termini that ensure high water solubility and prevent diffusion across phospholipid membranes. The presence of 32 terminal negative charges stabilizes the dicationic species and brings the apparent pK of the dye up to a range useful for biological experiments. A concern about porphyrins with the protonated state stabilized by a charged cage is its sensitivity to ionic strength: The salt concentration of the buffer may affect the probe pK. In Paper II we address this by making pH-titrations of Glu^3 in buffers containing different concentrations of monovalent (K$^+$ and Na$^+$) and divalent ions (Mg^{2+}). For this purpose, we have developed the automated titration system Maxwell, described below.

The pK of Glu^3 was indeed found to vary with cation concentrations, with higher ionic strength lowering the pK (see Figure 4, Paper II). This effect is much more pronounced in the case of Mg^{2+}. The salt effect is reproducible and stable, and can thus be taken into account. It even provides a means by which to fine-tune the probe toward a desired pK. By selecting the appropriate ionic environment for Glu^3, it can be used with good resolution from pH 4.5 to pH 7.5. However, caution must be taken in experiments where intravesicular ion concentrations are expected to vary, such as when investigating K$^+$/H$^+$ antiporters. To avoid pK variations with varying ionic strength, a relatively high salt concentration can be used. At 100 mM K$^+$, Glu^3 pK variation with ion concentration is moderate (see Figure 4, Paper II), and small ion flows across the bilayer are negligible compared to the total salt concentration. Conversely, used at high buffer strength and low ionic strength, Glu^3 may be indicative of other ion flows.
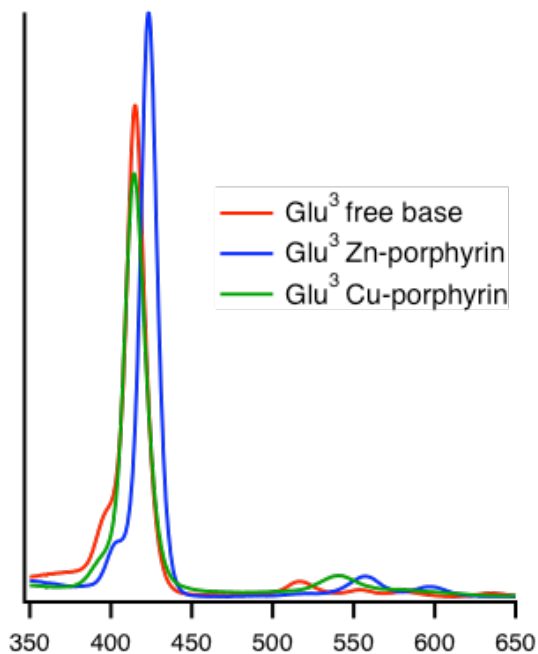
Figure 4. Spectra of Glu³ as a free base, as a zinc-porphyrin and as a cupper-porphyrin.

During these titrations it was found that the free-base porphyrin dyes are very sensitive to exposure to Zn^{2+} and Cu^{2+}, which are spontaneously and irreversibly incorporated into the porphyrin core. Even nanomolar concentrations of these metal ions will inhibit the probe, resulting in zinc- and cupper-porphyrin spectra (see Figure 4). This problem is avoided by ensuring that alloys in syringes and other lab equipment are Zn-free, and including EDTA in all buffers used in porphyrin-probe experiments. Fortunately, common divalent cations such as Ca^{2+} or Mg^{2+} do not form stable complexes with porphyrins in aqueous solution and do not affect the measurements.

Glu³ was also tested for compatibility with different detergents and the hydrophobic beads used for detergent removal. The probe showed excellent compatibility with the beads, as more than 99% of the dye was still in solution after incubation for one hour. This was far better than for any of the tested commercially available probes (see Table 1, Paper II).

In conclusion, Glu³ comes quite close to the ideal probe called for above. In Papers IV and V, its usefulness is demonstrated in a revealing investigation of the A/M2 proton channel. There is still some room for improvement: it has a slightly low pK for some applications, and is moderately sensitive to ionic strength. These issues are addressed in the development of the probe TCHpH, described below and in Paper III.

Probe TCHpH

The pH-sensitive nanoprobe TCHpH, shown in Scheme 1 of Paper III, is based on a highly non-planar tetraaryltetracyclohexenoporphyrin core modified with eight Newkome-type dendrons and then peripherally PEGylated, rendering a neutral, water-soluble probe. The non-planar core eliminates the need for electrostatic shielding to move the pK of the probe into a physiologically interesting range (31-33). The advantage of avoiding electrostatic shielding by terminal charges as for Glu[3] is that the pK of the probe should be much less sensitive to variations in ionic strength of the buffer. This is verified in Paper III. Unlike most tetraarylporphyrins, TCHpH exhibits two distinct protonation steps (pK_a 7.8 and 6.3). These unexpected separable protonation steps result in a much broader pH-range than offered by a single-protonation probe (such as Glu[3]), making TCHpH a very dynamic pH sensor with a practical measurement range of at least pH 5–9.

TCHpH was included into LUVs without any detectable effects on the spectral properties. Passive permeability of TCHpH-containing liposomes to protons was estimated and found to be in agreement with corresponding values for Glu[3]-containing liposomes. The probe was also tested for compatibility with hydrophobic beads. After 90 min incubation with beads, 89% of the probe was still in solution. This is not as good as for Glu[3], which was dissolved to >99%, but still better than for the least adsorbing of the commercially available pH dyes, SNARF-dextran, for which 72% remains in solution (see Table 1, Paper II). Only preliminary protein experiments has so far been conducted with TCHpH but they look very promising and my guess is that this probe will become a future working horse of this lab.

Automatic titrations by Maxwell

Performing pH-titrations in small volumes is a tedious and error-prone venture. To enhance precision and quality (and to unburden the laborant), an instrument was constructed for this purpose. The instrument, called Maxwell (see Figure 5), combines a UV-vis spectroscopic line with temperature control,

magnetic stirring, bulk pH measurement with a micro-combination electrode and computer-controlled injection of titrants. Maxwell is controlled by software written in LabView, including a user-friendly interface. The desired pH range and resolution are specified, after which the instrument administers calculated additions of acid or base until the electrode
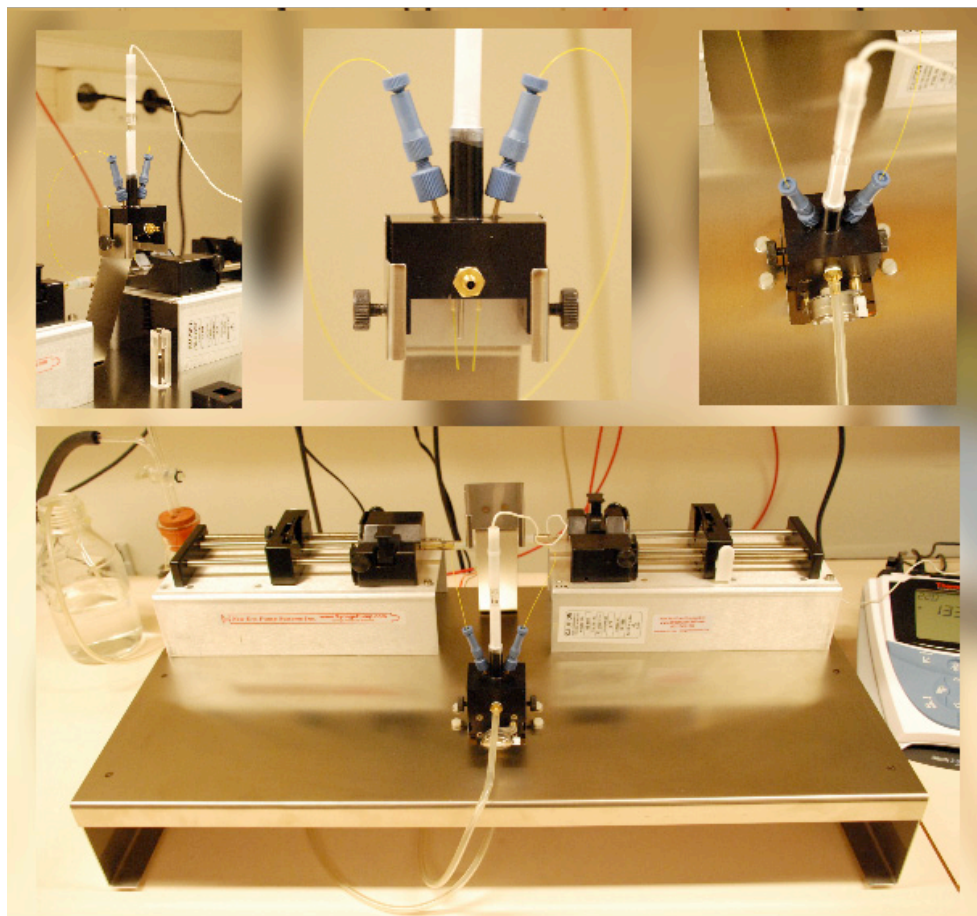
Figure 5. Maxwell, an automatic titration system. Very useful indeed.

feedback confirms that the setpoint has been reached. At each setpoint value, spectra are collected, a new setpoint is calculated, and the procedure is repeated through the entire titration range. In this way a full titration of

approximately 20 pH points can be performed autonomously and without human assistance in less than half an hour.

The Maxwell software was further enhanced for monitoring the development of intravesicular pH: The Glu^3 absorbance spectra are converted in real-time to R_{fb} (see Paper IV) and plotted vs time, enabling real-time experimental assessment.

Maxwell produces precise data with minimal error and at minimal cost in time and material. For robust analysis of the sometimes vast amounts of data procured, a set of procedures have been developed in Igor (Wavemetrics).

3. (Lipids + Detergent) – Detergent = Liposomes

In Paper IV we take on the challenges of predictable liposome assembly and membrane-protein reconstitution into proteoliposomes. The method we describe and assess is based on pioneering work done in Jean Louis Rigaud's lab, starting more than twenty years ago (17). The method makes use of the fact that detergent-solubilized phospholipids form lipid aggregates when the solubilizing detergent is removed below its critical micelle concentration (CMC). Before Rigaud's work, detergent removal was mostly done by dilution, often in the form of dialysis. Complete detergent removal is impossible with any dilution method, and thus these methods exclude detergents with low CMC. Residual detergent in the bilayer also promotes passive permeability of ions. Rigaud introduced hydrophobic polystyrene beads, which adsorb detergent molecules. Using bead-assisted detergent removal, a wide selection of detergents can be used, the rate of detergent removal can be controlled, and virtually complete detergent removal is achieved (17).

Lipids and preformed vesicles

One thing I have learned over the years is that the origin and purity of the lipids used in liposome production are crucial to the outcome. In Paper II we used phosphatidyl choline from egg yolk, of high purity but inherently poorly defined. When deposited as film on the walls of a glass vial and sonicated with aqueous buffer, this starting material gave SUVs with a diameter of 20-50 nm (in accordance with previous reports (39)). Such small vesicles are not optimal as starting material for LUV production, and therefore a step of liposome

formation by reversed-phase evaporation is often added to the procedure [(40), Paper II].
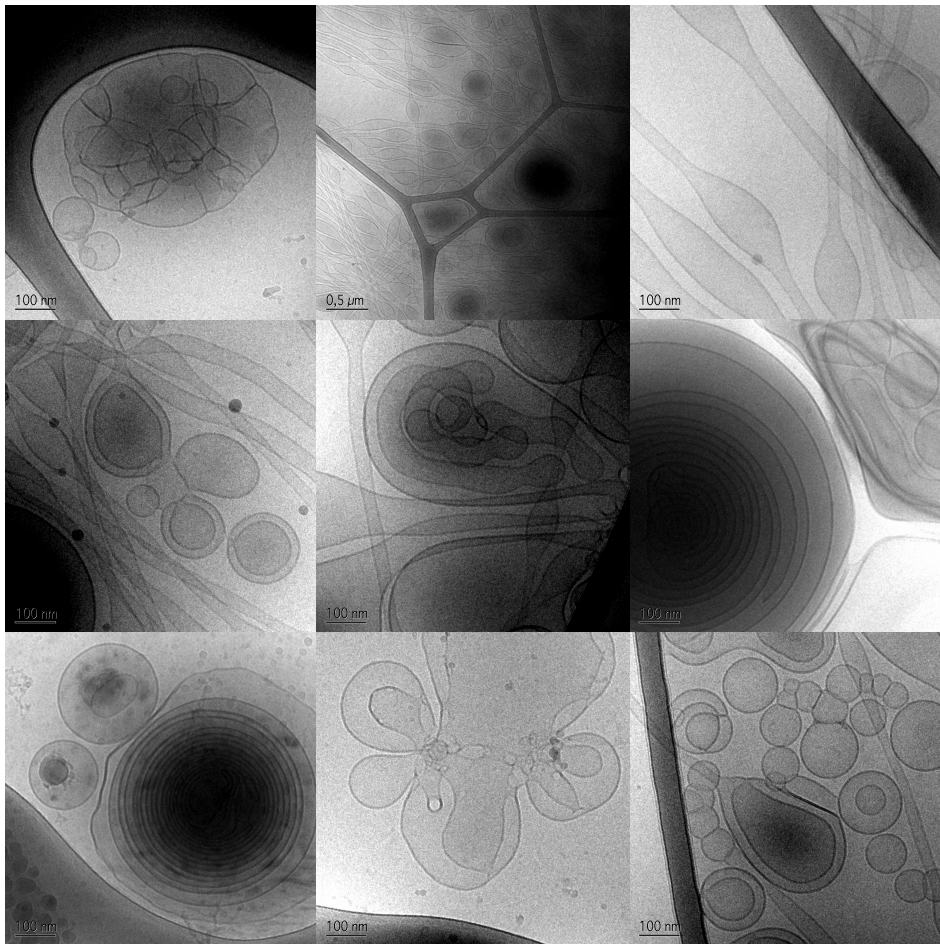
Figure 6. A collection of beautiful but failed vesicle experiments.

Starting instead with well-defined synthetic phospholipids, carefully protected from oxidation, sonication produces larger, multilamellar vesicles. Extrusion through a 200-nm polycarbonate filter results in mono- and bi-lamellar vesicles with diameters ranging from 30 to 200 nm, as depicted in Figure 1A, Paper IV. Such vesicles are quickly equilibrated with detergent and can be solubilized in a predictable and reproducible manner. These properties make it possible to attain standard detergent-to-lipid ratios that correspond to specific

aggregation states of the lipid-detergent complexes and to determine well-defined equilibration times. This also eliminates the need for reversed-phase evaporation, which in turn saves time and minimizes exposure to organic solvents. The effect of residual organic solvent in the lipid mixture can be enjoyed in Figure 6.

Making preformed vesicles from synthetic phospholipids is easy, and it provides a starting material that makes the whole liposome-production process predictable, facilitating the systematic optimization of protein-reconstitution parameters.

Detergents and solubilization

As seen in the solubilization of mitochondrial membranes presented in Paper I, different detergents give different results for membrane-protein solubilization. Not only do different detergents solubilize different amounts of total membrane protein, but also different protein species. This is likely related to the local membrane constitution around specific proteins. When reconstituting into proteoliposomes it is an advantage to be able to use the same detergent as was used in the purification process. This makes it easier to predict PFV solubilization levels compared to with a mixed detergent system. In contrast to methods using dialysis for detergent removal, the beads method is more liberal to choice of detergent as it also works with low-CMC detergents (40).

In Paper IV (Figure 2) we investigate the solubilizing properties of four different detergents on pre-formed phospholipid vesicles. Turbidity is plotted versus detergent. Detergent is given as the detergent-to-lipid ratio R (mol/mol). Only the detergent free to take part in lipid-detergent aggregation is considered, and this amount is calculated by $D_{tot} = D_{aq} + D_{agg}$ where D_{aq} is detergent in the buffer (estimated by the CMC for the detergent) and D_{agg} is the detergent available to take part in detergent-lipid aggregates. For example, if R=2 there are two detergent molecules taking part in aggregation for every lipid molecule present. From each solubilization curve two values for R are extracted, R_{sat} and R_{sol}, giving the detergent-to-lipid ratios for detergent-

saturated liposomes and fully solubilized vesicles in the form of detergent-lipid mixed micelles, respectively. With knowledge of the solubilization behavior of a lipid/detergent mixture, an informed choice can be made as to the degree of PFV solubilization used in subsequent reconstitution experiments. The degree of solubilization chosen for a specific protein reconstitution has been shown to influence the direction of insertion and the activity of the reconstituted protein (41). Prior to the solubilization study, we established the equilibration times for each detergent-lipid combination used. We found that equilibration times differ drastically between detergents, from five minutes for OG up to 180 minutes for DM and DDM.

Liposome formation and morphology

When creating liopsomes by detergent removal, two main variables (apart from temperature) can influence liposome morphology. First, there is lipid composition. The geometry of the participating lipids determines the curvature and thickness of the bilayer and thereby the size of the liposomes. Second is the rate of detergent removal. More precisely, the time passed between R_{sol} and R_{sat} is significant because this is where the initial lioposome formation occurs. The detergent-removal rate is governed by the choice of detergent, by the amount of beads added, and by the timing of bead additions. By administering many small bead additions rather than a few large ones, we reduce the risk of sudden or local rate changes in the sensitive region.
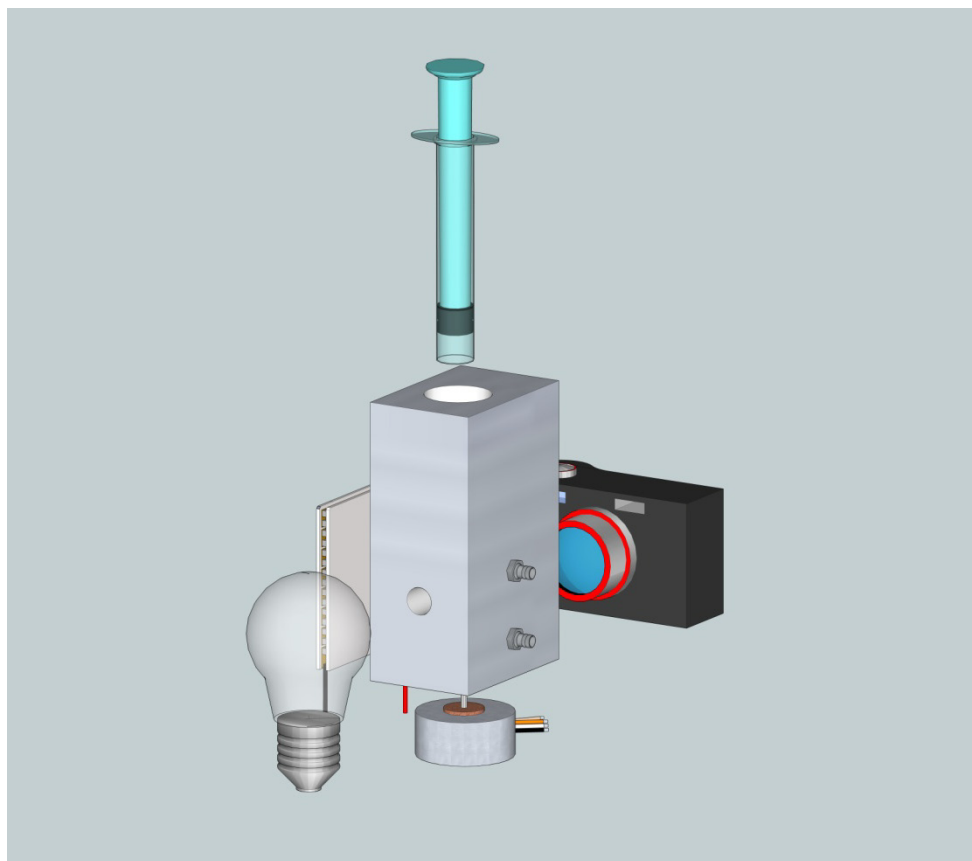
Figure 7. Schematic figure of Lips Inc consisting of sample holder, spectroscopic line, stirring, temperature control and automatic bead dispenser.

To investigate the influence of detergent-removal rate on liposome size and size dispersion, a second instrument was constructed and built (see Figure 7). The instrument takes 8 or 16 ml vials in its sample holder and features temperature control, stirring, a CCD-detected spectroscopic line and computer-controlled administration of hydrophobic beads. It was named "Lips Inc" for its ability to incorporate lipids (and to celebrate the group with the same name for their 1980 super hit "Funky Town"). With this instrument the turbidity of the sample could be continuously monitored and plotted as a function of time (see Figure 2, Paper IV). As with the first instrument, "Lips Inc" runs autonomously after the parameters are set and the start-button has been pressed.

For a typical run (Figure 2, Paper IV), PFV were completely solubilised to mixed micelles before the first addition of beads. After an initial lag period when excess detergent is adsorbed to the beads, aggregates start to form, as seen by a sharp increase in turbidity. The turbidity increases until it reaches a maximum and the vesicles reach their largest form as detergent-saturated vesicles. After the maximum, turbidity slowly decreases while detergent is drawn out of the vesicles. This is a slow process that is limited by three detergent-concentration equilibria: between bulk detergent and detergent in the outer leaflet, between the outer and inner leaflets and between the inner leaflet and the encapsulated buffer. After the plateau is reached it can take up to two hours for the residual detergent to be absorbed by the beads and the turbidity level to stabilize.

From these experiments we conclude that slower detergent removal gives larger vesicles (17), probably because larger bilayer aggregates have time to form before they wrap and close to form spherical liposomes. An influence of detergent removal rate on size distribution could not be seen.

Passive ion permeation through bilayers

When trying to quantify proton translocation through membrane-bound proteins, it is important to know if there is passive permeability to protons and other ions through the lipid bilayer itself. To assess this, the internal acidification of LUV in the absence of protein was monitored after an external acidification(see Figure 4, PaperIV). Following the acid pulse protons start to equilibrate over the membrane, but electrostatic forces almost instantly retard the influx. To make it possible for further protons to move in to the vesicles another cation, in this case potassium, has to move out. By the presence of either the K^+-selective ionophore valinomycin or the protonophore CCCP, the rate-limiting process was set to be either H^+ or K^+ diffusion. The permeability of H^+ and K^+ was tested for five different membrane compositions. No significant difference in proton or K^+ flux was seen between compositions. Passive proton flux was estimated to 17 s^{-1} μm^2. For potassium ions the

recorded flux was approximately the double. The addition of cholesterol did not show any significant effect on the passive permeability of the membrane.

4. The Influenza A/M2 Protein

The three types of influenza viruses (A, B and C) belong to the orthomyxoviridae family. Influenza A (42) viruses can infect multiple hosts, including humans, swine, ferrets and birds, while influenza B (43) infects humans only, and influenza C (44) viruses infect humans and swine (45). The most serious human symptoms are caused by influenza A and, to a somewhat lesser extent, influenza B strains (46, 47). Influenza C is believed to cause mild infection more similar to a common cold (48).

Influenza viral particles are enclosed in a lipid-membrane envelope, and contain a genome made up of 7-8 single-strand RNA segments, each segment encoding for particular proteins used by the virus.

The influenza virus lipid envelope contains three types of membrane proteins: hemagglutinin, neuraminidase, and the much less abundant M2 protein (49). Hemagglutinin and neuraminidase are key antigenic determinants of the virus, and their variants are reflected in the nomenclature of influenza virus subtypes, e.g. H1N1 or H3N2.

In a typical type A infection cycle, reviewed in (50), hemagglutinin on the viral particle binds to sialic-acid residues on the target epithelial-cell surface. The viral particle is incorporated in a cell endosome, where the extraviral pH is lowered. The M2 protein transports protons from the endosomal lumen into the viral interior, dissociating the viral RNA genome from the matrix. This acidification causes the influenza hemagglutinin to undergo a dramatic conformational change, triggering fusion of the viral envelope with the target-cell endosomal membrane. The viral RNA is thus released into the target cell and subsequently replicated in the target cell nucleus. newly synthesized viral proteins enter the Golgi-apparatus membrane for assembly and export to the

plasma membrane, from which new viral particles will form. For some strains, M2 plays its second role in this phase of the infection cycle, allowing proton efflux from the slightly acidic Golgi lumen to prevent premature hemagglutinin pH-triggering (51, 52). Finally, after new viral particles have assembled and budded off from the cell surface, neuraminidase facilitates detachment of the virion from the cell membrane, and a new infection can take place.

The influenza A/M2 protein is a 97-residue, tetrameric integral membrane protein containing a short N-terminal extracellular domain, a transmembrane (TM) helix, and a 54-residue cytoplasmic tail (53, 54). Four M2 TM domains associate into a highly selective proton channel (55, 56), which mediates viral infection as described above (57, 58). Given its very small size and modular structure, M2 has captured the attention of scientists as a pharmacologically relevant model system for understanding proton translocation and gating. The TM segment of the M2 peptideis both necessary and sufficient to reproduce its proton-translocating and drug-binding activity (59).

M2 has a single ionizable group in its TM domain, His37, which acts as both a pH sensor (60, 61) and determinant of its proton selectivity; variants in which His37 is mutated to other polar residues loose their selectivity for protons (62). Trp41 acts in concert with His37 as a "gate", helping to define the rate of proton flux, and to kinetically trap protons within an acidified virus (63-65). Recent studies have shown that Val27 at the entrance of the pore may act as a secondary gate of the A/M2 channel (64-66).

M2 is the target of the adamantane-containing anti-influenza drugs as well as related hydrophobic-amine containing structures (6, 55, 56, 67-69). Unfortunately the use of amantadine-related drugs is limited by side effects on the central nervous system and the rapid emergence of drug-resistant viruses (70-72).

The conductance of the M2 channel has been most thoroughly studied by measuring macroscopic whole-cell current in oocytes and mammalian cells. A

long-standing question has been how M2 can conduct a substantial number of protons into the very small interior volume of the virus without creating a substantial electrical gradient. Diffusion of a few protons down their concentration gradient from the acidic environment of the endosome would result in an electrical gradient that would abruptly halt further proton flow, preventing acidification of the viral interior.

Reconstitution of A/M2 into liposomes

In Paper V we use the reconstitution method to insert the full-length M2 protein into large unilamellar vesicles, with the N terminus out as in its native membrane. We examine a range of protein-to-lipid ratios to find the most feasible compromise between assay sensitivity and time resolution. For accurate determination of specific activity, reliable protein quantification is necessary. This is technically challenging in membrane preparations with low protein and high lipid concentrations, such as proteoliposomes, and it is common practice to assume that all added protein has been successfully incorporated into the liposomes. However, we were able to modify a commercially available protein-determination method for use with lipid concentrations up to 25 mg/ml and protein concentrations down to 10 µg/ml. We found that >95% of the added M2 protein was present in the liposome membrane.

Determination of A/M2 orientation

The orientation of reconstituted M2 was assessed for a previous reconstitution protocol, reporting random, symmetrical orientation (73). Up until now there have been no reports of unidirectional insertion of M2 into liposomes. In Paper IV we conduct a full MS-MS investigation of the directionality of protein insertion by proteoliposome trypsination, comparing a previously used reconstitution method (73) with ours. We find that with the method presented in this thesis, we get a fully asymmetrical orientation with the N-terminus out as in its native membrane, while the old method, as expected, gives a random orientation of the protein.

The unidirectionally oriented M2 liposomes allow facile measurements of the asymmetric aspects of conduction.

The influence of cholesterol

In Paper IV (Figure 6B) we also investigate the effect of different amounts of cholesterol on the proton flux of M2. As cholesterol had no effect on passive permeation through protein-free liposomes, any effect we see is related to the presence of M2. What we find is that with the phospholipids we use (POPC and POPG), cholesterol is crucial for M2-mediated proton flux. The more cholesterol, the more active the M2 proteoliposomes are - up to the level where the membrane is saturated and cholesterol starts to precipitate out of solution. If cholesterol served to seal the protein-lipid interface against non-specific ion leakage, the low-cholesterol liposomes would leak and rapidly preempt the driving potassium gradient, causing a rapid stop to proton tranfer. Rather, we see slow but persistent M2 activity, with gradual liposomal acidification progressing even after 25 minutes. This behavior reminds more of an inhibited channel, and belies a fast depletion of the K^+ membrane potential. It appears that under these conditions, cholesterol has a more specifically activating effect on M2. A possible explanation is the effect cholesterol has on bilayer thickness (74), affecting the relative tilt angle of the TM helices and thus M2 activity (75). A way to investigate this possibility would be to use phospholipids with longer acyl chains (e.g. SOPC/SOPG or SAPC/SAPG) and see if the greater thickness in this case makes cholesterol redundant. Cholesterol is present in influenza viral membranes, and has been shown to be necessary for effective fusion of the viral membrane to the endosomal membrane (76). There are several potential contributing factors to this phenomenon – and inhibition of M2-mediated acidification could be one of them. The cholesterol effect is intriguing and worth looking further into.

Inhibition

In Paper V we subject the M2 proteoliposomes to amantadine inhibition. Amantadine inhibition is a signature property of A/M2 and is often used to

verify M2 experimental procedures. We see almost full amantadine inhibition of M2-mediated proton flux, with IC_{50} to 1.3 μM, in good agreement with the literature (67, 73). To demonstrate the suitability of the reconstitution method/ proton-flux assay for M2 inhibitor assessment, we performed an initial inhibitor screen with known (69) Spiro-Piperidine-based inhibitors in Paper IV.

ΔpH-driven flux

The physiological role of M2 is to transfer protons from the acidifying endosome into the viral interior, whose primary cationic electrolyte is K^+. In Paper V we therefore examine the proton flux through M2 upon acidification of the liposome exterior. These experiments were performed in the presence of K^+ and valinomycin, in order to allow unhampered proton movement through M2. In- and outside were isotonic and the buffering capacity inside the vesicles was significantly smaller than $[K^+]_{in}$ to keep the change in the chemical potential of K^+ as small as possible (77). As observed in electrophysiological investigations, the rate of proton flux increased with decreasing pH_{out} (Figure 2A, Paper V). The experiments were repeated without valinomycin to see if M2 might allow K^+ efflux. As expected from the work of Busath et al (78), the proton-transfer rates were slower, but approximately 1/3 of the flux with valinomycin was left. This suggests that inward flux of protons is balanced by outward flux of K^+ through the M2 channel. We repeated the experiment in symmetrical $[Na^+]$ (again without valinomycin)and saw similar results but with approximateky ½ of the rates achieved with K^+ and valinomycin. This shows that Na+ exits the liposome faster than K^+. Importantly, this difference in K^+ and Na^+ flux establishes that cation efflux is not mediated through the membrane, as Na^+ has much lower bilayer permeability than K^+. Rather, this indicates K^+ and Na^+ flux through M2.

Electrically induced proton flux

In Paper IV and V (Figure 6 and 4, respectively) we also performed experiments in which a transmembrane electrical potential was generated by

rapidly diluting vesicles prepared in K^+ buffer into Na^+ buffer containing valinomycin. Valinomycin is very selective for K^+ relative to Na^+, and facilitates rapid diffusion of K^+ out of the vesicle. This generates an electrical potential which leads to inward proton flux. This kind of experiment only gives an acidification of the liposome interior if the reconstituted protein has a very high selectivity for protons over Na^+ and K^+ and if the vesicles are tight. In theory the internal acidification would continue until a Donnan equilibrium has been reached, and the driving force of the K^+ gradient matches the force of the induced proton gradient. The internal pH would then remain constant. For a ten-fold difference in K^+ concentrations the induced electrical gradient is 60 mV, and the Donnan equilibrium should be reached when $\Delta pH = 1$. What we see is a development of pH over time with two distinct phases of opposite sign (Figure 3, Paper V). The first phase is a rapid acidification of the liposomes as protons are driven into the vesicles through M2 by the electric force created by K^+ flowing out through valinomycin. The proton influx of the first phase gradually slows down and reaches an apparent equilibrium where the net proton flux is zero. At this point there is a balance between the induced pH gradient and the electric gradient formed by the remaining difference in potassium concentrations. Since we know the pH, it is now possible to calculate the remaining $[K^+]$ in the vesicles.

The initial proton flux rates decrease with decreasing pH, from 47 protons per tetramer and second at pH 7.0 to 7 protons per tetramer and second at pH 5.5. This is also the case for the ΔpH present at the Donnan equilibrium, where ΔpH decreases from 0.8 to 0.45 when the symmetrical starting pH is lowered from 7.0 to 5.5. By analyzing the ion concentrations at the Donnan equilibrium, we found that as pH_{in} was lowered, the rate of proton flux decreased but the rate of outward cation flux increased. This indicates that the relative influx of other cations than protons (namely Na^+) is increasing. I.e. the selectivity for protons over Na^+ and K^+ decreases with pH.

Following the apparent equilibrium each time-course also shows a second phase, which occurs at a much slower time scale and results in a gradual relaxation of the pH gradient induced during the first phase. We interpret this

slow decrease in pH_{in} as a loss in the electrical potential due to slow M2-dependent equilibration of the sodium and potassium ion concentrations across the bilayer(77) along the lines discussed above.

To examine the symmetry of this behavior, these experiments were repeated in the reverse direction: High $[K^+]$ in the bulk, low $[K^+]$ in the vesicles and valinomycin present creatse a positive-inside electrical potential, resulting in an efflux of protons. The result of these experiments are basically reciprocal to the first set of data (see Figure 3B, Paper V), in accordance with Chizhmakovs findings that voltage has no or little effect on the conducting pK_a (79).

Antiporter properties of A/M2

The biological function of the M2 protein is to pass protons down a pH gradient towards the interior of the virus. What has been less clear from electrophysiological studies is how protons can accumulate within a virus without developing a large electrical gradient when no other ion channels are present (49). Could M2 actually be an antiporter? Well, let's examine our data so far. We make the assumption that the anions present, in this case sulphate and phosphate, do not move across the membrane. For electroneutrality, the sum of cations in the vesicles must therefore remain constant. When subjected to a pH-gradient at symmetrical $[K^+]$ of 130 mM, pH can equilibrate through M2 even without valinomycin present (Paper V, Figure 1). Even if the rate of proton flux is a factor three lower than with valinomycin, it is still substantial. When K^+ was exchanged for Na^+, known to diffuse slower than K^+ across lipid bilayers, the rate goes up by 50%. This shows that (a) counterions do move across the M2 bilayer, and (b), they do not diffuse passively. In other words, as protons enter the liposome through M2, K^+ (or Na^+) moves through M2 in the opposite direction. So by definition, M2 is an antiporter.

Given that M2 serves as an antiporter, it is intriguing to ask whether it acts through a classical transporter mechanism. Proton-dependent transporters couple the diffusion of protons down a pH gradient to the transport of a second molecule or ion, or vice versa. M2 resembles cotransporters in many

ways as we discuss in Paper V, and we conclude that there are many arguments corroborating this proposal. However, the definitive assignment of M2 as a cotransporter must await additional experiments.

5. What's next?

It is still unclear if M2 works as a classic coupled cotransporter or if it functions in a different way. We got very far with our work on this protein in a relatively short period of time, and it would be satisfying to elucidate it further.

It would also be a natural step to apply our gained knowledge of reconstitutions and ion-current assessment to a new target. One fascinating group of targets is the antiporter-like subunits NuoL, NuoM and NuoN from the mitochondrial Complex I, described in Paper VI. These subunits are homologous to the MrpA and MrpD antiporters of *B. subtilis*, and we therefore suspect them of having antiporter activity within the Complex I ensemble. The Complex I subunits and the antiporters have been genetically fused to cytochrome c and equipped with a his-tag in this lab, facilitating overexpression and purification of each separate subunit. The next step would be to find the right reconstitution conditions for them and investigate them with the ion-assessment assays we established with M2.

Acknowledgement

References

1.   Hooke, R. 1665. Micrographia: or some physiological descriptions of minute bodies made by magnifying glasses with observations and inquiries thereupon. The Royal Society, London.

2.   Schwann. 1839. Microscopical researches into the accordance in the structure and growth of animals and plants.

3.   Singer, S. J., and G. L. Nicolson. 1972. FLUID MOSAIC MODEL OF STRUCTURE OF CELL-MEMBRANES. Science 175:720-&.

4.   Izumi, H., T. Torigoe, H. Ishiguchi, H. Uramoto, Y. Yoshida, M. Tanabe, T. Ise, T. Murakami, T. Yoshida, M. Nomoto, and K. Kohno. 2003. Cellular pH regulators: potentially promising molecular targets for cancer chemotherapy. Cancer Treatment Reviews 29:541-549.

5.   Stock, C., and A. Schwab. 2006. How ion channels and transporters affect metastasis. Physiology News Spring 2006:19-20.

6.   Davies, W. L., R. R. Grunert, R. F. Haff, J. W. McGahen, E. M. Neumayer, M. Paulshock, J. C. Watts, T. R. Wood, E. C. Herman, and C. E. Hoffman. 1964. Antiviral activity of 1-adamantanamine (amantadine). Science 144:862-863.

7.   Marcus, R. A. 1964. CHEMICAL + ELECTROCHEMICAL ELECTRON-TRANSFER THEORY. Annual Review of Physical Chemistry 15:155-&.

8.   Marcus, R. J., B. J. Zwolinski, and H. Eyring. 1954. THE ELECTRON TUNNELLING HYPOTHESIS FOR ELECTRON EXCHANGE REACTIONS. Journal of Physical Chemistry 58:432-437.

9.   Dani, J. A., and D. G. Levitt. 1981. BINDING CONSTANTS OF LI+, K+, AND TL+ IN THE GRAMICIDIN CHANNEL DETERMINED FROM WATER PERMEABILITY MEASUREMENTS. Biophys J 35:485-499.

10.   Dani, J. A., and D. G. Levitt. 1981. WATER TRANSPORT AND ION-WATER INTERACTION IN THE GRAMICIDIN CHANNEL. Biophys J 35:501-508.

11.   Levitt, D. G., S. R. Elias, and J. M. Hautman. 1978. NUMBER OF WATER-MOLECULES (N) COUPLED TO TRANSPORT OF K+ AND NA+ VIA NONACTIN AND GRAMICIDIN. Biophys J 21:A72-A72.

12. Rosenberg, P. A., and A. Finkelstein. 1978. INTERACTION OF IONS AND WATER IN GRAMICIDIN-A CHANNELS - STREAMING POTENTIALS ACROSS LIPID BILAYER MEMBRANES. Journal of General Physiology 72:327-340.

13. Rosenberg, P. A., and A. Finkelstein. 1978. WATER PERMEABILITY OF GRAMICIDIN-A-TREATED LIPID BILAYER MEMBRANES. Journal of General Physiology 72:341-350.

14. Burykin, A., and A. Warshel. 2003. What really prevents proton transport through aquaporin? Charge self-energy versus proton wire proposals. Biophys J 85:3696-3706.

15. Chakrabarti, N., B. Roux, and R. Pomes. 2004. Structural determinants of proton blockage in aquaporins. Journal of Molecular Biology 343:493-510.

16. Ilan, B., E. Tajkhorshid, K. Schulten, and G. A. Voth. 2004. The mechanism of proton exclusion in aquaporin channels. Proteins-Structure Function and Bioinformatics 55:223-228.

17. Levy, D., A. Bluzat, M. Seigneuret, and J. L. Rigaud. 1990. A SYSTEMATIC STUDY OF LIPOSOME AND PROTEOLIPOSOME RECONSTITUTION INVOLVING BIO-BEAD-MEDIATED TRITON-X-100 REMOVAL. Biochimica et Biophysica Acta 1025:179-190.

18. Borisov, S. M., and I. Klimant. 2008. Optical nanosensors - smart tools in bioanalytics. Analyst 133:1302-1307.

19. Auslander, W., and W. Junge. 1975. Neutral Red, a Rapid Indicator for Ph-Changes in Inner Phase of Thylakoids. Febs Letters 59:310-315.

20. Galkin, A., S. Drose, and U. Brandt. 2006. The proton pumping stoichiometry of purified mitochondrial complex I reconstituted into proteoliposomes. Biochimica Et Biophysica Acta-Bioenergetics 1757:1575-1581.

21. Manente, S., S. De Pieri, A. Lero, C. Rigo, and M. Bragadin. 2008. A comparison between the responses of neutral red and acridine orange: Acridine orange should be preferential and alternative to neutral red as a dye for the monitoring of contaminants by means of biological sensors. Analytical Biochemistry 383:316-319.

22. Lancz, G. J., and T. M. Chavez. 1977. Spectrophotometric Method for Monitoring the pH of Tissue Culture Medium. TCA (Tissue Culture Association) Manual 3:667-670.

23. Galkin, A. S., V. G. Grivennikova, and A. D. Vinogradov. 1999. -> H+/2(e)over-bar stoichiometry in NADH-quinone reductase reactions catalyzed by bovine heart submitochondrial particles. Febs Letters 451:157-161.

24.   Wikstrom, M. 1984. 2 Protons Are Pumped from the Mitochondrial Matrix Per Electron Transferred between Nadh and Ubiquinone. Febs Letters 169:300-304.

25.   Vecer, J., A. Holoubek, and K. Sigler. 2001. Fluorescence behavior of the pH-sensitive probe carboxy SNARF-1 in suspension of liposomes. Photochemistry and Photobiology 74:8-13.

26.   Giuliano, K. A., and R. J. Gillies. 1987. DETERMINATION OF INTRACELLULAR PH OF BALB/C-3T3 CELLS USING THE FLUORESCENCE OF PYRANINE. Analytical Biochemistry 167:362-371.

27.   Holoubek, A., J. Vecer, and K. Sigler. 2007. Monitoring of the proton electrochemical gradient in reconstituted vesicles: Quantitative measurements of both transmembrane potential and intravesicular pH by ratiometric fluorescent probes. Journal of Fluorescence 17:201-213.

28.   Slayman, C. L., V. V. Moussatos, and W. W. Webb. 1994. ENDOSOMAL ACCUMULATION OF PH INDICATOR DYES DELIVERED AS ACETOXYMETHYL ESTERS. Journal of Experimental Biology 196:419-438.

29.   Thiebaut, F., S. J. Currier, J. Whitaker, R. P. Haugland, M. M. Gottesman, I. Pastan, and M. C. Willingham. 1990. ACTIVITY OF THE MULTIDRUG TRANSPORTER RESULTS IN ALKALINIZATION OF THE CYTOSOL - MEASUREMENT OF CYTOSOLIC PH BY MICROINJECTION OF A PH-SENSITIVE DYE. Journal of Histochemistry & Cytochemistry 38:685-690.

30.   Hambright. 2000. Chemistry of water soluble porphyrins. In The Porphyrin Handbook. S. Kadish, Guilard, editor. Academic Press, New York.

31.   Barkigia, K. M., M. D. Berber, J. Fajer, C. J. Medforth, M. W. Renner, and K. M. Smith. 1990. NONPLANAR PORPHYRINS - X-RAY STRUCTURES OF (2,3,7,8,12,13,17,18-OCTAETHYL-5,10,15,20-TETRAPHENYLPOPHINATO)ZINC(II) AND (2,3,7,8,12,13,17,18-OCTAMETHYL-5,10,15,20-TETRAPHENYLPORPHINATO)ZINC(II). Journal of the American Chemical Society 112:8851-8857.

32.   Craig. 1990. The synthesis and solution conformation of dodecaphenylporphyrin. Tetrahedron Letters 31:5583-5586.

33.   Takeda, J., T. Ohya, and M. Sato. 1992. A FERROCHELATASE TRANSITION-STATE MODEL - RAPID INCORPORATION OF COPPER(II) INTO NONPLANAR DODECAPHENYLPORPHYRIN. Inorganic Chemistry 31:2877-2880.

34.   Kohata, K., H. Higashio, Y. Yamaguchi, M. Koketsu, and T. Odashima. 1994. SYNTHESIS AND CHARACTERIZATION OF NEW STYLE OF WATER-SOLUBLE GLYCOSYLATED PORPHYRINS AS A

SPECTROPHOTOMETRIC REAGENT FOR METAL-IONS. Bulletin of the Chemical Society of Japan 67:668-679.

35. Valiotti, A., A. Adeyemo, R. F. X. Williams, L. Ricks, J. North, and P. Hambright. 1981. A WATER-SOLUBLE PICKET FENCE PORPHYRIN AND ITS ISOMERS. Journal of Inorganic & Nuclear Chemistry 43:2653-2658.

36. Vinogradov, S. A., and D. F. Wilson. 2000. Electrostatic core shielding in dendritic polyglutamic porphyrins. Chemistry-a European Journal 6:2456-2461.

37. Finikova, O. S., A. V. Cheprakov, P. J. Carroll, S. Dalosto, and S. A. Vinogradov. 2002. Influence of nonplanarity and extended conjugation on porphyrin basicity. Inorg Chem 41:6944-6946.

38. Finikova, O. S., A. V. Cheprakov, I. P. Beletskaya, P. J. Carroll, and S. A. Vinogradov. 2004. Novel versatile synthesis of substituted tetrabenzoporphyrins. J Org Chem 69:522-535.

39. Finikova, O., A. Galkin, V. Rozhkov, M. Cordero, C. Hagerhall, and S. Vinogradov. 2003. Porphyrin and tetrabenzoporphyrin dendrimers: tunable membrane-impermeable fluorescent pH nanosensors. J Am Chem Soc 125:4882-4893.

40. Rigaud, J. L., and D. Levy. 2003. Reconstitution of membrane proteins into liposomes. Methods Enzymol 372:65-86.

41. Rigaud, J. L., B. Pitard, and D. Levy. 1995. RECONSTITUTION OF MEMBRANE-PROTEINS INTO LIPOSOMES - APPLICATION TO ENERGY-TRANSDUCING MEMBRANE-PROTEINS. Biochimica Et Biophysica Acta-Bioenergetics 1231:223-246.

42. Smith, W., C. H. Andrewes, and P. P. Laidlaw. 1933. A virus obtained from influenza patients. Lancet 2:66-68.

43. Francis Jr, T. 1940. A new type of virus from epidemic influenza. Science 92:405-408.

44. Taylor, R. 1951. A further note on 1233 influenza C virus. Archiv Gesamte Virusforschung 4:485-495.

45. Treanonor, J. 2005. Influenza Virus. In Principles and Practice of Infectious Diseases. M. B. Dolin, editor. Elsevier, Philadelphia.

46. Baine, W. B., J. P. Luby, and S. M. Martin. 1980. SEVERE ILLNESS WITH INFLUENZA-B. American Journal of Medicine 68:181-189.

47. Nigg, C., C. M. Eklund, D. E. Wilson, and J. H. Crowley. 1942. Study of an epidemic of influenza B. American Journal of Hygiene 35:265-284.

48. Mogabgab, W. J. 1963. VIRUSES ASSOCIATED WITH UPPER RESPIRATORY ILLNESSES IN ADULTS. Annals of Internal Medicine 59:306-&.

49. Brooks, G. B. 2004. Jawetz, Melnick, & Adelberg's Medical Microbiology. McGraw-Hill Medical, New York.

50. Lagoja, I. M., and E. De Clercq. 2008. Anti-influenza virus agents: Synthesis and mode of action. Medicinal Research Reviews 28:1-38.

51. Sakaguchi, T., G. P. Leser, and R. A. Lamb. 1996. The ion channel activity of the influenza virus M2 protein affects transport through the Golgi apparatus. J. Cell. Biol. 133:733-747.

52. Sugrue, R. J., G. Bahadur, M. C. Zambon, M. Hall-Smith, A. R. Douglas, and A. J. Hay. 1990. Specific structural alteration of the influenza haemagglutinin by amantadine. EMBO J. 9:3469-3476.

53. Lamb, R. A., S. L. Zebedee, and C. D. Richardson. 1985. Influenza virus M_2 protein is an integral membrane protein expressed on the infected-cell surface. Cell 40:627-633.

54. Zebedee, S. L., C. D. Richardson, and R. A. Lamb. 1985. Characterization of the influenza virus M2 integral membrane protein and expression at the infected-cell surface from cloned cDNA. J. Virol. 56:502-511.

55. Pinto, L. H., L. J. Holsinger, and R. A. Lamb. 1992. Influenza virus M_2 protein has ion channel activity. Cell 69:517-528.

56. Chizhmakov, I. V., F. M. Geraghty, D. C. Ogden, A. Hayhurst, M. Antoniou, and A. J. Hay. 1996. Selective proton permeability and pH regulation of the influenza virus M_2 channel expressed in mouse erythroleukaemia cells. J. Physiol. 494:329-336.

57. Martin, K., and A. Helenius. 1991. Nuclear transport of influenza virus ribonucleoproteins: the viral matrix protein (M1) promotes export and inhibits import. Cell 67:117-130.

58. Takeda, M., A. Pekosz, K. Shuck, L. H. Pinto, and R. A. Lamb. 2002. Influenza a virus M2 ion channel activity is essential for efficient replication in tissue culture. J. Virol. 76:1391-1399.

59. Cady, S. D., W. Luo, F. Hu, and M. Hong. 2009. Structure and function of the influenza A M2 proton channel. Biochemistry 48:7356-7364.

60. Hu, J., R. Fu, K. Nishimura, L. Zhang, H. X. Zhou, D. D. Busath, V. Vijayvergiya, and T. A. Cross. 2006. Histidines, heart of the hydrogen ion channel from influenza A virus: Toward an understanding of conductance and proton selectivity. Proceedings of the National Academy of Sciences of the United States of America 103:6865-6870.

61. Takeuchi, H., A. Okada, and T. Miura. 2003. Roles of the histidine and tryptophan side chains in the M2 proton channel from influenza A virus. FEBS Lett 552:35-38.

62. Venkataraman, P., R. A. Lamb, and L. H. Pinto. 2005. Chemical rescue of histidine selectivity filter mutants of the M2 ion channel of influenza A virus. J Biol Chem 280:21463-21472.

63. Tang, Y., F. Zaitseva, R. A. Lamb, and L. H. Pinto. 2002. The gate of the influenza virus M2 proton channel is formed by a single tryptophan residue. J Biol Chem 277:39880-39886.

64. Stouffer, A. L., R. Acharya, D. Salom, A. S. Levine, L. Di Costanzo, C. S. Soto, V. Tereshko, V. Nanda, S. Stayrook, and W. F. DeGrado. 2008. Structural basis for the function and inhibition of an influenza virus proton channel. Nature 451:596-599.

65. Balannik, V., V. Carnevale, G. Fiorin, B. G. Levine, R. A. Lamb, M. L. Klein, W. F. Degrado, and L. H. Pinto. 2010. Functional studies and modeling of pore-lining residue mutants of the influenza a virus M2 ion channel. Biochemistry 49:696-708.

66. Yi, M., T. A. Cross, and H. X. Zhou. 2008. A secondary gate as a mechanism for inhibition of the m2 proton channel by amantadine. The journal of physical chemistry 112:7977-7979.

67. Wang, C., K. Takeuchi, L. H. Pinto, and R. A. Lamb. 1993. The ion channel activity of the influenza A virus M_2 protein: characterization of the amantadine block. J. Virol. 67:5585-5594.

68. Balannik, V., J. Wang, Y. Ohigashi, X. Jing, E. Magavern, R. A. Lamb, W. F. Degrado, and L. H. Pinto. 2009. Design and Pharmacological Characterization of Inhibitors of Amantadine-Resistant Mutants of the M2 Ion Channel of Influenza A Virus. Biochemistry.

69. Wang, J., S. D. Cady, V. Balannik, L. H. Pinto, W. F. DeGrado, and M. Hong. 2009. Discovery of spiro-piperidine inhibitors and their modulation of the dynamics of the M2 proton channel from influenza A virus. J Am Chem Soc 131:8066-8076.

70. Bright, R. A., M. J. Medina, X. Y. Xu, G. Perez-Oronoz, T. R. Wallis, X. H. M. Davis, L. Povinelli, N. J. Cox, and A. I. Klimov. 2005. Incidence of adamantane resistance among influenza A (H3N2) viruses isolated worldwide from 1994 to 2005: a cause for concern. Lancet 366:1175-1181.

71. Bright, R. A., D. Shay, J. Bresee, A. Klimov, N. Cox, J. Ortiz, W. H. O. C. Ctr, and Cdc. 2006. High levels of adamantane resistance among influenza A (H3N2) viruses and interim guidelines for use of antiviral agents - United States, 2005-06 influenza season (Reprinted from MMWR, vol 55, pg 44-46, 2006). Jama-Journal of the American Medical Association 295:881-882.

72. Deyde, V. M., X. Y. Xu, R. A. Bright, M. Shaw, C. B. Smith, Y. Zhang, Y. L. Shu, L. V. Gubareva, N. J. Cox, and A. I. Klimov. 2007. Surveillance of resistance to adamantanes among influenza A(H3N2) and A(H1N1) viruses isolated worldwide. Journal of Infectious Diseases 196:249-257.

73. Ma, C., A. L. Polishchuk, Y. Ohigashi, A. L. Stouffer, A. Schon, E. Magavern, X. Jing, J. D. Lear, E. Freire, R. A. Lamb, W. F. DeGrado, and L. H. Pinto. 2009. Identification of the functional core of the influenza A virus A/M2 proton-selective ion channel. Proceedings of the National Academy of Sciences of the United States of America 106:12283-12288.

74. Luckey, M. 2008. Membrane Structural Biology with Biochemical and Biophysical Foundations. Cambridge University Press, New Yourk.

75. Ahyayauch. 2010. Detergent Effects on Membranes at Subsolubilizing Concentrations: Transmembrane Lipid Motion, Bilayer Permeabilization and Vesicle Lysis / Reassembly Are independent Phenomena. Langmuir In press DOI: 10.1021/1a904194a.

76. Biswas, S., S. R. Yin, P. S. Blank, and J. Zimmerberg. 2008. Cholesterol promotes hemifusion and pore widening in membrane fusion induced by influenza hemagglutinin. Journal of General Physiology 131:503-513.

77. Moffat, J. C., V. Vijayvergiya, P. F. Gao, T. A. Cross, D. J. Woodbury, and D. D. Busath. 2008. Proton transport through influenza A virus M2 protein reconstituted in vesicles. Biophys J 94:434-445.

78. Busath, D. D. 2009. Influenza A M2: Channel or Transporter? In Advances in Planar Lipid Bilayers and Liposomes. A. Leitmannova Liu, and A. Ȯgli editors. Academic Press, Burlington. 161-201.

79. Chizhmakov, I. V., D. C. Ogden, F. M. Geraghty, A. Hayhurst, A. Skinner, T. Betakova, and A. J. Hay. 2003. Differences in conductance of M2 proton channels of two influenza viruses at low and high pH. J. Physiol. 546:427-438.

I

ELSEVIER

Efficient and non-denaturing membrane solubilization combined with enrichment of membrane protein complexes by detergent/polymer aqueous two-phase partitioning for proteome analysis

Henrik Everberg, Thom Leiding, Anna Schiöth, Folke Tjerneld, Niklas Gustavsson [*]

Department of Biochemistry, Center for Chemistry and Chemical engineering, Lund University, P.O. Box 124, SE-22100 Lund, Sweden

Abstract

It is of central interest in membrane proteomics to establish methods that combine efficient solubilization with enrichment of proteins and intact protein complexes. We have investigated the quantitative and qualitative solubilization efficiency of five commercially available detergents using mitochondria from the yeast *Saccharomyces cerevisiae* as model system. Combining the zwitterionic detergent Zwittergent 3-10 and the non-ionic detergent Triton X-114 resulted in a complementary solubilization of proteins, which was similar to that of the anionic detergent sodium dodecyl sulfate (SDS). The subsequent removal of soluble proteins by detergent/polymer two-phase system partitioning was further enhanced by addition of SDS and increasing pH. A large number of both integral and peripheral membrane protein subunits from mitochondrial membrane protein complexes were identified in the detergent phase. We suggest that the optimized solubilization protocol in combination with detergent/polymer two-phase partitioning is a mild and efficient method for initial enrichment of membrane proteins and membrane protein complexes in proteomic studies.

© 2006 Elsevier B.V. All rights reserved.

Keywords: Detergents; Solubilization; Enrichment; Membrane proteins; Aqueous two-phase systems; Proteomics

1. Introduction

A membrane proteome contains both integral membrane proteins, which span the lipid bilayer one or several times, and peripheral proteins associated with the integral membrane proteins or the membrane surface by covalent or non-covalent interactions. Two-dimensional gel electrophoresis (2DE) and mass spectrometry (MS) are traditionally employed for separation and identification of soluble proteins. However, membrane proteomics has been hampered due to the poor solubility of integral membrane proteins in the first dimension iso-electric focusing step of 2DE [1,2]. Proteomic strategies currently used for successful identification of membrane proteins are mainly based on high-resolution separation of peptides by liquid chromatography in combination with tandem mass spectrometry (LC–MS/MS) [3–5]. Proteins are subjected to enzymatic proteolysis in solu-

tion generally resulting in very complex peptide mixtures, and multi-dimensional separation by LC is often required to reduce sample complexity enough for protein identification by MS/MS [6]. Although this so-called shotgun proteomic approach has been successful in identifying large numbers of membrane proteins, a major drawback derived from the peptide-based nature of the approach is that protein-specific information, such as size, iso-electric point, isoforms and post-translational modifications, is lost during the proteolysis step [7]. Thus, data derived from the peptide level of a shotgun experiment is in many cases difficult to interpret to yield information on the protein level, and even more on the level of protein–protein interactions such as for multi-subunit membrane protein complexes and alternative methods are thus needed. Conventional one-dimensional SDS-PAGE (1DE) is compatible with membrane protein separation although the resolving power is relatively low, compared to 2DE. Therefore, reduction of sample complexity by pre-fractionation is crucial prior to 1DE separation. We have previously reported on the use of aqueous two-phase partitioning and ion-exchange chromatography for

---

[*] Corresponding author. Tel.: +46 46 2228115; fax: +46 46 2224116.
  E-mail address: niklas.gustavsson@biochemistry.lu.se (N. Gustavsson).

pre-fractionation of yeast mitochondrial proteins prior to SDS-PAGE [8].

In the present study, this experimental strategy was modified to evaluate the efficiency of optimized solubilization and detergent/polymer two-phase partitioning for enrichment of a model membrane proteome. Mitochondria isolated from the yeast *Saccharomyces cerevisiae* were chosen since it represents a relatively small proteome from a fully sequenced organism, which contains, besides both soluble and membrane-bound proteins, a number of multi-subunit membrane protein complexes. Five commercially available detergents, representing three detergent classes, were selected for optimization of solubilization. The zwitterionic detergent *n*-decyl-*N*,*N*-dimethyl-3-ammonio-1-propanesulfonate with the commercial name Zwittergent 3-10 (Zw 3-10) was studied, based on results from an initial detergent screening (data not shown), although this detergent has previously been shown to be inefficient for membrane solubilization [9,10]. The three non-ionic detergents dodecyl maltoside (DDM), Triton X-100 (TX-100) and Triton X-114 (TX-114) are commonly used for solubilization of membranes when keeping protein structure and function intact is of importance, often at the expense of low extraction yields. The anionic detergent sodium dodecyl sulfate (SDS) is generally considered as the most efficient detergent for protein solubilization [11]. However, SDS disrupts the native structure of the solubilized proteins leaving essentially only electrophoresis for further separation. Thus, information about protein–protein interactions and the possibility for pre-fractionation will be lost after SDS solubilization. In this report, we show that, at optimized conditions, Zw 3-10 is highly efficient for membrane protein solubilization and that by combining Zw 3-10 and TX-114 a membrane protein extraction, both quantitatively and qualitatively comparable to that by SDS, can be obtained.

The optimized membrane solubilization by Zw 3-10 and TX-114 was also demonstrated to be compatible with protein pre-fractionation by detergent/polymer aqueous two-phase partitioning. As described in earlier works from our laboratory, many non-ionic detergents will form aqueous two-phase systems when mixed with a polymer in sufficient concentrations [12,13]. Detergent/polymer two-phase systems can be designed to increase the partitioning of soluble proteins to the polymer phase, which results in an enrichment of membrane proteins in the detergent phase [8,12]. This approach was extended in this work, based on the previously studied two-phase system, TX-114/poly-(ethylene glycol) (PEG), and optimized membrane protein solubilization using a combination Zw 3-10 and Triton X-114. The protein fraction partitioned to the detergent phase was separated by SDS-PAGE and protein bands were excised for protein identification. After in situ proteolysis and LC–MS/MS analysis of the peptide extracts, a large fraction (82%) of previously reported yeast respiratory chain components, including both peripheral and integral membrane components, were identified at a high level of confidence (99.95%).

This study demonstrates the importance of optimizing experimental conditions for efficient membrane solubilization. Moreover, the optimized solubilization combined with detergent/polymer two-phase partitioning, are suggested to be suitable for proteomic studies of membrane protein complexes and protein–protein interactions.

2. Experimental

2.1. Preparation of mitochondria from S. cerevisiae

Commercially processed *S. cerevisiae* was purchased from a grocery store. Pressed yeast (400 g) was suspended in 200 ml mitochondria isolation buffer (MIB) containing 0.6 M mannitol, 20 mM *N*-(2-hydroxyethyl)piperazine-*N*′-(2-ethanesulfonic acid) (HEPES)–KOH, pH 7.4, using a Dounce homogenizer. The mitochondria were isolated according to McAda and Douglas [14]. Glass beads (450–600 μm) and the yeast suspension were added to a Beadbeater (BioSpec Products Inc., Bartlesville, OK, USA) and the suspension was homogenized 5×20 s with 1 min rest on ice between each treatment. The homogenized cell suspension was pooled and centrifuged three times at $3500 \times g$ for 10 min to remove cell debris. To the supernatant, complete protease inhibitor cocktail tablet (Boehringer Mannheim, GmbH, Germany) dissolved in MIB was added according to the manufacturers instructions. The supernatant was centrifuged at +4 °C for 20 min at $17\,000 \times g$, to pellet the mitochondria. The pellet was washed once and the centrifugation step was repeated. The mitochondrial pellet was resuspended in 6 ml MIB (with protease inhibitor cocktail) and stored at −80 °C. Protein concentration of the suspension was determined (∼23 mg/ml) by the BCA protein assay [15].

2.2. Solubilization studies

The mitochondrial suspension was homogenized by freeze–thawing twice. Detergent (DDM, TX-100, TX-114, Zw3–10 and SDS) was added from stock solutions to the homogenized mitochondrial suspension, to obtain the desired detergent/protein ratio after dilution with Tris–HCl (final concentration: 10 mM) pH 9.0 in a final solubilization volume of 200 μl. The suspensions were incubated at +4 °C for 30 min and centrifuged at $100\,000 \times g$, 45 min. The amount of protein in the supernatant and the pellet was determined using the BCA protein assay. The amount of solubilized membrane protein was calculated by subtracting the soluble protein fraction (amount of protein in the supernatant without detergent) from the total amount of protein in the supernatant after solubilization and centrifugation. The total amount of protein in the supernatant and in the pellet was set to 100%. Mitochondrial membranes for assaying qualitative differences in extraction efficiency among the detergents were prepared by freeze–thawing the mitochondrial suspension twice followed by centrifugation for 30 min at $165\,000 \times g$. To remove soluble proteins trapped in the membrane vesicles or proteins attached to the mitochondrial membranes, the mitochondrial membrane pellet was resuspended in 100 μl 0.1 M Na$_2$CO$_3$, pH 11.5 and incubated on ice for 15 min followed by another centrifugation for 30 min at $165\,000 \times g$ [16].

2.3. Phase diagram determination

The phase diagram for the TX-114/PEG system was determined according to Sivars et al. [12,13]. Detergent and polymer (PEG; M_r: 40 000) were mixed at concentrations necessary to form two distinct phases at equilibrium. The phase systems were weighed in to a total of 0.5 g. The phase boundaries (binodial curves), where the change from a one-phase to a two-phase system occurs, were determined by titration of a two-phase system with small additions of water [17]. When no phase separation could be detected after centrifugation at $1800 \times g$, 5 min, the systems were considered to be monophasic. The concentrations of the phase components were calculated. To a TX-114/PEG system, glycine–NaOH, pH 10.0 was added to a final concentration of 10 mM and the system was titrated to the phase boundary by addition of 10 mM glycine–NaOH buffer, pH 10.0. In a TX-114/PEG phase system containing 10 mM glycine–NaOH, pH 10.0 and 2% (w/w) Zw 3-10 the phase boundary was determined by addition of 10 mM glycine–NaOH buffer, pH 10, 2% Zw 3-10. In a TX-114/PEG phase system containing 10 mM glycine–NaOH, pH 10.0, 2% (w/w) Zw 3-10 and 3 mM SDS the phase boundary was determined by addition of 10 mM glycine–NaOH buffer, pH 10, 2% Zw 3-10 and 3 mM SDS. All measurements were made at +4 °C.

2.4. Two-phase partitioning

Isolated mitochondria (0.5 mg total protein) were freeze–thawed twice. From stock solutions 6% (w/w) Zw 3-10 and 0.14% (w/w) TX-114 were added to obtain a total volume of 200 μl followed by incubation for another 30 min, by gentle agitation at +4 °C for membrane solubilization. The samples were centrifuged at $100\,000 \times g$ for 45 min to remove unsolubilized material and 167 μl of the supernatant was transferred to the two-phase systems. Maximum recovery 1.5 ml tubes (Axygen, Union City, CA, USA) were used and the total weight of each system was 0.5 g. The system components were weighed in from stock solutions (0.075 g TX-114 (100% stock solution), 0.080 g PEG (25% stock solution)) to obtain final concentrations (all concentrations are given in % w/w) of 15% TX-114, 2% Zw 3-10 and 4% PEG (M_r: 40 000). The systems also contained different buffers depending on the desired pH: HEPES pH 7.0; Tris–HCl pH 8.0 or 9.0; glycine–NaOH pH 10 or 11, all added from 0.2 M stock solutions to a final concentration of 10 mM (25 μl). SDS was added from a 100 mM stock solution to a final concentration of 3 mM (15 μl) and 138 μl water was added to the desired total system weight of 0.5 g. All components were thoroughly mixed and phase equilibration was performed by gentle agitation at 4 °C for 15 min. To speed up phase separation the systems were centrifuged at $1800 \times g$ in an Eppendorf centrifuge for 10 min at +4 °C. The phases were isolated using a Pasteur pipette and analyzed for total protein concentration with the BCA method. A partition coefficient (K-value) was calculated to evaluate the partitioning of proteins between the polymer phase and the detergent phase [18]. The K-value was here defined as the total concentration of protein in the top phase divided by the total

protein concentration in the bottom phase. The volumes of the phases in the used two-phase systems were equal in all the partitioning experiments.

2.5. SDS-PAGE

All samples were prepared for electrophoresis using the PlusOne SDS-PAGE Clean-Up Kit (Amersham Biosciences, Uppsala, Sweden) according to the manufacturers instructions. NuPAGE Bis-Tris pre-cast gradient gels 4–12% from Novex (San Diego, CA, USA) were used for SDS-PAGE with 3-(N-morpholino) propane sulfonic acid (MOPS) running buffer according to the manufacturers instructions. Electrophoresis conditions were set to 200 V, 125 mA for 80 min. The gels were stained with colloidal Coomassie [19] and destained in water. The protein band profiles of individual lanes on the gels were determined by densitometric analysis using a Personal Densitometer SI (Molecular Dynamics, Sunnyvale, CA, USA). Protein bands of interest were picked from the gel using glass capillaries with an inner diameter of 1 mm and put in maximum recovery 1.5 ml tubes. For LC–MS/MS a gel lane with the protein content in the detergent phase after two-phase partitioning was cut into 27 pieces of different size depending on the staining intensity. Larger sections were taken from weakly stained regions of the gel, and smaller sections were excised from strongly stained regions.

2.6. In-gel digestion

The gel pieces were destained in 75 μl 50 mM NH$_4$HCO$_3$, 50% ethanol for 60 min. The liquid was removed and 50 μl ethanol was added to shrink the gel pieces for 15 min. The liquid was removed and the gel pieces were dried in a Speed-Vac concentrator (Savant, Farmingdale, NY, USA). The gel pieces were rehydrated in 10 μl digestion buffer containing 25 mM NH$_4$HCO$_3$, and 12.5 ng/μl of sequencing-grade trypsin (Promega, Madison, WI, USA) on ice for 45 min. Digestion buffer without trypsin (10 μl) was added to cover the pieces and keep them wet during enzyme cleavage. The samples were incubated at +37 °C overnight and the supernatant was collected. To increase the peptide extraction yield from the gel pieces, 20 μl, 10 mM NH$_4$HCO$_3$, 50% ethanol, 0.5% trifluoroacetic acid (TFA) was added and incubated for 60 min at 37 °C. The gel particles were spun down and the supernatant was collected and pooled with the supernatant from the overnight incubation. The samples were dried using a SpeedVac concentrator. The same procedure was used for samples to be analyzed by LC–MS/MS with the exception of the volumes used for destaining (250 μl), shrinking (250 μl), digestion (50 μl) and extraction (50 μl).

2.7. Matrix-assisted laser desorption/ionization time-of-flight mass spectrometry (MALDI-TOF-MS), MS/MS and protein identification

The dried extracts were redissolved in 5 μl 0.1% TFA (10 μl for the LC experiments) and 0.5 μl of each sample was spotted directly onto a stainless steel MALDI target and were left to

dry. 0.5 μl of a matrix solution containing 5 mg/ml α-cyano-4-hydroxy cinnamic acid, 50% acetonitrile, 0.1% TFA and 5 mM $NH_4H_2PO_4$ [20] was added and allowed to dry. MALDI-TOF-MS and MS/MS spectra were recorded automatically using a 4700 Proteomics Analyzer (Applied Biosystems, Framingham, CA, USA) mass spectrometer in positive reflector mode. The obtained MS spectra were internally calibrated using two trypsin autoproteolysis peptides with the m/z values 842.51 and 2211.097 Da. Protein identification was performed using the GPS Explorer software, with an in-house Mascot search engine (Matrix Science, London, UK) [21] searching the Swiss-Prot database. Parameters specified in the search were as follows: taxa, *S. cerevisiae*; missed cleavages, 1; peptide mass tolerance, ±25 ppm; fragment ion mass tolerance, ±0.2 Da; variable modifications, oxidation of methionines. A protein was considered as identified when the level of confidence for the total ion score exceeded 99.95%.

2.8. Liquid chromatography

Peptides resulting from tryptic digestion of proteins enriched in the detergent phase after two-phase partitioning were separated by reversed phase nanoLC using an 1100 Series Nanoflow LC system (Agilent technologies, Waldbronn, Germany). The mobile phases used for separation were (A) 1% (v/v) acetonitrile and 0.05% (v/v) TFA and (B) 90% (v/v) acetonitrile and 0.04% (v/v) TFA. Five microliters of the in-gel digested peptide extract was loaded on the column from glass vials. The samples were loaded onto a pre-column (Zorbax 300 SB C18, 5 mm × 0.3 mm) at a flow rate of 0.050 ml/min of buffer A. After 10 min the separation column (Zorbax 300 SB C18, 150 mm × 0.075 mm) was connected in-line with the pre-column to the nanopump, flow-controlled by a micro six-port/two-position module. The separation was carried out at a flow rate of 200 nl/min with the following elution profile: 10–11 min, 0–30% B; 11–36 min, 30–90% B; 36–37 min, 90–100% B; 37–40 min, 100% B; 40–43 min, 100–0% B. Fractions were collected on MALDI targets from time 25.5 to 41.5 min with 15 s intervals using the 1100 Series LC micro collection/spotting system.

2.9. LC–MS/MS protein identification

A matrix solution consisting of 5 mg/ml α-cyano-4-hydroxy cinnamic acid, 50% acetonitrile, 0.1% TFA was added post-column manually onto the dried peptide fractions and was allowed to dry. The matrix solution also included 50 mM citric acid for suppression of matrix signals [22] and three standard peptides (angiotensin I, m/z: 1296.685; neurotensin, m/z: 1672.918 and ACTH 18-39, m/z: 2465.199) for internal calibration. MS and MS/MS spectra were recorded automatically using a 4700 Proteomics Analyzer mass spectrometer in positive reflector mode. Precursors were selected by using the jobwide interpretation function excluding masses derived from tryptic autoproteolysis and commonly occurring keratin peptides. A minimum signal to noise value of 50 and a spot-to-spot difference between precursor masses of ±50 ppm were set as requirements for precursor selection and a maximum of 10 pep-

tides in each fraction were selected for MS/MS acquisition. The acquired MS/MS data were used for database searches using GPS Explorer software and the in-house Mascot search engine searching the Swiss-Prot database. Search parameters were set as above and a protein was considered identified when the significance level for the total ion score exceeded 99.95%, which means that 0.05% of the identified proteins could statistically be false positives. A FASTA-formatted list of the identified proteins was created by submitting the Swiss-Prot accession numbers to Expasy (http://www.expasy.org/sprot/sprot-retrieve-list.html). The retrieved list was submitted to a topology prediction server using the so-called transmembrane hidden Markov model (TMHMM) (http://www.cbs.dtu.dk/services/TMHMM-2.0/) to predict the number of transmembrane helices in each identified protein [23]. Proteins were classified as integral membrane proteins when predicted to have one or more transmembrane regions or were annotated as an integral membrane protein in Swiss-Prot. By manual examination of the protein annotations a protein was classified as a peripheral membrane protein when annotated as: (1) membrane-associated by electrostatic and/or hydrophobic interactions; (2) subunit of a membrane protein complex; (3) attached to the membrane by a lipid anchor. Proteins reported to be functionally assigned to mitochondrial membranes such as ribosomal and chaperone proteins, glycolytic enzymes, tRNA-transport complex proteins and dehydrogenase complex proteins were classified as membrane-associated. Proteins not annotated in the database were classified as soluble/unknown.

3. Results

3.1. Optimization of membrane solubilization
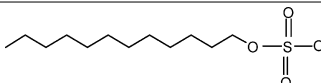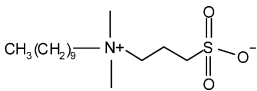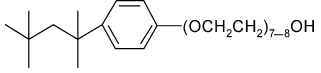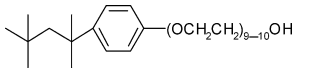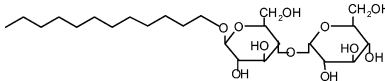
We have studied the solubilization efficiency of one zwitterionic detergent (Zw 3-10) and three commonly used non-ionic detergents (DDM, TX-100, TX-114) (Table 1), all compatible with subsequent fractionation and separation methods such as two-phase partitioning and liquid chromatography. For evaluation, the commonly used anionic detergent SDS was used as reference. Yeast mitochondria were incubated with increasing concentrations of the detergents followed by centrifugation to remove unsolubilized material. The solubilization efficiency is presented in Fig. 1. It is defined (Eq. (1)) as the fraction of solubilized membrane protein found in the supernatant of the total amount of membrane protein in pellet plus supernatant.

$$\text{Detergent solubilization efficiency (\%)} = \frac{A - B}{C + (A - B)} \times 100 \tag{1}$$

where A stands for total protein amount in the supernatant; B for soluble protein amount in the supernatant; and C for protein amount in the pellet. The soluble protein amount was determined as the amount of protein found in the supernatant when no detergent was added.

The maximum protein extraction yield using Zw 3-10 for solubilization was >90% while the maximum yield for all three non-ionic detergents DDM, TX-100 and TX-114 was ~80%.

Table 1
Structures and properties of detergents used

Detergent	Structure	Type	CMC (mM)	n	M_r (monomer)
SDS		A	10^a	60^a	288^a
Zw 3-10	$CH_3(CH_2)_9$—N+ ... S ... O−	Z	40^a	40^a	308^a
TX-114	$(OCH_2CH_2)_{7-8}OH$	N	0.25^a	n.d.[b]	537^c
TX-100	$(OCH_2CH_2)_{9-10}OH$	N	0.35^a	140^b	625^c
DDM		N	0.6^a	100^b	511^a

n: aggregation number, A: anionic, Z: zwitterionic, N: non-ionic. n.d.: not determined.

[a] Ref. [47].

[b] Dependent on detergent concentration and temperature [25,26,48].

[c] Ref. [49].

Solubilization by SDS extracted ~95% of the total membrane protein. The high extraction yield of Zw 3-10 was found to be stable over a wide concentration range while the extraction yield of the non-ionic detergents was relatively sensitive for changes in the detergent concentration. For the non-ionic detergents the maximum extraction efficiency was reached at low detergent/protein ratios around 5 mmol/g, probably due to their low CMC-values. The higher detergent/protein ratio of ~30 mmol/g needed to reach the maximum level of protein extraction for Zw 3-10 is probably due to the high CMC of this detergent (Table 1).

To investigate the qualitative differences in extraction of integral membrane proteins among the detergents, membranes were solubilized at the optimum conditions for each detergent. The membranes were first treated with 0.1 M Na$_2$CO$_3$ at high pH (11.5) for alkaline stripping of the membranes from soluble proteins and non-integral membrane proteins [16]. After solubilization, equal amounts (25 μg) of the protein extracts were analyzed by SDS-PAGE (Fig. 2). The protein pattern after extraction with the three non-ionic detergents DDM, TX-100 and TX-114, respectively, was very similar (data not shown). Therefore, TX-114 was selected as representative for the non-ionic detergents. The proteins extracted by Zw 3-10 showed a different pattern compared to those solubilized by TX-114. The staining intensity of the protein bands from the Zw 3-10 and TX-114 extracted proteins were compared by densitometric analysis. The intensity ratio (Zw/TX) was used to detect proteins more efficiently extracted by one of the detergents. A Zw/TX ratio of 1 denotes equal efficiency in extraction. Zw/TX ratios above 2 or below 0.5 were considered to indicate proteins more efficiently extracted by Zw 3-10 or TX-114, respectively, and were selected for analysis by MALDI-TOF-MS and MS/MS

for identification (Fig. 2, Table 2). Protein identifications with a level of confidence >99.95% was considered reliable. The proteins more efficiently extracted by Zw 3-10 (Zw/TX ratios > 2), were all integral membrane proteins as predicted by the software TMHMM 2.0 or peripheral membrane proteins annotated in the Swiss-Prot database. The proteins more efficiently extracted by TX-114 (Zw/TX ratios < 0.5) were also identified as integral membrane proteins. Among the proteins with a Zw/TX ratio below 0.5 were a phosphate carrier and a putative mitochondrial carrier protein, both annotated in Swiss-Prot with four probable transmembrane regions not predicted by TMHMM 2.0. Together with the group of membrane proteins with a Zw/TX ratio below 0.5 there were also a number of ribosomal proteins, which indicate association with the membranes despite the high pH treatment used for removal of proteins attached to the membranes.

In addition to using Zw 3-10 and TX-114 separately for membrane solubilization, we also assessed their solubilization efficiency by combining them at optimum conditions. The resulting protein pattern was very similar to that obtained by solubilization with SDS when analyzed by SDS-PAGE (Fig. 2). Given the high protein extraction efficiency of Zw 3-10 and the complementary extraction yield from using Zw 3-10 in combination with TX-114, we decided to assess this combination of detergents for its compatibility with protein pre-fractionation by aqueous two-phase partitioning.

3.2. Detergent/polymer aqueous two-phase partitioning

A phase diagram can be used to demonstrate the phase behavior of a two-phase system (Fig. 3). The phase boundary shows
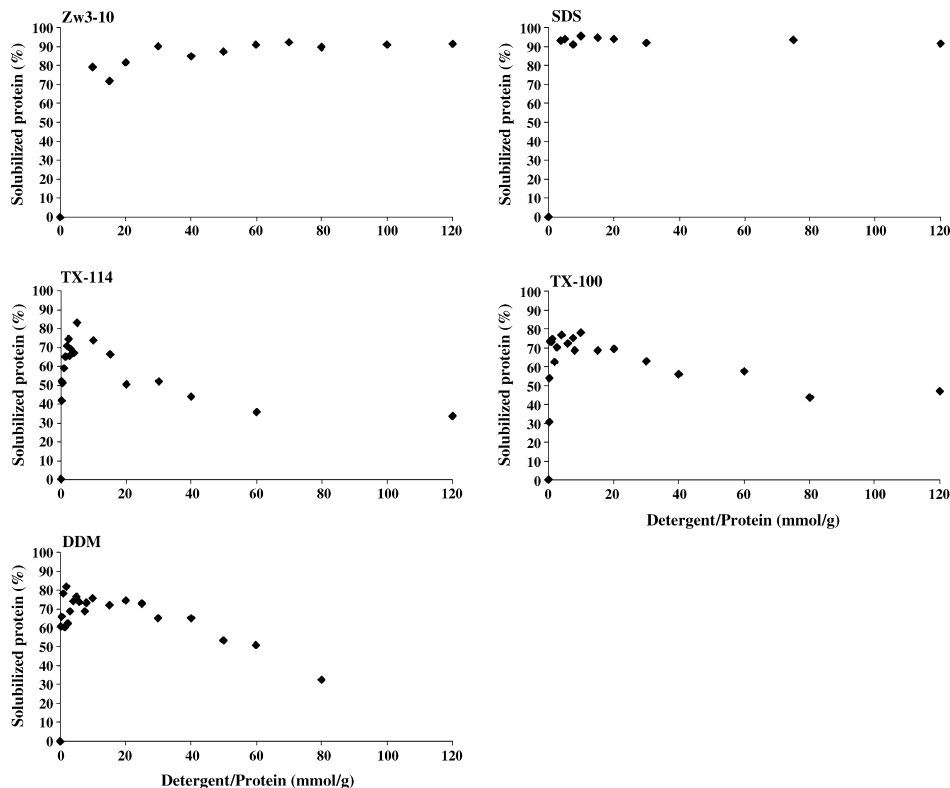
Fig. 1. Quantitative comparison of solubilization efficiency. Mitochondria were freeze–thawed twice and incubated in different detergent/protein molar ratios for 30 min on ice followed by centrifugation at $100\,000 \times g$ for 45 min. The soluble protein fraction (amount of protein in the supernatant without added detergent) was subtracted and the remaining protein content in the supernatant was considered as solubilized membrane proteins (See (Eq. (1)). The total amount of membrane proteins was defined as: membrane protein in the supernatant + protein in the pellet. SDS: sodium dodecyl sulfate; Zw 3-10: Zwittergent 3-10; TX-114: Triton X-114; TX-100: Triton X-100; DDM: dodecyl maltoside.

the concentrations of the two components needed for a transition from one homogenous phase to two distinct phases enriched in detergent micelles and polymer, respectively. Introducing a zwitterionic detergent, such as Zw 3-10 to a phase system influences the phase behavior. The phase diagram of a two-phase system composed of TX-114/PEG in water was determined and the influence on the phase boundary by the successive addition of (i) 10 mM glycine–NaOH, pH 10, (ii) 2% (w/w) Zw 3-10 and (iii) 3 mM SDS was determined (Fig. 3). The phase boundary was only slightly affected by the addition of glycine–NaOH, buffering the system at pH 10. The effect on the phase boundary was significantly larger upon addition of Zw 3-10, moving the phase boundary towards a smaller two-phase region. The addition of a small amount of SDS resulted in shifting the phase boundary even further. The fact that the TX-114/PEG phase system still separates into two distinct phases upon addition of zwitterionic and charged detergents demonstrates the robustness of the TX-114/PEG system.

Previously, we have established detergent/polymer two-phase partitioning as a suitable method for pre-fractionation of proteins prior to further separation by SDS-PAGE and protein identification by mass spectrometry [8]. In the present study protein partitioning was investigated by adding mitochondria solubilized at optimized conditions as described above, followed by centrifugation for removal of non-solubilized material. Thus, both the membrane bound and the soluble protein fraction of the mitochondria were included in the two-phase system. The partitioning coefficient (K) is defined as the protein concentration in the top-phase divided by the protein concentration in the bottom phase. As the phase volumes were equal in these experiments, a K-value > 1 denotes a predominant partitioning to the polymer-enriched top phase. As seen in Fig. 4, the K-value in a system including 3 mM SDS was increased from ~0.5 to ~2.5 by raising the pH from 7 to 10. This equals a five-fold shift in overall protein partitioning by raising the pH. The system at pH 10 was chosen for further evaluation of
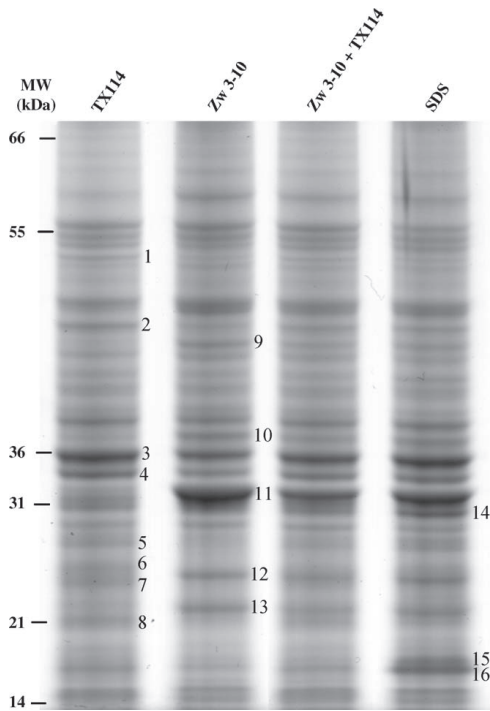
Fig. 2. Qualitative comparison of solubilization efficiency. SDS-PAGE of supernatants after solubilization at optimized conditions (as determined from Fig. 1) of mitochondrial membranes treated with sodium carbonate to remove soluble proteins trapped inside the membrane vesicles or attached to membranes. From each supernatant 25 μg protein was applied to the gel. The numbers indicate identified proteins found to be solubilized more efficiently by either Zw 3-10 or TX-114 as evaluated by densitometry (see Table 2).

Fig. 3. Phase diagram of the TX-114/PEG aqueous two-phase system. The influence on the phase boundary was studied by successive addition of 10 mM glycine–NaOH pH 10, Zwittergent 3-10 and SDS to TX-114/PEG two-phase systems. At concentrations below the phase boundary a homogenous one-phase system was obtained, above the phase boundary two distinct phases were obtained. PEG M_r: 40 000; temperature: +4 °C.

Table 2
Proteins identified (>99.95% confidence) with MALDI-TOF MS and MS/MS analysis after solubilization at optimized detergent/protein molar ratio (Fig. 1) and SDS-PAGE separation (Fig. 2)

No.	Swiss-Prot name	Acc. no.	TMD	Zw/TX
				<0.5
1	NADH-ubiquinone oxidoreductase	P32340	1	0.18
2	Mitochondrial outer membrane 45	P16547	1	0.24
3	ADP, ATP carrier protein 2	P18239	6	0.47
	Prohibitin	P40961	1	–
4	Mitochondrial phosphate carrier protein	P23641	4	0.40
	Putative mitochondrial carrier	P38988	4	
5	Hypothetical 27.7 kDa protein	P40098	2	0.31
	60S ribosomal protein L15-A	P05748	–	
	60S ribosomal protein L13-B	P40212	–	
6	Hypothetical 25.3 kDa protein	P53721	3	0.27
	Peroxisomal membrane protein PMP27	Q12462	MA	
7	60S ribosomal protein L16-B	P26785	–	
8	Elongation factor 1-alpha	P02994	–	0.47
				>2.0
9	Mitochondrial import subunit TOM40	P23644	–[a]	8.84
	S-adenosylmethionine synthetase 2	P19358		
10	NADH-cytochrome b5 reductase	P36060	1	7.22
11	Outer mitochondrial membrane porin 1	P04840	–[a]	6.46
12	ATP synthase subunit 4	P05626	2	3.58
13	ATP synthase D chain	P30902	MA	3.74
14	Cytochrome c1, heme protein	P07143	MA	1.16
	60S ribosomal protein L2	P05736	–	
	40S ribosomal protein S3	P05750	–	
15	60S ribosomal protein L28	P02406	–	n.d.
16	60S ribosomal protein L25	P04456	–	n.d

No.: number on gel; Acc. no.: Swiss-Prot accession number; TMD: number of transmembrane α-helices as predicted by TMHMM 2.0 or as annotated in Swiss-Prot, MA: protein associated to the membrane, subunit of an integral membrane protein complex or attached to the membrane by a lipid-anchor; Zw/TX: ratio of staining intensity between protein bands on SDS-PAGE after solubilization with Zw 3-10 and TX-114 as analyzed by densitometry; n.d.: not detectable.
[a] Channel with transmembrane β-strands not predicted as an integral membrane protein by the software TMHMM.

the protein content in the membrane protein-enriched detergent phase.

3.3. Identification of proteins partitioned to the detergent phase

To minimize discrimination against integral membrane proteins we have here applied an experimental approach based on peptide liquid chromatography for identification of proteins partitioned to the detergent phase. The protein content in the detergent phase after (i) solubilization with the combination of Zw 3-10 and TX-114 at optimized conditions and (ii) partitioning in the PEG/TX-114 aqueous two-phase system at pH 10, was separated by SDS-PAGE (Fig. 5). The gel was stained with Coomassie brilliant blue and the lane containing the proteins from the detergent phase was cut into 27 slices according to the staining intensity as indicated in the figure. The pro-

Fig. 4. Effect of pH on protein partitioning in the TX-114/PEG aqueous two-phase system. By increasing the pH of the system including SDS, the partitioning coefficient (K = (protein concentration in the top phase)/(protein concentration in the bottom phase)) is shifted from a partitioning predominantly to the detergent phase (K = 0.5) at pH 7, to a more pronounced partitioning t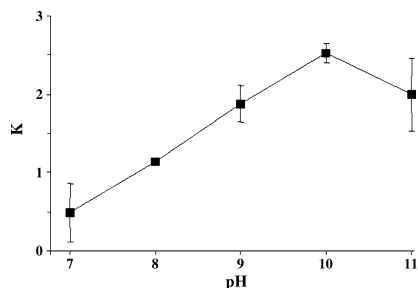o the polymer phase (K = 2.5) at pH 10. All systems were composed of 4% (w/w) PEG 40 000, 15% (w/w) Triton X-114, 2% (w/w) Zwittergent 3-10, 3 mM SDS and 10 mM buffer (pH 7.0 HEPES; pH 8.0 and 9.0 Tris–HCl; pH 10.0 and 11.0 glycine–NaOH).

teins present in each gel slice were digested with trypsin and the resulting peptides were extracted from the gel and separated by nanoflow reversed phase LC. Fractions were collected directly onto a MALDI target, analyzed by MALDI-TOF-MS, followed by automatic selection of peptides suitable for MS/MS-analysis. The obtained MS/MS-data was submitted for searching the Swiss-Prot database using the Mascot search engine. Using the default settings of a 95% confidence level (5% false positives) in Mascot for protein identification, which is a widely used criterion in proteomic research, 399 proteins were identified in the detergent phase.

To minimize the amount of false positives in our identification results, we used a confidence level of 99.95% (0.05% false positives). Using this strict criterion, 186 proteins were identified (Table 4, supplementary data). Fig. 6 shows a pie chart representation of the total number of identified proteins, divided into four different categories. Of the 186 identified proteins, 34 were integral membrane proteins with one to twelve transmembrane helices as predicted by TMHMM 2.0 or as annotated in Swiss-Prot and another 34 proteins were annotated as peripheral membrane proteins. In Table 3, protein components of multi-subunit membrane protein complexes identified in the detergent phase are presented. A large fraction (82%) of the known integral and peripheral components in the yeast respiratory chain
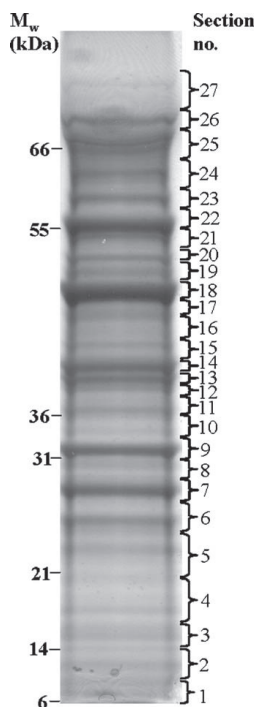

Fig. 5. SDS-PAGE of the protein content in the detergent phase after two-phase partitioning in the TX-114/PEG system containing Zw 3-10 and SDS. Solubilized protein (50 g) partitioned to the detergent phase was added to the gel, which was stained with colloidal Coomassie brilliant blue and cut into 27 sections according to staining intensity. The gel pieces were treated with trypsin and the peptide extracts were analyzed by LC–MS/MS.

Fig. 6. Summary of protein identifications. After LC–MS/MS analyses and database searches, a total of 186 proteins were reliably identified using a high significance level (99.95%). Integral membrane proteins were either predicted by the software TMHMM 2.0 or annotated as membrane bound in Swiss-Prot. Peripheral membrane proteins were defined as: proteins without transmembrane domains associated to the membrane by electrostatic and/or hydrophobic interactions; subunits of membrane protein complexes; proteins attached to membranes by a lipid anchor. Membrane-associated denotes proteins functionally assigned to mitochondrial membranes such as ribosomal and chaperone proteins, glycolytic enzymes, tRNA-transport complex proteins and dehydrogenase complex proteins. Proteins without annotation on cellular localization were included in the soluble/unknown fraction.

Table 3
Protein components of known multi-subunit membrane protein complexes identified in the detergent phase after solubilization, two-phase partitioning, SDS-PAGE and LC–MS/MS

Complex	Subunit	Accession Number	TM	>99.95%	99.95–95%
I	Rotenone-insensitive NADH-ubiquinone oxidoreductase	P32340	1	X	
II	Succinate dehydrogenase [ubiquinone] flavoprotein subunit	Q00711		X	
	Succinate dehydrogenase [ubiquinone] iron–sulfur protein	P21801		X	
	Succinate dehydrogenase cytochrome *B* subunit	P33421	3	X	
	Succinate dehydrogenase [ubiquinone] cytochrome *b*	P37298	2		X
III	Cytochrome c1, heme protein	P07143		X	
	Cytochrome b	P00163	9	X	
	Ubiquinol–cytochrome *c* reductase 8.5 kDa protein	P37299	1	X	
	Ubiquinol–cytochrome *c* reductase 14 kDa protein	P00128		X	
	Ubiquinol–cytochrome *c* reductase ubiquinone-binding protein QP-C	P08525	1	X	
	Ubiquinol–cytochrome *c* reductase iron–sulfur subunit	P08067		X	
	Ubiquinol–cytochrome *c* reductase core protein I	P07256		X	
	Ubiquinol–cytochrome *c* reductase core protein 2	P07257		X	
IV	Cytochrome *c* oxidase polypeptide I	P00401	12	X	
	Cytochrome *c* oxidase polypeptide II	P00410	2	X	
	Cytochrome *c* oxidase polypeptide IV	P04037			X
	Cytochrome *c* oxidase polypeptide Va	P00424	1	X	
	Cytochrome *c* oxidase polypeptide VI	P00427		X	
	Cytochrome *c* oxidase polypeptide VIa	P32799	1	X	
	Cytochrome *c* oxidase polypeptide VIIA	P07255	1		X
	Cytochrome *c* oxidase assembly protein COX11	P19516	1		X
	MSS51 protein	P32335		X	
	SCO1 protein	P23833		X	
V	ATP synthase alpha chain	P07251		X	
	ATP synthase beta chain	P00830		X	
	ATP synthase gamma chain	P38077		X	
	ATP synthase delta chain	Q12165		X	
	ATP synthase epsilon chain	P21306		X	
	ATP synthase e chain	P81449		X	
	ATP synthase D chain	P30902		X	
	ATP synthase J chain	P81450			X
	ATP synthase K chain	P81451		X	
	ATP synthase oligomycin sensitivity conferral protein	P09457		X	
	ATP synthase subunit 4	P05626	2	X	
	ATP11 protein	P32453			X
	ATP13 protein	P22136			X
	ATPase inhibitor	P01097			X
TOM	Mitochondrial import receptor subunit TOM40	P23644	TM-channel	X	
	Mitochondrial import receptor subunit TOM20	P35180	1		X
	Mitochondrial import receptor subunit TOM22	P49334	TM-channel		X
	Mitochondrial import receptor subunit TOM5	P80967	1		X
TIM	Mitochondrial import inner membrane translocase subunit TIM10	P87108		X	
	Mitochondrial import inner membrane translocase subunit TIM22	Q12328	2	X	
	Mitochondrial import inner membrane translocase subunit TIM9	O74700		X	
	Translocase of the inner membrane protein 11 (TIM11)	P81449	TM-channel	X	
	Mitochondrial protein import protein MAS5 (mtHSP70)	P25491		X	

Proteins identified at 99.95–95% confidence level were included after manual verification of the data. Transmembrane helices (TM) were predicted by the software TMHMM 2.0 or obtained from annotations in Swiss-Prot. TM-channel denotes proteins where the transmembrane region consists of β-strands.

complexes I–V was identified in the detergent phase. In addition, several subunits from the membrane protein translocase complexes TOM (outer membrane) and TIM (inner membrane) were detected in the detergent phase.

Another 36 proteins also identified in the detergent phase were classified as membrane-associated and the remainder of the identified proteins was either annotated as soluble or did not have any annotation about cellular localization in the Swiss-Prot database.

4. Discussion

4.1. Efficient and non-denaturing membrane solubilization

We present here a method, based on a combination of detergents, for efficient extraction of membrane proteins and membrane protein complexes, which allows for subsequent multi-dimensional separation of intact membrane protein complexes. We show that experimental parameters such as detergent/protein

molar ratio and detergent concentration in relation to the CMC are important for optimal solubilization.

At optimized conditions Zw 3-10 demonstrated a high solubilization efficiency of >90% extracted protein and also compatibility with pre-fractionation by aqueous two-phase partitioning. SDS solubilization yielded 95% extracted protein but was incompatible with two-phase partitioning as aggregation and precipitation occurred at the interphase of the system (results not shown). The three non-ionic detergents showed solubilization efficiencies at optimized conditions with levels around 80%, which is in agreement with other studies [10,24]. While the high solubilization efficiency of Zw 3-10 was retained also at high detergent/protein molar ratios, the non-ionic detergents showed rather narrow operational windows for efficient solubilization. An explanation for this behavior of the non-ionic detergents may be the formation of larger detergent micelles as the concentration is increased. Elongation of cylindrical micelle structures at increased detergent concentration is well studied for the poly-(oxyethylene) detergents $C_{10}EO_4$ [30], TX-100 and TX-114 [25]. Also DDM has been reported to form larger micelle structures at increasing detergent concentration [26]. Micelle enlargement may result in large detergent–protein complexes, which could result in precipitation and thereby apparent low solubilization efficiencies. Thus, using a fixed concentration of different detergents, regardless of the CMC, may result in a low yield of solubilized membrane proteins. In the case of zwitterionic and ionic detergent micelles, electrostatic repulsion between the charged micelles hinders micelle growth, given that the concentration of counter ions in the solution is kept low. This could explain the robust solubilization efficiency of Zw 3-10 at higher detergent concentrations, which in turn could be advantageous in cases where it is of importance to keep the solubilized proteins in a small volume for subsequent analysis.

As demonstrated in Fig. 2 and Table 2, the solubilization efficiency of individual proteins was different between non-ionic, zwitterionic and ionic detergents. This qualitative difference between the detergent classes can be explained by protein and lipid heterogeneity found in mitochondrial membranes resulting in specific detergent extraction profiles, which also depends on the properties of the detergents [27]. Our results demonstrate the importance of screening experimental conditions for optimized solubilization efficiency depending on the biological membrane system studied. The individual protein extraction profiles obtained from Zw 3-10 and TX-114 were found to be complementary to each other when the detergents were mixed prior to solubilization, yielding a SDS-PAGE protein pattern very similar to that from solubilization with SDS. Thus, this combination of detergents provides an extraction of membrane proteins from yeast mitochondria, quantitatively and qualitatively comparable to SDS, but with the advantage of being compatible with subsequent protein separation.

4.2. TX-114/PEG two-phase system: phase behavior and protein partitioning

When the zwitterionic detergent Zw 3-10 was introduced to the TX-114/PEG two-phase system used for protein pre-

fractionation, the phase separation behavior was changed. The phase behavior of detergent/polymer two-phase systems can be compared to a polymer/polymer two-phase system, e.g. the much used dextran/PEG system [18] and the detergent micelles can be regarded as the second polymer [28,29]. By addition of zwitterionic detergent, mixed micelles of TX-114 and Zw 3-10 are formed. The charged head group of Zw 3-10 introduced to the mixed micelles should lead to a shift in the phase diagram towards an increased one-phase area similar to the phase behavior in systems composed of non-charged and charged polymers [12,30]. This corresponds well with the phase separation behavior found in the two-phase system studied in this work (Fig. 3). There was a distinct change of the phase boundary upon addition of Zw 3-10 and SDS, which resulted in the need for higher concentrations of polymer and detergent for the system to separate into two phases.

Partitioning of membrane proteins in a detergent/polymer two-phase system is mainly dependent on hydrophobic interactions between the proteins and the detergent micelles [12]. The partitioning behavior of soluble proteins is more complex and is mainly governed by similar mechanisms as in polymer/polymer systems [31]. Here we have employed the electrostatic driving force to influence the partitioning of soluble proteins. Increased partitioning of proteins to the polymer phase was obtained by addition of a negatively charged detergent, SDS, at a concentration below its CMC. Monomers of SDS get incorporated in the mixed micelles of non-ionic and zwitterionic detergents, thus introducing negative charges [12,13,32,33]. This results in repulsion of negatively charged soluble proteins from the negatively charged mixed micelles in the detergent phase. The denaturing properties of SDS will be insignificant due to the low concentration of SDS monomers in the solution. By raising the pH, increased protein negative net charge leads to stronger repulsion between proteins and negatively charged mixed micelles, which enhances the partitioning of soluble proteins to the polymer-enriched top phase. Membrane proteins are not affected since the hydrophobic interaction between membrane protein and the hydrophobic core of the mixed micelles govern the partitioning for these proteins. The results shown in Fig. 4 demonstrate an increased partitioning of proteins to the polymer phase as an effect of including SDS and increasing the pH of the system from 7 to 10. The fact that the K-value decreased at pH 11 might be explained by the exposure of hydrophobic surfaces due to protein denaturation at the high pH, leading to an increased partitioning of the proteins to the detergent bottom phase or the interphase between the two phases.

4.3. Preservation of membrane protein complexes during solubilization and two-phase partitioning

As summarized in the pie chart diagram in Fig. 6, a total of 186 proteins were identified from the detergent phase with >99.95% confidence. Out of these, 68 proteins were classified as either integral membrane proteins with transmembrane domains (TMD), or peripheral membrane proteins. The 34 integral membrane proteins were predicted to contain up to 12 transmembrane-spanning helices by TMHMM 2.0 or up to 16

membrane-spanning β-strands in the case of a number of β-barrel proteins. Membrane topology prediction software tools are widely used for assessment of the number of integral membrane proteins in proteome research. Although predictions are never completely reliable and as all of the currently available methods have their individual strengths and weaknesses, no method can be distinguished as superior to all the others [34]. In this work we have employed TMHMM 2.0, which is frequently used for evaluation of large amounts of proteomic data.

In addition to characterization of integral membrane proteins, membrane proteomics also comprises the study of membrane protein complexes including peripheral subunits and other protein interaction partners. Thus, the development of non-denaturing solubilization and pre-fractionation methods is important. The 34 proteins classified as peripheral membrane proteins in Fig. 6 are characterized as (i) subunits of membrane protein complexes, (ii) attached to the membrane by a lipid anchor or (iii) annotated in the literature to be attached to mitochondrial membrane surfaces by electrostatic or hydrophobic interactions. Among these 34 proteins were several subunits of membrane protein complexes. If non-covalent interactions between the peripheral and the integral membrane protein subunits are broken during solubilization and fractionation, the peripheral subunits would most likely behave as soluble proteins in a two-phase system and would thus be partitioned to the polymer phase. On the other hand, if the interactions are preserved, the peripheral membrane proteins will co-partition with the integral membrane protein subunits to the detergent phase.

We have previously demonstrated that a number of peripheral membrane protein complex subunits are indeed highly enriched in the detergent phase after detergent/polymer two-phase partitioning, as judged by 2DE differential analysis of both the polymer and the detergent phase [8]. The results reported here further support the conclusion of intact membrane protein complexes partitioning to the detergent phase. A more complete coverage of the yeast respiratory chain complexes was obtained after LC–MS/MS analysis of the detergent phase. The respiratory chain of yeast is composed of five major components: a transmembrane NADH-dehydrogenase, which substitutes for the mammalian complex I, and complexes II–V, which all consist of several integral and peripheral protein subunits (II: 4; III: 10 [35]; IV: 12 [36]; V: 18 [37]). Altogether, 37 of the 45 (82%) reported protein components of the yeast respiratory chain were detected in the detergent phase, comprising both transmembrane and peripheral membrane subunits. Also, 10 of 18 components [38] from the mitochondrial protein translocation complexes TOM (outer membrane) and TIM (inner membrane) were identified in the detergent phase.

A group of 36 proteins, often detected in membrane preparations and regarded as contaminants [24,39] were here classified as functionally associated to the mitochondrial membranes based on earlier reports. These proteins were, for example, a group of chaperones and ribosomal proteins, also identified in the protein extracts obtained from the membrane preparations washed with Na_2CO_3 (high pH) which is regarded as an efficient method for stripping membranes of peripheral and loosely attached proteins. Although, it cannot be excluded that these pro-teins, are contaminating soluble proteins, we suggest that their interaction with the membranes are kept intact due to the mild conditions of the two-phase partitioning fractionation.

Ribosomal proteins are involved in translation of proteins expressed in the mitochondria at the matrix side of the inner membrane [40] and are suggested to be bound to membranes by electrostatic and/or hydrophobic interactions [39]. It has also been demonstrated that the interaction between mitochondrial ribosomal proteins and the inner mitochondrial membrane are partly resistant against treatment with TX-100. These mitochondrial ribosomes are suggested to be associated with large oligomeric complexes in the membrane [41]. Also cytosolic ribosomal proteins have been shown to associate with the outer membrane of mitochondria by both specific interactions with integral membrane proteins and non-specific interactions, possibly to lipids of the outer membrane [42,43].

Chaperone proteins such as members of the Hsp70 family are involved in protein translocation across the two mitochondrial membranes and membrane protein assembly [44] and are thus often found in membrane preparations. Another group of proteins identified in the detergent phase comprised a number of glycolytic enzymes previously suggested to be functionally associated with the outer mitochondrial membrane in *Arabidopsis thaliana* [45]. Mitochondrial dehydrogenases have been assigned to membrane-bound complexes in yeast including a number of tricarboxylic acid (TCA) cycle components [46]. In addition we identified a number of proteins proposed to be parts of protein complexes involved in tRNA import into mitochondria and have been co-purified in yeast mitochondrial membrane preparations (Brandina et al., personal communication). The remaining 82 identified proteins were annotated in the database as either soluble or with unknown cellular localization. As the software used for prediction of integral membrane proteins is never completely reliable, unknown integral membrane proteins may be included in this fraction. Furthermore, proteins included in the soluble/unknown fraction may actually be proteins functionally associated with the mitochondrial membrane surfaces, by analogy with the previously mentioned reports.

Our results suggest that optimized solubilization with the zwitterionic detergent Zwittergent 3-10 and TX-114 in combination with detergent/polymer two-phase partitioning provide an efficient and non-denaturing initial recovery of membrane proteomes. The method is suggested to maintain the integrity of membrane protein complexes to a great extent, allowing proteins that are non-covalently linked to membranes or integral membrane proteins to co-partition to the detergent phase as demonstrated by the identification of a large number of respiratory chain complex subunits. Thus, detergent/polymer two-phase partitioning enables isolation and analysis of interacting proteins and subunits for functional membrane proteomic studies, not only including integral membrane proteins.

Appendix A. Supplementary data

Supplementary data associated with this article can be found, in the online version, at doi:10.1016/j.chroma.2006.04.020.

References

[1] C. Adessi, C. Miege, C. Albrieux, T. Rabilloud, Electrophoresis 18 (1997) 127.
[2] V. Santoni, M. Molloy, T. Rabilloud, Electrophoresis 21 (2000) 1054.
[3] M.P. Washburn, D. Wolters, J.R. Yates III, Nat. Biotechnol. 19 (2001) 242.
[4] C.C. Wu, J.R. Yates III, Nat. Biotechnol. 21 (2003) 262.
[5] Y. Zhao, W. Zhang, Y. Kho, Anal. Chem. 76 (2004) 1817.
[6] C.C. Wu, M.J. MacCoss, K.E. Howell, J.R. Yates III, Nat. Biotechnol. 21 (2003) 532.
[7] A.I. Nesvizhskii, R. Aebersold, Mol. Cell Proteomics 4 (2005) 1419.
[8] H. Everberg, U. Sivars, C. Emanuelsson, C. Persson, A.K. Englund, L. Haneskog, P. Lipniunas, M. Jornten-Karlsson, F. Tjerneld, J. Chromatogr. A 1029 (2004) 113.
[9] R. Navarrete, R. Serrano, Biochim. Biophys. Acta 728 (1983) 403.
[10] V. De Pinto, R. Benz, F. Palmieri, Eur. J. Biochem. 183 (1989) 179.
[11] M.N. Jones, Int. J. Pharm. 177 (1999) 137.
[12] U. Sivars, K. Bergfeldt, L. Piculell, F. Tjerneld, J. Chromatogr. B 680 (1996) 43.
[13] U. Sivars, F. Tjerneld, Biochim. Biophys. Acta 1474 (2000) 133.
[14] P.C. McAda, M.G. Douglas, Methods Enzymol. 97 (1983) 337.
[15] P.K. Smith, R.I. Krohn, G.T. Hermanson, A.K. Mallia, F.H. Gartner, M.D. Provenzano, E.K. Fujimoto, N.M. Goeke, B.J. Olson, D.C. Klenk, Anal. Biochem. 150 (1985) 76.
[16] Y. Fujiki, A.L. Hubbard, S. Fowler, P.B. Lazarow, J. Cell Biol. 93 (1982) 97.
[17] P.A. Albertsson, F. Tjerneld, Methods Enzymol. 228 (1994) 3.
[18] D.E. Brooks, R. Norris-Jones, Methods Enzymol. 228 (1994) 14.
[19] V. Neuhoff, N. Arold, D. Taube, W. Ehrhardt, Electrophoresis 9 (1988) 255.
[20] I.P. Smirnov, X. Zhu, T. Taylor, Y. Huang, P. Ross, I.A. Papayanopoulos, S.A. Martin, D.J. Pappin, Anal. Chem. 76 (2004) 2958.
[21] D.N. Perkins, D.J. Pappin, D.M. Creasy, J.S. Cottrell, Electrophoresis 20 (1999) 3551.
[22] E. Mirgorodskaya, C. Braeuer, P. Fucini, H. Lehrach, J. Gobom, Proteomics 5 (2005) 399.
[23] A. Krogh, B. Larsson, G. von Heijne, E.L. Sonnhammer, J. Mol. Biol. 305 (2001) 567.
[24] D. Schluesener, F. Fischer, J. Kruip, M. Rogner, A. Poetsch, Proteomics 5 (2005) 1317.
[25] Y.J. Nikas, C.L. Liu, T. Srivastava, N.L. Abbott, D. Blankschtein, Macromolecules 25 (1992) 4797.
[26] O. Lambert, D. Levy, J.L. Ranck, G. Leblanc, J.L. Rigaud, Biophys. J. 74 (1998) 918.
[27] M. le Maire, P. Champeil, J.V. Moller, Biochim. Biophys. Acta 1508 (2000) 86.
[28] L. Piculell, B. Lindman, Adv. Colloid Interface Sci. 41 (1992) 149.
[29] L. Piculell, K. Bergfeldt, S. Gerdes, J. Phys. Chem. 100 (1996) 3675.
[30] L. Piculell, S. Nilsson, L. Falck, F. Tjerneld, Polym. Commun. 32 (1991) 158.
[31] H.O. Johansson, G. Karlstrom, F. Tjerneld, C.A. Haynes, J. Chromatogr. B 711 (1998) 3.
[32] R. Schomäcker, R. Strey, J. Phys. Chem. 98 (1994) 3908.
[33] M. Jonströmer, R. Strey, J. Phys. Chem. 96 (1992) 5993.
[34] H. Viklund, A. Elofsson, Protein Sci. 13 (2004) 1908.
[35] T. Joseph-Horne, D.W. Hollomon, P.M. Wood, Biochim. Biophys. Acta 1504 (2001) 179.
[36] A. Barrientos, M.H. Barros, I. Valnot, A. Rotig, P. Rustin, A. Tzagoloff, Gene 286 (2002) 53.
[37] I. Arnold, K. Pfeiffer, W. Neupert, R.A. Stuart, H. Schagger, EMBO J. 17 (1998) 7170.
[38] D. Leuenberger, N.A. Bally, G. Schatz, C.M. Koehler, EMBO J. 18 (1999) 4816.
[39] C. Klein, C. Garcia-Rizo, B. Bisle, B. Scheffer, H. Zischka, F. Pfeiffer, F. Siedler, D. Oesterhelt, Proteomics 5 (2005) 180.
[40] U. Krause-Buchholz, K. Barth, C. Dombrowski, G. Rodel, Curr. Genet. 46 (2004) 20.
[41] M.Q. Liu, L. Spremulli, J. Biol. Chem. 275 (2000) 29400.
[42] K.S. Crowley, R.M. Payne, J. Biol. Chem. 273 (1998) 17278.
[43] J.A. MacKenzie, R.M. Payne, J. Biol. Chem. 279 (2004) 9803.
[44] W. Voos, K. Rottgers, Biochim. Biophys. Acta 1592 (2002) 51.
[45] P. Giege, J.L. Heazlewood, U. Roessner-Tunali, A.H. Millar, A.R. Fernie, C.J. Leaver, L.J. Sweetlove, Plant Cell 15 (2003) 2140.
[46] X. Grandier-Vazeille, K. Bathany, S. Chaignepain, N. Camougrand, S. Manon, J.M. Schmitter, Biochemistry 40 (2001) 9758.
[47] M.S. Bhairi, A Guide to the Properties and Uses of Detergents in Biological Systems, Calbiochem, San Diego, 1997.
[48] B. Jönsson, B. Lindman, K. Holmberg, B. Kronberg, Surfactants and Polymers in Aqueous Solution, Wiley, Chichester, 1998.
[49] G. von Jagow, T.A. Link, H. Schägger, Purification Strategies for Membrane Proteins, Academic Press, San Diego, 1994.

II

Precise detection of pH inside large unilamellar vesicles using membrane-impermeable dendritic porphyrin-based nanoprobes

Thom Leiding [a], Kamil Górecki [a], Tomas Kjellman [b], Sergei A. Vinogradov [b], Cecilia Hägerhäll [a], Sindra Peterson Årsköld [a,*]

[a] Department of Biochemistry, Center for Chemistry and Chemical Engineering, Lund University, P.O. Box 124, 22100 Lund, Sweden
[b] Department of Biochemistry and Biophysics, University of Pennsylvania, Philadelphia, PA 19104, USA

ARTICLE INFO

ABSTRACT

Accurate real-time measurements of proton concentration gradients are pivotal to mechanistic studies of proton translocation by membrane-bound enzymes. Here we report a detailed characterization of the pH-sensitive fluorescent nanoprobe Glu^3, which is well suited for pH measurements in microcompartmentalized biological systems. The probe is a polyglutamic porphyrin dendrimer in which multiple carboxylate termini ensure its high water solubility and prevent its diffusion across phospholipid membranes. The probe's pK is in the physiological pH range, and its protonation can be followed ratiometrically by absorbance or fluorescence in the ultraviolet-visible spectral region. The usefulness of the probe was enhanced by using a semiautomatic titration system coupled to a charge-coupled device (CCD) spectrometer, enabling fast and accurate titrations and full spectral coverage of the system at millisecond time resolution. The probe's pK was measured in bulk solutions as well as inside large unilamellar vesicles in the presence of physiologically relevant ions. Glu^3 was found to be completely membrane impermeable, and its distinct spectroscopic features permit pH measurements inside closed membrane vesicles, enabling quantitative mechanistic studies of membrane-spanning proteins. Performance of the probe was demonstrated by monitoring the rate of proton leakage through the phospholipid bilayer in large vesicles with and without the uncoupler gramicidin present. Overall, as a probe for biological proton translocation measurements, Glu^3 was found to be superior to the commercially available pH indicators.

© 2009 Elsevier Inc. All rights reserved.

Advanced molecular sensors is a rapidly developing area of research [1], and proton nanosensors attract special interest because of their applicability in monitoring proton concentrations in biological microcompartments. Proton concentration gradients play a pivotal role in the processes of respiratory and photosynthetic energy conversion and regulation. These gradients are created and maintained by bioenergetic proton-translocating membrane-bound protein complexes, the reactions of which involve highly reactive intermediates that can produce damaging radicals. These bioenergetic enzymes are implicated in natural aging [2] and serious degenerative conditions such as Parkinson's disease [3–6]. Furthermore, misbalanced pH in cellular compartments is a key miscreant in cancer drug resistance, and the proton pumps and channels involved in tumor biology are under intense scrutiny [7–10].

Much structural information on bioenergetic proteins has emerged over the past decade. However, to understand the molecular mechanisms of their action, it is crucial to accurately measure electron transfer and proton translocation stoichiometries, and for this, quantitative methods for monitoring proton translocation are needed.

In proton translocation studies, the enzyme of interest must reside in the membrane of a closed vesicle, and the membrane itself must be proton impermeable on the time scale of the translocation process. The closed vesicle may be the native membrane of the protein (see, e.g., Ref. [11]) or one artificially prepared from a known phospholipid composition. The latter offers a well-defined experimental system where no unknown or unwanted proteins are present. To monitor proton concentrations in this system, non-invasively and dynamically, pH-sensitive molecular probes are used. Ideally, the proton concentration inside the vesicles and that of the bulk solution should be monitored simultaneously. Unfortunately, the characteristics of the available pH probes do not accommodate such measurements; many of them are membrane permeable, and most of them have too weak spectroscopic signals to report pH from the interior of vesicles dispersed in a bulk solution. These difficulties have been cleverly sidestepped in proton translocation studies on several important protein complexes

Table 1
Comparison of pH and membrane-potential probes.

Indicator	Membrane permeable?	Detection[a]	Indicates[b]	Residual dye after bead incubation	Reference
Neutral red	Yes	A	[H+]	n.a.	[41]
Phenol red	No	A	[H+]	<1%	[16]
Pyranine (HPTS)	No	A, F	[H+]	44%	[42]
BCECF	No	A, F	[H+]	67%	[43]
SNARF	No	A, F	[H+]	< 1%	[22]
SNARF–dextran (10 kDa)	No	A, F	[H+]	72%	[23]
Glu[3]	No	A, F	[H+]	> 99%	
Oxanol	Yes	A	$\Delta\psi$	n.a.	[44]
ACMA	Yes	F	Δ[H+]	n.a.	[45]

Note. n.a., not applicable; HPTS, hydroxypyrenetrisodium; BCECF, bis(carboxyethyl) carboxyfluorescein; ACMA, aminochloromethoxy acridine.

[a] Absorbance (A) and/or fluorescence (F).

[b] Proton concentration ([H+]), membrane potential (ψ), or proton concentration difference (Δ[H+]).

(see, e.g., Refs. [12–14]). However, experiments with available probes have reached their full potential; further progress requires better molecular pH sensors.

Several common commercial colorimetric pH indicators are presented in Table 1. Membrane-permeable pH-sensitive dyes, such as neutral red, have been used to monitor intravesicular pH changes using a solution of low buffer strength inside the vesicle and high buffer strength in the bulk phase. Although neutral red could diffuse freely in and out of the vesicle, the different buffer concentrations ensured that the detected spectral changes arose exclusively from the probe present inside the vesicles. However, a probe that diffuses through and associates with the membrane is likely to alter the membrane properties, affecting the measurements in an unpredictable manner. Neutral red was reported to show significant protonophore activity, facilitating proton transfer across the membrane [15]. A permeable probe may also accumulate on one side of the membrane as the pH changes. In addition, the difference in the buffering capacities required for these experiments excludes simultaneous pH measurements on both sides of the membrane. Phenol red [16] is less likely to diffuse across the membrane but displays relatively weak spectroscopic signals, making it less suitable for intravesicular pH determination. A combination of experiments using membrane-permeable neutral red and membrane-impermeable phenol red resulted in pumping stoichiometries of 2 H^+/e^- for the respiratory complex I [17,18], and 3.6 H^+/e^- for complex I reconstituted in proteoliposomes were obtained [14,19]. The seminaphthofluorescein chromophore SNARF[1,2] also monitors pH and does not diffuse significantly through lipid bilayers. It was, however, shown to bind to the membrane surface of large unilamellar vesicles (LUVs) and small unilamellar vesicles (SUVs), resulting in a sensor subpopulation with characteristics different from those of the dissolved probe [20]. The ratiometric fluorescence probe pyranine is more suitable for monitoring intravesicular pH and has been combined with the membrane potential probe oxonol for mechanistic studies of H^+-ATPase [21]. However, the modest brightness of pyranine fluorescence limits the sensitivity of these measurements. These problems may be avoided by using improved membrane-impermeable pH probes.

Ideal characteristics of a pH probe for proton translocation measurements include membrane impermeability, high molar extinction coefficients in both protonated and nonprotonated forms,

high water solubility, and no tendency to aggregate or form complexes with biological macrostructures. If measurements involve fluorescence, the emission quantum yields of both protonated and nonprotonated forms should be high enough to allow ratiometric pH detection. The only commercially available probes of this kind are SNARF–dextrans, which have been used in several proton-pumping studies [22,23]. The ligation of a dextran moiety to the SNARF chromophore effectively eliminates probe diffusion through membranes, but the SNARF group in these conjugates can still bind to membrane lipids. Furthermore, the molecular compositions of SNARF–dextrans are not uniquely defined, and although they permit ratiometric measurements, the spectral changes accompanying their protonation are not large.

Dendritic pH probes offer a number of advantages over SNARF–dextran complexes. Porphyrin-based probes, such as Glu[3] (see Fig. 1) [24], possess distinctly different absorption and fluorescence features in protonated and nonprotonated forms (see below). Their absorption (Soret) bands are sharper and stronger than those of SNARF, facilitating detection of small pH changes. Hydrophilic dendritic cages render probes like Glu[3] very water soluble, whereas multiple peripheral carboxylates prevent interactions with biological membranes. Furthermore, we found that the SNARF chromophore is easily lost during the preparation of proteoliposomes (see "Probe adhesion to hydrophobic beads" section in Materials and methods), whereas Glu[3] remains stable and in solution throughout the procedure. This combination of properties makes Glu[3] an attractive alternative to SNARF–dextrans for biological proton translocation measurements.

In this work, we characterize the pH-sensitive, membrane-impermeable probe Glu[3] (generation 3 polyglutamic porphyrin dendrimer [25]) and validate its potential for biological pH measurements. Glu[3] consists of a tetraarylporphyrin core with four covalently attached polyglutamic dendrons, terminated by carboxylic acid groups. The optical spectra of the porphyrin are distinctly different in the nonprotonated (free-base) and doubly protonated (dication) forms (see Fig. 2A). The negative charges of the ionized carboxylates shift the pK of the intrinsically weakly basic porphyrin to higher pH values, placing it in the physiological pH range [25]. The peripheral charges also render Glu[3] highly water soluble and membrane impermeable [24]. These qualities allow monitoring of proton translocation across membranes by nonintrusive detection of pH inside closed phospholipid vesicles.

Glu[4] (generation 4 polyglutamic porphyrin dendrimer), a dendritic probe similar to Glu[3], was used in our previous experiments involving SUVs (20–30 nm in diameter). Glu[4] was demonstrated to be retained inside the vesicles and to report on their internal pH [24]. Later, this probe was used to demonstrate formation of synthetic membrane-spanning channels made of dendritic dipeptides [26,27]. The current probe Glu[3] exhibits a pK similar to that of Glu[4]

---

[1] *Abbreviations used:* SNARF, seminaphthorhodafluor; LUV, large unilamellar vesicle; SUV, small unilamellar vesicle; Glu[3], generation 3 polyglutamic porphyrin dendrimer; Glu[4], generation 4 polyglutamic porphyrin dendrimer; CCD, charge-coupled device; UV, ultraviolet; PMT, photomultiplier tube; H₂TPP, tetraphenylporphyrin; SNR, signal-to-noise ratio; fb, free base; dc, dication; EDTA, ethylenediaminetetraacetic acid; cryo-TEM, transmission electron microscopy at cryogenic temperatures; DMSO, dimethyl sulfoxide; H₂P, tetraarylporphyrin chromophore.

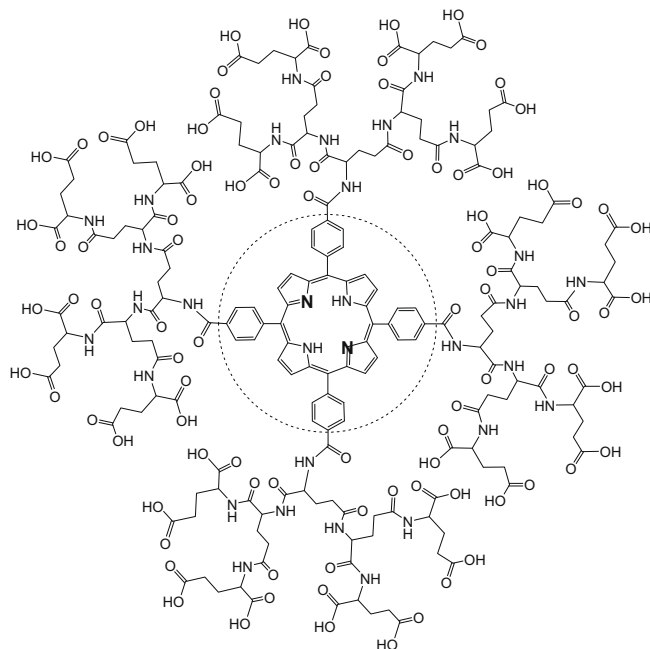[2] SNARF pH indicators (Invitrogen).

Fig. 1. Molecular structure of probe Glu[3]. The tetraarylporphyrin chromophore (H$_2$P) is shown inside the dashed circle, and the nitrogen atoms undergoing protonation are shown in bold. The molecular weight of the probe is 4406 Da as the polycarboxylic acid and 5110 Da as the poly-Na$^+$ salt.

but can be synthesized in fewer steps. Neither probe has yet been calibrated with the precision required for mechanistic studies of proton-translocating enzymes. For such measurements, the ability to monitor small pH changes at low dye concentrations is required; many proton-pumping studies have been carried out in the absence of buffer, with exact control of the buffering capacity being sacrificed so as to obtain detectable signals [12,13,28]. Furthermore, the behavior of the probe in the presence of metal cations, biological macromolecules, and phospholipid membranes needs to be evaluated accurately.

Rather than using poorly defined SUVs with small internal volumes (on the order of 10^{-21} L/vesicle), we have adapted methods for probe incorporation into well-characterized LUVs of uniform size (on the order of 10^{-18} L/vesicle). The LUVs have an approximately 10 times larger diameter than the SUVs, accommodating larger amounts of the probe and, thus, permitting accurate determination of pH not only by fluorescence but also by absorption.

In this work, Glu[3] was investigated using a newly developed semiautomatic titration system.[3] The system is based on a charge-coupled device (CCD) spectrometer from which output is fed automatically into an analysis program. This setup ensures precision, eliminates user-to-user variability, and significantly reduces the time required for titration experiments. CCD detection enables the full absorption spectrum to be collected in 1.1 ms, providing the user with continuous control of all chromophores in the sample. The evaluation presented in this article provides the basis for a robust, quantitative pH detection method, optimized specifically for pH measurements in the interior of liposomes. This method can be ap-

plied directly to determination of proton-pumping stoichiometries of bioenergetic enzymes. By adding a different pH probe to the bulk solution or monitoring the bulk pH with an electrode, the pH change on each side of the vesicle membrane can be monitored simultaneously [24]. This excludes proton concentration changes incurred by reactions other than proton translocation and enhances the sensitivity of the measurements. If the protein contains optically detectable cofactors, these will be monitored as well, giving a uniquely comprehensive picture of the proton translocation process.

Materials and methods

Optical spectroscopy and titrations

Optical absorption spectra were recorded either on a PerkinElmer Lambda 35 ultraviolet-visible spectrophotometer or by using an in-house-constructed CCD-based spectrometer (see below). Steady-state fluorescence measurements were performed on an SPEX Fluorolog-2 spectrofluorometer (HORIBA Jobin Yvon) equipped with Hamamatsu R2658P photomultiplier tube (PMT). Emission spectra were obtained using aqueous solutions (50 mM phosphate buffer, total [K$^+$] = 50 mM) of Glu[3] (4–5 μM) with absorbance of approximately 0.05 OD at the excitation maxima. The emission quantum yields of Glu[3] as the free base (pH 8.0) and dication (pH 4.0) were determined relative to the fluorescence of free-base tetraphenylporphyrin (H$_2$TPP) in deoxygenated benzene ($\phi_{fl} = 0.11$) [29]. For pH titration by fluorescence, the pH of a buffered solution of the probe (~30 ml total volume) was adjusted by adding small portions of concentrated solutions of HCl and KOH (5 M). The pH step was 0.5 to 1.0 units. At each pH, two emission spectra, excited at 515 nm (free base) and 600 nm (dication),
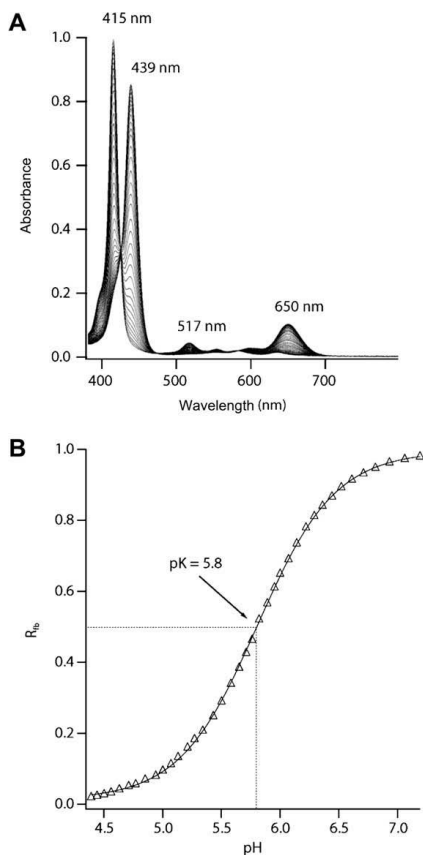
_____
[3] Autonomous Science Machines.

Fig. 2. (A) Absorption spectra of Glu^3 in 5 mM potassium phosphate buffer with total [K$^+$] = 9 mM and [Mg^{2+}] = 1 mM, recorded with pH varying from 7.2 to 4.4. (B) Fraction of free-base Glu^3 derived from the data in panel A using Eq. (1). The data were fitted by Eq. (3) (solid line), giving pK = 5.8 (n = 1.3).

were recorded. The spectra were integrated, and the ratio of the integrals (plotted against pH) was analyzed (see below) to yield the value of the apparent pK. Three independent titrations were averaged to obtain the calibration curve.

Titrations by absorption were performed using an in-house-constructed system. The spectra were recorded using a fiber-optic absorption spectrometer (AvaSpec-2048, Avantes) with a tungsten/halogen light source. The spectrometer was coupled to a sample holder featuring stirring, a controlled atmosphere, an electrode duct, and two capillary inlets. Two Hamilton syringes (100 μl total volume), attached to computer-controlled syringe pumps (NE-500, New Era Pump Systems), were connected to the capillary inlets of the sample holder. The syringe pumps administered precise volumes of 0.5 M HCl and KOH solutions, calculated by the controlling software to achieve the desired pH. The actual pH of the bulk solution was measured by a combination pH microelectrode (Orion ROSS, Thermo Scientific) fitted to the electrode duct of the sample holder. The software was configured to set a series of pH points and acquire the absorption spectrum at each pH.

To investigate the effects of metal cations, Glu^3 was added to solutions of potassium or magnesium salts to a final probe concen-

tration of approximately 2 μM. The acquisition time for each spectrum was 1.1 ms, and 1024 spectra were averaged for each pH point. This configuration results in an extremely high signal-to-noise ratio (SNR) throughout the entire spectral range, with a temporal resolution of 1.2 s. If a lower SNR is acceptable, the system achieves millisecond time resolution.

Data analysis

The fraction of nonprotonated Glu^3 at a given pH (R_{fb}) was derived from the absorbances at the Soret peaks of the free base (fb, where A_{415} is absorbance at 415 nm) and the dication (dc, where A_{439} is absorbance at 439 nm):

$$R_{fb} = \frac{1.04 \times A_{415} - 0.22 \times A_{439}}{A_{415} + A_{439}} \quad (1)$$

In Eq. (1), the absorbances were corrected for the slightly differing extinction coefficients of the free-base and cation Soret maxima ($\varepsilon_{fb}/\varepsilon_{dc}$ = 1.17) and for the partial overlap of the absorption bands. The correction values were determined experimentally using the spectra acquired at pH 4.5 for the dication and at pH 7.2 for the free base. (Complete protonation of the porphyrin requires very acidic conditions at which polyglutamic branches might undergo partial hydrolysis. At pH 4.5, less than 5% of the probe is deprotonated, introducing less than 1% error in Eq. 1.) Measurements involving liposome-encapsulated Glu^3 required subtraction of the scattering baseline prior to determination of A_{415} and A_{439}.

The equation for the analysis of the fluorescence data was

$$R_{fb} = \frac{I_{E515} - 0.18 \times I_{E600}}{0.77 \times I_{E515} + 2.12 \times I_{E600}}, \quad (2)$$

where I_{E515} is the integrated fluorescence spectrum when exciting at 515 nm, corresponding to the free base, and I_{E600} is the integrated fluorescence spectrum when exciting at 600 nm, corresponding to the dication. As in Eq. (1), corrections for different band intensities and spectral overlap were made. The protonation state of the dye, determined by absorbance (Eq. 1) or fluorescence (Eq. 2), was fitted with a sigmoidal curve according to the Hill equation [30]:

$$R_{fb}(pH) = \frac{10^{n(pH-pK)}}{1 + 10^{n(pH-pK)}}, \quad (3)$$

where pK refers to the apparent protonation constant (see below) and corresponds to the pH at which R_{fb} = 0.5. The Hill equation with n = 1 is valid for a protonation reaction involving a single proton. However, it can be applied to protonations involving more than one proton by using the floating parameter n if the protonations have close equilibrium constants. The resulting apparent pK represents the average of the protonation constants. Notably, constant K in Eq. (3) corresponds to the equilibrium where the forward reaction is the dissociation of protons from the dication (see Scheme 1) rather than the protonation of the free base.

Glu^3 can also be analyzed ratiometrically by monitoring the absorbance ratio $R = A_{415}/A_{439}$ or the ratio of fluorescence intensities or inetgrals (vide infra). Plotting R versus pH results in a sigmoidal curve, displaying a midpoint that is significantly higher than the apparent pK and a larger dynamic range along the y axis.

$$H_4P^{2+} \underset{+H^+}{\overset{K_1}{\rightleftharpoons}} \left(H_3P^+ \right) \underset{+H^+}{\overset{K_2}{\rightleftharpoons}} H_2P$$
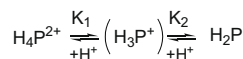
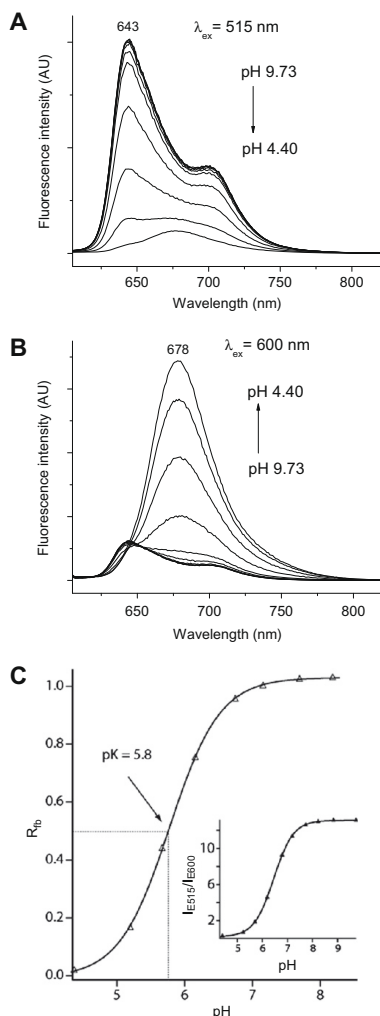**Scheme 1.** Protonation of the core porphyrin (H$_2$P) in Glu^3.

A

B

C

Fig. 3. (A, B) Fluorescence spectra of Glu[3] in 50 mM potassium phosphate buffer: (A) λ_{ex} = 515 nm; (B) λ_{ex} = 600 nm. (C) Fraction of free-base Glu[3] derived from the integrated fluorescence spectra from panels A and B using Eq. (2). The data were fitted by Eq. (3) (solid line), giving pK = 5.8 (n = 1.2). The inset shows the ratio of the integrated fluorescence spectra, I_{E515}/I_{E600}, plotted against pH and fitted to a sigmoidal curve. The midpoint pH derived from the inset is 6.45. [Glu[3]] = 4–5 μM; total [K^{+}] = 50 mM.

Liposome preparation and dye inclusion

LUVs were prepared following the method described by Rigaud and Levy [31]. High-purity phosphatidyl choline from egg yolk (Sigma–Aldrich) was used to prepare multilamellar vesicles by re-verse-phase evaporation. In each preparation, 0.5 ml of lipid in chloroform at 100 mg/ml was used. The chloroform was evaporated under vacuum, and the resulting lipid film was dissolved in 3 ml of diethyl ether and sonicated with 1 ml of 20 mM potassium phosphate buffer with 0.5 mM ethylenediaminetetraacetic acid

(EDTA, pH 7.2). This resulted in a water-in-oil emulsion. Sonication was performed on ice during four periods of 30 s separated by periods of 15 s. The organic phase was removed by evaporation under 0.5 atm of nitrogen for 2 h. Also, 2 ml of the buffer was added to the resulting material, and the suspension was dried for 1 h to remove the remaining traces of diethyl ether. The suspension was extruded in series through polycarbonate filters with pore sizes of 400 and 200 nm using an extruder (LiposoFast, Avestin) [32]. A total of nine extrusions were performed. The preformed liposomes were diluted in a buffer to a final lipid concentration of 5 mg/ml, solubilized by the addition of 80 mg of the detergent Triton X-100 to achieve a 2:1 (w/w) detergent/lipid ratio, and stirred for 20 min or until the solution became optically transparent. Glu[3] was added to a final concentration of approximately 0.2 mM. Detergent was removed by adding moist beads (SM-2 Bio-Beads, Bio-Rad) in four portions of 800 mg, with 1 h of gentle stirring between the additions. The removal of the detergent was monitored optically by the OD at 700 nm, which represents light scattering caused by the assembling liposomes. The vesicles were harvested 15 min after the OD became constant. Prior to use, the beads were washed with methanol and deionized water alternatively (three cycles) and then with deionized water (three times) to remove traces of methanol. To remove Glu[3] from the bulk solution, the liposomes were purified by size exclusion chromatography [24] on a Sephadex G200 column (GE Healthcare) containing a layer of Sephadex A50 anion exchange resin (GE Healthcare) at the bottom [24]. The resin was degassed under vacuum before use. The resulting vesicles were stored at 4 °C.

Probe adhesion to hydrophobic beads

Five commercially available pH-sensitive dyes and Glu[3] (see Table 1) were each added to a separate 2-ml sample of 20 mM potassium phosphate buffer solution at pH 7.2 to give the final dye concentration of 200 μM. Each probe solution was divided into two aliquots of 1 ml, one of which was put aside for control. Pre-washed SM-2 beads (100 mg) were added to each sample, followed by 60 min of stirring. Then a second portion of 50 mg of beads was added, followed by 60 min of stirring. The dye solutions were separated from the beads, and the absorbance spectra of these solutions were compared with those of the reference samples.

Cryo-TEM

The morphology of the liposomes was investigated by transmission electron microscopy at cryogenic temperatures (cryo-TEM) [33]. For the preparation of the unstained, frozen, hydrated liposome specimen, a 5-μl droplet of the liposome suspension (∼4 mg of lipid/ml) was deposited on an electron microscopy grid. After removing the excess solution with a filter paper, the thin layer of aqueous solution was rapidly plunged into liquid ethane at −178 °C. The grid, kept under liquid nitrogen, was then transferred into a cryoholder maintained at −170 °C, which in turn was introduced into the electron microscope for observation at the same temperature. Liposomes from several cryo-TEM images were measured to estimate the size distribution.

Monitoring the probe inside liposomes

Titration measurements were performed using LUV suspensions in potassium phosphate buffer (20 mM) at 20 °C in the absence and presence of gramicidin. Gramicidin was added as a solution in dimethyl sulfoxide (DMSO) to a final concentration of approximately 1 μg/ml. In the pH jump experiment (see Fig. 8), pH was changed from 7.2 to 5.6 by a single addition of 0.5 M solution of HCl. Following the addition, the spectrum of the probe was

monitored for 30 min, after which gramicidin was added and the final spectrum was recorded. The net flux of protons and hydroxyl ions, J_{net}, was calculated as

$$J_{net} = \frac{\Delta pH_i}{\Delta t} \times \frac{B_i \times V_i}{A}, \tag{4}$$

where ΔpH_i is the change of internal pH during the time interval Δt, V_i is the internal volume, B_i is the buffer capacity of the internal volume, and A is the total membrane area [34].

Results and discussion

Probe Glu³

The molecular structure of the probe Glu³ is shown in Fig. 1. The probe was synthesized by the mixed convergent/divergent method described previously [24,25,35]. The probe's molecular weight as a polyglutamic acid is 4402 Da. The porphyrin macrocycle in Glu³ (tetraarylporphyrin chromophore [H₂P], shown inside the circle in Fig. 1) undergoes two sequential protonations, resulting in the formation of the dication. It is more common to consider dissociation of the protons from the dication as the forward reaction rather than the protonation of the free base. The dication H_4P^{2+} can then be viewed as a Brønsted acid characterized by two ionization constants K_1 and K_2 (Scheme 1).

Protonation of porphyrins is accompanied by distinct changes in the optical spectra, for example by red shifts of the Soret bands (see Fig. 2A). The protonations can be followed spectroscopically by plotting a characteristic absorbance intensity of either of the forms, or their ratio, versus pH (Fig. 2B). For the majority of porphyrins, constants K_1 and K_2 are very close, and the monocation H_3P^+ is an elusive species whose concentration is extremely low at all proton concentrations [36]. Accordingly, instead of fitting the data to a function describing two sequential protonations, it is more practical to use the analytical equation describing a single protonation (Eq. 3), allowing variation of the parameter n. The derived apparent constant K is suitable for the characterization of the overall equilibrium [37].

The use of a floating parameter n in Eq. (3) is also justified by the fact that the pK values of the multiple glutamic carboxylates at the periphery of Glu³ span a broad range. Although the pK values of an isolated glutamic acid are well defined, 2.19 and 4.25, in Glu³, 16 closely positioned peripheral glutamic residues affect each other's protonation states and significantly broaden the protonation range of the core porphyrin. The net effect of the ionized glutamates is stabilization of the porphyrin dication and a shift of the pK to higher values compared with the "naked" porphyrin [24,25].

Automated pH titration spectroscopy

We have constructed an automated titration system coupled to a fiber-optic CCD spectrometer, as detailed in Materials and methods. CCD detection sidesteps baseline drift problems associated with monochromators and provides full spectral coverage suitable for monitoring the state of the sample continuously. Automated titration eliminates user-to-user variability, minimizes titration errors, and facilitates fast and reproducible titrations and analyses of large numbers of samples. Once the experimental parameters have been set and the titration has been initiated, this system performs the complete titration without user attendance. A typical pH titration experiment consisting of 20 spectral measurements at pH values separated by $\Delta pH = 0.1$ is completed within 25 min. The resulting spectra are automatically analyzed to reveal the protonation state of the sample at each pH (Eq. 1), after which the data are fitted to Eq. (3).

Porphyrin dendrimers as pH sensors

The change of the Glu³ absorption spectrum during titration is shown in Fig. 2A. Overall, this titration features a stable baseline, a clean isosbestic point, and an accurate fit of the data points to Eq. (3) (Fig. 2B). The titration starts with the free-base form, exhibiting absorption maxima at 415 nm (Soret band) and 517 nm (Q band). These features decrease with a decrease in pH in favor of the peaks at 439 and 650 nm, originating from the doubly protonated (dicationic) form. The spectra of Glu³ are virtually identical to those reported previously for Glu⁴ [24].

The relative amount of the probe in its free-base form at any given pH can be estimated by comparing the intensity of the Soret peaks at 415 and 439 nm, as detailed in Materials and methods (Eq. 1). Plotting this fraction, R_{fb}, as a function of pH and fitting it with Eq. (3) yields the pK value of 5.8 for Glu³ in 20 mM potassium phosphate buffer with total [K⁺] = 34 mM.

In the free-base form, Glu³ fluoresces with quantum yield $\phi_{fl}(fb) = 0.16$. In spite of the strong nonplanar deformation of the porphyrin macrocycle induced by protonation [38], the Glu³ dication fluoresces with nearly the same quantum yield, $\phi_{fl}(dc) = 0.15$, as the free base. On protonation, the emission spectra undergo a red shift (Fig. 3A and B) mirroring that of the absorption. The probe was excited at wavelengths corresponding to the free base and the dication: 515 and 600 nm, respectively. Using the integrated fluorescence spectra (Fig. 3A and B) as indicators of the dication and free-base concentrations, the fraction of free-base Glu³ was calculated using Eq. (2), plotted versus pH, and fitted with Eq. (3) (Fig. 3C). The fit yields pK = 5.8, in good agreement with that derived from the titration by absorption (Fig. 2B).

Fig. 3 clearly demonstrates that Glu³ can be used as a ratiometric fluorescent pH sensor, as it exhibits practically equal brightness (molar extinction times quantum yield) in its nonprotonated and protonated forms. This property is rare for fluorescent pH indicators, most of which fluoresce only in one form and do not permit ratiometric measurements. The accuracy of R_{fb} (Eqs. 1 and 2) is enhanced considerably when both states are followed spectroscopically. When the ratio of the integrated fluorescence spectra, I_{E515}/I_{E600} is, plotted against pH, as is shown in the inset of Fig. 3C, the midpoint of the plot occurs at a pH higher than the pK (6.45 compared to 5.8).

The following experiments were based on absorption measurements conducted using the system described above.

Ion effects on the dye

The absorption spectrum of Glu³ changes gradually and irreversibly in the presence of Zn²⁺ ions, probably as a result of the insertion of Zn²⁺ into the porphyrin. Subsequently, all zinc-containing materials were excluded from the experimental system and 0.5 mM EDTA was added to all solutions studied. Cu²⁺ effects similar spectroscopic changes (data not shown), and other metal ions with high affinity to the tetrapyrrole macrocycle can potentially influence the signal. Fortunately, common two-valent cations, such as Ca²⁺ or Mg²⁺, do not form stable complexes with porphyrins in aqueous solution and do not affect the measurements.

The pK values of dendritic polyglutamic probes such as Glu³ can be influenced by the complexation between the peripheral carboxylate groups and metal cations. Such complexation can reduce the effective negative charge around the porphyrin, decreasing its apparent pK [24,25]. To quantify this effect, we performed a series of pH titrations in the presence of K⁺ and Mg²⁺ ions. [K⁺] was varied between 2.5 and 200 mM, and [Mg²⁺] was varied between 0 and 8 mM. The results are displayed in Fig. 4. For both K⁺ and Mg²⁺, the pK of the probe decreases with an increase in the cation concentration. This effect is much more pronounced in the case of
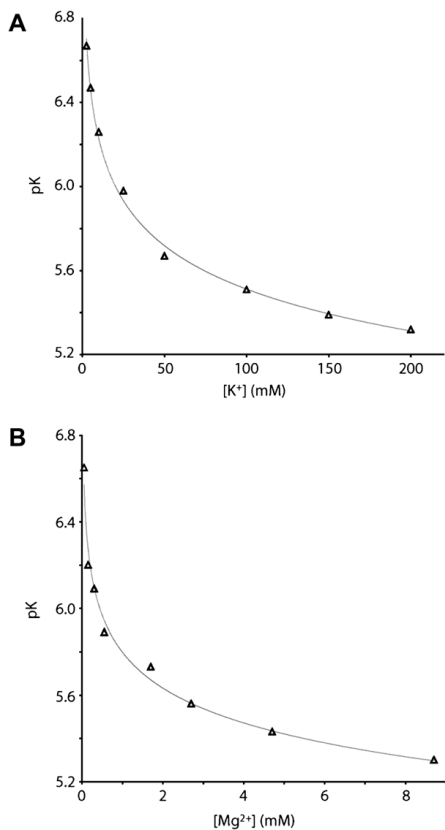
Fig. 4. pK values of Glu[3] as a function of [K⁺] (A) and [Mg²⁺] (B). For clarity, the data were fitted with these functions: $7.04 \times pH^{-0.00531}$ (K⁺) and $5.82 \times pH^{-0.00417}$ (Mg²⁺).

Mg²⁺. The salt effect is reproducible and stable, and it provides a means by which to tune Glu[3] toward a desired pK.

At the concentrations [K⁺] = 50 mM and [Mg²⁺] = 1 mM, typical for many protein assays, the pK of Glu[3] at 2 µM is close to 5.6. At a lower ion concentration, [K⁺] = 10 mM and no Mg²⁺, pK is approximately 6.3. This pK enables pH measurements at physiological pH values, and the pK is increased further when monitoring intravesicular pH (see below). The effect of Na⁺ was similar to that of K⁺ (data not shown).

Dye adsorption to hydrophobic beads

Most protein reconstitution methods include a step of detergent removal conducted by dilution, dialysis, or the use of detergent-absorbing hydrophobic polystyrene beads [31,39]. Hydrophobic beads are preferable because they guarantee virtually complete detergent removal, a narrow distribution of vesicle sizes, and no sample dilution. For the dye to be included in the liposomes, it needs to be added prior to detergent removal. Therefore, it is crucial that the probe remains dissolved throughout this process. We have tested several commercially available pH probes with respect to their adsorption to beads (see Table 1). All of the membrane-impermeable colorimetric probes were found to adsorb to hydrophobic beads to some extent. Glu[3] stands out, showing a very

low propensity to adsorb to the beads. This makes this probe particularly suitable for inclusion into proteoliposomes.

Inclusion of the probe into liposomes

To calibrate Glu[3] for intravesicular pH measurements, it was characterized while encapsulated in LUVs. Glu[3] was enclosed in phospholipid LUVs, and the excess probe was rigorously removed from the bulk solution outside the vesicles as described in Materials and methods. The probe concentration was 200 µM (i.e., ∼100 times higher than that in the bulk experiments, Figs. 2–4). A cryo-TEM image of the Glu[3]-containing vesicles is shown in Fig. 5A. The vesicles are predominantly unilamellar. The darkening of the vesicle centers reveal that they protrude out of the surface of the isomorphous ice, suggesting that they have not been flattened during the TEM sample preparation procedure. The excellent mechanical stability of the vesicles is also confirmed by the fact that close-lying vesicles do not coalesce but rather show slight signs of deformation. The LUVs have a mean diameter of 150 nm and exhibit a relatively homogeneous size distribution; the diameters of 80% of the vesicles are distributed within ±50 nm of the mean value (Fig. 5B).

The spectra and pK of Glu[3] in liposomes were measured in the presence of gramicidin (Fig. 6A). Gramicidin is a pore-forming pep-
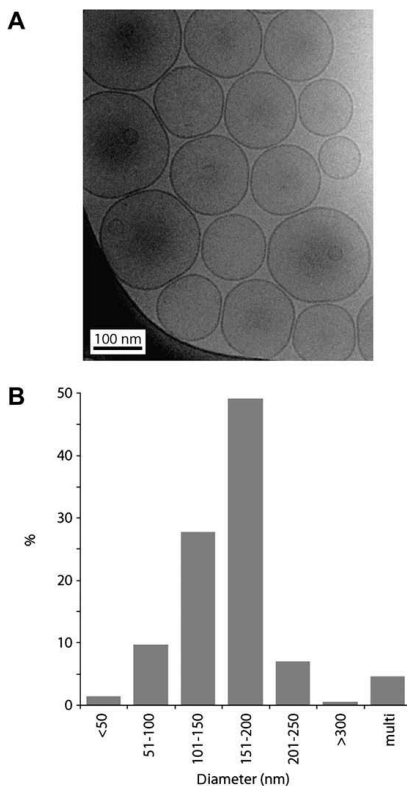

Fig. 5. (A) Transmission electron micrograph of LUVs made from egg yolk phosphatidyl choline containing Glu[3]. (B) Size distribution of 216 vesicles.

tide [40] in which oligomers form membrane-spanning channels, allowing protons, but not large charged molecules such as Glu^3, to pass through the lipid bilayer. Thus, in the presence of gramicidin, the bulk pH and the pH inside the vesicles are rapidly equilibrated, whereas Glu^3 remains inside. The spectra of protonated and nonprotonated Glu^3 captured inside the vesicles are shown in Fig. 6A. The slope of the baseline is caused by the scattering of the vesicles; however, the spectra themselves are identical to those in Fig. 2A. Since the scattering does not vary with pH, the SNR of the titration curve is practically unaffected by the vesicle encapsulation. The strength of the measured signal suggests that the probe concentration and/or the spectral averaging time can be decreased considerably without compromising measurement accuracy.

Notably, when titrated inside the gramicidin-containing vesicles, the probe showed significantly higher pK than in the solution experiments (6.3 vs. 5.8) (Fig. 6B). This increase may be explained by the cation effect discussed above. Although the ion concentration is the same within the vesicles as in the solution ($[K^+] = 34$ mM), the probe concentration inside the vesicles is 100 times higher than it was in the solution experiments. Thus, the salt concentration per probe molecule is lower, and the pK attenuation effect (Fig. 4) is diminished. To test this hypothesis, we determined
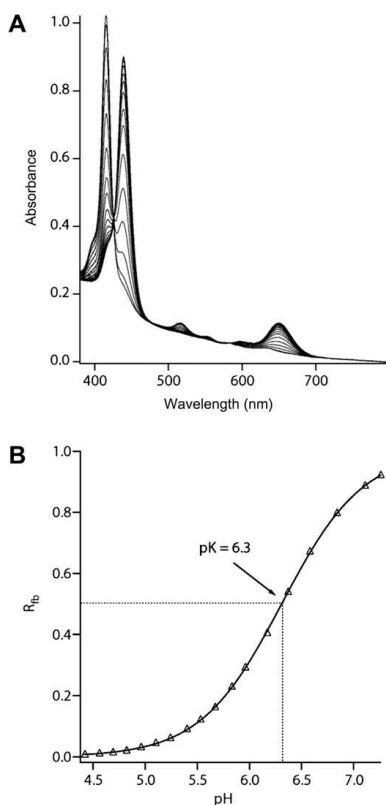
the pK of Glu^3 in 4 mM K^+ solution at $[Glu^3] = 20$ and 2 μM. This 10-fold increase of Glu^3 concentration led to a 1% increase in pK (pK = 6.55 and 6.48, respectively, $n = 1.1$ in both cases [data not shown]), consistent with a minor effect of the Glu^3 concentration on the pK value.

Fig. 7 displays the results of an experiment identical to that in Fig. 6 but performed in the absence of gramicidin. While pH in the medium was titrated from 7.5 to 4.6, the probe inside the liposomes remained virtually unaffected (solid spectra). When gramicidin was added at the end of the titration, rendering the lipid bilayer proton permeable, the probe was immediately protonated (dashed spectrum, lowest data point in Fig. 7B). The titration curve of the encapsulated probe in Fig. 6B is superimposed on Fig. 7B (inversed with the inversed x axis), demonstrating nearly perfect reproducibility at the end points of the titration. The slight increase in the pH after the addition of gramicidin is due to the accessibility of the encapsulated buffer ions and dye molecules (which also have buffering capacity) to the bulk protons. The buffer is near its pK inside the vesicles and so only 50% protonated, whereas the bulk buffer ions have nearly no buffering capacity at the end of the titration (pH 4.6). When gramicidin is added, the encapsulated buffer and dye molecules bind protons from the bulk, causing

Fig. 6. (A) Absorption spectra of Glu^3 enclosed in LUVs with membranes percolated by gramicidin. (B) Fraction of free-base Glu^3 derived from the data in panel A using Eq. (1) as a function of pH. The experimental data (solid line) were fitted by Eq. (3), giving pK = 6.31 at $[K^+] = 34$ mM ($n = 1.1$).
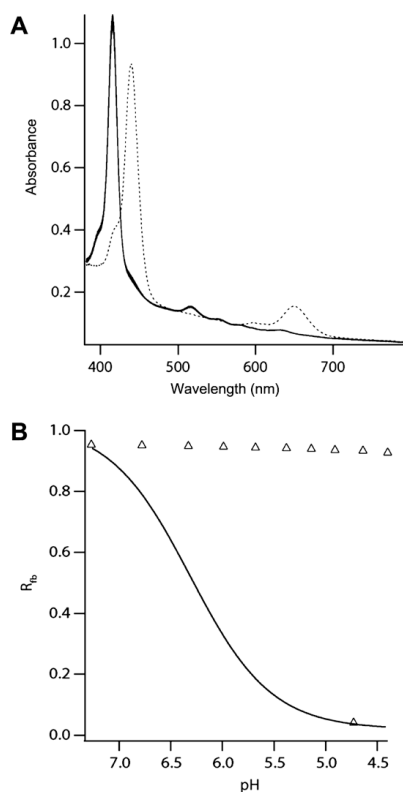

Fig. 7. (A) Absorption spectra of Glu^3 enclosed in LUVs in the absence of gramicidin. (B) Fraction of free-base Glu^3 derived from the data in panel A using Eq. (1) as a function of pH. The lowest point was recorded last, after the addition of gramicidin. The fit from Fig. 6B is indicated.

the observed increase in pH. The total volume of intravesicular solution is approximately 2% of the total sample volume.

Vesicle stability and leakage

A sample of the liposomes with Glu^3 inside was stored for 6 days in the dark at 4 °C, and the spectra from day 1 and day 7 were virtually indistinguishable (data not shown). This demonstrates that the liposomes are extremely stable and that the probe does not change characteristics inside the LUVs over time. This experiment shows that the observed changes in Figs. 7 and 8 are not caused by dye variation over time but rather are a true reflection of the intravesicular pH.

Proton leakage through the phospholipid bilayer was investigated by exposing the liposomes, containing a probe solution equilibrated with the bulk at pH 7.2, to a sharp decrease of external pH to 5.6. Fig. 8 shows the temporal evolution of R_{fb} after this pH jump administered at time = 0. There was no baseline drift over time; such a drift would be immediately evident from the spectra that were recorded throughout the measurement. Thus, the slope in Fig. 8 represents the change in pH inside the vesicles. It is clear that the decrease in external pH affected the internal pH only very slowly.

After 35 min, gramicidin was added, effecting an immediate pH equilibration across the membrane. At this point, the intravesicular pH had drifted from its original value by only 0.2 pH units. From these data, the half-time of proton leakage is estimated to be 130 min. This corresponds to an approximate leak rate of one proton per second and vesicle or 10 protons per second and μm². This very low leakage rate shows that our vesicles are virtually proton impermeable in the absence of proteins and under the current experimental conditions, providing a good system for studying proton translocation.

Sensitivity of Glu^3 as an intravesicular pH indicator

The previously reported experiment with Glu^4 in SUVs [24] had one dye molecule per 1000 to 10,000 vesicles, leaving the majority of vesicles spectroscopically silent. Nonetheless, distinct fluorescence changes of Glu^4, encapsulated in gramicidin-containing SUVs, were observed on a pH jump of 1 unit. In the current study, we used 200 μM Glu^3 in the dye incorporation step, resulting in an average of 170 probe molecules per LUV. Our vesicle concentration is on the order of 10 times lower than that in the SUV experiment [24]. Thus, the current setup should yield an approximately 100-fold higher intrinsic signal level, with all LUVs acting as detection
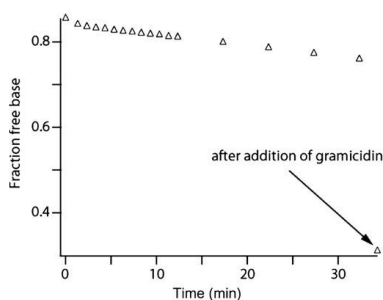
units and each one reporting an average readout from 170 dye molecules. As is evident from the data in Figs. 2–4 and Fig. 6, at such a high signal level, the detection of ΔpH = 0.01 in the linear regime of the indicator is entirely feasible. If necessary, even smaller effects can be monitored by using fluorescence rather than absorbance and/or by following a single wavelength with a PMT detector that is more sensitive than the CCD system.

Conclusions

The probe/liposome system presented is well suited for measurements of biological proton transfer across phospholipid bilayers, and the titration/spectroscopy system enhances efficiency and accuracy. The probe Glu^3 has a pK appropriate for biological applications. The probe was successfully included into liposomes and did not traverse the membrane, displaying excellent localizability. The absorbance signal from Glu^3 enclosed in liposomes is intense and dominates the spectrum over the scattering caused by the vesicles. LUVs loaded with the probe show good stability over time and can be stored for several days. The proton permeability of the LUV phospholipid bilayer is very low under our experimental conditions, approximately 10 protons per second and μm².

Acknowledgments

References

[1] S.M. Borisov, I. Klimant, Optical nanosensors: smart tools in bioanalytics, Analyst 133 (2008) 1302–1307.

[2] G. Lenaz, Role of mitochondria in oxidative stress and ageing, Biochim. Biophys. Acta 1366 (1998) 53–67.

[3] P.M. Abou-Sleiman, M.M.K. Muqit, N.W. Wood, Expanding insights of mitochondrial dysfunction in Parkinson's disease, Nat. Rev. Neurosci. 7 (2006) 207–219.

[4] B.B. Seo, E. Nakamaru-Ogiso, T.R. Flotte, A. Matsuno-Yagi, T. Yagi, In vivo complementation of complex I by the yeast Ndi1 enzyme: possible application for treatment of Parkinson disease, J. Biol. Chem. 281 (2006) 14250–14255.

[5] T.M. Dawson, V.L. Dawson, Molecular pathways of neurodegeneration in Parkinson's disease, Science 302 (2003) 819–822.

[6] T.B. Sherer, J.R. Richardson, C.M. Testa, B.B. Seo, A.V. Panov, T. Yagi, A. Matsuno-Yagi, G.W. Miller, J.T. Greenamyre, Mechanism of toxicity of pesticides acting at complex I: relevance to environmental etiologies of Parkinson's disease, J. Neurochem. 100 (2007) 1469–1479.

[7] A. De Milito, S. Fais, Proton pump inhibitors may reduce tumour resistance, Expert Opin. Pharmacother. 6 (2005) 1049–1054.

[8] S. Harguindey, G. Orive, J.L. Pedraz, A. Paradiso, S.J. Reshkin, The role of pH dynamics and the Na⁺/H⁺ antiporter in the etiopathogenesis and treatment of cancer: two faces of the same coin—one single nature, Biochim. Biophys. Acta 1756 (2005) 1–24.

[9] N. Altan, Y. Chen, M. Schindler, S.M. Simon, Defective acidification in human breast tumor cells and implications for chemotherapy, J. Exp. Med. 187 (1998) 1583–1598.

[10] S.R. Sennoune, R. Martinez-Zaguilan, Plasmalemmal vacuolar H⁺-ATPases in angiogenesis, diabetes, and cancer, J. Bioenerg. Biomembr. 39 (2007) 427–433.

[11] F. Johansson, M. Olbe, M. Sommarin, C. Larsson, Brij-58, a polyoxyethylene acyl ether, creates membrane-vesicles of uniform sidedness: a new tool to obtain inside-out (cytoplasmic side-out) plasma-membrane vesicles, Plant J. 7 (1995) 165–173.

[12] J. Reimann, U. Flock, H. Lepp, A. Honigmann, P. Adelroth, A pathway for protons in nitric oxide reductase from *Paracoccus denitrificans*, Biochim. Biophys. Acta 1767 (2007) 362–373.

[13] H. Lepp, L. Salomonsson, J.P. Zhu, R.B. Gennis, P. Brzezinski, Impaired proton pumping in cytochrome *c* oxidase upon structural alteration of the D pathway, Biochim. Biophys. Acta 1777 (2008) 897–903.

[14] A. Galkin, S. Drose, U. Brandt, The proton pumping stoichiometry of purified mitochondrial complex I reconstituted into proteoliposomes, Biochim. Biophys. Acta 1757 (2006) 1575–1581.

Fig. 8. Fraction of free-base Glu^3 enclosed in LUVs without gramicidin as a function of time. The initial pH was 7.2. At time 0, the bulk pH was changed to 5.6. After 35 min, gramicidin was added.

[15] S. Manente, S. De Pieri, A. Lero, C. Rigo, M. Bragadin, A comparison between the responses of neutral red and acridine orange: Acridine orange should be preferential and alternative to neutral red as a dye for the monitoring of contaminants by means of biological sensors, Anal. Biochem. 383 (2008) 316–319.

[16] G.J. Lancz, T.M. Chavez, Spectrophotometric method for monitoring the pH of tissue culture medium, Methods Cell Sci. 3 (1977) 667–670.

[17] M. Wikstrom, Two protons are pumped from the mitochondrial matrix per electron transferred between NADH and ubiquinone, FEBS Lett. 169 (1984) 300–304.

[18] A.S. Galkin, V.G. Grivennikova, A.D. Vinogradov, $\vec{H}^+/2\bar{e}$ stoichiometry in NADH–quinone reductase reactions catalyzed by bovine heart submitochondrial particles, FEBS Lett. 451 (1999) 157–161.

[19] A.S. Galkin, V.G. Grivennikova, A.D. Vinogradov, $H^+/2\bar{e}$ stoichiometry of the NADH:ubiquinone reductase reaction catalyzed by submitochondrial particles, Biochemistry (Mosc.) 66 (2001) 435–443.

[20] J. Vecer, A. Holoubek, K. Sigler, Fluorescence behavior of the pH-sensitive probe carboxy SNARF-1 in suspension of liposomes, Photochem. Photobiol. 74 (2001) 8–13.

[21] A. Holoubek, J. Vecer, K. Sigler, Monitoring of the proton electrochemical gradient in reconstituted vesicles: quantitative measurements of both transmembrane potential and intravesicular pH by ratiometric fluorescent probes, J. Fluoresc. 17 (2007) 201–213.

[22] F. Thiebaut, S.J. Currier, J. Whitaker, R.P. Haugland, M.M. Gottesman, I. Pastan, M.C. Willingham, Activity of the multidrug transporter results in alkalinization of the cytosol: measurement of cytosolic pH by microinjection of a pH-sensitive dye, J. Histochem. Cytochem. 38 (1990) 685–690.

[23] C.L. Slayman, V.V. Moussatos, W.W. Webb, Endosomal accumulation of pH indicator dyes delivered as acetoxymethyl esters, J. Exp. Biol. 196 (1994) 419–438.

[24] O. Finikova, A. Galkin, V. Rozhkov, M. Cordero, C. Hagerhall, S. Vinogradov, Porphyrin and tetrabenzoporphyrin dendrimers: tunable membrane-impermeable fluorescent pH nanosensors, J. Am. Chem. Soc. 125 (2003) 4882–4893.

[25] S.A. Vinogradov, D.F. Wilson, Electrostatic core shielding in dendritic polyglutamic porphyrins, Chemistry 6 (2000) 2456–2461.

[26] M.S. Kaucher, M. Peterca, A.E. Dulcey, A.J. Kim, S.A. Vinogradov, D.A. Hammer, P.A. Heiney, V. Percec, Selective transport of water mediated by porous dendritic dipeptides, J. Am. Chem. Soc. 129 (2007) 11698–11699.

[27] V. Percec, A.E. Dulcey, V.S.K. Balagurusamy, Y. Miura, J. Smidrkal, M. Peterca, S. Nummelin, U. Edlund, S.D. Hudson, P.A. Heiney, D.A. Hu, S.N. Magonov, S.A. Vinogradov, Self-assembly of amphiphilic dendritic dipeptides into helical pores, Nature 430 (2004) 764–768.

[28] U. Flock, N.J. Watmough, P. Adelroth, Electron/Proton coupling in bacterial nitric oxide reductase during reduction of oxygen, Biochemistry 44 (2005) 10711–10719.

[29] P.G. Seybold, M. Gouterma, Porphyrins: XIII. Fluorescence spectra and quantum yields, J. Mol. Spectr. 31 (1969) 1–13.

[30] A.V. Hill, The possible effects of the aggregation of molecules of hemoglobin on its dissociation curve, J. Physiol. (Lond.) 40 (1910) 4–7.

[31] J.L. Rigaud, D. Levy, Reconstitution of membrane proteins into liposomes, Methods Enzymol. 372 (2003) 65–86.

[32] R.C. Macdonald, R.I. Macdonald, B.P.M. Menco, K. Takeshita, N.K. Subbarao, L.R. Hu, Small-volume extrusion apparatus for preparation of large, unilamellar vesicles, Biochim. Biophys. Acta 1061 (1991) 297–303.

[33] J. Dubochet, M. Adrian, J.J. Chang, J.C. Homo, J. Lepault, A.W. McDowall, P. Schultz, Cryo-electron microscopy of vitrified specimens, Q. Rev. Biophys. 21 (1988) 129–228.

[34] M. Seigneuret, J.L. Rigaud, Use of the fluorescent pH probe pyranine to detect heterogeneous directions of proton movement in bacteriorhodopsin reconstituted large liposomes, FEBS Lett. 188 (1985) 101–106.

[35] S.A. Vinogradov, L.W. Lo, D.F. Wilson, Dendritic polyglutamic porphyrins: Probing porphyrin protection by oxygen-dependent quenching of phosphorescence, Chemistry 5 (1999) 1338–1347.

[36] P. Hambright, Chemistry of water soluble porphyrins, in: K. Kadish, K. Smith, R. Guilard (Eds.), The Porphyrin Handbook, Academic Press, San Diego, 2000 (Chapter 18).

[37] O.S. Finikova, A.V. Cheprakov, P.J. Carroll, S. Dalosto, S.A. Vinogradov, Influence of nonplanarity and extended conjugation on porphyrin basicity, Inorg. Chem. 41 (2002) 6944–6946.

[38] V.S. Chirvony, A. van Hoek, V.A. Galievsky, I.V. Sazanovich, T.J. Schaafsma, D. Holten, Comparative study of the photophysical properties of nonplanar tetraphenylporphyrin and octaethylporphyrin diacids, J. Phys. Chem. B 104 (2000) 9909–9917.

[39] R. Schubert, Liposome preparation by detergent removal, Liposomes A 367 (2003) 46–70.

[40] A. Finkelstein, O.S. Andersen, The gramicidin channel: a review of its permeability characteristics with special reference to the single-file aspect of transport, J. Membr. Biol. 59 (1981) 155–171.

[41] W. Auslander, W. Junge, Neutral red, a rapid indicator for pH-changes in inner phase of thylakoids, FEBS Lett. 59 (1975) 310–315.

[42] K.A. Giuliano, R.J. Gillies, Determination of intracellular pH of Balb/c-3t3 cells using the fluorescence of pyranine, Anal. Biochem. 167 (1987) 362–371.

[43] T.J. Rink, R.Y. Tsien, T. Pozzan, Cytoplasmic pH and free Mg^{2+} in lymphocytes, J. Cell Biol. 95 (1982) 189–196.

[44] Y.P. Loh, W.W.H. Tam, J.T. Russell, Measurement of pH and membrane-potential in secretory vesicles isolated from bovine pituitary intermediate lobe, J. Biol. Chem. 259 (1984) 8238–8245.

[45] C.S. Huang, S.J. Kopacz, C.P. Lee, Mechanistic Differences in the energy-linked fluorescence decreases of 9-aminoacridine dyes associated with bovine heart submitochondrial membranes, Biochim. Biophys. Acta 722 (1983) 107–115.

III

A membrane-impermeable ratiometric pH nanoprobe based on a highly non-planar dendritic porphyrin

Sujitha Thyagarajan,[1] Thom Leiding[2], Jonas Martinsson[2], Sindra Peterson Årsköld,[2]* and Sergei A. Vinogradov[1]*

Department of Biochemistry and Biophysics, University of Pennsylvania, Philadelphia, PA 19104; Department of Biochemistry and Structural Biology, Center of Chemistry and Chemical Engineering, Lund University, 221 00 Lund, Sweden.

E-mail: vinograd@mail.med.upenn.edu

Running title: Non-planar porphyrin-dendrimer: ratiometric pH nanosensor

[1]University of Pennsylvania; [2] Lund University.

Abstract

Metal-free porphyrin-dendrimers provide a convenient platform for construction of membrane-impermeable ratiometric probes for pH measurements in compartmentalized biological systems. In all so far reported molecules, electrostatic stabilization (shielding) of the core porphyrin core by peripheral negative charges (carboxylates) was required in order to move the intrinsically low porphyrin protonation pK_a's ($pK_a \sim 3$-4) into the physiological pH range (pH 6-9). However, binding of metal cations (such as K^+, Na^+, Ca^{2+}, Mg^{2+}) by the carboxylate groups on the dendrimer could affect the protonation behavior of the probes in biological environments. Here we report a new pH nanosensor based on a highly non-planar tetraaryltetracyclohexenoporphyrin (Ar_4TCHP), whose intrinsic proton affinity is significantly higher than that of regular tetraarylporphyrins, thereby eliminating the need for electrostatic shielding. The porphyrin was modified with eight Newkome-type dendrons, which were subsequently PEGylated at the periphery, rendering a neutral water-soluble probe (TCHpH), suitable for measurements in a broad pH range (pH 5-9). The protonation of TCHpH was followed by absorption (ε_{Soret}(free-base)$\sim$150,000 $cm^{-1}M^{-1}$) or by weak but detectable fluorescence (ϕ_{fl}=0.02 in aq. buffer, pH 4). Unlike most tetraarylporphyrins, TCHpH exhibits two distinct protonation steps, with pK_a's 7.8 and 6.3. In the region between the pK_a's, an intermediate species with distinct spectroscopic signature, presumably a TCHpH monocation, could be observed in the mixture. The performance of TCHpH was evaluated by pH-gradient measurements in large unilamellar vesicles. The probe was retained inside the vesicles and did not pass through or interact with vesicle membranes, proving useful for quantification of proton transport across phospholipid bilayers in the physiological pH range.

Keywords: porphyrin, dendrimer, non-planar, pH sensor, ratiometric, porphyrin protonation, porphyrin monocation, proton flux, proton pumping, liposomes, LUV, pH gradient, lipid bilayer

Introduction

Over the past decade, porphyrin-dendrimers have continuously attracted attention in numerous areas of chemistry, including light harvesting, electron transfer, host-guest chemistry, photodynamic therapy and design of biological sensors and imaging agents.[1,2] Dendritic encapsulation[3,4] offers a straightforward way of isolating the porphyrin moiety from components of biological systems, improving its solubility and controlling distribution in multiple-compartment systems. At the same time, the ability to place multiple functional units at the dendrimer periphery makes it possible to modulate the porphyrin nanoenvironment, and by doing so fine-tune the properties of the sensor in order to meet the application requirements.

As molecular nanosensors, porphyrin-dendrimers have been proven particularly useful in biological imaging of oxygen[5] and as membrane-impermeable ratiometric probes for pH measurements in microcompartmentalized environments.[6] The latter application makes use of the fact that protonation of two pyrollenine nitrogens in the core of the tetrapyrrole macrocycle leads to dramatic changes in the porphyrin optical spectra; yet both protonated and de-protonated forms have strong absorption bands and, in some cases, substantial fluorescence, enabling ratiometric pH sensing. Compared to existing macromolecular pH indicators,[7] porphyrins offer an advantage of extremely high extinction coefficients (reaching as high as 400,000 $M^{-1}cm^{-1}$ in the Soret region), which helps to improve signal-to-noise (SNR) ratios and increase measurement accuracy. Once encapsulated inside dendrimers with hydrophilic peripheral groups, porphyrins become highly water-soluble, while unable to pass through or interact with lipid bilayers, enabling pH measurements in micro-compartmentalized systems.[6b,8] Such systems include biological organelles whose membranes contain proton-translocating proteins, e.g. mitochondria. Such proteins play pivotal roles in bioenergetics and photosynthesis, and are implied in aging,[9] Parkinson's disease,[10] cancer[11] as well as in mechanisms of viral infection.[12] An improved assay for quantitative investigations of biological proton channels an assay is being developed,[8] in which proteins are reconstituted in lipid bilayers of artificial liposomes, while proton translocation is monitored optically using porphyrin-dendrimer based membrane-impermeable probes.

Intrinsic protonation pK's of tetaarylporphyrins[13] are typically too low to be suitable for pH measurements in the physiological pH range (pH 6-8). However, there are several ways by which proton affinity of the porphyrin macrocycle can be modulated, including electronic substitution,[13] structural deformations[14] and electrostatic core stabilization.[15] In the dendritic probes developed to date, electrostatic stabilization (shielding) of porphyrin cations by peripheral negative charges (carboxylates) was used to shift their protonation pK's (typically, for tetraarylporphyrins apparent protonation pK's are ~3-4) into the physiological pH range (pH 6-9).[6] Some of these probes proved useful in functional studies;[6b,8,16] however, dependence of the protonation state of the sensor on the ionization of the peripheral exposed layer makes such probes vulnerable to the adverse effects of the environment. For example, in biological systems, binding of divalent metal cations (e.g. Ca^{2+} and Mg^{2+}) by the peripheral carboxylates on the dendrimer and/or alterations in K^{+} or Na^{+} concentrations can unpredictably affect the protonation state of the porphyrin, skewing the measurements.

A preferred way to tune the probe's pK would be to modulate the intrinsic proton affinity of the porphyrin, while leaving the dendrimer periphery neutral and insensitive to the components of biological systems. Such modulation can be accomplished by affecting the planarity of the porphyrin macrocycle. It is well-known that proton affinities of non-planar porphyrins are much higher than of their planar analogues.[14] Although protonation pK is a purely thermodynamic parameter, this effect is typically explained by an "increased accessibility" of the core nitrogens to protons in distorted macrocycles,[17] which, at least intuitively, implies a kinetic nature of the effect. An alternative, non-

contradicting explanation[18] is based on factorization of the porphyrin protonation free-energy (ΔG_{prot}) into electronic (ΔG_{el}) and structural (ΔG_{struct}) components ($\Delta G_{prot}=\Delta G_{el}+\Delta G_{struct}$) and suggests that in regular planar porphyrins, the structural factor always disfavors protonation ($\Delta G_{struct}>0$), while in non-planar porphyrins it is relatively small ($\Delta G_{struct}\approx0$). Indeed, accommodation of two extra protons in the core of a planar free-base porphyrin requires its distortion: with rare exceptions,[19,20] porphyrin cations are known to be strongly non-planar species.[21,22,23] Distortion decreases aromatic stabilization of the macrocycle and thereby disfavors protonation. In intrinsically non-planar porphyrins only a small extra distortion should arise from protonation; therefore, the structural factor becomes small ($\Delta G_{struct}\approx0$) and the overall protonation energy becomes more negative. Electronic changes accompanying de-planarization, such as an increase in conjugation between *meso*-aryl groups and the macrocycle π-system,[24] should favor protonation of planar porphyrins, but not be very significant in the case of intrinsically non-planar porphyrins. Overall, the net change in the electronic term is apparently smaller than in the structural term, and non-planar porphyrins exhibit significantly higher proton affinities. The above model[18] provides a simple mechanistic framework for employing structural effects in practical design of porphyrin-based pH probes.

An interesting aspect of porphyrin protonation behavior is that in the overwhelming majority of cases two sequential protonations of pyrrolenine nitrogens are inseparable, and with rare exceptions[25,26,27] porphyrin monocations (or monoacids) remain elusive. Apparently, protonation of the first pyrrolenine nitrogen induces strong de-planarization of the macrocycle, cooperatively enhancing the second protonation by reducing the associated structural penalty (ΔG_{struct}). Since structural changes induced by protonations in non-planar porphyrins are small, one would expect that the two protonation steps should be distinguishable and monocation species readily observable.

Here we present a new dendritic pH nanoprobe TCHpH, based on a highly non-planar tetraaryltetracyclohexenoporphyrin (Ar_4TCHP), which is modified with eight Newkome-type dendrons and terminated by polyethyleneglycol (PEG) residues. TCHpH is highly water-soluble, has no peripheral charges and is suitable for colorimetric and fluorescence pH measurements in the physiological range. pH titrations of TCHpH revealed two sequential protonation steps (pK_a's 7.8 and 6.3) and formation of an intermediate species with distinct spectroscopic signature, presumably a TCHpH monocation. The probe proved useful in proton-gradient measurements in unilamellar phospholipid vesicles.

Experimental

General. All solvents and reagents were obtained from commercial sources and used as received. Tetrahydroisoindole ethyl ester (pyrrole ester) (**1**)[28] and dibutyl-5-formylisophthalate (aromatic aldehyde)[29] were synthesized as described previously. Tris{[2-(*tert*-butoxycarbonyl)ethoxy]methyl}methylamine (Gen 1 Newkome-type dendron) was synthesized according to the published method.[30] Thin-layer chromatography was performed on aluminum-supported silica gel plates (Aldrich). Column chromatography was performed on Selecto silica gel (Fisher). Preparative GPC was performed on S-X1 beads (Bio-Rad), using THF as a mobile phase. ^{1}H and ^{13}C NMR spectra were recorded on a Brucker DPX-400 spectrometer. The mass spectra were obtained on a MALDI-TOF Voyager- DE[TM] RP BioSpectrometry workstation, using α-cyano-4-hydroxycinnamic acid as the matrix.

Quartz fluorometric cells (Starna Cells, Inc., 1 cm optical path length) were used in both UV-Vis and fluorescence experiments. Optical absorption spectra were recorded on a Perkin-Elmer Lambda 40 UV-

Vis spectrophotometer or an Avantes AvaSpec-2048 fiberoptic spectrometer with a Tungsten-Halogen light-source, the latter connected to an in-house constructed titration system.[8] Steady-state fluorescence measurements were performed on FS-900 spectrofluorometer (Edinburgh Instruments). The fluorescence quantum yields were determined relative to the fluorescence of Rhodamine 6G (ϕ_{fl}=0.95 in EtOH)[31] or tetraphenylporphyrin (ϕ_{fl}=0.11 in deox. C_6H_6).[32] Dynamic light-scattering (DLS) measurements were performed on a Zetasizer Nano-S instrument from Malvern Instruments.

Synthesis

Tetraaryltetracyclohexenoporphyrin octabutyl ester (**3**). A mixture of pyrrole ester (**1**) (300 mg, 1.55 mmol) and potassium hydroxide (~85 %, 140 mg, 2.55 mmol) in ethylene glycol (9 ml) was refluxed under Ar for 1 h. The mixture was cooled to 0 °C and CH_2Cl_2 (20 ml) was added. The organic phase was washed with water and with brine. The product, pyrrole **2**, was extracted with CH_2Cl_2. The solution was washed with water and brine, dried over Na_2SO_4, and the solvent was evaporated in a vacuum. The residue was purified by column chromatography (Selecto silica gel/CH_2Cl_2). The resulting pyrrole **2** was dissolved in CH_2Cl_2 (150 ml). The flask was protected from ambient light and flushed with Ar, after which dibutyl-5-formylisophthalate (430 mg, 1.41 mmol) was added in one portion. The solution was stirred for 10 min, after which $BF_3·Et_2O$ (40 mg, 0.28 mmol) was added, and the mixture was stirred at rt for 2 h. DDQ (350 mg, 1.55 mmol) was added, and the mixture was stirred overnight. The resulting green solution was washed with 10% aq Na_2SO_3, 10% aq Na_2CO_3, 5% aq HCl, and finally with brine. The organic layer was dried over Na_2SO_4 and reduced in volume by rotary evaporation. The green colored residue was purified by column chromatography on silica gel using CH_2Cl_2/EtOAc (85:15 by volume) as a mobile phase. After evaporation of the solvent, and drying in vacuum, porphyrin **3** was isolated as green-brown solid. Yield: 230 mg, 10% (based on **1**). UV-vis (CH_2Cl_2-TFA, 9:1) λ_{max} (log ϵ) 464 (5.29), 611 (4.08), 671 nm (4.29); ^{1}H NMR (CDCl$_3$) δ 8.40-8.37 (m, 12H), 4.90 (s, 16H), 2.64-2.44 (m, 32H), 1.86-1.84 (m, 16H), 1.68-1.65 (m, 16H), 0.89 (s, 24H), 0.31 (br s, 2H); ^{13}C NMR (CDCl$_3$) δ 159.6, 140.6, 135.0, 131.1, 127.7, 124.1, 123.7, 88.8, 56.1, 39.1, 28.9, 24.0, 15.6, 12.3; MALDI, m/z for $C_{100}H_{118}N_4O_{16}$ calcd. 1630.8, found 1630.8.

Tetraaryltetracyclohexenoporphyrin octacarboxylic acid (**4**). Porphyrin **3** (46 mg, 0.028 mmol) was dissolved in THF (6 ml) at 0 °C, and two-three pellets of NaOH and MeOH (~0.5 ml) were added to the mixture. The mixture was left to stir at r.t. overnight, after which it was concentrated in vacuum, and several drops of water were added to dissolve the brown precipitate. The solution was stirred for 1 h at r.t. and THF was removed by rotary evaporation. The solution was acidified with conc. HCl. The precipitate was isolated by centrifugation and washed with water three times to give **4** as a dark green powder. Yield: 33 mg, 94%. ^{1}H NMR (DMSO-d$_6$) δ 8.33-8.05 (m, 12H), 1.45-0.94 (m, 32H), 0.39 (br s, 2H); MALDI, m/z for $C_{68}H_{54}N_4O_{16}$ calcd. 1182.3, found 1182.7.

Porphyrin-dendrimer poly-^{t}Bu-ester (**5**). Porphyrin **4** (52 mg, 0.044 mmol) and HBTU (250 mg, 0.66 mmol) were dissolved in dry NMP (25 ml). DIPEA (520 mg, 4.05 mmol) was added to the solution at r. t., immediately followed by addition of the Newkome G1 dendron (334 mg, 0.66 mmol). The resulting mixture was stirred for 4 days at r.t., after which it was poured into aq. NaCl (3%). The resulting precipitate was collected by centrifugation, washed with water by suspension/centrifugation cycles (3×30 ml) and dried in vacuum. The green-brown viscous solid was re-dissolved in THF and purified by SEC (Bio-Rad S-X1 Beads, 200-400 mesh, THF) to yield the porphyrin-dendrimer **5**. Yield: 191 mg, 86%. MALDI, m/z for $C_{268}H_{414}N_{12}O_{80}$ calcd. 5080.9, found 5080.3.

Porphyrin-dendrimer polycarboxylic acid (**6**). To a well-stirred solution of **5** (198 mg, 0.039 mmol) in CH_2Cl_2 (12 ml), TFA (10 ml) was added dropwise at 0°C over a period of 20 min. The solution was

allowed to react for 2 h, after which the solvent and the excess TFA were evaporated in vacuum at r.t. The residual TFA was removed by re-dissolving the precipitate in CH_2Cl_2 (10 ml) and evaporating it in vacuum. This procedure was repeated several times, leaving polyacid **6** as a dark green viscous solid. Yield: 142 mg, 98%. MALDI, *m/z* for $C_{172}H_{222}N_{12}O_{80}$ calcd. 3735.4, found 3735.4.

Porphyrin-dendrimer poly-PEG-ester (TCHpH). Polyacid **6** (129 mg, 0.035 mmol) was dissolved in CH_2Cl_2 (10 ml), monomethoxyoligoethyleneglycol (Av. MW 750, 3 ml) was added, and the solution was left under stirring for 15 min at r.t., after which it was cooled on an ice bath. *sym*-Collidine (8-10 drops), HOBt (1.18 g, 8.75 mmol) and DCC (1.81 g, 8.75 mmol) were added to the mixture, and it was left to react under stirring for 4 days at r.t. Ice-cold 0.05 N aq. HCl (50 ml) was added to the mixture to quench the reaction, and the mixture was stirred for 30 min in order to decompose the unreacted DCC. The mixture was filtered through a Whatman 55 filter paper. The filtrate was extracted with CH_2Cl_2 and the solvent was removed in vacuum. The product was purified by size-exclusion column chromatography (Bio-Rad S-X1 beads, 200-400 mesh, THF) to yield target TCHpH probe as a green viscous solid. Yield: 396 mg, 53%.

pH titrations. Bulk titrations of TCHpH were performed using 5 mM, 20 mM or 50 mM potassium phosphate buffers. To suppress possible interference by traces of two-valent cations (particularly Zn^{2+} and Cu^{2+}), which can bind in the porphyrin cavity, titrations were performed in the presence of 250 μM EDTA. pH was adjusted by addition of HCl, H_2SO_4 or KOH. K_2SO_4 and $MgSO_4$ were used to test influence of high metal ion concentrations. In the titrations by absorption, absorbances of solutions at Soret peaks were kept ca 1 OD. In titrations by fluorescence, absorbances at the excitation wavelengths were below 0.1 OD.

The titration curves were constructed by plotting absorbances at selected wavelengths, or, in the case of fluorescence titrations, by plotting integrated fluorescence signals *vs* pH. In ratiometric titrations, ratios of the integrated fluorescence spectra upon excitation at selected wavelenghts (e.g. Soret peaks corresponding to the free-base and dication forms) were plotted *vs* pH.

The titration data were fitted to the Henderson-Hasselbalch-type equations derived for the cases of single (eq. 1) and two sequential protonations (eq. 2):

$$A_\lambda(pH) = P_1 \frac{10^{n(pH-pK)}}{1+10^{n(pH-pK)}} + P_2 \qquad\qquad\text{(Eq. 1)}$$

$$A_\lambda(pH) = \frac{P_3 \times 10^{-2pH} + P_2 \times 10^{-pH} + P_1}{10^{-2pH} + P_4 \times 10^{-pH} + P_5}, \qquad\qquad\text{(Eq. 2)}$$

where $A_\lambda(pH)$ designates the absorbance at a selected wavelength λ, and fitting parameters P_1-P_5 are the functions of the equilibrium constant(s), probe concentration and molar extinction coefficients of the free-base, monocation and dication (see supplement for derivation).

Liposome experiments. Large unilamellar liposomes containing TCHpH were prepared from palmitoyl-oleoyl phosphatidylcholine (Avanti Polar Lipids) according to the protocol described previously.[8] The buffer was potassium phosphate (20 mM, pH 7), containing EDTA (250 μM) and K_2SO_4 to bring the total K^+ concentration to 50 mM. This procedure is designed specifically for preparation of proteoliposomes, and, therefore, it includes a step of partial liposome dissolution using a detergent (octylglucoside, Avanti Polar Lipids), followed by detergent removal using polystyrene beads (Bio-

Beads, SM-2, Bio-Rad). TCHpH was added to the mixture prior to the step of detergent removal to a total concentration of 4.67 mg/ml. After vesicle formation, the probe not enclosed in the liposomes was removed by centrifugation of the liposomes at 40,000 rpm for 2h, discarding the supernatant and re-suspending the formed pellet in 6 ml buffer. This procedure was repeated three times. Based on the DLS measurements, the liposomes were characterized by a homogenous size distribution with average size 200 nm.

For calibration of the signal from the encapsulated probe, gramicidin (Sigma) dissolved in DMSO was added to liposome suspensions to a final concentration of ~1 µg/ml. This treatment renders the liposomes permeable to hydrogen ions, but not to large molecules such as TCHpH. The bulk pH was titrated, and the absorption spectra were corrected for the scattering background arising from the turbidity of the liposome suspension. Quantity R, used for fitting in these experiments, was determined using absorbances at 430 nm (blue edge of the Soret band of the free-base) and 456 nm (Soret peak of the dication):

$$R = \frac{A_{430} - A_{456} \cdot a}{A_{430} \cdot b + A_{456} \cdot a}$$
(Eq. 3)

where constants a and b account for the difference in the extinction coefficients of differently protonated forms, band overlaps and scattering.

The pH-jump experiment (Fig. 7) was performed using a suspension of liposomes in a mixture of Mes buffer (20 mM), potassium phosphate buffer (20 mM) and EDTA (250 µM). The intraliposomal pH was 7, and the extraliposomal (bulk) pH was set at pH 4.75. The spectra were recorded every 5 s during ~16 min, after which gramicidin in DMSO was added to a final concentration of 1 µg/ml.

The passive proton permeability of the liposome bilayer was calculated by considering the difference in pH between times t_1 (pH$_1$) and t_2 (pH$_2$) during the initial period (Fig. 7), that is prior to the addition of gramicidin, taking into account the capacity of the buffer inside the liposomes (20 mM, pK$_a$ 6.87):
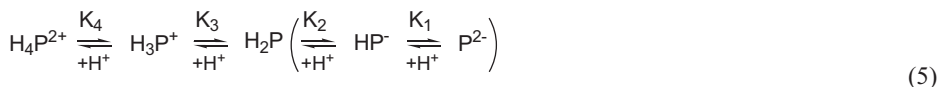
$$\Delta[H^+] = \frac{20 \cdot 10^{(6.87 - pH_2)}}{1 + 10^{(6.87 - pH_2)}} - \frac{20 \cdot 10^{(6.87 - pH_1)}}{1 + 10^{(6.87 - pH_1)}}$$
(Eq. 4)

Eq. 4 gives the change in proton concentration $[H^+]$ (in mM) inside the liposomes between times t_1 and t_2. When multiplied by the total internal liposome volume, this quantity gives the total amount of protons that traversed the phospholipid membrane.

Adhesion of TCHpH to polystyrene beads was tested by adding the beads (100 mg) to a solution of the probe in the buffer (1 ml, 8.5 mg/ml of TCHpH, pH 7.2), incubating the suspension under stirring for 1 h, adding more beads (50 mg) and continuing stirring for 1 h.

Results and Discussion

*Choice of porphyrin.* Free-base porphyrins (H$_2$P) are able to sequentially bind two protons to the core pyrrolenine nitrogen atoms with formation of *mono-* (H$_3$P$^+$) and *di-* (H$_4$P$^+$) cations (5). These two protonation/deprotonation reactions are usually described by equilibrium constants K$_3$ and K$_4$, while symbols K$_1$ and K$_2$ are reserved for reactions leading to porphyrin anions.[13]

$$H_4P^{2+} \underset{+H^+}{\overset{K_4}{\rightleftharpoons}} H_3P^+ \underset{+H^+}{\overset{K_3}{\rightleftharpoons}} H_2P \left(\underset{+H^+}{\overset{K_2}{\rightleftharpoons}} HP^- \underset{+H^+}{\overset{K_1}{\rightleftharpoons}} P^{2-} \right)$$

(5)

The choice of tetraaryltetracyclohexenoporphyrin (Ar_4TCHP) (Fig. 1) as a core for the construction of dendritic pH probe was motivated by our earlier observations of water-soluble non-planar porphyrins,[18] which revealed that apparent protonation pK's of Ar_4TCHP's are significantly higher than those of regular tetraarylporphyrins. To explain these results we proposed a model, which separates the total free-energy of protonation (ΔG_{prot}) into electronic (ΔG_{el}) and structural (ΔG_{struc}) components (summarized in the Introduction). This model suggests that the high proton affinity of Ar_4TCHP core should be related to its highly non-planar structure in the non-protonated (free-base) state; whereas its distortion upon protonation should be much smaller than that encountered in the case of regular tetraarylporphyrins.[17] To test this assumption, we performed ground-state DFT (B3LYP/6-31G(d)) calculations on the free-base and protonated forms of Ph_4TCHP and TPP. The resulting optimized structures (minima confirmed by frequency calculations) were analyzed by Normal Mode Structural Decomposition (NSD) analysis,[33] which proved to be a useful tool for quantifying distortions of porphyrins.[34] The difference in the mean square out-of-plane displacements (D_{oop}) between the free-base and dication forms (ΔD_{oop}) was used as a measure of the macrocycle distortion effected by protonation. The results are depicted in Fig. 2, clearly showing that the macrocycle distortion induced by protonation of TPP (ΔD_{oop}=2.7Å) is much higher than that of Ph_4TCHP (ΔD_{oop}=0.8Å), suggesting that protonation pK's (pK_3 and pK_4) of the latter should be shifted significantly towards higher pH values. In fact, electron-donor alkyl groups in β-pyrrolic positions of Ar_4TCHP could shift the pK's way too high, passed the physiological pH range. To partially offset this effect we contemplated adding electron-withdrawing groups (carboxyls) into the meta-positions of the *meso*-aryl rings, which could simultaneously provide anchor points for linking solubilizing dendrons.

Another observation from the computation model was that the structure of the Ar_4TCHP monocation was also very similarly distorted compared to the free-base form. Therefore, no cooperativity could be expected for binding of the second proton, and the protonation steps were expected to be well resolved. Consequently, one could expect that in the pH region between the pK's (pK_3 and pK_4) the porphyrin monocation could be detected spectroscopically.

Synthesis. The synthesis of probe TCHpH (Scheme 1) followed protocols developed previously in our laboratory for synthesis of phosphorescent Pt and Pd porphyrin dendrimers.[5e] Pyrrole **2** with fused cyclohexene rings was obtained by decarboxylation of pyrrole-ester **1**, which was synthesized by the modified Barton-Zard method, as reported previously.[28] Octabutoxycarbonyltetracyclohexenoporphyrin **3** was synthesized by the Lindsey method[35] and converted into the corresponding octa-carboxylic acid **4** by base-mediated hydrolysis. The eight carboxylic groups on **4** were modified with Newkome-type dendrons using HBTU/DIPEA coupling chemistry, and the resulting porphyrin-dendrimer **5** was purified by SEC on polystyrene beads using THF as a mobile phase. MALDI-TOF analysis of this intermediate dendritic porphyrin (**5**) revealed only a small (<5%) contamination with dendrimers containing seven and six dendritic wedges. The peripheral *tert*-butyl ester groups on **5** were cleaved by TFA, giving polyacid **6**, whose peripheral carboxyl groups were subsequently esterified with monomethoxyoligo(ethylene glycol) (Av. MW 750) using DCC/HOBt chemistry.[36] The final PEGgylated porphyrin-dendrimer (TCHpH) was purified twice by SEC on polystyrene beads.
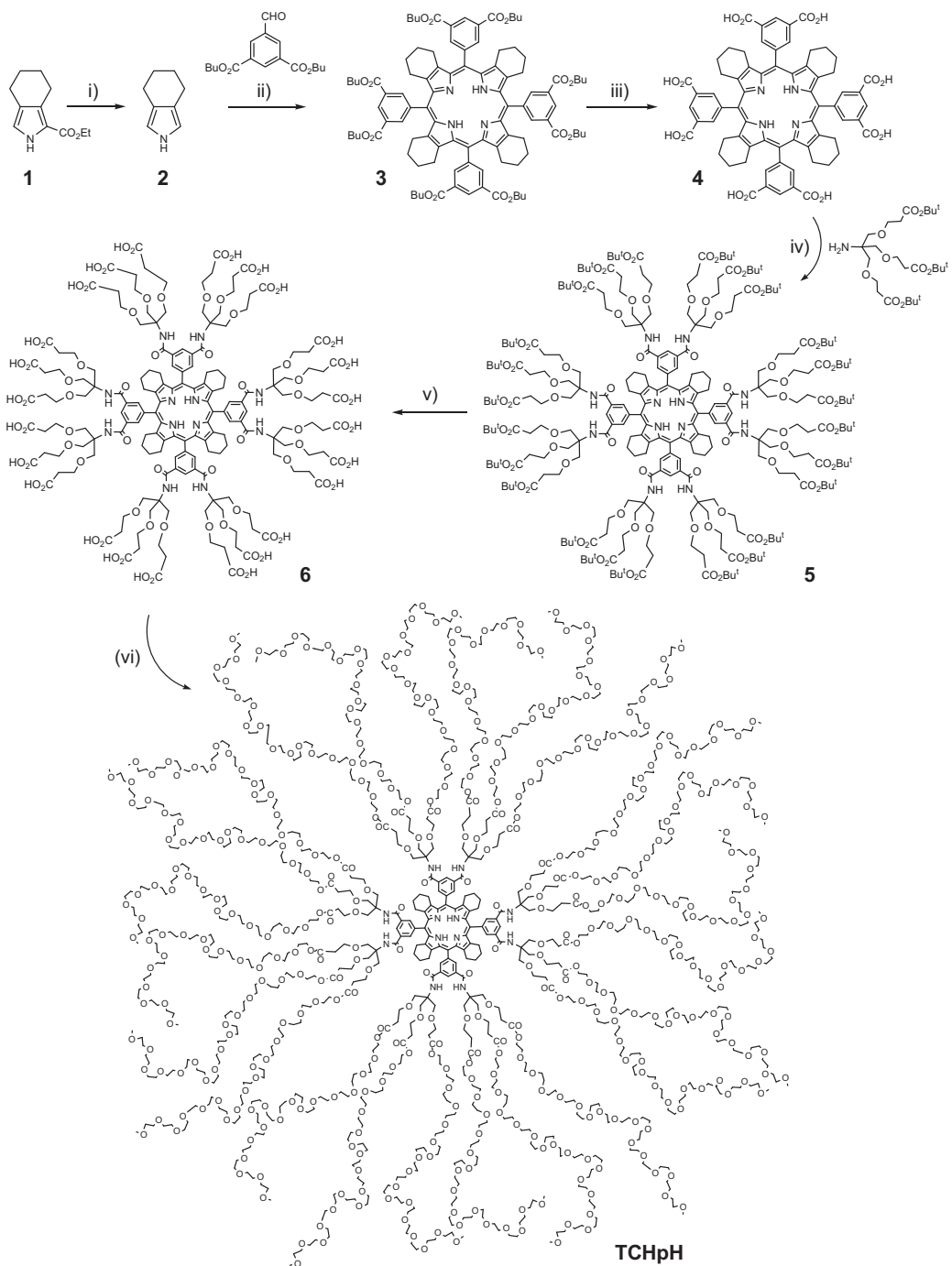
TCHpH

Scheme 1. (Previous page.) Synthesis of probe TCHpH.

Reagents and conditions: (i) KOH, HOCH$_2$CH$_2$OH, reflux, 1 h; (ii) a) BF$_3$·Et$_2$O, CH$_2$Cl$_2$, r.t., 2 h; b) DDQ, r.t., 12h, 10% for two stages; (iii) NaOH, THF, r.t., 12 h, 94%; (iv) HBTU, DIPEA, NMP, r.t., 4 days, 86% ; (v) TFA, 0°C, 20 min, 98%; (vi) PEG750, DCC, HOBt, *Sym*-collidine, CH$_2$Cl$_2$, r.t., 4 days, 53%.

Abbreviations: NMP=N-methylpyrrolidone; HBTU=2-(1H-benzotriazol-1-yl)-1,1,3,3-tetramethyluronium hexafluorophosphate; DIPEA=N,N-diisopropylethylamine; TFA=Tri fluoroacetic acid; PEG750=oligoethyleneglycol monomethyl ether, Av. MW 750; DCC=N,N-dicyclohexylcarbodiimide; HOBt = 1-hydroxybenzoytriazole.

Spectroscopic properties and pH titrations of TCHpH. The optical absorption spectra of TCHpH are shown in Fig. 3. The spectrum of the free-base spectrum, acquired at pH 10.6, shows the Soret band at 442 nm and a characteristic four-Q-band pattern, typical of tetraarylporphyrins. All bands, however, are significantly broadened, which is a well-known signature of porphyrin non-planarity. The spectrum of the fully protonated species (porphyrin dication), acquired at pH 4.0, shows a red-shifted Soret band (λ_{max}=456 nm) and Q maxima at 600 nm and 655 nm.

The Soret band extinction coefficient was measured for the dication form of parent porphyrin **3** in CH$_2$Cl$_2$/TFA, and it was assumed to be altered insignificantly by addition of dendrons. To calculate the extinction coefficient of the PEGylated dendrimer in aqueous media, we assumed the same oscillator strength as for the parent porphyrin, which resulted in the values of $\varepsilon_{\text{free base}}$(441 nm)=10$^{5.18}$ cm^{-1}M^{-1} and $\varepsilon_{\text{dication}}$(456 nm)= 10$^{5.38}$ cm^{-1}M^{-1}.

In Fig. 3C, *R* (3) is plotted as a function of pH. The data was fitted with eq. 1 with a single apparent pK of 7.49. Despite the floating parameter *n*, this fit was not satisfactory; two components were necessary to accurately fit the data (eq. 2). The pK-values thus obtained were pK_3=6.09 and pK_4=7.83, weighted with constants C_1=0.29 and C_2=0.71, respectively. The behavior of TCHpH as the pH is lowered thus appears to be more complex than a double protonation of the porphyrin core at a single apparent pK.

Notably, the spectral progression in Fig. 3A and 3B shows intensity in the 580–600 nm region that is maximal near pH 6.9, but absent in both free-base and dication spectra. There is also a conspicuous absence of isosbestic points through-out the spectral region. In Fig. 4A and 4B, the spectrum recorded at pH 6.9 is compared to the free-base and dication spectra. A species absorbing to the red of doubly protonated TCHpH seems to present at intermediate pH. The pH-6.9 spectrum was deconvoluted by subtracting amounts of the alkali and acidic spectra, weighted manually to null the contributions of their respective bands while avoiding negative intensities anywhere in the resulting difference spectrum. Subtracting 0.3×(acidic spectrum) and 0.18×(alkali spectrum) resulted in the dashed curves, representing a tentative spectral shape of the intermediate species. This tentative spectrum displays maxima at 465 nm, 585 nm, 630 nm and 685 nm, represents approximately 60% of the total population, and has an ε(465 nm) of approximately 10$^{5.1}$ cm^{-1}M^{-1}.

In Fig. 4C, the relative populations of the free base, the dication and the intermediate species are plotted vs pH. The free base is represented by the absorbance intensity at 415 nm, where none of the other species absorb, normalized to 1 at pH 10.6. The dication population is taken as the absorbance at 446 nm, corrected for overlap with the free-base spectrum using the absorbance intensity at 415 nm, and finally normalized to 1 at pH 4. The gray trace in Fig. 4C represents the sum of the free-base and dication populations, subtracted from 1. I.e., it shows an apparent population deficit in the intermediate pH range when only the free-base and dication species are taken into account: At most 50% of the TCHpH population appears to be missing. This figure is near the 60% estimated from spectral deconvolution, above. The population of the intermediate species is taken as the absorbance intensity at

498 nm, normalized so that the sum of the three populations is 1 at pH 7. This curve coincides with the gray trace through-out the region.

Fig. 4C shows that a species that is spectrally distinct from the free base and the dication appears at intermediate pH. It is maximal at pH 6.9, where it accounts for approximately 50% of the TCHpH population. Figure 3C shows a TCHpH protonation process that spans a very broad pH range and is not well described by a single pK. Introducing two pK values yields a good fit, and the pK values obtained fall symmetrically around the optimal pH for the intermediate species, as seen in Figure 4C. Based on this, it is tempting to assign this species to the singly protonated state of TCHpH. However, such a state would be expected to display a Soret maximum between the deprotonated and the doubly protonated species. The presently observed red-shift of the Soret band compared to the TCHpH dication is difficult to reconcile with a porphyrin monocation.

Having uncovered the spectral component at 465 nm, we now know that the absorbance at 456 nm, used in Eq. 1 to evaluate the presence of TCHpH dication, in fact includes a significant contribution from this species at intermediate pH. It can be seen as representing the sum of the dication and the intermediate species, albeit not adjusted for the different extinction coefficients. If necessary, this can be corrected for using the absorbance intensity at 498 nm to evaluate the contribution from the intermediate species – but not without introducing a substantial amount of noise, due to the low oscillator strength in the 498-nm region. For our purposes, we will use Eq.1 as is, with the calibration curve yielded by Eq. 3.

Suitability of TCHpH for sensing pH in biological systems. The unexpected spectral pH-dependence results in a much broader pH-range than offered by a single-protonation probe (such as Glu[3]),[8] making TCHpH a very dynamic pH sensor. Figure 3C indicates a measurement range of pH 5–9 or more.

For biological measurements, small monovalent ions are often present, and in some cases the ion concentrations may change during an experiment. We therefore investigated the ion dependence of TCHpH read-out. The probe was calibrated at several different K^+ concentrations, with no notable effect, as seen in Fig. 5. This differs from the Glu[3] probe, whose negatively charged dendrites render the porphyrin pK slightly sensitive to ionic strength. With Glu[3], we have circumvented this difficulty by working at sufficiently high salt concentrations to render minor changes in salt concentrations insignificant.[8] With TCHpH this will not be necessary, and small proton fluxes can be detected in the presence of low or varying salt concentrations.

The effect of Mg^{2+} was also addressed, but as Mg^{2+} precipitates at the high pH required for a full calibration of TCHpH, the results were not conclusive. The indications are that up to 5 mM Mg^{2+} has no effect on TCHpH – but such high Mg^{2+} concentrations can not be present during probe calibration or measurements at pH>8.

TCHpH as pH reporter inside phospolipid vesicles. TCHpH was present during preparation of large unilamellar phosphatidyl choline vesicles, and the TCHpH in the bulk of the final liposome suspension was removed. For calibration of the encapsulated probe, the non-specific ion pore gramicidin was added, rendering the liposomes permeable to protons and other ions but not to larger molecules. The suspension was titrated as in Fig. 3A. The resulting spectra were superimposed on a scattering slope from the liposome turbidity, but otherwise identical to those of Fig. 3 (not shown). After subtracting the scattering background, the data were processed according to Eq. 1 and fit to Eq. 3, producing the results displayed in Figure 6. The fit parameters were nearly identical to those obtained in bulk, showing that encapsulation and high local concentration have no effect on the spectral characteristics of the probe.

In the absence of gramicidin, a pH gradient was created over the lipsome bilayer, while monitoring the (encapsulated) TCHpH absorbance continuously (Fig. 7). The initial internal pH was 7, and at time t=0, the liposomes were diluted in a buffer solution of pH 4.75. The absorbance spectra were converted into R_{fb}-values, which were converted into pH values using the calibration curve obtained in Figure 6. The weak slope of pH_{in} in Figure 7 reflects a slow passive permeability of protons across the bilayer. After approximately 16 minutes gramicidin was added, allowing protons to flow into the liposomes. pH_{in} dropped at this point, reflecting the fast decrease of internal pH from 6.7 to 5.3.

This demonstrates that TCHpH is membrane-impermeable, as it reported the inside pH near 7 while the bulk pH was 4.75. It kept reporting internal pH for over 15 minutes, and was only protonated when the interior of the liposomes was acidified.

A key feature of the porphyrin-based probe Glu^3 is that it does not adsorb to the hydrophobic beads used for liposome preparations. This feature makes it possible to use beads in the liposome formation procedure, resulting in detergent-free liposomes in a relatively short period of time. It also enables experimental determination of the total internal volume in the final liposome suspension: Since the encapsulated Glu^3 concentration is the same as the initial, known concentration, the absorbance of the suspension reports directly on the encapsulated volume. TCHpH in solution was found to adsorb to a limited extent to the hydrophobic beads used for liposome production: After 90 min incubation with beads, 89% of the probe was still in solution. This is a higher adsorbance than for Glu^3, which was dissolved to >99% after the same treatment, and indicates a certain affinity of the PEG groups to the hydrophobic grooves. The adsorbance is much higher for commercially available pH dyes, including SNARF-dextran, for which 72% remains in solution. The relatively low adsorption of TCHpH makes it suitable for incorporation in bead-generated liposomes, but not for precise volume determination.

The liposomes of Figure 7 had a diameter of 200 nm determined by DLS, and we deduce the internal volume to 1.5% of the suspension, as determined for similarly prepared Glu^3 liposomes. Taking the internal buffer strength into account, pH_{in} was recalculated into the number of protons translocated from the bulk into the liposome interior. The time-averaged passive permeability of the liposomes in Figure 7 under $\Delta pH=2$ was thus determined to 30 protons/s·μm^2. This is in agreement with estimations obtained using Glu^3.

This establishes TCHpH as capable of quantitative, noninvasive, intravesicular pH determination. As such, it is a useful pH probe for studies of proton-translocation by proteins reconstituted in liposomes. TCHpH is currently being used to investigate the Influenza virus A protein M2.

Conclusions

The newly developed pH probe TCHpH is suitable for pH measurements in microcompartmentalized systems. The probe can operate as a ratiometric colorimetric or fluorescent sensor, does not interact with or traverse lipid bilayers and shows no apparent sensitivity to changes in ionic strength. It can therefore be used for pH measurements in systems with varying salt concentrations. Compared to previously reported dendritic probes Glu^4 and Glu^3, TCHpH covers wider pH range with maximal sensitivity around pH 7.5, thereby being ideally suitable for physiological measurements.

Supporting Information. Derivation of expressions used for fitting the spectroscopic data, results of NSD analyses.

References

1.   W. S. Li, T. Aida, *Chem. Rev.* **2009**, *109*, 6047.

2.   W. Maes, W. Dehaen, *Eur. J. Org. Chem.* **2009**, 4719.

3.   S. Hecht, J. M. J. Fréchet, *Angew. Chem. Int. Ed.* **2001**, *40*, 74.

4.   C. B. Gorman, J. C. Smith, *J. Am. Chem. Soc.* **2000**, *122*, 9342.

5.   (a) Vinogradov, S. A.; Lo, L. W.; Wilson, D. F. *Chem. Eur. J.* **1999**, *5*, 1338; (b) Dunphy, I.; Vinogradov, S. A.; Wilson, D. F. *Anal. Biochem.* **2002**, *310*, 191; (c) Rietveld, I. B.; Kim, E.; Vinogradov, S. A. *Tetrahedron* **2003**, *59*, 3821; (d) Finikova, O. S.; Lebedev, A. Y.; Aprelev, A.; Troxler, T.; Gao, F.; Garnacho, C.; Muro, S.; Hochstrasser, R. M.; Vinogradov, S. A. *ChemPhysChem* **2008**, *9*, 1673; (e) Lebedev, A. Y.; Cheprakov, A. V.; Sakadzic, S.; Boas, D. A.; Wilson, D. F.; Vinogradov, S. A. *ACS Applied Materials & Interfaces* **2009**, *1*, 1292.

6.   (a) Vinogradov, S. A.; Wilson, D. F. *Chem. Eur. J.* **2000**, *6*, 2456-2461; (b) Finikova, O. S.; Galkin, A. S.; Rozhkov, V. V.; Cordero, M. C.; Hagerhall, C.; Vinogradov, S. A. *J. Am. Chem. Soc.* **2003**, *125*, 4882.

7.   *Invitrogen*, SNARF pH indicators, 2003.

8.   Leiding, T.; Gorecki, K.; Kjellman, T.; Vinogradov, S. A.; Hagerhall, C.; Arskold, S. P. *Anal. Biochem.* **2009**, *388*, 296.

9.   G. Lenaz, *Biochimica Et Biophysica Acta-Bioenergetics*, 1366 (1998) 53-67.

10.   T.M. Dawson, V.L. Dawson, *Science* **302** (2003) 819-822.

11.   (a) N. Altan, Y. Chen, M. Schindler, S.M. Simon, *Journal of Experimental Medicine* **187** (1998) 1583-1598; (b) S.R. Sennoune, R. Martinez-Zaguilan, *Journal of Bioenergetics and Biomembranes*, **39** (2007) 427-433.

12.   M. Takeda, A. Pekosz, K. Shuck, L.H. Pinto, R.A. Lamb, *J. Virol.* **76** (2002) 1391-1399.

13.   Hambright, P. *Chemistry of water soluble porphyrins*, Ch. 18 in *The Porphyrin Handbook*, Kadish, K. M., Smith, K. M., Guilard, R. Eds., Academic Press, 2000.

14.   (a) Medforth, C. J.; Smith, K. M. *Tetr. Lett.* **1990**, *31*, 5583-5586; (b) Barkigia, K. M.; Berber, M. D.; Fajer, J.; Medforth, C. J.; Renner, M. W.; Smith, K. M. *J. Am. Chem. Soc.* **1990**, *112*, 8851-8857; (c) Takeda, J.; Ohya, T.; Sato, M. *Inorg. Chem.* **1992**, *31*, 2877-2880.

15.   (a) Valiotti, A.; Adeyemo, A.; Williams, R. F. X.; Ricks, L.; North, J.; Hambright, P. *J. Inorg. Nucl. Chem.* **1981**, *43*, 2653-2658; (b) Kohata, K.; Higashio, H.; Yamaguchi, Y.; Koketsu, M.; Odashima, T. *Bull. Chem. Soc. Jpn.* **1994**, *67*, 668.

16.   (a) Percec, V.; Dulcey, A. E.; Balagurusamy, V. S. K.; Miura, Y.; Smidrkal, J.; Peterca, M.; Nummelin, S.; Edlund, U.; Hudson, S. D.; Heiney, P. A.; Hu, D. A.; Magonov, S. N.;

Vinogradov, S. A. *Nature* **2004**, *430*, 764; (b) Kaucher, M. S.; Peterca, M.; Dulcey, A. E.; Kim, A. J.; Vinogradov, S. A.; Hammer, D. A.; Heiney, P. A.; Percec, V. *J. Am. Chem. Soc.* **2007**, *129*, 11698.

17. (a) Stone, A.; Fleisher, E. B. *J. Am. Chem. Soc.* **1968**, *90*, 2735; (b) Cheng, B.; Munro, O. Q.; Marques, H. M.; Scheidt, W. R. *J. Am. Chem. Soc.* **1997**, *119*, 10732.

18. Finikova, O. S.; Cheprakov, A. V.; Carroll, P. J.; Dalosto, S.; Vinogradov, S. A. *Inorg. Chem.* **2002**, *41*, 6944.

19. Cetinkaya, E.; Johnson, A. W.; Lappert, M. F.; McLaughlin, G. M.; Muir, K. W. *J. Chem. Soc. Dalton. Trans.* **1974**, 1236-1243.

20. Senge, M. O.; Forsyth, T.; Nguyen, L. T.; Smith, K. M. *Angew. Chem. Int. Ed.* **1994**, *33*, 2485-2487.

21. Senge, M. O *Highly substituted porphyrins*, Ch. 6 in *The Porphyrin Handbook*, Kadish, K. M.; Smith, K. M.; Guilard, R. Eds., Academic Press, 2000.

22. Stone, A.; Fleisher, E. B. *J. Am. Chem. Soc.* **1968**, *90*, 2735-2748.

23. Cheng, B.; Munro, O. Q.; Marques, H. M.; Scheidt, W. R. *J. Am. Chem. Soc.* **1997**, *119*, 10732-10742.

24. Rosa, A.; Ricciardi, G.; Baerends, E. J.; Romeo, A.; Scolaro, L. M. *Journal of Physical Chemistry A* **2003**, *107*, 11468.

25. Almarsson, O.; Blasko, A.; Bruice, T. C. *Tetrahedron* **1993**, *49*, 10239.

26. De Luca, G.; Romeo, A.; Scolaro, L. M.; Ricciardi, G.; Rosa, A. *Inorganic Chemistry* **2007**, *46*, 5979.

27. Honda, T.; Kojima, T.; Fukuzumi, S. *Chem. Commun.* **2009**, 4994.

28. Finikova, O. S.; Cheprakov, A. V.; Beletskaya, I. P.; Carroll, P. J.; Vinogradov, S. A. *J. Org. Chem.* **2004**, *69*, 522-535.

29. Finikova, O. S.; Aleshchenkov, S. E.; Briñas, R. P.; Cheprakov, A. V.; Carroll, P. J.; Vinogradov, S. A. *J. Org. Chem.* **2005**, *70*, 4617-4628.

30. Cardona, C. M.; Gawley, R. E. *J. Org. Chem.* **2002**, *67*, 1411.

31. Kubin, R. F.; Fletcher, A. N. *J. Luminescence* **1982**, *27*, 455-462.

32. Seybold, P. G.; Gouterman, M. *J. Mol. Spectrosc.* **1969**, *31*, 1.

33. Jentzen, W.; Song, X.-Z.; Shelnutt, J. A. *J. Phys.Chem. B* **1997**, *101*, 1684.

34.   (a) Rozhkov, V. V.; Khajehpour, M.; Vinogradov, S. A. *Inorg. Chem.* **2003**, *42*, 4253; (b) Lebedev, A. Y.; Filatov, M. A.; Cheprakov, A. V.; Vinogradov, S. A. *J. Phys. Chem. A* **2008**, *112*, 7723.

35.   Lindsey, J. S.; Schreiman, I. C.; Hsu, H. C.; Kearney, P. C.; Marguerettaz, A. M. *J. Org. Chem.* **1987**, *52*, 827-836.

36.   Dandliker, P. J.; Diederich, F.; Gross, M.; Knobler, C. B.; Louati, A.; Sanford, E. M. *Angew. Chem. Int. Ed.* **1994**, *33*, 1739–1742. (b) Dandliker, P. J.; Diederich, F.; Gisselbrecht, J. P.; Louati, A.; Gross, M. *Angew. Chem. Int. Ed.* **1996**, *34*, 2725–2728.
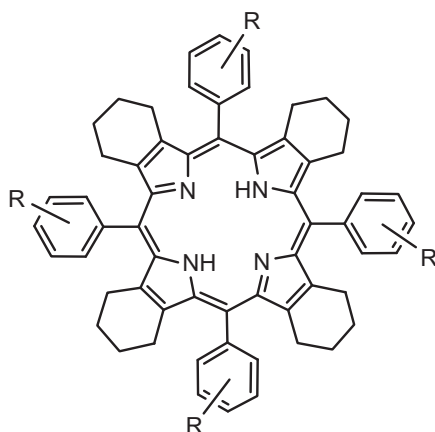
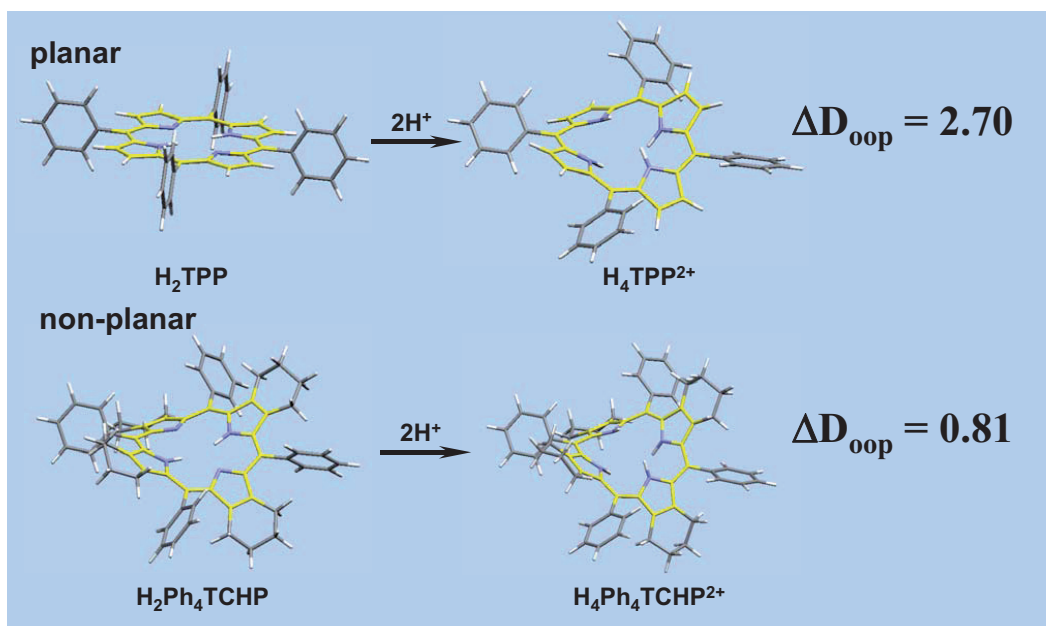**Figure 1.** Structure of tetraaryltetracyclohexenoporphyrin (Ar$_4$TCHP).

Figure 2. Structural changes accompanying protonation of H$_2$TPP (top) and Ar$_4$TCHP (bottom). Changes in total out-of-plane distortion (ΔD_{oop}) upon protonation were quantified by Normal Mode Structural decomposition analysis.
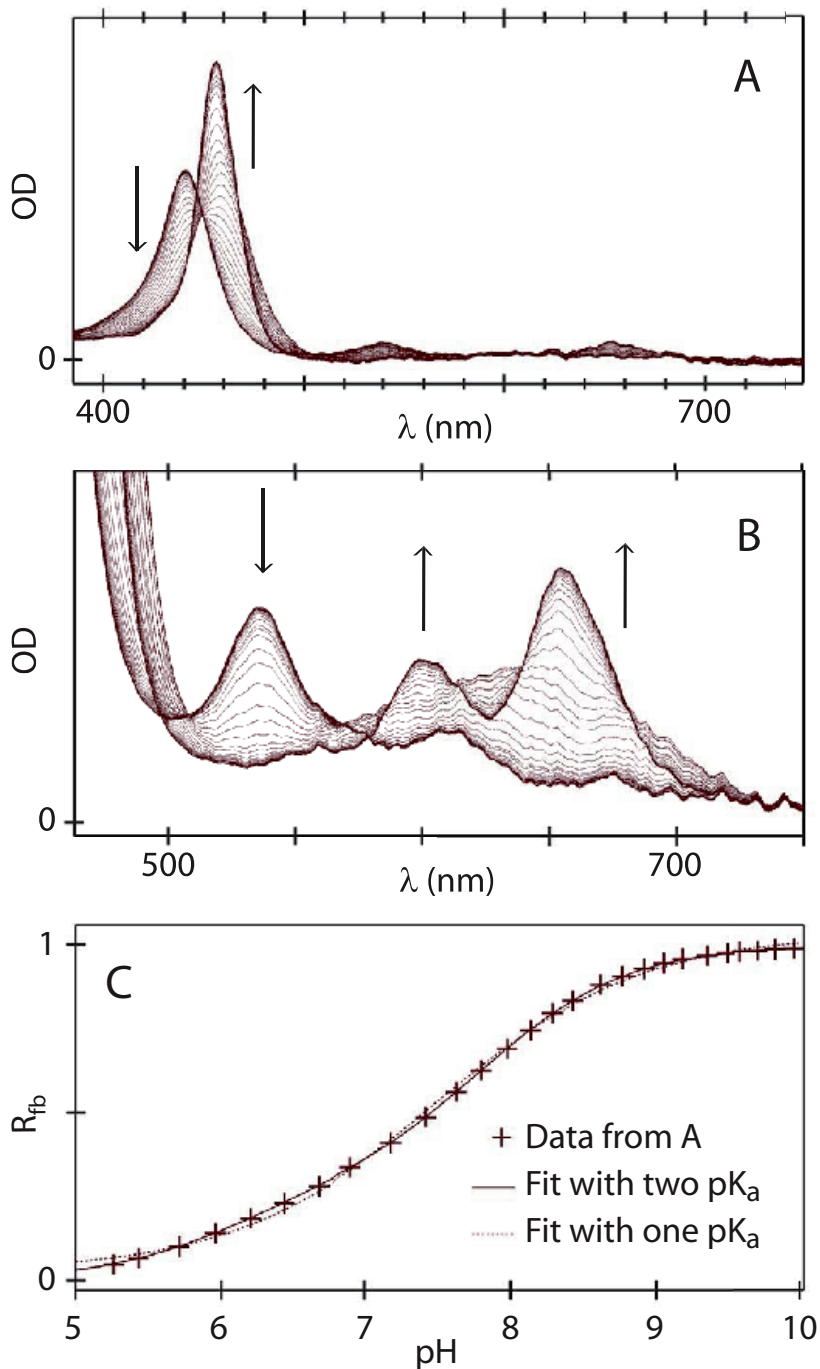
Figure 3. A, B: Absorption spectra of probe TCHpH, titrated from pH 10.6 to 4.0. The arrows indicate the change of peak intensities as pH decreases. C: Rfb (the relative amount of free-base TCHpH), calculated from the data in Figure 3A. Dotted line: Fit of the Hills equation assuming a single pK (Eq. 1) renders pK=7.49, n=0.62. Solid line: Fit of the Hills equation assuming two separate pK's (Eq. 2) renders pK3=6.09, C1=0.29, pK4=7.83, C2=0.71, n=0.88.
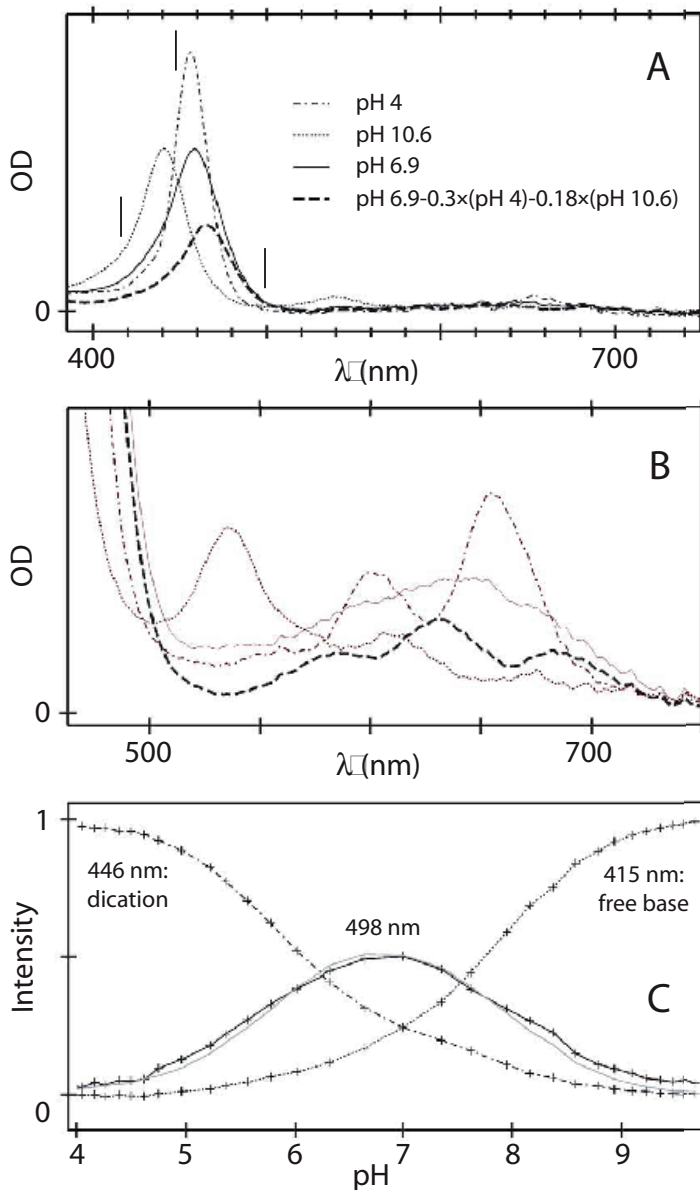
Figure 4. A, B: Selected absorption spectra from Figure 3: The dication spectrum (pH 4), the free-base spectrum (pH 10.6) and the spectrum acquired at pH 6.9. The heavy, dashed line is the estimated spectrum of the species present at intermediate pH, deconvoluted from the other three spectra as specified in the figure. **C:** The relative population of the free base, the dication and the intermediate species vs pH, from the data in Figure 4A. Free base: OD(415 nm) was normalized to 1 at high pH. Dication: OD(446 nm) was corrected for contributions from the free-base spectrum using OD(415 nm), then normalized to 1 at low pH. Intermediate species: OD(498 nm) was normalized so that the three curves add up to 1 at pH 7. The grey trace represents 1-(free base + dication), as determined by the present graph. 415 nm, 446 nm and 498 nm are indicated with bars in Figure 4A.
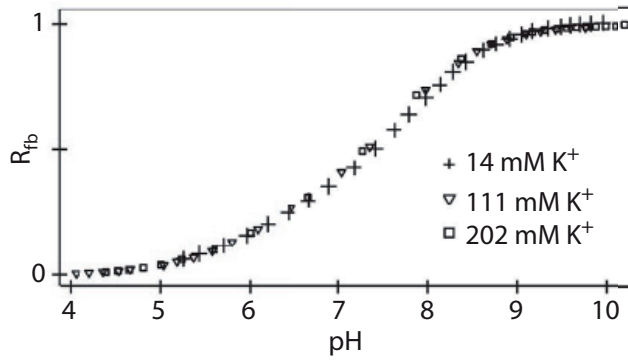
Figure 5. Rfb (the relative amount of free-base) of TCHpH in solution as a function of pH, in the presence of different K+ concentrations as specified. The lowest concentration is the data from Figure 3.
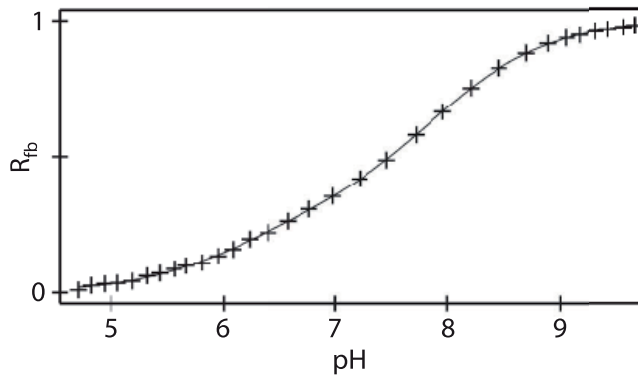
Figure 6. Rfb of TCHpH encapsulated in large unilamellar vesicles as a function of pH. Gramicidin was present during pH titration, facilitating ion exchange across the membrane. Fit to Eq. 3, yielding pK3=6.12, C1=0.30, pK4=7.89, C2=0.70, n=0.85.
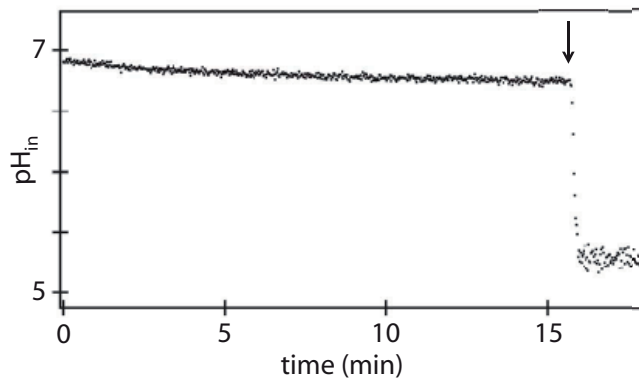

Figure 7. Interior liposome pH, determined using TCHpH absorbance. At time 0, liposomes of internal pH 7 were diluted into a buffer of pH 4.75. Gramicidin was added at the arrow.

IV

An Improved Detergent-Mediated Reconstitution Method Yields Unidirectional Influenza A/M2 Proteoliposomes.

Thom Leiding[1], Jonas Martinsson[1], Katja Bernfur[1], Alexandra Franzén[1], Björn Borgström[1], Alexei L. Polishchuk[2], William F. DeGrado[2] and Sindra Peterson Årsköld[1,*]

1. Department of Biochemistry and Structural Biology, Center of Chemistry and Chemical Engineering, Lund University, Box 124, SE-22100 Lund, Sweden.

2. Department of Biochemistry and Biophysics, University of Pennsylvania, Philadelphia, PA 19104-6059, USA.

* To whom correspondence should be addressed. Phone +46 46 222 8178, fax +46 46 222 4116, e-mail Sindra.peterson_arskold@biochemistry.lu.se.

Abstract

An improved method for reconstituting membrane proteins into artificial liposomes for quantitative functional analysis is presented. Optimization for reconstitution of the drug target M2 from Influenza virus A resulted in fully unidirectional reconstitution. The pH sensor Glu[3] was used to quantify proton flux through the reconstituted protein, reporting rates up to 47 protons per M2 tetramer and second under an electrical gradient of 62 mV, in the N → C direction. This value is considerably higher than previously reported rates of 5-10 for reconstituted M2 under an electrical gradient of 120 mV. The effect on M2 proton flux of a range of known inhibitors was quantified, demonstrating this method as suitable for drug screening. The reconstitution process utilizes detergent solubilization of a preformed liposome suspension followed by slow detergent removal by hydrophobic beads. Protein-free liposomes produced this way allowed a passive permeability of approximately 17 protons $(s \cdot \mu m^2)^{-1}$ and 30 K^+ ions $(s \cdot \mu m^2)^{-1}$, under a pH gradient of one pH unit (60 mV). This high liposome integrity enables uncompromised proton-translocation measurements, spanning hours if necessary. A number of key parameters for reconstitution by detergent removal are assessed in this paper: The lipid-to-protein ratio, the detergent-to-lipid ratio and the lipid and cholesterol composition. Starting with preformed liposomes rather than a poorly defined lipid suspension resulted in predictable solubilization behavior, facilitating optimization of the reconstitution parameters and ensuring reproducible results. While the presence of cholesterol did not affect ion leakage in the protein-free liposomes, it had a significant effect on the proton flux rates of M2 proteoliposomes, indicating an activating effect of cholesterol on M2 proton transfer under these conditions. The precise intravesicular volume was determined experimentally by

absorbance, rendered possible by the unilamellar nature of the liposomes and the bilayer impermeability of Glu[3]. The Biorad DC Protein Assay was adapted to samples with high lipid and low protein content to quantify the protein in the proteoliposomes. Together, this enabled absolute proton-flux quantitation. Based on this systematic, comprehensive approach to protein reconstitution, we present a robust system for quantitative proton-flux analysis, as demonstrated by M2 reconstitution into large unilamellar vesicles.

Abbreviations

ACN: Acetonitrile, CCCP: carbonylcyanide chlorophenylhydrazone, CMC: critical micelle concentration, DDM: dodecyl maltoside, DM: decyl maltoside, DMSO: dimethyl sulfoxide, EDTA: ethylene-diamine-tetraacetic acid, LPR: lipid-to-protein ratio, LUV: large unilamellar vesicles, MS: mass spectrometry, OD: optical density, OG: octyl glucoside, PdI: polydispersity index, PFV: preformed vesicles, POPA: palmitoyl-oleoyl phosphatidic acid, POPC: palmitoyl-oleoyl phosphatidylcholine, POPG: palmitoyl-oleoyl phosphoglycerol, RNP: ribonucleoprotein, RMS: root mean square, SDS: sodium dodecyl sulfate, TFA: trifluoroacetic acid, TM: transmembrane, Triton: Triton X-100.

1. Introduction

Proteoliposome assays harbor great promise for a range of membrane-bound proteins, particularly ion channels and bioenergetic proton transporters. Reconstitution in artificial lipid bilayers recreates the membrane environment of the protein while removing the complexity of the native membranes and interferences with other membrane constituents. This is especially relevant when dealing with proteins that have influence on or are influenced by chemical gradients. The liposome assay also recreates sample compartmentalization, enabling measurements of ion concentration gradients across the bilayer; this is particularly effective in combinaton with ion-sensitive molecular probes.

However, producing proteoliposomes of reproducibly high quality has proven challenging. Bilayers with high ion permeability are unable to sustain concentration gradients for longer than a few minutes, thus limiting the measurement window and giving rise to systematic errors in measured ion-translocation rates. Morphological heterogeneity, such as varying liposome size and multilamellar populations, increases noise levels and obstructs quantification. Uncertainty as to how much protein has been successfully incorporated in the bilayer and in which orientation it has been inserted thwarts accurate data analysis. Finally, the reproducibility of the liposome production process has proven problematic, as the factors that lead to successful reconstitution of proteins have been elusive. Probe-related issues such as probe leakage or probe interaction with the membrane or proteins can also cause problems, particularly in the absence of reliable intravesicular probe-calibration procedures. These challenges make it difficult to calculate specific protein activities, and therefore many liposome assays result in inherently qualitative or relative data.

Despite these difficulties, a number of successful proteoliposome studies have been accomplished using different reconstitution methods. Signeuret and Rigaud used reversed-phase evaporation

followed by detergent solubilization and detergent removal by hydrophobic beads to reconstitute Bacteriorhodopsin and measure light-induced proton transport [1, 2]. Proton pumping was estimated using Pyranine fluorescence. Galkin and coworkers used a similar method, replacing the reversed-phase evaporation with direct solubilization of dried lipid film with detergent and sonication, to reconstitute mitochondrial Complex I. Using Neutral red in a weakly buffered external bulk, the proton-pumping stoichiometry was determined by absorbance to 3.6 protons translocated per two electrons transferred through the complex [3]. A number of methods have been employed for recosntitution of the Influenza A virus protein M2. Schroeder et al. used detergent removal by dialysis, detecting pH with Pyranine fluorescence [4]. Moffat et al. reconstituted M2 by a two-step method where protein-rich proteoliposomes were created with dialysis [5], then mixed with protein-free vesicles, vortexed and freeze-thawed. Proton movement was monitored using a weakly buffered external bulk and a pH electrode. Ma and coworkers added a truncated form of the protein in ethanol to dried lipid film, followed by hydration, vortexing, freeze-thawing and extrusion, and used Pyranine for proton-flux detection [6].

1.1 Systematizing protein reconstitution

In this paper, we attempt to systematically resolve the factors that determine the outcome of a reconstitution experiment. We address the lipid starting material, the detergent-to-lipid ratio, the protein-to-lipid ratio, the rate of detergent removal, and the choice of detergent and lipid composition. We map out the behavior of lipid-detergent dispersions under relevant conditions, providing an overview of key parameters and a basis for systematic optimization of protein reconstitution. The result is reproducably tight, homogenous, unilamellar vesicles. Absorbance measurements of the membrane-impermeable pH sensor Glu[3] [7] enables precise intraliposomal volume determination as well as quantitative proton-flux measurements. We also present a protein-determination method adjusted to samples with high lipid and low protein concentrations, in order to determine the amount of protein present in the final proteoliposomes. These steps exclude a number of common assumptions and minimize error in the evaluation of specific proton-translocating activity. As a proof of concept, we chose to reconstitute the structurally determined and well characterized M2 protein of Influenza virus A, which has been the subject of a number of previous reconstitution investigations (see section 1.3) [4-6, 8-11]. The mechanism of M2 conductance is of general interest with respect to the topic of proton transport as well as the development of new antivirals, and a comprehensive investigation of ion translocation by unidirectionally reconstituted M2 is presented elsewhere [12].

1.2 Protein M2 of Influenza Virus A

The influenza A virus M2 protein is a tetrameric integral membrane protein containing a short N-terminal extracellular domain, a transmembrane (TM) helix, and a 54-residue cytoplasmic tail [13, 14]. Four M2 TM domains associate into a highly selective proton channel [15, 16], whose activity is essential for viral replication [17, 18]. Influenza virus enters cells via the endosomal pathway, and the M2 protein functions to equilibrate the pH of the virus interior with that of the acidic endosome. The lowering of pH within the virus leads to disruption of the interactions between the viral ribonucleoprotein (RNP) complex and the M1 protein [17], an important step in viral uncoating [19]. Additionally, for some subtypes of influenza A virus, the M2 proton channel activity helps maintain a neutral pH in the lumen of the trans-Golgi network to prevent premature triggering of the hemagglutinin to the low-pH form [20-23]. M2 is the target of the adamantane-containing anti-

influenza drugs amantadine and rimantadine [15, 16, 24, 25], as well as spiro-piperidines [26] related spiro-cyclohexylamines [27]. Structures of the A/M2 TM domain have been determined by X-ray crystallography [28] and a structure of the TM domain with 17 residues of the cytoplasmic tail was determined by solution NMR [29].

The conductance of the M2 channel has been most thoroughly studied by measuring macroscopic whole-cell current in oocytes and mammalian cells at mildly acidic pH [15, 16, 18, 24, 30-32]. From first principles, it is known that the rate is limited by the low proton concentrations under physiological conditions [33]. Given the physical dimensions of the channel[33], the most rapid rate at which protons might be expected to diffuse through the pore would be on the order of 10^8 to 10^9 $M^{-1}sec^{-1}$, corresponding to a proton flux of 10 to 10^4 sec^{-1} at the proton concentrations corresponding to pH 7 and 5. The low conductance of the channel has made single-channel studies in transfected cells technically infeasible. However, the mean flux per tetramer has been determined by normalizing the current observed in a series of oocytes with the amount of protein expressed in the same oocytes (as determined from quantitative immunoblotting). A time-average inward proton current of 0.5 fA (corresponding to about 3000 ions per second) was determined when the driving force was approximately 0.2 V.

1.3 M2 proteoliposomes

Given the problems associated with measurements of the single-channel current of M2, there has been considerable interest in reconstituting the protein in phospholipid bilayers and vesicles, although these studies have met with varying degrees of success. M2 has been reconstituted in large unilamellar vesicles (LUV), and shown to have a conductance similar to that measured in whole cells. Schroeder [4, 10, 11] confirmed the proton-selectivity of the channel, and observed a conductance of 10^{-18} A (1.2 aA) with pH_{out} = 7.4, a temperature of 18° C, and a TM potential of 150 mV. Although this current is lower than that in transfected cells, the discrepancy is partly a result of the use of reduced temperature in the vesicle studies, which provides an experimentally convenient rate of conduction. One recent study has confirmed the original work of Schroeder et al [6], while another carefully conducted series of experiments found the proton flux was approximately 10-fold lower [9, 34]. Moreover this latter study found the rate of proton flux decreased rather than increased at low pH [9, 34]. Chou and coworkers have examined a series of single-site mutants of a functional fragment of M2 using the vesicle flux assay [8]; Lamb, Pinto and their coworkers examined the same set of mutants in full-length M2 in oocytes as well as in reverse-engineered viruses[32] [35, 36]. There was very little qualitative or quantitative agreement between the magnitude of proton flux and drug-sensitivity seen in the two studies. Finally, electrophysiological studies of M2 show that it has significant rectification that varies in a functionally interesting manner with respect to the M2 proteins from different viral strains; by contrast the current/voltage curves from M2 proteoliposomes are highly linear, probably because the channel is randomly inserted in the bilayer with the N-terminus oriented either inward or outward [10, 11].

Liposome assays offer great promise for M2, because they allow convenient correlation between function versus ssNMR and optical spectroscopic measurements of M2 in vesicles [37-42] or bilayers [43-49]. Along these lines, there is encouraging agreement between liposome studies and electrophysiological studies of M2 concerning its proton-selectivity, and qualitative agreement that the channel is relatively small, although the estimates from vesicle flux assays tend to be significantly lower by about one to three orders of magnitude. There have been no reports of unidirectional

insertion, which would allow facile measurements of the asymmetric aspects of conduction.

Using the present reconstitution system, we have identified conditions for unidirectional insertion of the full-length M2 protein into large unilamellar vesicles, with the N-terminal out as in its native membrane. We characterize the M2 proteoliposomes morphologically and functionally and quantify M2-catalyzed proton flux with unprecedented precision.

2. Materials and Methods

2.1 Preparation of preformed vesicles

All phospholipids were from Avanti Polar Lipids. Preformed vesicles (PFV) were prepared with almitoyl-oleoyl phosphatidylcholine (POPC), palmitoyl-oleoyl phosphoglycerol (POPG), palmitoyl-oleoyl phosphatidic acid (POPA) and cholesterol (Sigma), at the molar ratio specified for each experiment. A total of 28.6 mg POPC, POPG and POPA in chloroform was added to an evaporation flask. When cholesterol was used, it was added as a chloroform solution at this time. The chloroform was evaporated under nitrogen gas. 4 ml K buffer (potassium phosphate 20 mM / di-potassium sulphate 50 mM / 250 µM EDTA pH 7.0; $[K^+]_{total}$=130 mM) or Na buffer (sodium phosphate 20 mM / di-sodium sulphate 50 mM / 250 µM EDTA pH 7.0; $[Na^+]_{total}$=130 mM) was added to the resulting lipid film and the sample was sonicated on ice 4×40 s separated by 20 s periods, using a micro-horn on a Branson Sonifier 250. This resulted in large multilamellar vesicles. The suspension was extruded nine times through a 200 nm polycarbonate filter in an Avestin LiposoFast extruder to give a well-defined vesicle suspension (Figure 1A).

2.2 Solubilization of preformed vesicles

All detergents were from Anatrace/Affymetrix. The solubilization behavior of PFV was investigated as sample turbidity versus the detergent-to-lipid ratio (R). R was defined as the molar ratio of detergent concentration exceding the CMC to the total lipid concentration, not counting cholesterol. Turbidity was taken as the spectral background caused by scattering, detected optically in non-absorbing spectral regions: $OD_{480} - OD_{700}$. Stock detergent solutions of 77 mM Triton X-100 (Triton) [50], 380 mM octyl glucoside (OG) [51], 170 mM dodecyl-β-d-maltoside (DDM) [52] and 420 mM decyl maltoside (DM) [53] were used. The equilibration time was determined for each detergent-lipid combination by monitoring the turbidity after the addition of a non-solubilizing amount of detergent, noting the time required for the turbidity to stabilize. The equilibration times obtained were used for all subsequent solubilization protocols.

Detergent was titrated into a suspension of PFV, and the turbidity was recorded after each addition and equilibration. At every titration point, the size distribution of the dispersion was determined by dynamic light-scattering (DLS) with a Zetasizer Nano-S from Malvern Instruments. R_{sat} was defined as the R at the turbidity maximum preceding the decline towards total solubilization (see Figure 2) for Triton and OG, and the R preceding two-phase behaviour for DDM and DM. R_{sol} was defined as the R required for complete solubilization of the PFV, characterized by a turbidity level that does not decrease further with increasing R. All solubilization was performed with gentle stirring at 18°C.

Turbidity measurements were recorded on an Avantes AvaSpec-2048 fiberoptic spectrometer with a Tungsten-Halogen light-source.

2.3 Detergent removal and liposome self-assembly

PFV of molar composition POPC/POPA 9:1 were prepared as described above and completely solubilized with $R \geq R_{sol}$. Self-assembly of the thus solubilized phospholipids into liposomes was achieved by gradually removing detergent using hydrophobic polystyrene beads (Bio-Beads SM-2, Bio-Rad). Detergent removal was performed in an in-house constructed instrument combining a CCD vis-spectroscopy line with automated bead additions, temperature control and stirring. Prior to bead additions, the beads were washed with methanol, then water, repeated three times, and lastly with water three times to remove any traces of methanol. A total of 2.4 ml moist beads were added to the suspension. The detergent-removal rate was varied by adding the beads in several smaller portions: 1×2.4 ml, 4×0.6 ml, or 12×0.2 ml, at 16-minute intervals (see Table 1). Vesicle formation was monitored as turbidity over time (see Figure 3). When the turbidity had been steady for 30 minutes, the vesicles were harvested by removing the suspension from the beads with a syringe. Detergent removal was done with stirring at 18°C.

2.4 Reconstitution of M2 into proteoliposomes

Full-length M2 (A/Udorn/72, cys free W15F variant, W15F, C17S, C19S, C50S) was prepared as described in [6]. 0.5 ml 0.5 M OG, 3.4 ml K or Na buffer, and 3.5 ml PFV (POPC/POPG/cholesterol 3:1:1) were added to a glass vial. This results in $R = R_{sat} = 2.6$. Detergent and lipid were equilibrated at 18°C for 20 minutes with stirring, before 14 µl stock protein (340 µM) was added to yield a molar lipid-to-protein ratio of 6900 (not counting cholesterol). The protein-lipid-detergent mixture was equilibrated for 40 minutes at 18°C with stirring. 2 mg of the pH sensor Glu[3] [7], dissolved in 0.1 ml water, was added to the vial.

Detergent removal was performed as described above, adding 6×0.4 ml beads at 16-minute intervals at 18°C with stirring. Following the last bead addition, the sample was left with stirring at 18°C for 90 min to allow complete detergent removal. Liposome formation was monitored by recording turbidity ($OD_{610} - OD_{760}$) every 4 min throughout the proteoliposome formation process. The final liposome suspension was harvested and ultracentrifuged at 100,000×g at 4°C for 2 h. The pellet was gently resuspended in 1 ml reconstitution buffer and passed through a 1 ml HiTrap Q XL anion exchange column (GE Healthcare) to remove traces of external Glu[3]. The resulting Glu[3]-containing M2-proteoliposomes were stored at 4°C for up to three days.

2.5 Passive permeability of LUV

Glu[3]-containing liposomes were prepared as described for M2 proteoliposomes, with different lipid compositions and without adding protein. K buffer was used. For measurements, 0.1 ml liposome dispersion was diluted in K buffer to a total volume of 1 ml. Spectra were continuously recorded on

an Avantes AvaSpec-2048 fiberoptic spectrometer with a Tungsten-Halogen light source. 4 s signal-averaging per spectrum gave a time resolution of ~5 s. ΔpH $\approx$ 1 over the liposome bilayer was induced by adding 0.5 M sulphuric acid (Figure 4:1). The bulk pH was measured with an Orion ROSS 8220 combination pH microelectrode (Thermo Electron). The additions in Figure 4 were: valinomycin (Sigma) dissolved in dimethyl sulfoxide (DMSO), to a final concentration of 0.5 μM, CCCP (Sigma) dissolved in DMSO, to a final concentration of 0.5 μM, gramicidin (Sigma) dissolved in DMSO, to a final concentration of 1 μg/ml.

2.6 Protein quantification in proteoliposomes

Determination of the amount of protein incorporated in the M2 proteoliposomes was done with the "DC Protein Assay" from Biorad, modified for use with lipid concentrations up to 25 mg/ml and protein concentrations down to 10 μg/ml by including two solubilization steps as follows. Reagent A´: 20 μl of reagent S was added to each ml of reagent A needed. 180-μl samples were treated as follows, with vortexing immediately after each addition: add 100 μl reagent A´; add 800 μl reagent B; add 20 μl 10% SDS (Sigma); add 20 μl 10% Triton. The thus solubilized samples were incubated at room temperature for 15 minutes, after which the absorbance at 750 nm was recorded. Purified M2 of known concentration was used to establish a standard curve with which to interpret the results.

2.7 Mass spectrometry

Samples were enzymatically digested using trypsin, and the resulting peptides were analyzed by MALDI-TOF and MALDI-TOF/TOF mass spectrometry (MS). Trypsin (Seq. Grade Modified Trypsin, Porcine, from Promega) was added from a 100 ng/μl stock solution to a final trypsin-to-protein ratio of 1:10 (w/w), in a total sample volume of 100 μl. After overnight incubation at 37°C, 3 μl of 10% trifluoro acetic acid (TFA) was added to stop proteolysis. Samples were purified and concentrated using POPOS R2 microcolumns [54]. After washing the microcolumns with 10 μl 80% ACN and equilibration with 20 μl 0.1% TFA, 20 μl peptide mixture was added in 10 μl 0.1% TFA onto the microcolumn. After washing the microcolumns twice with 25 μl 0.1% TFA, peptides were eluted with 80% ACN directly onto a MALDI target plate. A matrix solution containing of 5 mg/ml α-cyano-4-hydroxy cinnamic acid, 50% acetonitrile, 1% TFA and 25 mM citric acid was added in 0.5 μl portions onto each of the dried peptide sample preparations.

MS and MS/MS spectra were acquired on a 4700 MALDI TOF/TOF mass spectrometer (Applied Biosystems, Framingham, CA, USA) in positive reflector mode. For each sample, a total of 1200 single-shot spectra were accumulated. All MS spectra were internally calibrated using three standard peptides: Angiotensin II, Neurotensin and ACTH (clip18-39), with *m/z* values 1046.564 Da, 1672.918 Da and 2465.199 Da.

2.8 Intravesicular pH monitored by Glu^3 spectra

R_{fb} , the fraction of deprotonated Glu[3] at a given pH, was derived from the Soret peak absorbances of the free base (A_{415}) and the dication (A_{439}) after correcting for the scattering baseline induced by the liposomes [7]:

$$R_{base} = \left(\frac{A_{415} - A_{439} \cdot q}{A_{415}(1 - m \cdot p) + A_{439}(m - q)} - B_n \right) \frac{1}{C_n} \qquad \text{(eq. 1)}$$

The constants m, p, q, B_n and C_n were determined by calibration of the encapsulated probe, as described below. m accounts for the different extinction coefficients of the free-base and dication Soret peaks. The partial overlap of the absorbance features is accounted for by the constant q, which corrects for the absorbance of the dication at 415 nm, and p, which corrects for the absorbance of the free base at 439 nm. B_n and C_n ensure that R_{fb} spans the range 0 - 1. In [7], we evaluated these constants from acid and alkali spectra obtained in bulk. Here, we have improved the precision by calibrating these parameters (along with the probe pK) *in situ* for each batch of liposomes, using an iterative process to evaluate the constants in each case. Typical values obtained are *m = 1.16, p = 0.03, q = 0.16, B_n = 0.001, and C_n = 0.99.*

2.9 Calibration of encapsulated Glu[3]

For maximal precision in pH determination, calibration of intravesicular Glu[3] was performed in connection to each set of proton-flux measurements. The spectral read-out was calibrated versus bulk pH in the presence of 1 µg/ml gramicidin.

Titrations were performed with an in-house constructed titration system, consisting of a sample holder featuring stirring, an electrode duct and a capillary inlet, and coupled to a spectrometer. A 100 µl gas-tight Hamilton syringe attached to a computer-controlled NE-500 syringe pump from New Era Pump Systems Inc is connected to the capillary inlet of the sample holder. The syringe pump administers precise volumes of 0.5 M H_2SO_4, calculated by the controlling software in combination with electrode feedback to achieve the desired pH. The bulk pH is monitored with an Orion ROSS 8220 combination pH microelectrode (Thermo Electron), fitted to the electrode duct of the sample holder. Glu[3] calibrations were run automatically by configuring the software to set pH and acquire a spectrum every 0.2 pH units from pH 7.4 to pH 4.5. The constants m, p and q of Eq. 1 were determined:

$$m = \frac{A_{415\,max}}{A_{439\,max}}, \quad p = \frac{A_{439\,min}}{A_{415\,max}} \text{ and } q = \frac{A_{415\,min}}{A_{439\,max}} \qquad \text{(eq. 2)}$$

where A_{415max} and A_{439min} are the absorbance values when Glu[3] is fully protonated, and A_{439max} and A_{415min} are the absorbances for fully deprotonated Glu[3]. R_{fb} (Eq. 1) vs. pH value was fitted with the Hill equation [7]:

$$R_{fb} = \frac{10^{n(pH - pK)}}{1 + 10^{n(pH - pK)}} \qquad \text{(eq. 3)}$$

where pK is the pH at which R_{fb} = 0.5. The sigmoidal curve yielded values for C_n and B_n of Eq. 1, and R_{fb} was adjusted iteratively.

2.10 Proton-flux assay

A positive electrical gradient was created over the proteoliposome membrane by establishing a K^+ concentration gradient: At time t=0 (Figure 6), 0.1 ml M2 proteoliposomes made with K buffer were diluted into 0.9 ml Na buffer. The two buffers were identical except for the cation species (see Section 2.1); Na^+ was present for isotonicity between the inside and outside of the LUV. Taking into account the 80 μl K buffer from the proteoliposome stock added, the final K^+ concentrations were $[K^+]_{in}$=130 mM, $[K^+]_{out}$=11 mM, creating a membrane potential of 62 mV, negative inside. The outside buffer contained 0.5 μM valinomycin, rendering the bilayer permeable to K^+. Glu^3 spectra were continuously recorded after the K^+ gradient was induced, with a 0.5-1 s time resolution.

2.11 Inhibitor screening

Spiro-piperidine (compound 9), 3-methyl-3-azoniaspiro[5,5]undecane chloride (compound 10), 1,5-dioxa-9-azaspiro[5,5]undecane (compound 17) and 1,5-dithia-9-azaspiro[5,5]undecane (compound 18) [27] were kind gifts from Jun Wang. Amantadine was from Sigma. M2 proteoliposomes were incubated with 0.1 mM of the compound for one hour in room temperature while stirring, then subjected to the proton-flux assay (section 2.10).

3. Results and Discussion

3.1 Liposome solubilization and self-assembly

3.1.1 Lipid starting material: Preformed vesicles

We used the method of liposome assembly by bead-mediated detergent removal from a lipid/detergent mixture [55], to produce liposomes with and without protein. For consistent and repeatable results, PFV were used as starting material rather than a less well defined lipid/buffer dispersion. PFV were produced by mixing lipids dissolved in chloroform, evaporating the chloroform, adding the aqueous buffer of choice, sonicating, and finally extruding through a 200 nm filter (see 2:1). This resulted in mono- and bilamellar vesicles with diameters ranging from 30 to 200 nm, as seen in Figure 1A. These vesicles equilibrate rapidly with detergent and are solubilized in a reproducible manner. We can thus identify detergent-to-lipid ratios corresponding to specific aggregation states of the lipid-detergent dispersion, and determine equilibration times for the aggregation process in each case. This well-defined starting material is easy to prepare and displays predictable solubilization behavior, which facilitates a systematic approach to successful protein reconstitution.

3.1.2 Solubilization of preformed vesicles

To gain an understanding of the LUV solubilization process and to establish the detergent concentrations that produce specific aggregation states, solubilization experiments were conducted on POPC/POPA (9:1) PFV. The detergent/lipid equilibration times for four detergents often used in protein preparations were determined: 15 min for Triton, 5 min for OG and 180 min for DM and DDM. We subjected the PFV to gradual solubilization by these detergents. Each detergent was titrated in, and the resulting vesicle morphology was investigated by turbidity measurements and DLS. The results are shown in Figure 2.

In Figure 2a, sample turbidity is plotted versus Triton detergent-to-lipid ratio (R, defined in Section 2.2). The initial turbidity reflects the size of the PFV. Turbidity increases with R until the liposomes are fully saturated with detergent; we define R_{sat} as the R at this turbidity maximum, 0.4 for Triton. The maximum is followed by a decrease in turbidity towards optical transparancy. We define R_{sol} as the R of complete solubilization, 1.7 for Triton. The equivalent graphs for detergents OG, DM and DDM are plotted in Figures 2B-D. Key points from the turbidity plots were examined by DLS, shown in the insets: No detergent, R_{sat}, R_{sol}, and one point between R_{sat} and R_{sol}. We note that the PFV sizes recorded by DLS in Figure 2 accurately reflect the size detected by cryo-TEM (Figure 1A), validating the use of DLS for vesicle size estimation.

DLS of Triton-treated PFV (Figure 2A, inset) shows a liposome diameter of 150 nm at R = 0, 190 nm at R_{sat} and 20 nm at R_{sol}. Interestingly, the point chosen on the turbidity slope between R_{sat} and R_{sol} (R=1.1) shows larger aggregates by DLS, 350 nm, than those at R_{sat}. This apparent discrepancy is due to the different nature of DLS and turbidity measurements. Turbidity reflects the static light scattering of a sample, related to the root mean square (RMS) radius of the particles. DLS, however, is based on Brownian motion, and reports on the hydrodynamic radius of the particles present, i.e. the largest radius. If the aggregates present were spherical, the RMS and hydrodynamic radii would be similar. However, elongated structures have a hydrodynamic radius corresponding to their longest axis, which exceeds their RMS radius. We therefore interpret the large DLS diameter recorded for $R_{sat} < R < R_{sol}$ as an aggregation phase of extended or elongated structures preceding the terminal state of mixed micelles.

 For OG (Figure 2B) the turbidity plot is similar to that of Triton, except for an initial decrease in turbidity. The decrease is mirrored by DLS: the PFV diameter of 160 nm decreases to 120 nm at R_{sat}. Again, elongated structures seem to appear after R_{sat}, before the final state of mixed micelles with a diameter of 10 nm.

DM and DDM display two-phase behavior with PFV in the R domain preceding R_{sat} (Figure 2C,D: shaded regions). Characteristically, these detergent-lipid dispersions do not equilibrate within the experimentally established equilibration time, but grow gradually more turbid. Eventually they separate into two macroscopic phases, one transparent and one turbid. The DM two-phase domain occurs at 0.5 < R < 1.4, and the DDM two-phase domain occurs at 1 < R < 1.8. Apart from the two-phase domain, the turbidity plots for DM and DDM are similar to that for Triton. For these detergents, we define R_{sat} as the highest R below the two-phase domain.

For DM, the final dispersion is dominated by 10-nm micelles (Figure 2C). DDM DLS data show a distribution of sizes at R_{sat}, and the final aggregates at optical transparency are considerably larger than for the other detergents.

Figure 2 shows a complex but predictable behavior of PFV under subsolubilizing conditions, in agreement with a recent study of lipid dynamics under similar conditions [56]. The detergent concentration giving R_{sat} is of particular interest to protein-reconstitution procedures, as it may be preferable to insert a protein in the geometric context of an intact liposome - this can influence protein directionality and proteoliposome integrity.

3.1.3 Self-assembly into large unilamellar vesicles

Starting with completely solubilised PFV (mixed micelles, POPC/POPA 9:1), liposomes were allowed to form by gradually removing detergent using hydrophobic beads. We chose removal by hydrophobic beads rather than dilution or dialysis, as it is a relatively fast method that has been shown by isotope labeling to leave no detergent molecules in the resulting liposomes [55]. This is important as even sub-CMC concentrations of residual detergent induces dynamicity and permeability of the bilayer [56]. The progression of liposome formation during detergent removal was monitored as sample turbidity vs time in Figure 3, where each bead addition in indicated by a line. As expected, the plot shows the reverse shape of the turbidity plot from the gradual solubilization in Figure 2. Initially excess detergent is absorbed by the beads, after which a sharp increase in turbidity reflects the formation of larger complexes. The turbidity reaches a maximum when detergent-saturated vesicles have formed, and subsequently decreases as detergent is extracted from the vesicles. This is a slow process that is limited by three detergent-concentration equilibria: between bulk detergent and detergent in the outer bilayer leaflet, between the outer and inner leaflets and finally between the inner leaflet and the encapsulated solution. After the turbidity maximum is reached it can take up to two hours for the residual detergent to be absorbed by the beads and the turbidity level to stabilize, depending on the lipid-detergent system used. The vesicles are harvested when the turbidity level has been constant for 30 minutes.

The effect of detergent-removal rate on self-assembly was addressed by adding the beads at different rates, as detailed in Section 2.3. Table 1 summarizes the effect of removal rate on the final liposome size. For Triton a clear correlation was seen: The slower the removal rate, the larger the vesicles. The trend was less clear with OG, but the lowest removal rate still resulted in the largest vesicles. Under identical conditions, vesicles formed with Triton had a 50% larger diameter than those formed with OG. This may be explained by the higher molar concentration of OG; similar bead-adsorption rates would result in slower detergent removal for OG than for Triton. Larger vesicles are formed at slower removal rates [55], possibly due to larger bilayer aggregates having time to form before they close into spherical liposomes. Size distribution, as reported by the DLS polydispersity index (PdI), did not display a clear trend with detergent-removal rate.

The method of gradual detergent removal procures relatively uniform, unilamellar vesicles, as determined by cryo-TEM (Fig. 1 C,D). Comparing this to repeated freeze-thawing, another method sometimes employed for protein reconstitution, the same starting material produces multilamellar structures, shown in Fig. 1B.

3.2 Passive permeability of liposomes

The passive permeability of protons and potassium ions through lipid bilayers of different composition was assessed. The internal LUV pH was monitored continuously by Glu[3] absorption, as displayed on the y axis of Figure 4. At point 1 in the graph, the bulk pH was lowered by one pH-unit, creating a pH gradient over the bilayer. A minor decrease in pH is observed, possibly due to a few burst vesicles leaving a small population of Glu[3] in the bulk. At point 2 in the bottom trace, the protonophore CCCP was added. Although a proton gradient was present and protons could move freely across the membrane via CCCP, the influx was almost instantly retarded by electrostatic forces, and proton movement into the liposomes was very slow between points 2 and 3. At point 3 the K^+-selective ionophore valinomycin was added, allowing K^+ ions to move freely over the membrane and resulting in rapid release of the proton gradient. Gramicidin was added at point 4 to verify that the gradients were equilibrated.

This experiment illustrates that maintaining charge neutrality across the membrane is a much stronger driving force than concentration equilibration: In order for protons to move across the bilyer, other positively charged ions must move out. It also demonstrates that the passive permeation of K^+ across the LUV bilayer is small: The slope between points 2 and 3 represents the flux of K^+ across the bilayer in the absence of valinomycin under a driving force of 60 mV ($\Delta pH = 1$).

In the upper trace, the ionophores are added in the opposite order: Valinomycin is added at point 2, CCCP at point 3. In this trace, the slope between points 2 and 3 signifies the proton leakage across the bilayer under the same driving force, when the counter-ion K^+ is free to traverse the membrane.

The passive permeability of H^+ and K^+ was tested for five different bilayer compositions of POPC/POPA/cholesterol: 10:0:0, 9:1:0, 8:1:1, 8:2:0 and 7:2:1 (Table 2). The distribution of the values obtained is due to the very small differences measured in combination with measurements at the edge of the pH range of Glu[3]. Nonetheless, a clear trend is discernible: potassium permeation exceeds proton permeation through the bilayer, with an average proton flux of 17 $s^{-1}\mu m^{-2}$ and an average potassium flux of 30 $s^{-1}\mu m^{-2}$. No significant difference in proton or K^+ flux was observed for the different lipid compositions, and the addition of cholesterol did not influence the passive ion permeability of the membrane.

3.3 M2 proteoliposomes

3.3.1 Optimal M2 reconstitution conditions

The method presented above was used to successfully reconstitute the M2 Protein from Influenza virus A. We obtained the best M2 proteoliposomes by using the molar proportions 3:1:1 of POPC/POPA/cholesterol, similar to the 4:1:2 proportions used by Pinto and coworkers [6]. This composition yielded unilamellar proteoliposomes with an average diameter around 200 nm (Figure 1C,D) and a relatively narrow size distribution. A lipid-to-protein ratio of 6900 (not counting cholesterol) resulted in optimal balance between proton translocation rates and measurement resolution. OG was used at the solubilizing detergent-to-lipid ratio of 2.6 mol/mol. Successful

reconstitution was achieved at pH 6.5-7.5; lower reconstitution pH resulted in lower yield of insertion and M2 inactivaton.

3.3.2 Protein quantification in the presence of lipids

For accurate determination of specific activity, reliable protein quantification is necessary. This is technically challenging in membrane preparations with low protein and high lipid concentrations, such as proteoliposomes, and it is common practice to assume that all added protein has been successfully incorporated into the liposomes. The D_C protein assay (BioRad) proved incompatible with the amount of detergent needed to solubilize M2 proteoliposomes at concentrations necessary for protein determination. However, we were able to modify this protein-determination method (Section 2.6) for use with lipid concentrations up to 25 mg/ml and protein concentrations down to 10 µg/ml. We found that >95% of the added M2 protein was present in the liposome membrane for reconstitutions above pH 6.2.

3.3.7 Unidirectional protein orientation in the bilayer

The directionality of M2 in the liposomes was addressed with mass spectroscopy (MS). The M2 proteoliposomes were subjected to trypsin proteolysis, allowing trypsin access exclusively to protruding amino acids; peptide stretches in the bilayer or protruding into the enclosed liposome volume were not accessible to trypsin. MS of the peptides thus removed are displayed in Figure 5C, showing a main component at m/z 1948.013. This matches the calculated mass of M2 amino acids 1-17 - the N terminal of the protein. Figure 5B shows the equivalent investigation of M2 proteoliposomes prepared according to [6], expected to have random M2 orientation. In addition to the N-terminal peak, intensity is evident at m/z 1990.013; MS/MS analysis confirmed this peptide to be the N-terminal acetylated version of the m/z 1948.013 peptide. It also displays intensity at m/z 2089.942, matching the calculated mass of M2 amino acids 78-96 – the C terminal. For comparison, pure M2 (in the absence of lipids) was trypsinated and investigated, Figure 5A. The C- and N-terminal peptides dominate this spectrum, as well, in accordance with previously reported trypsin digestions of M2 [11, 57].

The data in Figure 5 conclusively show that the current M2 proteoliposomes feature unidirectionally inserted M2, with the N terminus out. We obtained the same results whether we reconstituted M2 at R_{sat} or R_{sol}, and also for different cholesterol concentrations (not shown). This orientation matches the native orientation of M2 in the viral membrane, and may be favorable with respect to membrane curvature. Using a slow reconstitution procedure likely allowed M2 to insert in the preferred, native orientation.

This enables detailed investigations of functional rectification of M2 outside its native membrane, and we present a more comprehensive functional study elsewhere [12].

3.3.8 Quantitative M2 proton flux determination

In Figure 6A, proton flux through M2, driven by a [K$^+$] gradient, is depicted as internal liposome pH vs time. At time 0, the potassium concentrations were [K$^+$]$_{in}$=130 mM, [K$^+$]$_{out}$=11 mM, creating an initial membrane potential of 62 mV, negative inside, with valinomycin present.

The inside was rapidly acidified by the proton influx through M2, and the system reached its Donnan equilibrium within 5 minutes, after which a slow relaxation of the established pH gradient was seen. The internal liposome volume was determined by Glu^3 absorbance to 15.6 µl (1.56% of the sample). Taking account of the volume, the internal buffer strength and the protein concentration, pH$_{in}$ was converted to number of protons transferred per s and tetramer, Figure 6B top trace. The initial rate was 45±2 protons per s and M2 tetramer, recorded at 18°C.

This value is considerably higher than previously reported for reconstituted M2 [4-6]. Significantly, the observed value approaches the rates inferred from conduction measured by electrophysiology,

which are on the order of 10^3 protons/sec at 37°C [58]. Given that M2-mediated proton flux M2 in vesicles increases about 5 to 10-fold between 18°C and 37° [11] and that the current rate was induced by a [K$^+$] gradient rather than a pH gradient, these values are comparable, if not identical. This enforces the liposome assay as a biologically relevant experimental system for M2, where whole-cell results eventually can be reproduced and expanded upon using the advantages of a cell-free system with complete control over ion gradients.

The high rate achieved may be explained by the integrity of the liposomes, the precision of the pH-detection method used [7] and the unidirectionality of M2: all proteins present are channeling protons in the N→C direction, as in the native viral system.

The experiment was repeated with liposomes with a varying amount of cholesterol present, as specified in Figure 6B. When we increased the cholesterol level above 1:4 (cholesterol: total lipid, M:M), there was a tendency for cholesterol precipitation over time.

The upper two traces of Figure 6B both contain significant amounts of cholesterol, and both show similar behavior, reaching Donnan equilibrium within 5 minutes. The two lower traces have low or no cholesterol, and show inhibited behavior: The proton translocation is slow, but there is no indication of a lowered maximum. After 25 minutes, the sample without cholesterol has reached 1100 accumulated protons per tetramer, and is still increasing (not shown). This establishes that for M2 liposomes of POPG/POPA (3:1) lipid composition, cholesterol has an activating effect.

As cholesterol had no effect on passive permeation through protein-free liposomes (Section 3.2), the effect is related to the presence of M2. If cholesterol served to seal the protein-lipid interface against a non-specific ion leakage, the low-cholesterol traces of Figure 6 would level off at a much lower value than the high-cholesterol traces, as the K$^+$ gradient would be rapidly depleted and the driving force lost. Rather, we see gradual liposomal acidification progressing even after 25 minutes, belying a fast depletion of the K$^+$ membrane potential. It appears that under these conditions, cholesterol has a more specifically activating effect on M2. A possible explanation is the effect cholesterol has on bilayer thickness [59], affecting the relative tilt angle of the TM helices and thus M2 activity [56].

3.3.9 M2 Inhibitor screening

In [12] we show the dose dependent inhibition of amantadine with an IC_{50} value of 1.3 µM. To see if the reconstitution method together with the proton-flux assay is feasible for M2 inhibitor assessment, an initial inhibitor screen with known Spiro-Piperidine-based M2 inhibitors [27] was performed. M2 inhibition by 0.1 mM amantadine was found to reach its maximal effect within 1h of incubation with M2 proteoliposomes; this incubation time and inhibitor concentration was used for all examined inhibitors. The resulting inhibitions can be seen in Table 3. The fractional inhibition found for these compounds are in good agreement with previously reported values [27], except for compound 18 (1,5-dithia-9-azaspiro[5,5]undecane), which effects considerably larger inhibition as detected with the current method. We conclude that the reconstitution method and proton-flux assay presented in this paper is suitable for inhibitor screening.

Table 1

Size and size distribution of LUV vs detergent and detergent removal rate, determined by DLS. Time indicates the time from the first to the last bead addition.

Bead additions [time]		Detergent	Average diameter (nm)	Size distribution (PdI)
1×2.4 ml	[0 min]	Triton	160	0,16
4×0.6 ml	[48 min]	Triton	190	0,19
12×0.2 ml	[192 min]	Triton	210	0,18
1×2.4 ml	[0 min]	OG	120	0,15
4×0.6 ml	[48 min]	OG	100	0,06
12×0.2 ml	[192 min]	OG	140	0,1

Table 2

Passive permeability of H^+ and K^+ vs LUV lipid and cholesterol composition (number of ions per s and μm^2).

Lipid composition	H^+ $(s \cdot \mu m^2)^{-1}$	$K^+ / (s \cdot \mu m^2)^{-1}$
POPC	11	38
POPC / POPA (9 : 1)	22	27
POPC / POPA / chol (8 : 1 : 1)	11	13
POPC / POPA (8 : 2)	15	35
POPC / POPA / chol (7 : 2 : 1)	27	38

Table 3

Inhibition of proton flux through M2 in proteoliposomes by Spiro-Piperidine-based M2 inhibitors [27], defined in Materials and methods, and amantadine.

Compound	Inhibition (%)
compound 17	36 ± 2
compound 10	75 ± 2
compound 18	82 ± 1
compound 9	87 ± 1
amantadine	87 ± 1

Figure Legends

Figure 1. Cryogenic transmission electron micrographs of POPC/POPG/cholesterol (3:1:1 mol/mol) vesicles. **A:** Preformed vesicles, after sonication and extrusion. **B:** Vesicles produced by freeze-thawing PFV six times. **C, D:** M2 proteoliposomes produced by method presented in this paper.

Figure 2. Solubilization of POPC/POPA (9:1 mol/mol) liposomes shown as turbidity vs detergent-to-lipid ratio (R) for different detergents. **A:** Triton, **B:** OG, **C:** DM, **D:** DDM. Main graphs: Suspension turbidity, detected as the difference in optical density, 480 nm – 700 nm. R_{sat}=0.4 and R_{sol}=1.7 (see text) are indicated for Triton in panel A. Shaded areas indicate two-phase behavior. Insets: The hydrodynamic diameters detected by DLS for four different DLR values. Solid green: R=0, preformed vesicles. Dashed blue: R=R_{sat}, saturated vesicles. Dotted red: R_{sat} < R < R_{sol} (Triton: 1.1, OG: 1.7), mixed aggregates. Dash-dotted black: R= R_{sat}, fully solubilized material.

Figure 3. The turbidity of fully solubilized pre-formed POPC/POPA (9:1 mol/mol) vesicles, monitored as in Figure 2 vs time during detergent removal by hydrophobic polystyrene beads. Each dotted line represents an addition of 200 μl beads.

Figure 4. Internal vesicle pH vs time for POPC/POPA (9:1 mol/mol) LUV without protein, monitored using Glu[3] absorbance. The initial internal and bulk pH was 7.2; the upper trace has been offset by 0.4 pH units for clarity. **1:** the bulk pH was lowered by one pH-unit. **2:** CCCP (lower trace) or valinomycin (upper trace) was added. **3:** Valinomycin (lower trace) or CCCP (upper trace) was added. **4:** Gramicidin was added. Cf. sections 2.5 and 3.2.

Figure 5. Mass spectra of **A:** solubilized M2, **B:** M2 proteoliposomes produced according to [6], and **C:** M2 proteoliposomes produced according to the current method. *m/z* 1948.013 corresponds to M2 amino acids 1-17, *m/z* 1990.013 corresponds to an acetylated form of the same peptide, and *m/z* 2089.942 corresponds to M2 amino acids 78-96.

Figure 6. A: Internal pH vs time for M2 proteoliposomes. At time t=0, a [K$^+$] gradient was placed over the membrane ([K$^+$]$_{in}$=0.13 M, [K$^+$]$_{out}$=0.011 M), creating a potential of +62 mV. Valinomycin was present. Liposome composition: POPC/POPG/cholesterol 6:2:3, lipid-to-protein ratio 6900. **B:** The number of protons accumulated inside the vesicles per M2 tetramer vs time. Experiment as in A, with varying amounts of cholesterol: POPC/POPG/cholesterol ratios are specified for each trace. The top trace is the data set displayed in 6A.

Acknowledgements

References

[1]   M. Seigneuret, J.L. Rigaud, Analysis of Passive and Light-Driven Ion Movements in Large
        Bacteriorhodopsin Liposomes Reconstituted by Reverse-Phase Evaporation .1. Factors
        Governing the Passive Proton Permeability of the Membrane, Biochemistry 25 (1986) 6716-
        6722.

[2]   M. Seigneuret, J.L. Rigaud, Analysis of Passive and Light-Driven Ion Movements in Large
        Bacteriorhodopsin Liposomes Reconstituted by Reverse-Phase Evaporation .2. Influence of
        passive permeability and back-pressure effects upon light-induced proton uptake.,
        Biochemistry 25 (1986) 6723-6730.

[3]   A. Galkin, S. Drose, U. Brandt, The proton pumping stoichiometry of purified mitochondrial
        complex I reconstituted into proteoliposomes, Biochimica Et Biophysica Acta-Bioenergetics
        1757 (2006) 1575-1581.

[4]   C. Schroeder, C.M. Ford, S.A. Wharton, A.J. Hay, Functional reconstitution in lipid vesicles of
        influenza virus M2 protein expressed by baculovirus: evidence for proton transfer activity, J
        Gen Virol 75 (1994) 3477-3484.

[5]   J.C. Moffat, V. Vijayvergiya, P.F. Gao, T.A. Cross, D.J. Woodbury, D.D. Busath, Proton
        transport through influenza a virus M2 protein reconstituted in vesicles, Biophys. J. 94
        (2008) 434-445.

[6]   C. Ma, A.L. Polishchuk, Y. Ohigashi, A.L. Stouffer, A. Schon, E. Magavern, X. Jing, J.D. Lear, E.
        Freire, R.A. Lamb, W.F. DeGrado, L.H. Pinto, Identification of the functional core of the
        influenza A virus A/M2 proton-selective ion channel, Proc Natl Acad Sci U S A 106 (2009)
        12283-12288.

[7]   T. Leiding, K. Górecki, T. Kjellman, S. Vinogradov, C. Hägerhäll, S. Peterson Årsköld, Precise
        detection of pH inside large unilamellar vesicles using membrane-impermeable porphyrin-
        based nanoprobes, Analytical Biochemistry. 388 (2009) 296-305.

[8]   R.M. Pielak, J.R. Schnell, J.J. Chou, Mechanism of drug inhibition and drug resistance of
        influenza A M2 channel, Proc Natl Acad Sci U S A 106 (2009) 7379-7384.

[9]   D.D. Busath, Influenza A M2: Channel or Transporter?, in: A. Leitmannova Liu, A. Iglič (Eds.),
        Advances in Planar Lipid Bilayers and Liposomes, vol. 10, Academic Press, Burlington, 2009,
        pp. 161-201.

[10]   T.-I. Lin, H. Heider, C. Schroeder, Different modes of inhibition by adamantane amine
        derivatives and natural polyamines of the functionally reconstituted influenza virus M2
        proton channel protein., J. Gen. Virol. 78 (1997) 767-774.

[11]   T.I. Lin, C. Schroeder, Definitive assignment of proton selectivity and attoampere unitary
        current to the M2 ion channel protein of influenza A virus, Journal of virology 75 (2001)
        3647-3656.

[12]   T. Leiding, J. Wang, J. Martinsson, W.F. DeGrado, S. Peterson Årsköld, Functional antiporter
        activity of the M2 proton channel from influenza A virus., Submitted to Proc. Nat. Acad. Sci.
        USA (2010).

[13]   R.A. Lamb, S.L. Zebedee, C.D. Richardson, Influenza virus M_2 protein is an integral membrane
        protein expressed on the infected-cell surface, Cell 40 (1985) 627-633.

[14]   S.L. Zebedee, C.D. Richardson, R.A. Lamb, Characterization of the influenza virus M2 integral
        membrane protein and expression at the infected-cell surface from cloned cDNA, J. Virol. 56
   (1985) 502-511.

[15]   I.V. Chizhmakov, F.M. Geraghty, D.C. Ogden, A. Hayhurst, M. Antoniou, A.J. Hay, Selective proton permeability and pH regulation of the influenza virus M_2 channel expressed in mouse erythroleukaemia cells, J. Physiol. 494 (1996) 329-336.

[16]   L.H. Pinto, L.J. Holsinger, R.A. Lamb, Influenza virus M_2 protein has ion channel activity, Cell 69 (1992) 517-528.

[17]   K. Martin, A. Helenius, Nuclear transport of influenza virus ribonucleoproteins: the viral matrix protein (M1) promotes export and inhibits import, Cell 67 (1991) 117-130.

[18]   M. Takeda, A. Pekosz, K. Shuck, L.H. Pinto, R.A. Lamb, Influenza a virus M2 ion channel activity is essential for efficient replication in tissue culture, J. Virol. 76 (2002) 1391-1399.

[19]   O.P. Zhirnov, Solubilization of matrix protein M1/M from virions occurs at different pH for orthomyxo- and paramyxoviruses, Virology 176 (1990) 274-279.

[20]   R.J. Sugrue, G. Bahadur, M.C. Zambon, M. Hall-Smith, A.R. Douglas, A.J. Hay, Specific structural alteration of the influenza haemagglutinin by amantadine, EMBO J. 9 (1990) 3469-3476.

[21]   A.J. Hay, The action of adamantanamines against influenza A viruses: inhibition of the M_2 ion channel protein, Seminars in Virology 3 (1992) 21-30.

[22]   S. Grambas, A.J. Hay, Maturation of influenza A virus hemagglutinin--estimates of the pH encountered during transport and its regulation by the M2 protein, Virology 190 (1992) 11-18.

[23]   T. Sakaguchi, G.P. Leser, R.A. Lamb, The ion channel activity of the influenza virus M2 protein affects transport through the Golgi apparatus, J. Cell. Biol. 133 (1996) 733-747.

[24]   C. Wang, K. Takeuchi, L.H. Pinto, R.A. Lamb, The ion channel activity of the influenza A virus M_2 protein: characterization of the amantadine block., J. Virol. 67 (1993) 5585-5594.

[25]   W.L. Davies, R.R. Grunert, R.F. Haff, J.W. McGahen, E.M. Neumayer, M. Paulshock, J.C. Watts, T.R. Wood, E.C. Herman, C.E. Hoffman, Antiviral activity of 1-adamantanamine (amantadine), Science 144 (1964) 862-863.

[26]   V. Balannik, J. Wang, Y. Ohigashi, X. Jing, E. Magavern, R.A. Lamb, W.F. Degrado, L.H. Pinto, Design and Pharmacological Characterization of Inhibitors of Amantadine-Resistant Mutants of the M2 Ion Channel of Influenza A Virus, Biochemistry (2009).

[27]   J. Wang, S.D. Cady, V. Balannik, L.H. Pinto, W.F. DeGrado, M. Hong, Discovery of spiro-piperidine inhibitors and their modulation of the dynamics of the M2 proton channel from influenza A virus, J Am Chem Soc 131 (2009) 8066-8076.

[28]   A.L. Stouffer, R. Acharya, D. Salom, A.S. Levine, L. Di Costanzo, C.S. Soto, V. Tereshko, V. Nanda, S. Stayrook, W.F. DeGrado, Structural basis for the function and inhibition of an influenza virus proton channel, Nature 451 (2008) 596-U513.

[29]   J.R. Schnell, J.J. Chou, Structure and mechanism of the M2 proton channel of influenza A virus, Nature 451 (2008) 591-595.

[30]   I.V. Chizhmakov, D.C. Ogden, F.M. Geraghty, A. Hayhurst, A. Skinner, T. Betakova, A.J. Hay, Differences in conductance of M2 proton channels of two influenza viruses at low and high pH, J. Physiol. 546 (2003) 427-438.

[31]   J.A. Mould, J.E. Drury, S.M. Frings, U.B. Kaupp, A. Pekosz, R.A. Lamb, L.H. Pinto, Permeation and activation of the M2 ion channel of influenza A virus, J. Biol. Chem. 275 (2000) 31038-31050.

[32]   V. Balannik, V. Carnevale, G. Fiorin, B.G. Levine, R.A. Lamb, M.L. Klein, W.F. Degrado, L.H. Pinto, Functional studies and modeling of pore-lining residue mutants of the influenza a virus M2 ion channel, Biochemistry 49 (2010) 696-708.

[33]   T.E. Decoursey, Voltage-gated proton channels and other proton transfer pathways, Physiol Rev 83 (2003) 475-579.

[34]   V. Vijayvergiya, R. Wilson, A. Chorak, P.F. Gao, T.A. Cross, D.D. Busath, Proton conductance of influenza virus M2 protein in planar lipid bilayers, Biophys J 87 (2004) 1697-1704.

[35]   X. Jing, C. Ma, Y. Ohigashi, F.A. Oliveira, T.S. Jardetzky, L.H. Pinto, R.A. Lamb, Functional studies indicate amantadine binds to the pore of the influenza A virus M2 proton-selective ion channel, Proc Natl Acad Sci U S A 105 (2008) 10967-10972.

[36]   Y. Ohigashi, C. Ma, X. Jing, V. Balannick, L.H. Pinto, R.A. Lamb, An amantadine-sensitive chimeric BM2 ion channel of influenza B virus has implications for the mechanism of drug inhibition, Proc Natl Acad Sci U S A 106 (2009) 18775-18779.

[37]   S.D. Cady, K. Schmidt-Rohr, J. Wang, C.S. Soto, W.F. Degrado, M. Hong, Structure of the amantadine binding site of influenza M2 proton channels in lipid bilayers, Nature 463 (2010) 689-692.

[38]   S.D. Cady, M. Hong, Effects of amantadine on the dynamics of membrane-bound influenza A M2 transmembrane peptide studied by NMR relaxation, J Biomol NMR 45 (2009) 185-196.

[39]   S.D. Cady, W. Luo, F. Hu, M. Hong, Structure and function of the influenza A M2 proton channel, Biochemistry 48 (2009) 7356-7364.

[40]   S.D. Cady, T.V. Mishanina, M. Hong, Structure of amantadine-bound M2 transmembrane peptide of influenza A in lipid bilayers from magic-angle-spinning solid-state NMR: the role of Ser31 in amantadine binding, J Mol Biol 385 (2009) 1127-1141.

[41]   H. Takeuchi, A. Okada, T. Miura, Roles of the histidine and tryptophan side chains in the M2 proton channel from influenza A virus, FEBS Lett 552 (2003) 35-38.

[42]   A. Okada, T. Miura, H. Takeuchi, Protonation of histidine and histidine-tryptophan interaction in the activation of the M2 ion channel from influenza a virus, Biochemistry 40 (2001) 6053-6060.

[43]   M. Yi, T.A. Cross, H.X. Zhou, Conformational heterogeneity of the M2 proton channel and a structural model for channel activation, Proc Natl Acad Sci U S A 106 (2009) 13311-13316.

[44]   C. Li, H. Qin, F.P. Gao, T.A. Cross, Solid-state NMR characterization of conformational plasticity within the transmembrane domain of the influenza A M2 proton channel, Biochim Biophys Acta 1768 (2007) 3162-3170.

[45]   J. Hu, T. Asbury, S. Achuthan, C. Li, R. Bertram, J.R. Quine, R. Fu, T.A. Cross, Backbone structure of the amantadine-blocked trans-membrane domain M2 proton channel from Influenza A virus, Biophys J 92 (2007) 4335-4343.

[46]   J. Hu, R. Fu, T.A. Cross, The chemical and dynamical influence of the anti-viral drug amantadine on the M2 proton channel transmembrane domain, Biophys J 93 (2007) 276-283.

[47]   J. Hu, R. Fu, K. Nishimura, L. Zhang, H.X. Zhou, D.D. Busath, V. Vijayvergiya, T.A. Cross, Histidines, heart of the hydrogen ion channel from influenza A virus: Toward an understanding of conductance and proton selectivity, Proceedings of the National Academy of Sciences of the United States of America 103 (2006) 6865-6870.

[48]   C. Tian, P.F. Gao, L.H. Pinto, R.A. Lamb, T.A. Cross, Initial structural and dynamic characterization of the M2 protein transmembrane and amphipathic helices in lipid bilayers, Protein Sci 12 (2003) 2597-2605.

[49]   K. Nishimura, S. Kim, L. Zhang, T.A. Cross, The closed state of a H+ channel helical bundle combining precise orientational and distance restraints from solid state NMR, Biochemistry 41 (2002) 13170-13177.

[50]   K.S. Rosenthal, F. Koussaie, CRITICAL MICELLE CONCENTRATION DETERMINATION OF NON-IONIC DETERGENTS WITH COOMASSIE BRILLIANT BLUE G-250, Analytical Chemistry 55 (1983) 1115-1117.

[51]   B. Lorber, J.B. Bishop, L.J. Delucas, PURIFICATION OF OCTYL BETA-D-GLUCOPYRANOSIDE AND REESTIMATION OF ITS MICELLAR SIZE, Biochimica et Biophysica Acta 1023 (1990) 254-265.

[52]   T. Vanaken, S. Foxallvanaken, S. Castleman, S. Fergusonmiller, ALKYL GLYCOSIDE DETERGENTS - SYNTHESIS AND APPLICATIONS TO THE STUDY OF MEMBRANE-PROTEINS, Methods in Enzymology 125 (1986) 27-35.

[53]   H. Alpes, H.J. Apell, G. Knoll, H. Plattner, R. Riek, RECONSTITUTION OF NA+/K+-ATPASE INTO PHOSPHATIDYLCHOLINE VESICLES BY DIALYSIS OF NONIONIC ALKYL MALTOSIDE DETERGENTS, Biochimica et Biophysica Acta 946 (1988) 379-388.

[54]   J. Gobom, E. Nordhoff, E. Mirgorodskaya, R. Ekman, P. Roepstorff, Sample purification and preparation technique based on nano-scale reversed-phase columns for the sensitive analysis of complex peptide mixtures by matrix-assisted laser desorption/ionization mass spectrometry, Journal of Mass Spectrometry 34 (1999) 105-116.

[55]   D. Levy, A. Bluzat, M. Seigneuret, J.L. Rigaud, A SYSTEMATIC STUDY OF LIPOSOME AND PROTEOLIPOSOME RECONSTITUTION INVOLVING BIO-BEAD-MEDIATED TRITON-X-100 REMOVAL, Biochimica et Biophysica Acta 1025 (1990) 179-190.

[56]   Ahyayauch, Detergent Effects on Membranes at Subsolubilizing Concentrations: Transmembrane Lipid Motion, Bilayer Permeabilization and Vesicle Lysis / Reassembly Are independent Phenomena, Langmuir In press DOI: 10.1021/1a904194a (2010).

[57]   G.G. Kochendoerfer, D. Salom, J.D. Lear, R. Wilk-Orescan, S.B. Kent, W.F. DeGrado, Total chemical synthesis of the integral membrane protein influenza A virus M2: role of its C-terminal domain in tetramer assembly, Biochemistry 38 (1999) 11905-11913.

[58]   J.A. Mould, H.-C. Li, C.S. Dudlak, J.D. Lear, A. Pekosz, R.A. Lamb, L.H. Pinto, Mechanism for Proton Conduction of the M2 Ion Channel of Influenza A Virus, J. Biol. Chem. 275 (2000) 8592-8599.

[59]   M. Luckey, Membrane Structural Biology with Biochemical and Biophysical Foundations, Cambridge University Press, New Yourk, 2008.
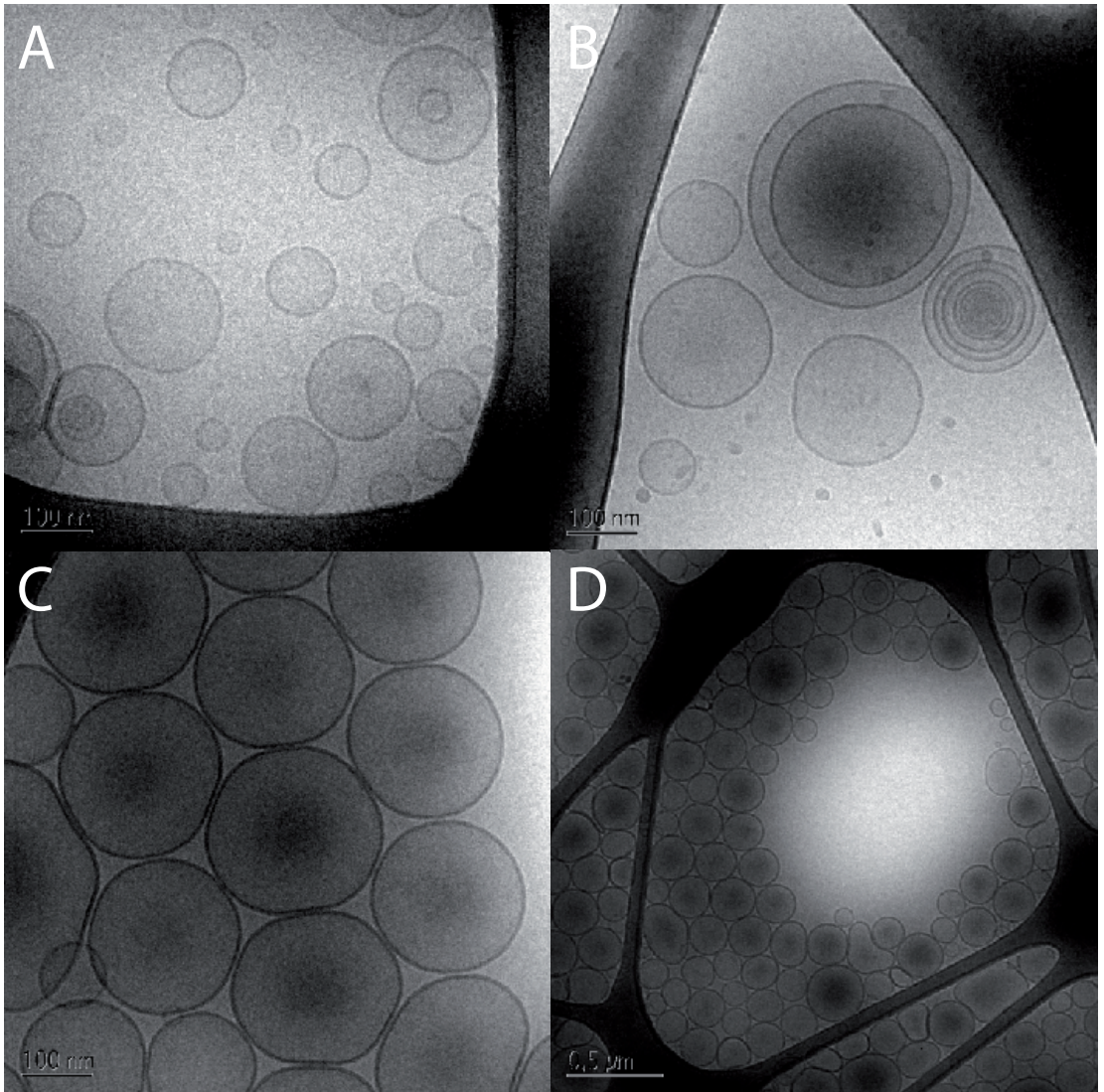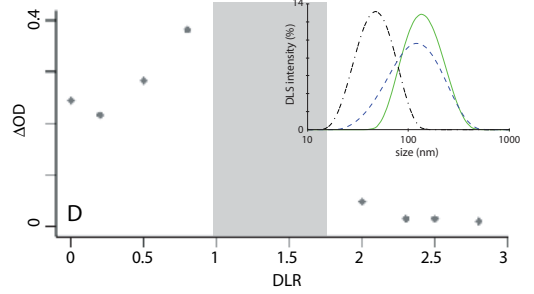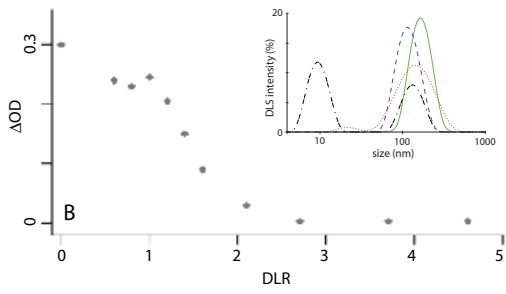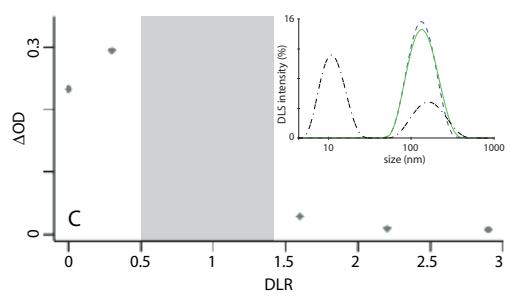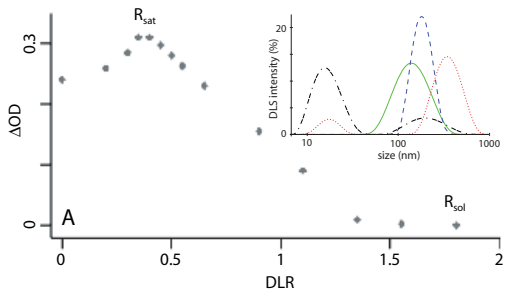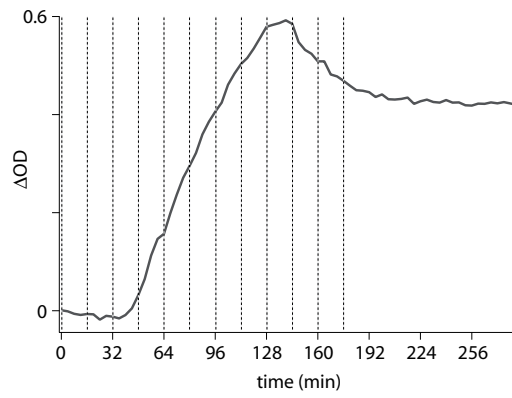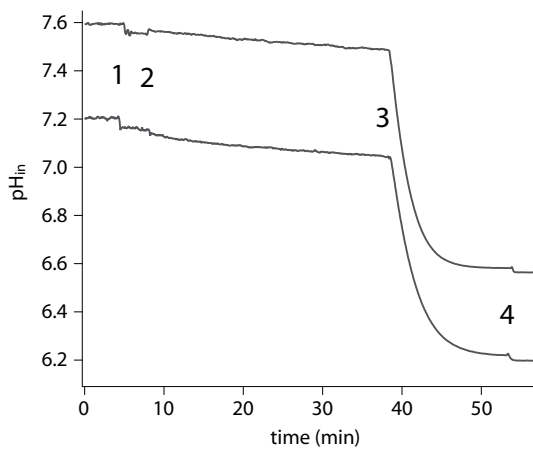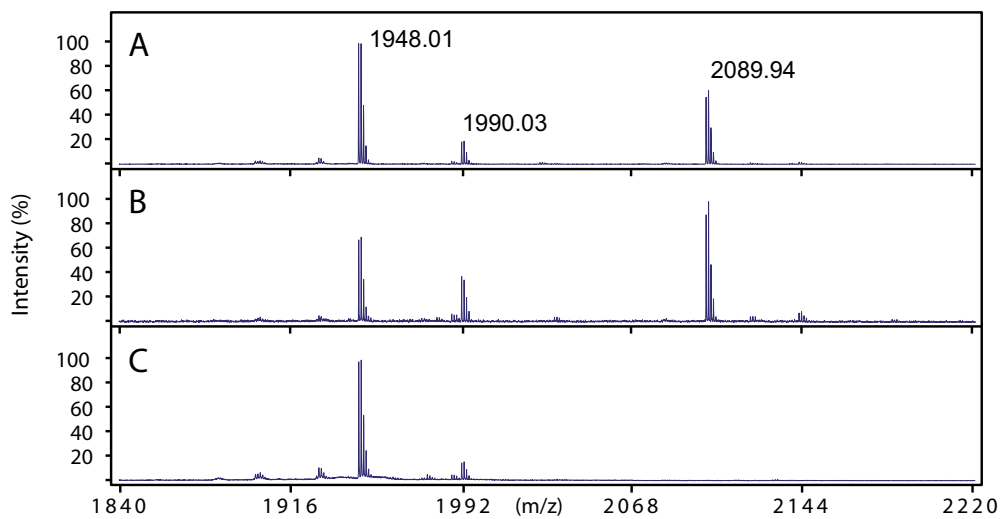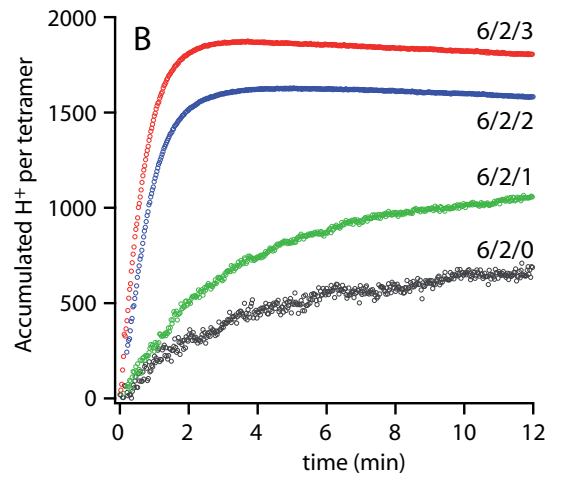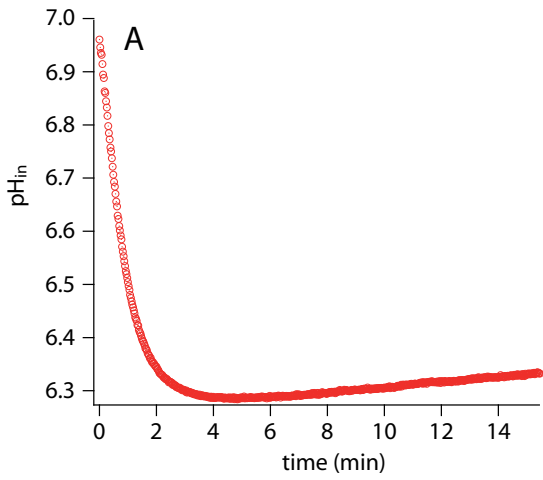
--

V

Functional antiporter activity of the M2 proton channel from influenza A virus.

Thom Leiding[a], Jun Wang[b], Jonas Martinsson [a], William F. DeGrado[b, c, †], and Sindra Peterson Årsköld[a, †]

TITLE RUNNING HEAD: Antiporter activity of Influenza protein A/M2

[a] Department of Biochemistry and Structural Biology, Center for Chemistry and Chemical Engineering, Lund University, PO Box 124, S-221 00 Lund, Sweden; [b] Department of chemistry [c] Department of Biochemistry and Biophysics, University of Pennsylvania, Philadelphia, PA 19104-6059;
[†] Correspondence to: William F. DeGrado, Department of Biochemistry and Biophysics, University of Pennsylvania, Philadelphia, PA 19104-6059. Tel: (215) 898-4590; Fax: (215)-573-7299; E-mail: wdegrado@mail.med.upenn.edu or Sindra Peterson Årsköld, Department of Biochemistry and Structural Biology, Center for Chemistry and Chemical Engineering, Lund University, PO Box 124, S-221 00 Lund, Sweden. Tel +46 46 222 8178; Fax: +46 46 222 4116; E-mail: sindra.peterson_arskold@biochemistry.lu.se.

Keywords: H^+, protons, influenza A virus, M2 channel, antiporter, liposome, ion channels

Manuscript information: 21 text pages, 4 figures

ABSTRACT

The M2 protein is a small, single-span transmembrane (TM) protein, which plays an important role in the life cycle of influenza A virus and is the target of the adamantane series of anti-influenza drugs. This virus enters cells via the endosomes; as the endosomes acidify M2 facilitates proton transport into the viral interior, thereby disrupting matrix protein/RNA interactions required for infectivity. M2 associates into a tetramer, whose four TM helices form a pore-like structure containing the "proton-sensing residue", His37. A mystery has been how protons can accumulate in the viral interior without developing a large electrical potential that impedes further inward proton translocation, which is required to effect a significant change in the internal effective pH. Progress in addressing this question has been limited by the availability of robust

methods of unidirectional insertion of the protein into virus-like vesicles. Using an optimized procedure for reconstitution, we show that M2 has antiporter-like activity, facilitating K^+ or Na^+ efflux from vesicles when protons flow into the vesicles. The rate of cation efflux is small in the absence of the buildup of an internal electrical potential, and is greater when protons are flowing through the channel than when there is little or no net movement of protons across the bilayer. Its antiporter-like activity defines M2 as a very simple and biologically relevant system for understanding this class of proteins. The present studies, together with the known biophysical properties of the M2 protein, suggest that it might act as a classical cotransporter, binding and releasing one or more protons with each translocation of a cation. However, other gated-channel models cannot be ruled out. Thus, the demonstration of the essential antiporter-like activity of M2 should lead to future investigations of the biophysical mechanism of transport, which will have implications for the design of new generations of M2-targeting drugs as well as furthering our understanding of cotransport.

INTRODUCTION

The influenza A virus M2 protein is a tetrameric integral membrane protein containing a short N-terminal extracellular domain, a transmembrane (TM) helix, and a 54-residue cytoplasmic tail (1, 2). Four M2 TM domains associate into a highly selective proton channel (3, 4), whose activity is essential for viral replication (5, 6). Influenza virus enters cells via the endosomal pathway, and the M2 protein functions to equilibrate the pH of the virus interior with that of the acidic endosome. The lowering of the pH within the virus leads to disruption of the interactions between the viral ribonucleoprotein (RNP) complex and the M1 protein (5), an important step in viral uncoating (7). Additionally, for some subtypes of influenza A virus, the M2 proton channel activity helps maintain a neutral pH in the lumen of the trans-Golgi network to prevent premature triggering of the hemagglutinin to the low-pH form (8-11). A long-standing question has been how M2 can conduct a substantial number of protons into the very small-volume interior of the virus without developing a substantial electrical gradient. Diffusion of a few protons down their concentration gradient from the acid environment of the endosome into the viral interior would result in an electrical gradient that would abruptly halt further proton flow and thereby prevent acidification of the viral interior. Here we demonstrate that under physiological pH gradients of low pH_{out} M2 mediates a significant outward flux of K^+, abrogating the buildup of a large electrical potential.

Given its very small size and modular structure, M2 has already captured the attention of biophysicists and biochemists as a pharmacologically relevant model system for understanding proton translocation and gating; the discovery of antiporter-like activity should heighten interest in this protein. Peptides spanning M2's TM helix are both necessary and sufficient to reproduce its proton-translocating and drug-binding activity (12). M2 has a single ionizable group in its TM domain, His37, which acts as both a pH sensor (13, 14) and determinant of its proton selectivity; variants in which

His37 is mutated to other polar residues loose their selectivity for protons (15). Trp41 acts in concert with His37 as a "gate", helping to define the rate of proton flux, and to kinetically trap protons within an acidified virus (16-18). Recent studies have shown that Val27 at the entrance of the pore may act as a secondary gate of the A/M2 channel (17-19).

M2 is the target of the adamantane-containing anti-influenza drugs as well as related hydrophobic amine-containing structures (3, 4, 20-23). Structures of the A/M2 TM domain in complex with amantadine have been determined by X-ray crystallography (17) and solid-state NMR (24). The X-ray structure of M2TM crystallized from micelles as well as the solid-state NMR structure in phospholipid bilayers showed that a single molecule of amantadine binds in the N-terminal half of the pore, surrounded by residues Val27, Ala30, Ser31, and Gly34 (24); a second low-affinity site on the outside of the protein has been observed (25), although this site is not pharmacologically relevant (26). These studies demonstrated the presence of a substantial pore, which is hydrated in the absence of drug (27).

The conductance of the M2 channel has been most thoroughly studied by measuring macroscopic whole-cell current in oocytes and mammalian cells at mildy acidic pH (3, 4, 6, 18, 20, 28, 29). Under these conditions, the channel is approximately 10^6 to 10^7-fold more permeable to protons relative to alkali metal cations such as Na^+ and K^+. Numerous investigations have shown that the channel is activated by low exterior pH (pH_{out}), and its current/pH profile is sigmoidal with a midpoint near pH 6, reaching a limiting rate near pH 4.5 to 5. This behavior is reminiscent of transporters, and quite different from most channels, whose conductance increases with increasing permeant ion concentration, well into the high-mM range (30). The saturation of the rate at low pH has been hypothesized to be associated with additional kinetic barriers involving protonation/deprotonation of His37 (31) or the formation of significant energy barriers at low pH (32). The rate of proton flux through the M2 channel, which has been reported to range from 10 to 1,000 sec^{-1}, depending on the electrical and chemical potential driving conduction (33), is also similar to that of transporters. Moreover, the electrophysiologically determined selectivity of 10^6 for proton vs Na^+/K^+ suggests that cation flux might be on the same order of magnitude as that of proton flux, given that the physiologically relevant proton concentration is 10^{-6} M while that of K^+ is 0.15 M, as selectivity ratios are normalized to the concentration of the permeant ions.

Full-length M2 and various variants of M2TM have been reconstituted in large unilamellar vesicles (LUVs), and shown to have a conductance similar to that measured in whole cells in terms of selectivity and rate of proton conduction (33-39). However, electrophysiological studies of M2 show that its conductance is asymmetric with regard to the direction of the proton gradient; by contrast the current/voltage curves from M2 in the vesicle assay are highly linear, probably because the channel is randomly inserted in the bilayer in two orientations with the N-terminus oriented either inward or outward (34, 35). Here, we describe conditions for unidirectional insertion of full-length M2 into LUVs (40). Under these conditions, the conduction properties depend on voltage and

pH$_{out}$ in a similar manner to that observed in M2-expressing cells. Unidirectional insertion allowed examination of asymmetric ion conduction under controlled conditions. We demonstrate that M2 has antiporter-like activity; diffusion of external protons (H$_{out}$) into vesicles activates the protein for outward conduction of K$^+$ ions (K$_{in}$) as the concentration of H$_{in}$ increases. Thus, the high inner concentration of K$^+$ provides an adequate reservoir of cations to exchange for protons until the buffering capacity of the viral interior has been overcome and equilibration of protons between the endosome and virus is reached.

RESULTS

Reconstitution of M2 in proteoliposomes (M2PLs) – The M2 protein used in these studies is a full-length construct that has been extensively studied for a variety of biophysical and proton-transport experiments (37). Full-length M2 protein corresponding to the sequence of WT Udorn strain (GenBank accession no. CAD22815) was expressed with a C-terminal His-tag and four extra mutations (W15F, C17S, C19S, C50S). These mutations significantly improve the protein expression yield and do not affect M2 function (41). Final M2 protein was solublized with octyl glucoside (OG) and eluted from superflow Ni-NTA column (Qiagen) with 300 mM imidazole. The purity of the M2 protein was verified by both gel electrophoresis and HPLC to be >98%. The M2 protein was reconstituted in liposomes by solubilization of preformed vesicles in the presence of M2 followed by slow detergent removal by hydrophobic beads (40). Using this method, we obtain a good yield for reconstitution between pH 6.5 and 7.5, but poorer reconstitution below pH 6.5. To establish the directionality of insertion, proteoliposomes were exhaustively proteolyzed and the released fragments were analyzed by MS. Although both the N-terminal extodomain and C-terminal cytoplasmic domain of the protein are highly susceptible to proteolysis (42), the only fragments detected in our M2PLs were derived from the N-terminal domain, which faces the outside of the virus. Moreover, the vesicle size was approximately 200 nm, which represents a compromise between the curvature encountered in spherical influenza particles (approximately 100 nm) and M2-expressing cells for which electrophysiological data are available. Thus, M2 proteoliposomes are excellent mimics in terms of size and protein orientation.

Δ **pH-driven flux** - The physiological role of M2 is to transfer protons from the acidifying endosome into the viral interior whose primary cationic electrolyte is K$^+$ (SO$_4^{2-}$ serves as a membrane-impermeant counterion). We therefore examined proton flux under conditions of pH$_{in}$ (initial) = 7, while varying pH$_{out}$. These experiments were performed in the presence of K$^+$, and valinomycin was included to allow K$^+$ to diffuse rapidly out of the vesicles as protons diffused in, thereby maintaining electrical neutrality. The salt composition was the same inside and out (symmetrical K$^+$; [K$_{in}$] = [K$_{out}$] = 0.13 M), and the buffering capacity inside the vesicles was significantly smaller than [K$_{in}$] to prevent

the formation of a large change in the chemical potential of K^+ as it flowed outward in response to proton influx (43).

As observed in electrophysiological investigations, the rate of proton flux increases with decreasing pH_{out} (i.e., increasing proton activity, Fig. 1A). Under these conditions, 90% of the time course followed a single-exponential decay. No significant flux on this time scale was observed in control liposomes lacking M2, and proton flux was >90% blocked by amantadine (see below).

To determine whether M2 might allow K^+ efflux concomitant with proton influx, pH_{out}/flux curves were measured under the same conditions, but in the absence of valinomycin (Fig. 1B). As expected from the work of Busath et al. (33), the rates were slower, but they were not decreased to the background rate of proton flux for control M2-free liposomes or M2PLs inhibited by amantadine. Single-exponential kinetics were again observed; however, the rate was approximately three-fold slower than in the presence of valinomycin. Together with previous studies (33), these findings suggest that inward flux of protons is balanced by outward flux of K^+ through the M2 channel. To confirm that the K^+ flux was not due to non-specific diffusion of the ion through the bilayer, we repeated the experiment in symmetrical Na^+ (without valinomycin), which has much lower bilayer permeability due to its greater dehydration energy. Similar kinetics were again observed (Fig. 1C), and the rate was approximately 50% greater than the corresponding rate with K^+ ions in the absence of valinomycin.

Figure 2A illustrates the dependence of the initial rate of proton flux on pH_{out} with constant initial $pH_{in} = 7.0$ under various conditions. Similar to whole-cell recordings, the curves can be described by a simple conductance scheme with an effective pK_a of 5.9 ± 0.2 (see supplement). The rate of conduction at pH 6 and symmetrical $K^+ = 0.13$ M was three-fold greater in the presence of valinomycin than its absence. Finally, no flux was observed in the presence of amantadine. These findings demonstrate that M2 mediates outward conduction of potassium ions in response to an inward proton flux. If the cation efflux were a simple consequence of passive diffusion, the rate of K^+ efflux (in the absence of valinomycin) would be significantly greater than that of Na^+, since K^+ is a larger and much more easily dehydrated cation.

Electrically induced proton flux – To investigate further the possibility of cation transport through M2, we performed experiments in which a transmembrane electrical potential was generated by rapidly diluting vesicles prepared in K^+ buffer into Na^+ buffer containing valinomycin. Valinomycin is very selective for transport of K^+ relative to Na^+, and facilitates very rapid diffusion of K^+ out of the vesicle that generates an electrical potential, leading to inward proton flux. Fig. 3 illustrates data for M2PLs diluted into buffer with Na^+ and K^+ concentrations adjusted to induce a 62 mV potential (initial pH_{in} = pH_{out}). In the absence of valinomycin or a transmembrane proton gradient, diffusion of the alkali metals was too slow to drive a significant proton flux (per-tetramer flux < 1 – 2 protons/sec). However, addition of valinomycin allowed rapid efflux of K^+, establishing an electrical potential and inducing rapid acidification of the vesicle interior.

The observed time-courses for vesicle acidification of M2PLs are biphasic for initial symmetrical pH (pH_{in} = pH_{out}) between 5.5 and 7 (Fig. 3A). The first phase requires approximately 1 to 5 min, and results in acidification of the interior of the vesicle. In marked contrast to the experiment in which only the initial pH_{out} was varied, while holding pH_{in} constant, the rate of proton flux actually decreased with low pH when pH_{in} and pH_{out} were the same. This behavior has been seen in an earlier study of reconstituted M2 protein (43), and does not contradict electrophysiological studies, which did not examine proton flux at pH_{in} < 6 for technical reasons. When considered in relation to the experiment with variable pH_{out} these data suggest that proton flux is activated by low pH_{out} but inhibited by low pH_{in}; indeed, a plot of the initial rate of proton flux vs. pH_{in} is well described by a single-site isotherm with a pK_a = 6.0 ± 0.16 (Fig. 4A). The same pK_a was also observed when the potential was reversed (Fig. 3B, 4A), consistent with previous findings of small to no effect of voltage on the conducting pK_a (29).

Each time-course of vesicle acidification also shows a second phase, which occurs at a much slower time scale and results in a gradual increase of the interior pH towards the initial value (Fig. 3A). We ascribe this slow increase in pH_{in} to a loss in the electrical potential (43) due to slow M2-dependent equilibration of the sodium and potassium ion concentrations across the bilayer. With high K^+_{in}/low K^+_{out} (and low Na^+_{in}/high Na^+_{out}) M2LPs containing valinomycin, the carrier allows rapid outward flux of K^+ generating the electrical potential. Under these conditions, M2 promotes not only inward flux of protons but also Na^+, ultimately leading to equilibration of the K^+ and Na^+ across the membrane (43). Our data now show that the magnitude of this inward Na^+ flux is strongly pH-dependent, displaying opposite dependence on pH than the corresponding proton flux: The Na^+ flux increases markedly with decreasing pH_{in} (= pH_{out}), while the proton flux decreases (Fig. 3, 4).

The apparent Na^+ flux during the slow phase can be computed from the rate of the depolarization as described previously (43). The per-channel flux increases from 1 to 10 ions per sec as the pH is lowered from 7.0 to 5.5. These values are smaller in magnitude and in reverse order from the initial rate of proton flux, which decreases from 40 to 5 protons/sec over the same pH range (Fig. 4A). To allow a better comparison of the rates, the Na^+ and H^+ fluxes were converted to chord conductance (g_i = flux/(V − E_i), in which V is the electrical potential created by the rapid valinomycin-dependent diffusion of K^+ ions, and E_i is the chemical potential difference of Na^+ or H^+ ions). The same trends and magnitudes are observed as when the raw fluxes were compared; both curves conform to a classical binding isotherm with a pK_a of 6.0 ± 0.15 for proton conductance and 6.0 ± 0.4 for Na^+ conductance (Fig. 4B).

The partial depolarization associated with the slow inward Na^+ flux is also responsible for the fact that the maximal pH change, $\triangle pH_{max}$, observed in the first phase does not reach the limit of 1.0 expected from the 62 mV potential from the initial potassium gradient (Fig. 3A). The value of $\triangle pH_{max}$ at pH 7 is near 0.8, and decreases

progressively with decreasing initial pH to a value of <0.5 at pH 5.5. At $\triangle pH_{max}$ the electrical potential should approximately equal the proton-motive force (PMF), allowing calculation of the inner and outer ionic composition from which the mean inward Na^+ flux can be estimated (as described in the supplement). A plot of the inner proton flux versus inner Na^+ flux has a shape similar to that of the initial pH flux, but trends upward rather than downward at low pH. Also, the apparent K_a for the curve is shifted from pH 6 for proton flux to pH 5.0 for Na^+ flux.

To determine the effect of reversing the potential, M2PLs were prepared with the salt concentrations reversed to drive outward flux of H^+ and Na^+ (Fig. 3B). The resulting initial outward proton flux is of similar shape and magnitude to the inner proton flux under otherwise identical conditions. These findings are consistent with electrophysiological studies, which showed symmetrical current/voltage curves between approximately -60 and 60 mV when the proton concentration is the same on both sides of the bilayer. Similar results were observed for the inward Na^+ flux.

M2 proton flux is fully inhibited by amantadine - The M2-mediated current induced by an electrical gradient was inhibited by amantadine in a dose-dependent manner and the sigmoidal inhibition curve is well described by a classical single-site binding isotherm with K_{diss} = 1.3 µM (Fig. 2B). This value compares well with IC_{50} values of 0.3 to 10 µM reported in the literature (20, 37). Previous studies of M2 proteoliposomes often showed only partial inhibition (33), which was ascribed to incomplete accessibility of the drug to randomly inserted protein. In contrast, our preparations show full inhibition at high amantadine concentrations.

DISCUSSION

The results of this investigation, although novel and somewhat surprising, are consonant with the biological function of the protein, and generally in good agreement with previous biophysical studies. The biological function of the protein is to pass protons down a pH gradient towards the interior of the virus. The experiments in which pH_{out} was varied (while maintaining the initial pH_{in} at 7.0, Fig. 2A) mimic this situation, and the results are in good agreement with previous electrophysiological studies (33, 44). Previously, there has been a lack of agreement between the rate of conduction measured by electrophysiology, which was on the order of 10^3 protons/sec (31), and vesicle measurements, which tended to provide a maximal conductance rate of 1 to 10 protons/sec. The improved reconstitution methods (40) used herein gave M2PLs with a proton flux that was too rapid to be easily measured in our system at 37°C. Therefore, the experiments were conducted at 18°C, at which a flux of 80 protons/sec was observed with pH_{in} = 7 and pH_{out} = 6 (0.013 fA; 0.2 fS). The corresponding conductance inferred from electrophysiological experiments at 37°C is approximately 4 fS (31). Given that M2-mediated proton flux M2 in vesicles increases about 5 to 10-fold

between 18°C and 37° (35), the expected conductance of M2 in vesicles at 37°C (1 to 4 fS) is the same in M2PLs and vesicles within experimental error.

What has been less clear from electrophysiological studies has been how protons can accumulate within a virus without developing a large electrical gradient. We show that the channel is in fact capable of outward K^+ flux to counterbalance the inward flux. With symmetrical K^+, the rate of proton inward flux is three-fold slower in the absence of valinomycin than in its presence; thus, proton flux is attenuated due to the slower rate of potassium ion efflux in the absence of a K^+ carrier. From the rate of proton flux in the presence and absence of valinomycin, and the concentration of protons and potassium ions, the selectivity of M2 at pH_{in} 7.0, $pH_{out} = 6.5$ is approximately 10^6, within the range obtained from electrophysiology (4, 45). The implications of this cation flux is that under these conditions M2 function is akin to that of a classical antiporter, exchanging protons for potassium ions.

It has been much more difficult to study the later stages of proton equilibration, in which the inside of the viral compartment becomes acidified. Electrophysiological measurements of M2 have been largely limited to whole-cell recordings, because the small conductance of the channel has precluded single-channel measurements of isolated membrane patches. Although this has limited the extent to which it has been possible to vary the interior pH, previous studies of proton and ion flux versus pH_{in} are in very good qualitative agreement with the present study (4, 45). Of particular interest is our current finding that as the pH_{in} was lowered, the rate of proton flux decreased and the rate of outward cation flux increased.

The pH-dependent behavior of M2 is consistent with the biological restraints and function of the protein as the virus moves through various portions of its infectivity cycle. When present on the cell surface prior to packaging it is important to minimize cell toxicity; high pH_{in} and pH_{out} assures minimal K^+ and Na^+ flow, which would disrupt the ionic balance of the host cell. Moreover, the very low concentration of protons at pH 7 minimizes the degree of proton flux. Once encapsulated in an endosome, the high but not absolute proton selectivity assures rapid acidification of the interior of a virus at a rate limited only by the low conductance of K^+ in the opposite direction. Finally, as the interior pH of the virus reaches the value required for disruption of viral RNA/M1 protein interactions the rate of proton flux decreases, essentially trapping protons in the virus. The minimization of reversed flow of protons might actually be advantageous if RNA uncoating leads to proton release from the M1 protein and/or RNA components due to changes in their substituents' pK_a values during the dissociation process.

Given that M2 serves as an antiporter, it is intriguing to ask whether it might act by a classical transporter mechanism. Proton-dependent transporters couple the diffusion of protons down a pH gradient to the transport of a second molecule or ion (or vice versa). M2 resembles cotransporters in many ways: 1) The rates of proton turnover in transporters (30) generally occurs at rates of 100 to 10,000 sec^{-1}. At a pH of 6 (10^{-6} M proton activity) this turnover corresponds to an overall second-order rate constant of 10^8

to 10^{10} M^{-1}sec^{-1}, approaching the diffusion-controlled rate and limited only by the architecture of typical proton-entry sites in proteins. Similarly, the rate of 100 to 1000 sec^{-1} observed for M2 at pH 6 corresponds to a second-order rate of 10^8 to 10^9 M^{-1}sec^{-1}, indicating that proton transport occurs at a rate close to the "speed limit" for proton translocation. 2) Proton-dependent transporters typically have proton-binding sites, which limit the turnover rate at low pH as saturation of the binding sites is approached. Along these lines, it is interesting to note that equilibrium studies show that one of the pK_a values for His37 is 6.2 – identical within experimental error with the conducting pK_a observed in this study. 3) With each turnover, transporters couple proton binding/dissociation events with conformational changes critical for cotransport. It is quite reasonable to expect that M2 might similarly become protonated by a proton diffusing through the channel, given that the sidechains of His37 in the tetrameric channel are directly positioned along the proton-diffusion pathway, and have pK_a values ranging from 8 to 5 assuring the availability of the basic form over a wide pH range. Moreover, given a pK_a of 6 for the "conducting pK_a" (13) and the overall second-order rate constant of 10^8 to 10^9 sec^{-1} for proton diffusion through the channel, the rate of deprotonation is calculated to be 100 to 1000 sec^{-1} ($K_a = 10^{-pKa} = k_{off}/k_{on}$). Thus, either the chemical rate of deprotonation or a conformational change that enables deprotonation is expected to occur on precisely the same time scale as proton turnover and provides an attractive explanation for the saturation of the rate at low pH. 4) The process of proton transport should couple to conformational changes that occur on the same time scale as translocation. M2 is known to undergo pH-dependent changes in dynamics, undergoing large-scale conformational changes that cause severe broadening of the mainchain amides as the pH is lowered below 6.5 (12, 46), indicative of motions on the same time scale as the dispersion of chemical shifts in distinct conformational states of proteins (10 to 1000 sec^{-1}), again matching the time scale of proton turnover. 5) The rate of translocation of the transported species should be similar to the rate of proton transport in a coupled system. The rate of Na$^+$ transport through M2 is indeed most rapid (up to 100 protons/sec) in the experiment with variable pH_{out} and initial pH_{in} = 7.0, which leads to rapid proton flux. By contrast, the rate of proton flux is slow during the second phase of the electrical-gradient experiment during which proton flux is minimal, despite the fact that the chemical potential of Na$^+$ ions and the electrical gradient are both favorable to Na$^+$ translocation.

M2's very low rate of passive transport is also consistent with an antiporter function. In the absence of high proton flux its basal rate of Na$^+$ conduction at 0.13 M salt is on the order of 1 sec^{-1}, corresponding to a second-order rate constant of 10 M^{-1}sec^{-1} – 10^6-fold slower than a typical cation channel. Thus, cations experience large energy barriers during conduction through M2, preventing unregulated basal conduction that could be toxic to the host cell prior to virus packaging.

While all of these considerations suggest that M2 acts as an antiporter, it might be possible to devise gated-channel models in which protonation of His37 gates the channel into an open state that allows protons to transverse the pore region without

formally protonating the His37 residues. Hybrid models are also possible in which protons are shared between clusters of water molecules and His37 residues as they pass this region of the channel. Thus the definative assignment of M2 as a cotransporter must await additional experiments.

MATERIALS AND METHODS

The supplement provides detailed materials, procedures for A/M2 SGC protein expression, purification, reconstitution in liposomes, trypsin digestion and MS analysis, proton-flux protocols and analysis, and equations and models for the proton-flux data fitting.

FIGURE LEGENDS

Fig. 1. pH change of the aqueous contents of M2PLs in response to the induction of a pH gradient induced at time=0. Initital interior pH=7 in all traces; external pH from top to bottom: pH_{out}=6.8, 6.5, 6.0, 5.5, 5.0. **A.** Symmetrical $[K^+]_{in}$=$[K^+]_{out}$=0.13 M, valinomycin present. **B.** Symmetrical $[K^+]_{in}$=$[K^+]_{out}$=0.13 M, no valinomycin. **C.** Symmetrical $[Na^+]_{in}$=$[Na^+]_{out}$=0.13 M. These data are displayed as proton flux in supplementary Fig. S1.

Fig. 2. A. The effect of varying pH_{out} (initial pH_{in}=7.0) on the magnitude of the net inward flux of protons into M2PL. The inner pH at the start of each experiment was 7, and the rates are quoted as protons per M2 tetramer and sec, extrapolated to time=0. Squares: K M2PLs with valinomycin (Fig 1A), Circles: K M2PLs without valinomycin (Fig. 1B), triangles: Na M2PLs (Fig. 1C). The smooth curves through the data were generated using a kinetic scheme based on a proton relay mechanism to fit a conducting pK_a and maximal rate to the data (see supplement). Other mechanisms such as a gated channel also provided a reasonable fit to the data. **B.** Inhibition of the initial rate of proton conduction driven by a K^+/valinomycin-induced potential (62 mV), as a function of amantadine concentration. The data were fit with a sigmoidal binding isotherm with K_{diss} = 1.3 μM.

Fig. 3. pH change of the aqueous contents of M2PLs in response to the induction of a 62 mV electrical potential, positive outside (**A**) or inside (**B**). The initial pH was symmetrical, and the [K$^+$] gradient was induced at time=0, with initial concentrations [K$^+$]$_{in}$=0.13 M, [Na$^+$]$_{in}$=0 M, [K$^+$]$_{out}$=0.011 M, [Na$^+$]$_{out}$=0.119 M (**A**) and [K$^+$]$_{in}$=0.01 M, [Na$^+$]$_{in}$=0.12 M, [K$^+$]$_{out}$=0.12 M, [Na$^+$]$_{out}$=0.01 M (**B**).

Fig. 4. **A** shows the effect of symmetrical pH on the magnitude of the initial rate of flux through the M2 channel in response to a K$^+$/valinomycin-induced potential of 62 mV. Circles: K-containing M2PLs (Fig. 3A), triangles: Na-containing M2PLs (Fig. 3B). **B** shows the chord conductance computed for the proton flux (open symbols) shown in panel A and the K$^+$/valinomycin-induced potential of 62 mV at t=0. (Note that the valinomycin allows distribution of potassium ions at a rate much greater than proton flux so that the full potential is essentially formed at time = 0.) Also shown in panel B is the value of the chord conductance for Na$^+$ ions vs. pH$_{in}$ (closed symbols; circles: K-containing M2PLs, triangles: Na-containing M2PLs). The Na$^+$ conductance was computed between t = 6 min and 10 min during which the pH changed relatively slowly, allowing computation of the mean V and E$_{Na+}$ over this interval (see supplement).

REFERENCES

1. Lamb, R. A., Zebedee, S. L., & Richardson, C. D. (1985) *Cell* **40,** 627-633.
2. Zebedee, S. L., Richardson, C. D., & Lamb, R. A. (1985) *J. Virol.* **56,** 502-511.
3. Pinto, L. H., Holsinger, L. J., & Lamb, R. A. (1992) *Cell* **69,** 517-528.
4. Chizhmakov, I. V., Geraghty, F. M., Ogden, D. C., Hayhurst, A., Antoniou, M., & Hay, A. J. (1996) *J. Physiol.* **494,** 329-336.
5. Martin, K. & Helenius, A. (1991) *Cell* **67,** 117-130.
6. Takeda, M., Pekosz, A., Shuck, K., Pinto, L. H., & Lamb, R. A. (2002) *J. Virol.* **76,** 1391-1399.
7. Zhirnov, O. P. (1990) *Virology* **176,** 274-279.
8. Sugrue, R. J., Bahadur, G., Zambon, M. C., Hall-Smith, M., Douglas, A. R., & Hay, A. J. (1990) *EMBO J.* **9,** 3469-3476.
9. Hay, A. J. (1992) *Seminars in Virology* **3,** 21-30.
10. Grambas, S. & Hay, A. J. (1992) *Virology* **190,** 11-18.
11. Sakaguchi, T., Leser, G. P., & Lamb, R. A. (1996) *J. Cell. Biol.* **133,** 733-747.
12. Cady, S. D., Luo, W., Hu, F., & Hong, M. (2009) *Biochemistry* **48,** 7356-7364.
13. Hu, J., Fu, R., Nishimura, K., Zhang, L., Zhou, H. X., Busath, D. D., Vijayvergiya, V., & Cross, T. A. (2006) *Proceedings of the National Academy of Sciences of the United States of America* **103,** 6865-6870.
14. Takeuchi, H., Okada, A., & Miura, T. (2003) *FEBS Lett* **552,** 35-38.
15. Venkataraman, P., Lamb, R. A., & Pinto, L. H. (2005) *J Biol Chem* **280,** 21463-21472.

16. Tang, Y., Zaitseva, F., Lamb, R. A., & Pinto, L. H. (2002) *J Biol Chem* **277,** 39880-39886.

17. Stouffer, A. L., Acharya, R., Salom, D., Levine, A. S., Di Costanzo, L., Soto, C. S., Tereshko, V., Nanda, V., Stayrook, S., & DeGrado, W. F. (2008) *Nature* **451,** 596-599.

18. Balannik, V., Carnevale, V., Fiorin, G., Levine, B. G., Lamb, R. A., Klein, M. L., Degrado, W. F., & Pinto, L. H. (2010) *Biochemistry* **49,** 696-708.

19. Yi, M., Cross, T. A., & Zhou, H. X. (2008) *The journal of physical chemistry* **112,** 7977-7979.

20. Wang, C., Takeuchi, K., Pinto, L. H., & Lamb, R. A. (1993) *J. Virol.* **67,** 5585-5594.

21. Davies, W. L., Grunert, R. R., Haff, R. F., McGahen, J. W., Neumayer, E. M., Paulshock, M., Watts, J. C., Wood, T. R., Herman, E. C., & Hoffman, C. E. (1964) *Science* **144,** 862-863.

22. Balannik, V., Wang, J., Ohigashi, Y., Jing, X., Magavern, E., Lamb, R. A., Degrado, W. F., & Pinto, L. H. (2009) *Biochemistry*.

23. Wang, J., Cady, S. D., Balannik, V., Pinto, L. H., DeGrado, W. F., & Hong, M. (2009) *J Am Chem Soc* **131,** 8066-8076.

24. Cady, S. D., Schmidt-Rohr, K., Wang, J., Soto, C. S., Degrado, W. F., & Hong, M. (2010) *Nature* **463,** 689-692.

25. Schnell, J. R. & Chou, J. J. (2008) *Nature* **451,** 591-595.

26. Ohigashi, Y., Ma, C., Jing, X., Balannick, V., Pinto, L. H., & Lamb, R. A. (2009) *Proceedings of the National Academy of Sciences of the United States of America* **106,** 18775-18779.

27. Luo, W. B. & Hong, M. (2010) *J Am Chem Soc* **132,** 2378-2384.

28. Mould, J. A., Drury, J. E., Frings, S. M., Kaupp, U. B., Pekosz, A., Lamb, R. A., & Pinto, L. H. (2000) *J Biol Chem* **275,** 31038-31050.

29. Chizhmakov, I. V., Ogden, D. C., Geraghty, F. M., Hayhurst, A., Skinner, A., Betakova, T., & Hay, A. J. (2003) *J. Physiol.* **546,** 427-438.

30. Decoursey, T. E. (2003) *Physiol Rev* **83,** 475-579.

31. Mould, J. A., Li, H.-C, Dudlak, C. S., Lear, J. D., Pekosz, A., Lamb, R. A., & Pinto, L. H. (2000) *J Biol Chem* **275,** 8592-8599.

32. Chen, H., Wu, Y., & Voth, G. A. (2007) *Biophys. J.* **93,** 3470-3479.

33. Busath, D. D. (2009) in *Advances in Planar Lipid Bilayers and Liposomes*, eds. Leitmannova Liu, A. & Iglič, A. (Academic Press, Burlington), pp. 161-201.

34. Lin, T.-I., Heider, H., & Schroeder, C. (1997) *J. Gen. Virol.* **78,** 767-774.

35. Lin, T. I. & Schroeder, C. (2001) *Journal of virology* **75,** 3647-3656.

36. Schroeder, C., Ford, C. M., Wharton, S. A., & Hay, A. J. (1994) *J Gen Virol* **75,** 3477-3484.

37. Ma, C., Polishchuk, A. L., Ohigashi, Y., Stouffer, A. L., Schon, A., Magavern, E., Jing, X., Lear, J. D., Freire, E., Lamb, R. A*., et al.* (2009) *Proceedings of the National Academy of Sciences of the United States of America* **106,** 12283-12288.

38. Vijayvergiya, V., Wilson, R., Chorak, A., Gao, P. F., Cross, T. A., & Busath, D. D. (2004) *Biophysical journal* **87,** 1697-1704.

39. Pielak, R. M., Schnell, J. R., & Chou, J. J. (2009) *Proceedings of the National Academy of Sciences of the United States of America* **106,** 7379-7384.

40. Leiding, T., Martinsson, J., Bernfur, K., Borgström, B., Franzén, A., DeGrado, W. F., & Peterson Årsköld, S. (2010) *Manuscript in preparation.*

41. Nguyen, P. A., Soto, C. S., Polishchuk, A., Caputo, G. A., Tatko, C. D., Ma, C. L., Ohigashi, Y., Pinto, L. H., DeGrado, W. F., & Howard, K. P. (2008) *Biochemistry* **47,** 9934-9936.

42. Kochendoerfer, G. G., Salom, D., Lear, J. D., Wilk-Orescan, R., Kent, S. B., & DeGrado, W. F. (1999) *Biochemistry* **38,** 11905-11913.

43. Moffat, J. C., Vijayvergiya, V., Gao, P. F., Cross, T. A., Woodbury, D. J., & Busath, D. D. (2008) *Biophysical journal* **94,** 434-445.

44. Pinto, L. H. & Lamb, R. A. (2006) *J Biol Chem* **281,** 8997-9000.

45. Shimbo, K., Brassard, D. L., Lamb, R. A., & Pinto, L. H. (1996) *Biophysical journal* **70,** 1335-1346.

46. Li, C., Qin, H., Gao, F. P., & Cross, T. A. (2007) *Biochim Biophys Acta* **1768,** 3162-3170.
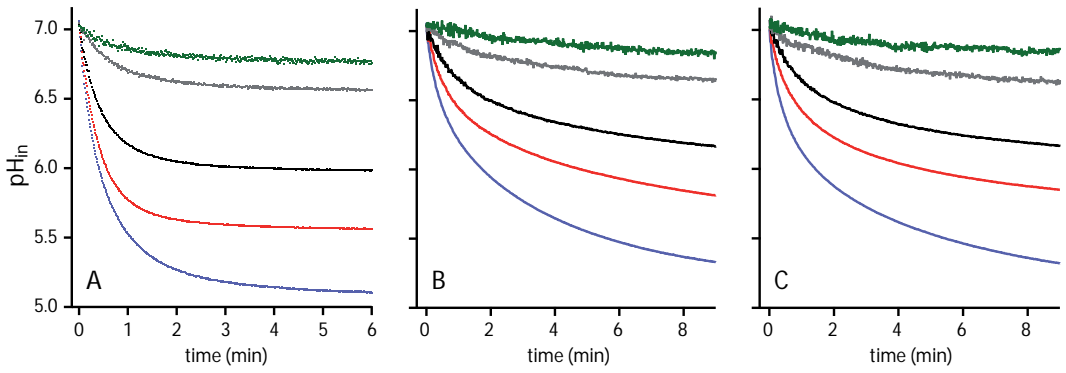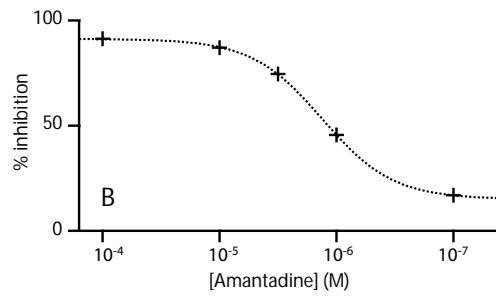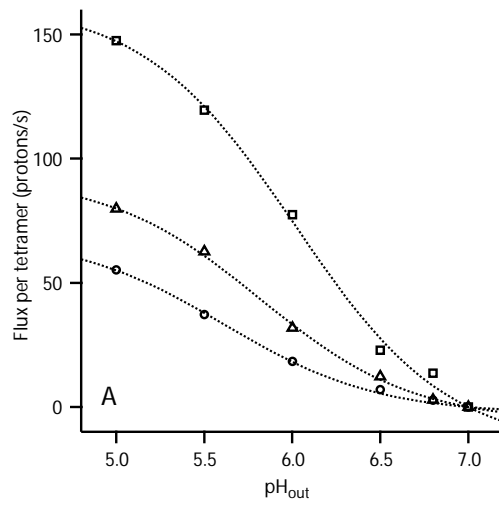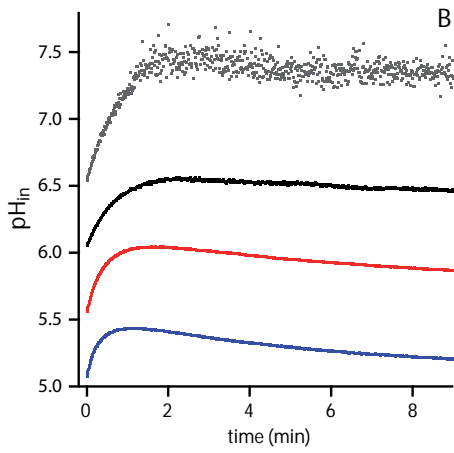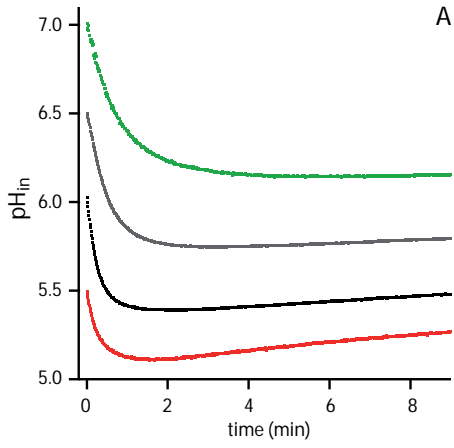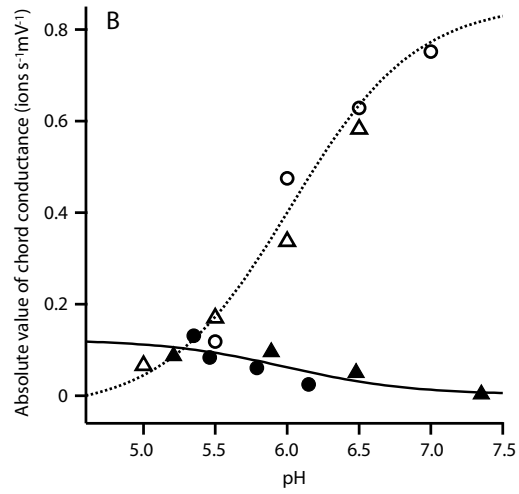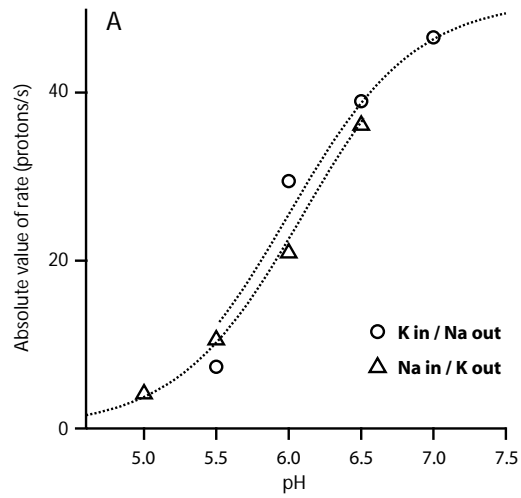
Functional antiporter activity of the M2 proton channel from influenza A virus.

SUPPLEMENTARY MATERIALS

Thom Leiding[a], Jun Wang[b], Jonas Martinsson[a], William F. DeGrado[b, c, †], and Sindra Peterson Årsköld[a, †]

Figure S1 Legend:
Fig S1. Number of accumulated intravesicular protons per tetramer, driven by a pH gradient induced at time=0. Initital pH_{in}=7 in all traces. Traces from bottom to top: pH_{out}=6.8, 6.5, 6.0, 5.5, 5.0. **A.** Symmetrical $[K^+]_{in}$=$[K^+]_{out}$=0.13 M, valinomycin present. **B.** Symmetrical $[K^+]_{in}$=$[K^+]_{out}$=0.13 M, no valinomycin. **C.** Symmetrical $[Na^+]_{in}$=$[Na^+]_{out}$=0.13 M.

Fitting of parameters to proton flux versus pH_{out} curves.
A variety of approaches were examined to fit the data, including gated-channel as well as proton-shuttle mechanisms. A good fit was obtained with the shuttle model, although the data were not extensive enough to rule out alternate mechanisms. For simplicity, we a protonation/deprotonation mechanism:

$$H_{out} + M2 \underset{k_{-1}}{\overset{k_1}{\rightleftarrows}} M2H \underset{k_2}{\overset{k_{-2}}{\rightleftarrows}} H_{in} + M2$$

Eq. 1

We define:

$$R = \frac{[M2]}{[M2H]}$$

Eq. 2

At steady state:

$$\frac{d[M2H]}{dt} = 0$$

Eq. 3

$$k_1 [H_{out}][M2] + k_2 [H_{in}][M2] = k_{-1}[M2H] + k_{-2}[M2H]$$

Eq. 4

$$R = \frac{[M2]}{[M2H]} = \frac{k_{-1} + k_{-2}}{k_1 * 10^{-pH_{out}} + k_2 * 10^{-pH_{in}}}$$

Eq. 5

In order to express k_2 in terms of k_1, k_{-1} and k_2, considering the following:
Net proton flux is defined as:

$$\frac{d[H_{out}]}{dt} = Flux_{out} - Flux_{in} = \frac{k_{-1}}{1+R}[M2]_{total} - k_1 * 10^{-pH_{out}} * \frac{R}{1+R}[M2]_{total}$$

Eq. 6

When $[H_{in}]$=$[H_{out}]$:

$$\frac{d[H_{out}]}{dt} = 0$$

Eq. 7

Rearrange Eq. 6, k_2 can be expressed as:

$$k_2 = \frac{k_1 * k_{-2}}{k_{-1}}$$

Eq. 8

Net flux per channel:

$$Flux/channel = \frac{k_{-1}}{1+R} - k_1 * 10^{-pH_{out}} * \frac{R}{1+R}$$

Eq. 9

$$R = \frac{k_{-1}+k_{-2}}{k_1 * 10^{-pH_{out}} + k_2 * 10^{-pH_{in}}} = \frac{k_{-1}+k_{-2}}{k_1 * 10^{-pH_{out}} + \frac{k_1 * k_{-2}}{k_{-1}} * 10^{-pH_{in}}} = \frac{k_{-1}+k_{-2}}{k_1(10^{-pH_{out}} + \frac{k_{-2}}{k_{-1}} * 10^{-pH_{in}})}$$

Eq. 10

$$Flux/channel = \frac{k_{-1}}{1 + \frac{k_{-1}+k_{-2}}{k_1(10^{-pH_{out}} + \frac{k_{-2}}{k_{-1}} * 10^{-pH_{in}})}} - k_1 * 10^{-pH_{out}} * \frac{\frac{k_{-1}+k_{-2}}{k_1(10^{-pH_{out}} + \frac{k_{-2}}{k_{-1}} * 10^{-pH_{in}})}}{1 + \frac{k_{-1}+k_{-2}}{k_1(10^{-pH_{out}} + \frac{k_{-2}}{k_{-1}} * 10^{-pH_{in}})}}$$

Eq. 11

at pH_{in}=7:

$$Flux/channel = \frac{k_{-1}}{1 + \frac{k_{-1}+k_{-2}}{k_1(10^{-pH_{out}} + \frac{k_{-2}}{k_{-1}} * 10^{-7})}} - k_1 * 10^{-pH_{out}} * \frac{\frac{k_{-1}+k_{-2}}{k_1(10^{-pH_{out}} + \frac{k_{-2}}{k_{-1}} * 10^{-7})}}{1 + \frac{k_{-1}+k_{-2}}{k_1(10^{-pH_{out}} + \frac{k_{-2}}{k_{-1}} * 10^{-7})}}$$

Eq. 12

Eq. 12 is used for the data fitting of Fig. 2A and the fitting result is presented in Table S1.

The proton dissociation constant for M2H is

$$K_a = \frac{k_{-1}}{k_1}$$

Curves were fit to the current vs. pH_{out} profiles by the method of non-linear least squares. The parameters k_1, k_{-1}, and k_2 in Eq. 12 were the fitting variables. The value of k_{-2} was well defined by the experimental data. The value of $K(a) = k_{-1}/k_1$ was well defined, although the value of k_{-1} was less well determined from the experimental data, due to the small degree of outward flux under these experimental conditions. Satisfactory fits were obtained so long at k_{-1} was

greater than 100 sec^{-1}, and the value of k_1 covaried to maintain a constant value of the proton dissociation constant for M2H.

Table S1. Parameters obtained from analysis of proton flux versus pH$_{out}$ curves (Fig. 2A).

Condition	k_1 (M^{-1} sec^{-1})	k_{-1} (sec^{-1})	k_{-2} flux(max) (sec^{-1})	pK(a) (M)
K$^+$ with valinomycin	1.23 * 10^9 (±.144 * 10^9)	1000 (fixed)	163 (± 5)	6.09 (±0.05)
K$^+$	0.443 * 10^9 (±0.030 * 10^9)	1000 (fixed)	68.9 (± 1.6)	5.65 (±0.03)
Na$^+$	0.725 * 10^9 (±0.052 * 10^9)	1000 (fixed)	93.4 (± 2.0)	5.86 (±0.03)

In the absence of valinomycin a transmembrane electrical potential develops that opposes the flow of protons. This buildup of an unfavorable electrical potential can be seen in the decrease in flux(max), as well as the pK$_a$ of the titratable group (presumably His37). The difference in the pK$_a$ for potassium ions in the presence and absence of valinomycin corresponds to 27 mV, which is small relative to the proton chemical potential created at low pH$_{out}$. This is consistent with the expectation that the electrical potential drop is only partial at His37 (1, 2).

For data fitting of Fig. 4A, pH$_{in}$ = pH$_{out}$. Rearrange Eq. 11:

$$Flux/channel = \frac{k_{-1}}{1 + \dfrac{k_{-1} + k_{-2}}{k_1 * 10^{-pH} * (1 + \dfrac{k_{-2}}{k_{-1}})}} - k_1 * \frac{\dfrac{k_{-1} + k_{-2}}{k_1(1 + \dfrac{k_{-2}}{k_{-1}})}}{1 + \dfrac{k_{-1} + k_{-2}}{k_1 * 10^{-pH} * (1 + \dfrac{k_{-2}}{k_{-1}})}}$$

Eq. 13

Supplemental Materials & Methods:

Materials. Reagents used in experiments were obtained from commercial sources unless otherwise stated.

M2 SGC expression, purification. Full-length M2 protein corresponding to the sequence of WT Udorn strain (GenBank accession no. CAD22815) was

expressed with a C-terminal His-tag and four extra mutations (W15F, C17S, C19S, C50S). Recombinant M2 was expressed in BL21(DE3)pLyS E. Coli (Invitrogen) cells that were transformed with pET23D(+) plasmid (EMD Bioscience) containing the M2 gene under T7 promoter (designated M2SGC wt, the sequence of M2 was verified by both forward and reverse sequencing). Previously reported expression and purification procedures were followed with some changes to simplify the process and enhance the purification yield (3). The final M2 protein was solublized with octyl glucoside (OG) and eluted from the Ni-NTA column with 300 mM imidazole. For storage purpose, the elution buffer was exchanged for storage buffer (4mM OG, 20% v/v glycerol, 50mM HEPES, pH 8) by repetitive displacement using a 3K molecular weight cut centrifugal concentrator (Milipore). The purity of the M2 protein was verified by both gel electrophoresis and HPLC to be >98%. It is noted that M2 eluted in HPLC is a mixture of two species showing one single peak with a right-hand shoulder. LC-MS analysis showed the major peak mass corresponding to the calculated mass of WT sequence (MW 11892 Da), and the shoulder showed +40 that of the calculated mass. Further trypsin digestion and MS/MS analysis identified the +40 mass as an N-terminal acetylation, and this modification does not affect the M2 tetramerization.

Protein expression: BL21(DE3)pLyS E. Coli cells were chemically transformed with pET23D(+) plasmids containing the M2 gene and grown in LB agar plates with 100 μg/ml ampicilin. A single colony was picked up from the plate to inoculate 5ml LB supplemented with 100 μg/ml ampicilin, and was allowed to incubate at 37°C with 200rpm shaking for 8hrs. Next, 0.5 ml of the above cell solution was used to inoculate 50ml of LB supplemented with 100 μg/ml ampicilin and shake at 37°C overnight. The overnight culture was used to inoculate 1 L of LB supplemented with 100μg/ml ampicilin. When OD600 reached 0.7-1.0 (normally after 2hrs), M2 expression was induced with 1mM IPTG. Three hours later, protein expression was halted by centrifugation at 4°C for 30 min.

Protein purification: The cell pellet was resuspended in 50ml of 50mM Tris (pH 8), 40mM OG, 150 mM NaCl, 0.25 μg/ml lysozyme, 0.02 μg/ml DNase I and 500 μM PMSF at 0°C. The mixture was sonicated on ice for 20 min (20% amplitude, 1s on 1s off), followed by further reconstitution using a homogenizer for 10 mins to make the solution homogeneous. The solution was then centrifuged at 15,000 g for 30 mins. The supernatant was saved for Ni-NTA column purification, and the pellet was subjected to another round of reconstitution as described above. Finally the supernatants from two rounds were combined and incubated with 10 ml Ni-NTA super flow resin (Qiagen) and 20mM imidazole at room temperature

for 30 min with gentle shaking. The column was washed successively with 50 mM Tris (pH 8), 150 mM NaCl, 40mM OG, 20% v/v glycerol, then 50mM Tris (pH 8), 20mM OG, 20% v/v glycerol, followed by 50mM Tris (pH 8), 4mM OG, 20% v/v glycerol, 20mM imidazole. Finally, the M2 protein was eluted with 50mM Tris (pH 8), 4mM OG, 20% v/v glycerol, 300 mM imidazole. To remove the interfering effect of high imidazole concentration on subsequent experiments, the elution buffer was exchanged with storage buffer (4mM OG, 20% v/v glycerol, 50mM HEPES, pH 8) by repetitive displacement using a 3K molecular weight cut centrifugal concentrator (Milipore). The concentration of the M2 stock solution was calculated based on UV absorbance at 280 nm with an extinction coefficient of 8,480 $M^{-1}cm^{-1}$ (calculated from the M2 sequence in ExPASy website), which corresponds to a yield of 55 mg/L of expression.

A/M2 Liposome (M2LP) Preparation.
<u>K buffer</u>: 20 mM KPO_4, 50 mM K_2SO_4, 250 μM EDTA, pH 7.0, $[K^+]_{total}$=130 mM.
<u>Na buffer</u>: 20 mM $NaPO_4$, 50 mM Na_2PO_4, 250 μM EDTA, pH 7.0, $[Na^+]_{total}$=130 mM.
Preformed vesicles of molar composition palmitoyl-oleoyl phosphatidylcholine (POPC) /palmitoyl-oleoyl phosphoglycerol (POPG) / cholesterol 3/1/1 were produced by mixing lipids (from Avanti Polar Lipids) and cholesterol (Sigma) dissolved in chloroform, evaporating the chloroform, adding the aqueous reconstitution buffer, sonicating, and extruding nine times through a 200 nm polycarbonate filter. These vesicles were solubilized with OG to a molar detergent-to-lipid ratio of 2.6 (not counting cholesterol; detergent exceeding CMC). M2 was added to a protein-to-lipid ratio of 6900 (not counting cholesterol). The pH sensor Glu^3 (4) was added to a final concentration of 60 μM. For K^+-containing M2PLs K buffer was used; For Na^+-containing M2PLs, Na buffer and K buffer were combined to obtain $[K^+]$=0.01 M, $[Na^+]$=0.12 M.
The detergent was gradually removed by adding 6 × 0.4 ml hydrophobic polystyrene beads (Bio-Beads SM-2, Bio-Rad) at 16-minute intervals at 18°C. 90 min after the last bead addition, the liposome suspension was removed from the beads and ultracentrifuged at 100,000×g at 4°C for 2 h, then passed through a 1 ml HiTrap Q XL anion-exchange column (GE Healthcare) to remove external Glu^3. The resulting Glu^3-containing M2-proteoliposomes were stored at 4°C for up to three days. The M2PL contained >95% of the added protein, and were consistently unilamellar with an average diameter of 200 nm.

Trypsin digestion of A/M2 Liposome (M2LP) and MS characterization. .
Trypsin (Seq. Grade Modified Trypsin, Porcine, from Promega) was added to M2PL samples from a 100 ng/μl trypsin stock to a final trypsin-to-protein ratio of

1:10 (w/w), in a total sample volume of 100 µl. After overnight incubation at 37°C, 3 µl of 10% trifluoroacetic acid (TFA) was added to stop proteolysis. Samples were purified and concentrated using POPOS R2 microcolumns (5). After washing the microcolumns with 10 µl 80% ACN and equilibration with 20 µl 0.1% TFA, 20 µl peptide mixture was added in 10 µl 0.1% TFA onto the microcolumn. After washing the microcolumns twice with 25 µl of 0.1% TFA peptides were eluted with 80% ACN directly onto a MALDI target plate. A matrix solution containing of 5 mg/ml α-cyano-4-hydroxy cinnamic acid, 50% acetonitrile, 1% TFA and 25 mM citric acid was added in 0.5 µl portions onto each of the dried peptide sample preparations.

MS and MS/MS spectra were acquired on a 4700 MALDI TOF/TOF mass spectrometer (Applied Biosystems, Framingham, CA, USA) in positive reflector mode. For each sample, 1200 single-shot spectra were accumulated. All MS spectra were internally calibrated using three standard peptides: Angiotensin II, Neurotensin and ACTH (clip18-39), with m/z values 1046.564 Da, 1672.918 Da and 2465.199 Da. For control spectra, pure M2 protein was treated equivalently.

The M2PL mass spectra showed a single intensity corresponding to (the N-terminal) amino acids 1-17 (m/z 1948.01). Solubilized M2 showed this peak, a second peak corresponding to an N-terminally acetylated form of the same sequence (m/z 1990.03), an intensity corresponding to (the C-terminal) amino acids 78-96 (m/z 2089.94), and a few lower-intensity peaks, corresponding to other M2 amino-acid stretches. Thus both M2 termini can be digested and detected using this protocol (in accordance with (6)), but trypsination of M2PLs digests the N terminus exclusively, demonstrating unidirectional M2 insertion.

A/M2 Liposome (M2LP) flux assay. A positive electrical gradient was created over the M2PL membrane by diluting 0.1 ml M2PL made with K buffer into 0.9 ml Na buffer, including 0.5 µM valinomycin. The final K^+ concentrations were $[K^+]_{in}$=130 mM, $[K^+]_{out}$=11 mM, creating a membrane potential of 62 mV, negative inside. A potential of opposite direction was created by diluting 0.1 ml Na M2PL in 0.9 ml K buffer. A pH gradient over M2PL with symmetrical Na or K concentrations was created by adding 0.5 M H_2SO_4.
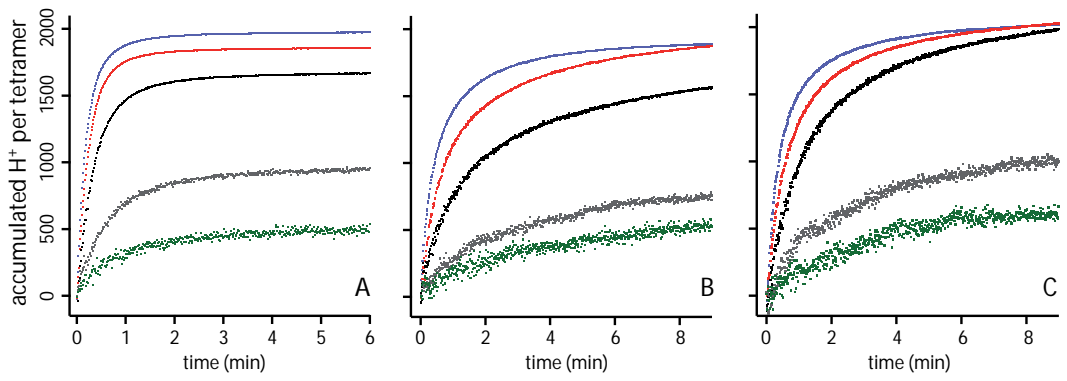
To lower the initial pH_{in} of M2PL reconstituted at pH 7 (Fig. 3), the bulk pH was set to the desired pH with 0.5 M H_2SO_4, allowing M2 to acidify the interior. The accompanying change in K^+ concentrations was taken into account when imposing an electrical gradient over the resulting M2PLs.

Absorbance spectra were continuously recorded at 0.5-1 sec time resolution using an Avantes AvaSpec-2048 fiberoptic spectrometer with a Tungsten-Halogen light-source.

Calibration of the enclosed Glu^3 was done on gramicidin-treated M2PL in connection to each set of experiments. Glu^3 Soret-band absorbance intensities were converted to internal pH values as described in (4). Proton flux was calculated from pH$_{in}$ utilizing the encapsulated volume as determined by Glu^3 absorbance and the average vesicle diameter as determined by cryo-TEM and DLS.

References

1. Mould, J. A., Li, H.-C., Dudlak, C. S., Lear, J. D., Pekosz, A., Lamb, R. A., & Pinto, L. H. (2000) *J Biol Chem* **275,** 8592-8599.
2. Gandhi, C. S., Shuck, K., Lear, J. D., Dieckmann, G. R., DeGrado, W. F., Lamb, R. A., & Pinto, L. H. (1999) *J Biol Chem* **274,** 5474-5482.
3. Ma, C., Polishchuk, A. L., Ohigashi, Y., Stouffer, A. L., Schon, A., Magavern, E., Jing, X., Lear, J. D., Freire, E., Lamb, R. A*., et al.* (2009) *Proceedings of the National Academy of Sciences of the United States of America* **106,** 12283-12288.
4. Leiding, T., Górecki, K., Kjellman, T., Vinogradov, S., Hägerhäll, C., & Peterson Årsköld, S. (2009) *Analytical Biochemistry.* **388,** 296-305.
5. Gobom, J., Nordhoff, E., Mirgorodskaya, E., Ekman, R., & Roepstorff, P. (1999) *Journal of Mass Spectrometry* **34,** 105-116.
6. Kochendoerfer, G. G., Salom, D., Lear, J. D., Wilk-Orescan, R., Kent, S. B., & DeGrado, W. F. (1999) *Biochemistry* **38,** 11905-11913.

VI

A cytochrome *c*- fusion protein domain for convenient detection, quantification and enhanced production of membrane proteins in *Escherichia coli* - expression and characterization of cytochrome-tagged complex I subunits.

Tobias Gustavsson, Maria Trane, Vamsi K. Moparthi, Egle Miklovyte, Lavanya Moparthi, Kamil Górecki, Thom Leiding, Sindra Peterson Årsköld and Cecilia Hägerhäll*

Dept. of Biochemistry and Structural biology, Center for Molecular Protein Science, Department of Chemistry, Lund University, Box 124, 22100, Lund, Sweden.

Running title: Cytochrome *c*- fusion proteins for convenient detection, quantification and enhanced production of membrane proteins.

Keywords:
cytochrome *c*, fusion proteins, covalently bound heme, NADH:quinone oxidoreductase, NuoH, NuoL, NuoM, NuoN, MrpA, MrpD, *Escherichia coli, Bacillus subtilis*

Abbreviations: Amp^r: ampicillin resistance, BCA: bicinchoninic acid, BSA: bovine serum albumin, BTP: bis-tris-propane, Cm^r: chloramphenicol resistance, EPR: electron paramagnetic resonance, FMN: flavin mononucleotide, GFP: green fluorescent protein, GST: glutathione S-transferase, IPTG: Isopropyl β-D-1-thiogalactopyranoside, LB: Luria Bertoni, LHON: Leber's Hereditary Optic Neuropathy, NuoHcyt: NuoH with a fused cytochrome *c* tag, NuoLcyt: NuoLcyt with a fused cytochrome *c* tag, NuoMcyt: NuoM with a fused cytochrome *c* tag, NuoNcyt: NuoN with a fused cytochrome *c* tag, MrpAcyt: MrpA with a fused cytochrome *c* tag, MrpDcyt: MrpD with a fused cytochrome *c* tag, ORP-electrode: oxidation/reduction potential electrode, PCR: polymerase chain reaction, PMSF: phenylmethanesulphonylfluoride, PVDF: Polyvinylidene fluoride, SDS-PAGE: sodiumdodecylsulfate polyacrylamide gel electrophoresis.

*corresponding author: FAX: +46-46-2224116, e-mail: Cecilia.Hagerhall@biochemistry.lu.se

Abstract

Overproduction of membrane proteins can be a cumbersome task, particularly if high yields are desirable. NADH:quinone oxidoreductase (complex I) contains several very large membrane-spanning protein subunits that hitherto have been impossible to express individually in any appreciable amounts in *Escherichia coli*. The polypeptides contain no prosthetic groups or visual redox pigments and are poorly antigenic, making optimization of protein production a challenging task. In this work the C-terminal ends of the complex I subunits NuoH, NuoL, NuoM and NuoN from *E. coli* complex I and the *bona fide* antiporters MrpA and MrpD were genetically fused to the cytochrome *c* domain of *Bacillus subtilis* cytochrome c_{550}. A naturally occurring transmembrane helix anchor was removed from cytochrome c_{550} and substituted by the membrane-spanning polypeptide to be tagged. Compared to other available fusion-protein tagging systems, the cytochrome *c* has several advantages. The heme is covalently bound, and is not lost from the polypeptide even under denaturing conditions, it renders the proteins visible by optical spectroscopy, and can be used to monitor, quantify and determine the orientation of the polypeptides in a plethora of experiments. The fusion proteins were expressed from plasmids in a wild-type *E. coli* strain. For the antiporter-like subunits NuoL, NuoM and NuoN and the real antiporters MrpA and MrpD, unprecedented amounts of fusion proteins could be obtained, containing nearly 100% holo-cytochrome. The NuoHcyt polypeptide was also efficiently produced, but heme insertion was less effective in this construct. The cytochrome c_{550} domain in all the holo-fusion proteins exhibited normal spectra and redox properties, with an E_m of about +170 mV. The MrpA and MrpD antiporters remained functional after being fused to the cytochrome *c*-tag. Finally, a his-tag could be added to the C-terminal end of the cytochrome domain, without any spectral changes or other perturbations to the cytochrome, allowing efficient purification of the overexpressed fusion proteins.

1. Introduction

1.1 Introduction

The most convenient way to express a prokaryote membrane protein is in *Escherichia coli*, where many suitable strains and vectors are available[1.]. However, there are many technical obstacles to overcome to obtain good yields of membrane proteins as compared to soluble proteins, the need for post-translational translocation through the Sec-machinery [2,3]and the limited physical space in the membrane being just the beginning. Many membrane proteins are also poorly antigenic, and most also stain poorly, making protein expression cumbersome to monitor and optimize.

The proton-pumping NADH:ubiquinone oxidoreductase (complex I) of prokaryotes has a molecular mass of about 500 kDa, where the NuoBCDEFGI domain constitutes the hydrophilic arm harboring all known prosthetic groups, and the NuoAHJKLMN domain constitutes the hydrophobic arm, embedded in the membrane. The structure of the hydrophilic arm from the bacteria *Thermus thermophilus* has been solved at 3.3 Å resolution[4,5], revealing the location of the FMN (flavin mononucleotide) and nine iron-sulfur clusters. The membrane-spanning domain of complex I harbors important components of the energy-conserving machinery, but remains poorly understood compared to the protruding, water-soluble part. 2D crystals of the membrane domain resulted in images with about 8 Å resolution[6], but no high resolution structure exists. The structural features of the membrane-spanning part of the complex I enzyme has been mapped by experimentally supported transmembrane topology models[7-10], crosslinking [11] and fractionation studies[12], combined with single particle analyses[13]. We and others have tried to express the individual membrane-spanning complex I polypeptides in *E. coli* using a variety of strains and state-of-the-art strategies, his-tagged proteins etc, without much success. Whereas the antiporters MrpA and MrpD from different organisms have been expressed in, and functionally complemented, *E. coli* strains deleted of their native antiporters, as summarized in [14], the homologous complex I subunits NuoL, NuoM and NuoN have never been expressed in *E. coli* in any appreciable amounts. Only a truncated form of NuoL was successfully expressed [15]. The whole NuoL, fused with a protein A domain, has been produced in yeast endoplasmatic reticulum with seemingly retained functionality [16].

Here, we present protein constructs where the C-terminal end of the complex I subunits NuoH, NuoL, NuoM and NuoN from *E. coli* have been genetically fused to a cytochrome *c* domain (Figure 1). The covalently bound heme in cytochrome *c* renders the proteins visible by optical spectroscopy and can be used to monitor, quantify and orient the polypeptides in a plethora of novel future experiments. Surprisingly, the cytochrome *c* fusion proteins could also be produced with much higher yields compared to all previous attempts to produce the proteins without the fused cytochrome *c*. We suggest that the compact cytochrome *c* domain protects the C-terminal of these polypeptides from proteolysis during growth.

1.2 The choice of cytochrome c

The *Bacillus subtilis* cytochrome c_{550} is a 13 kDa protein, encoded by the *cccA* gene, displaying a Q-band absorption peak at 550 nm. This cytochrome c contains an N-terminal transmembrane helix anchoring it to the membrane, as is common in Gram-positive organisms[17]. The heme is covalently bound by a classical c-type CXXCH motif, where the two cysteines form covalent thioether bonds to the heme group. The histidine in the motif and a C-terminally located conserved methionine serve as axial ligands to the heme iron. Cytochrome c_{550} has a redox midpoint potential of 178 mV[18]. The presence of a membrane anchor in the form of the N-terminal transmembrane helix made

this cytochrome a particularly suitable candidate for creating a cytochrome-containing fusion protein, since the membrane anchor helix could be replaced by a transmembrane helix from the target protein, without any anticipated structural modifications. Furthermore, large amounts of holo-cytochrome c_{550} have previously been produced in *E. coli* under aerobic or microaerophile conditions[19]. In bacteria, the cytochrome c-type covalent thioether bonds can only form in the oxidizing environment on the periplasmic side of the membrane. Thus, only proteins where the C-terminal end is located in the periplasm can be tagged with holo-cytochrome *c*. On the other hand, once the heme is incorporated, it won't be lost from the protein during purification or handling, and is retained even under the denaturing conditions of SDS-PAGE.

1.3 The choice of the membrane-spanning Nuo proteins.
The membrane-spanning domain of complex I is bound to harbor important components of the energy-coupling machinery. The NuoH subunit (Figure 1B) is located in the membrane-spanning domain of complex I, and has long been a strong candidate for harboring a quinone binding site. The NuoH subunit (denoted ND1 in mitochondria) has been specifically photo-labeled with a rotenone analogue [20]. A number of mitochondrial mutations correlating with the inherited disease Leber's Hereditary Optic Neuropathy (LHON) were found in the NuoH subunit [21]. Mutations mimicking some of the LHON mutants were introduced in NuoH (the equivalent of NQO8) of *Paracoccus denitrificans*, and shown to affect quinone reductase activity [22]. If the subunit could be overexpressed and purified without the rest of the enzyme complex, the putative quinone binding site could be probed by direct azidoquinone labelling and mass spectrometry. The C-terminal end of NuoH is located in the periplasm [7], making it a candidate for cytochrome c tagging (Figure 1).

The antiporter-like subunits NuoL, NuoM and NuoN (Figure 1, C and D) are all homologous to the *bona fide* antiporters MrpA and MrpD, making them strong candidates for containing proton and/or ion channels in complex I. An unresolved controversy exists over whether complex I translocates protons exclusively, or sodium as well. The proton/electron stoichiometry of complex I has been scrutinized in many labs over the years (summarized in [23]), reaching a consensus of $4H^+/2e^-$ in complex I in tightly coupled submitochondrial particles from bovine heart. At the same time, it was demonstrated that complex I from *Klebsiella pneumonie* translocated Na^+ [24], and other experiments suggested that complex I from *E. coli* [25] also functions as a primary sodium pump. It is not known whether the NuoL, NuoM and NuoN proteins retain an antiporter function or if they are mere proton channels in Complex I. Some functional specialization of each subunit seems likely, since NuoL more closely resembles MrpA whereas NuoM and N are more similar to MrpD [8]. If these subunits could be overexpressed and purified, the antiporter-function could be measured directly in liposomes. All the antiporters and antiporter-like proteins of this protein family are predicted to have the C-terminus in the periplasm [8], and can therefore be fused to cytochrome *c* (Figure 1). In this work we also added cytochrome-c domains to the the *bona fide* antiporters MrpA and MrpD from *B. subtilis,* to use them as antiporter control proteins to compare with NuoL, NuoM and NuoN in future experiments.

2. Results

2.1 *Construction of the expression vector for cytochrome c fusion proteins*

The membrane-anchored cytochrome c_{550} from *B. subtilis*, described in section 1.2, is encoded by the *cccA* gene. A plasmid for construction and expression of cytochrome-tagged membrane-spanning proteins was produced by cloning the truncated *cccA* gene, omitting the part of the gene encoding the N-terminal transmembrane helix, into the plasmid pUC19[26], that contains an IPTG-inducible *lac* promotor. This plasmid was named pTRC19 (see section 4.2.1). In principle, all membrane-spanning proteins with the C-terminal end located in the periplasm can be tagged with holo-cytochrome *c* by using the novel expression vector pTRC19.

2.2 *Construction of the NuoH, NuoL, NuoM, NuoN, MrpA and MrpD fusion proteins containing a cytochrome c domain.* The *E. coli nuoH, nuoL, nuoM* and *nuoN* genes were amplified by PCR from chromosomal DNA, using primers omitting the respective stop codon. The DNA fragments were ligated into pTRC19 (section 2.1) and transformed into *E. coli*. The resulting plasmids were named pHC1, containing the *nuoH* gene fused to the truncated *cccA*, and pLC1, pMC1 and pNC1, essentially identical to pHC1 but containing the *nuoL*, *nuoM* or *nuoN* gene instead of *nuoH*. The *mrpA* and *mrpD* genes were amplified from *B. subtilis* chromosomal DNA and cloned into pTRC19, resulting in plasmids pVM4 and pVM2 respectively (Table 1, section 4.2.2). The fusion proteins produced from these constructs are denoted NuoHcyt, NuoLcyt, NuoMcyt, NuoNcyt, MrpAcyt and MrpDcyt respectively.

2.3 *Expression of the fusion proteins in E. coli*

The aerobic respiratory chain in *E. coli* does not contain any c-type cytochromes, and therefore *E. coli* expresses the cytochrome c maturation genes exclusively under anaerobic conditions[19,27]. In order to produce the fusion proteins under aerobic conditions and minimize production of apo-cytochrome, the proteins were co-expressed with the *ccm* proteins responsible for heme insertion and cytochrome c maturation from the plasmid pEC86 (kindly provided by Linda Thöny-Meyer, see Table 1). pEC86 expresses the genes in the *ccm* operon constitutively from the tetracycline promoter [27]. Four different growth conditions, with different expected mRNA and/or protein-production rates were tested (Table 2). After growing and harvesting, the cells were broken with French press and the membranes isolated. To compare the amount of cytochrome c_{550} produced under the different growth conditions, the membrane proteins were solubilised with detergent, and the cytochrome c_{500} content was determined by optical spectroscopy using the extinction coefficient for cytochrome c_{550}, $\varepsilon_{550-535} = 24$ mM^{-1}cm^{-1} [18]. The best yield of intact cytochrome c_{550} in this expression system was achieved by growing the cells aerobically at 37°C and inducing the expression with 10 μM IPTG when the cells had reached an optical density of 0.5 (Table 2, a). Letting the cells grow for a longer time, omitting IPTG and instead relying on the small "leaky" expression from the lac-promotor was equally effective: This resulted in virtually the same amount of cytochrome c_{550} in the membranes (Table 2, b). For production of the NuoLcyt, NuoMcyt and NuoNcyt fusion proteins, it was more effective to grow the cells microaerophilically at lower temperature (Table 2, c and d). The highest yield was obtained when the cells were induced with 50 μM IPTG and grown for 42 hours before harvesting. These growth conditions were less effective for making the native cytochrome. The shortest and fastest option, aerobic growth at 37°C with IPTG induction, resulted in significantly less membrane-bound NuoNcyt (Table 2, a). This indicates

that the rate-limiting step is membrane translocation and insertion of the large, membrane-spanning NuoN, whereas the heme insertion, promoted by expression of *ccm* from pEC86, is faster and more efficient. The antiporter-like NuoLcyt, NuoMcyt and NuoNcyt proteins have similar size and overall structure (Figure 1, C and D) and were thus expected to behave very similar. Therefore, the growth conditions were optimized for NuoNcyt and subsequently implemented for the homologous NuoLcyt and NuoMcyt proteins. For NuoHcyt, significantly less holo-fusion protein was produced under all the conditions tested (but see also sections 2.4.3 and 4). As expected, the *E. coli* JM109 strain, containing only the pUC19 expression vector and pEC86, displayed no detectable levels of c-type cytochromes.

Since it has been suggested that expression of the antiporter-like NuoL, NuoM and NuoN might upset the salt and pH homeostasis and thus be toxic to the *E. coli* cells [15], we also grew the *E. coli* strains expressing NuoLcyt, NuoMcyt and NuoNcyt at two different NaCl concentrations (100mM and 300mM, not shown). Neither construct resulted in any significant growth impairment when the salt concentration was increased. Thus, the most likely explanation for the previously obtained poor yield of the full length NuoL, M and N polypeptides is that the proteins are prone to proteolysis when expressed independently, outside the complex I enzyme. It is not unlikely that the compactly folded cytochrome *c* domain could prevent proteolysis in what would otherwise be a more floppy c-terminal end of a protein complex subunit expressed alone.

2.4 *Detecting and characterizing the fusion proteins*
2.4.1 *Optical spectra.*
C-type cytochromes are distinguished by a relatively high redox potential, and thus they are typically reducible by ascorbate. Figure 2 shows the spectra of solubilised membranes containing NuoHcyt, NuoNcyt, intact cytochrome c_{550} , and spectra of membranes from wild-type bacteria containing only the empty vector. All cultures were grown under identical, microaerophilic conditions (Table 2, c). The intact cytochrome c_{550} was expressed from plasmid pLUW1900 (Table 1). As seen in Figure 2, membranes from *E. coli* JM109 containing only plasmids pEC86 and pUC19 do not contain any ascorbate-reducible cytochromes, whereas the cells containing the pEC86 and pLUW1900 encoding the full length cytochrome c_{550} showed the expected ascorbate-reducible peak at 550 nm. Membranes from cells harboring either pHC19 (encoding NuoHcyt) or pNC19 (encoding NuoNcyt) in combination with pEC86 also show a peak at 550 nm after ascorbate reduction. Upon dithionite reduction, another spectral feature with a peak at 559 nm appears in all the samples (Figure 2). The spectra from membranes harboring NuoLcyt, NuoMcyt, MrpAcyt and MrpDcyt are like those of NuoNcyt under the same growth conditions (not shown). Taken together, this demonstrates that the cytochrome c_{550} domain can be readily detected in *E. coli* membranes, even when present in relatively low amounts.

2.4.2 *Redox properties of the fused cytochrome moiety.*
The membranes containing either NuoHcyt, NuoNcyt or intact cytochrome c_{550} were solubilised with Thesit. The redox potential of the heme group in each solubilized protein was determined using a semi-automatic titration system integrated with an optical spectrometer (see section 4.6). The corresponding wild-type membranes were treated the same way. Redox titrations of all the samples from microaerophilic growth conditions (Table 2, c) showed the presence of a redox component with maximal absorbance at 559 nm (see also Figure 2A), with midpoint redox potentials ranging from 50 mV to 78 mV (Figure 4B and D). In the samples from membranes

expressing c-type cytochromes an additional feature was present, with maximal absorbance at 550 nm, corresponding to cytochrome c_{550}. This redox component showed an E_m ranging from 162 mV to 205 mV (Figure 3A and C). The low-potential component is endogenously produced under both aerobic and microaerophilic growth conditions and is probably a mixture of cytochromes from the cytochrome bo_3 oxidase and succinate:quinone reductase, with previously reported midpoint redox potentials of 55 mV [28] and 36 mV [29] respectively. The aerobic samples (Table 2, a and b) contain similar amounts of other cytochromes (not shown). The E_m of the cytochrome c_{550} domain was essentially the same in NuoHcyt, NuoNcyt and in full length, native cytochrome c_{550}, irrespective of whether microaerophilic (Figure 3) or aerobic (not shown) growth conditions were used. Taken together, this demonstrated that the cytochrome c_{550} domain had retained its normal redox properties [17, 18] in the fusion proteins, and that the cytochrome c could be resolved from the other endogenous *E. coli* membrane redox components also when present in low amounts.

2.4.3 *Heme staining and western blot*.

The cytochrome-containing polypeptides could be detected in polyacrylamide gels after SDS-PAGE, either by conventional western blot using antibodies against the cytochrome c_{550} as primary antibody, or the gel can be directly stained for peroxidase activity (so called heme staining). The former method is much more sensitive than the latter, and can detect both apo- and holo-cytochrome c. The latter method demonstrates the presence of a covalently bound heme, and since aerobically grown *E. coli* lack endogenous cytochrome c, the fusion proteins are the only protein bands visible. produced directly in the gel. The *E. coli* membranes expressing NuoHcyt and NuoNcyt were subjected to SDS-PAGE. After electrophoresis, the gels were transferred to PVDF membranes and subjected to western blot using anti-cytochrome c_{550} antibodies (Figure 4A and not shown) or were directly stained for peroxidase activity (Figure 4B and not shown). Membranes from *E. coli* cells containing only pUC19 did not show any band after heme staining, since only c-type cytochromes retain the covalently bound heme group after denaturing SDS-PAGE (not shown) This can be compared with Figure 2 and 3, where other endogenous *E. coli* cytochromes are resolved. Membranes from cells harboring pNC1 show a distinct band of the expected size for the NuoNcyt fusion protein (62 kDa), whereas membranes from pHC1-containing cells only show a faint band, albeit of the expected size of around 46 kDa for NuoHcyt (Figure 4B). This is not surprising since lower amounts of NuoHcyt holo-cytochrome is produced under all growth conditions tested (Table 2). Using immunodection (Figure 4A), we could however detect the fusion proteins using antibodies produced against intact cytochrome c_{550}. When loading equal amounts of membrane protein, the NuoHcyt band appears at least as prominent as the NuoNcyt band, using membranes from the same batch and growth condition as was used for heme staining. This demonstrated that similar amounts of apo-cytochrome fusion protein were in fact produced and inserted into the membrane, whereas heme insertion must be less effective in the NuoHcyt than in the NuoNcyt fusion protein and the other antiporter-like proteins.

2.4.4 *Investigating the function of the cytochrome-tagged antiporters*

B. subtilis cells deleted for their native MrpA or MrpD antiporters exhibit distinct salt and pH sensitive growth phenotypes [37, 38] To test whether the cytochrome-tagged MrpA and MrpD antiporters retained their native function, the MrpAcyt- and MrpDcyt-encoding genes were subcloned into the shuttle vector pCW6, and transformed into *B. subtilis* deleted for the respective antiporters (Table 1). As seen in Figure 5, neither *B. subtilis* ΔMrpA nor *B. subtilis* ΔMrpD are able

to grow at 200 mM NaCl, but when the respective cytochrome-c antiporter fusion proteins are expressed from plasmids, the wild-type growth properties were restored. The lag phase seen particularly in *B. subtilis* ΔMrpD expressing MrpDcyt probably reflects that the Mrp antiporter proteins form a complex [35], and are normally expressed as an operon. By producing one subunit *in trans*, the complex assembly will be somewhat delayed. This effect observed also when the antiporters are expressed from plasmid without cytochrome c. It can be concluded that the cytochrome *c* tagged MrpA and MrpD retained their antiporter function when expressed in the *B. subtilis* antiporter-deletion strains, and thus the cytochrome domain did not interfere with the ion-translocation mechanism or the protein-complex formation.

2.4.5 *Introduction of a his-tag in the c-terminal end of the cytochrome domain*

To further facilitate purification of the cytochrome-tagged proteins, a C-terminal his-tag was added to the cytochrome *c* domain. An insert of a short sequence encoding 6 His residues was introduced by amplifying the respective whole plasmids using a primer pair phosphorylated in the 5'-end especially designed for this purpose (Table 1). The forward primer was completely complimentary to the plasmid region downstream of the fusion gene. The initial part of the reverse primer contained a 15 kb long sequence which was totally complimentary to the end of *cccA* gene but excluding the stop codon, followed by the overhanging 6 His-encoding codons terminated by a phosphorylated stop-codon TAA. After a number of PCR cycles the insert was completely incorporated in the DNA sequence. Self-circularization of the 5' phosphorylated linear PCR product catalyzed by ligase occurred right after the introduced his-tag was terminated by the stop codon, and thus, the risk of introducing a shift in the reading frame was minimized. The constructs were first transformed into *E. coli* XL1-Blue and their sequence was verified, and were subsequently transformed into *E.coli* JM109 harboring plasmid pEC86. The cells were grown as described in section 4.3. The cells expressing fusion proteins with a cytochrome domain and a his-tag at the C-terminal end where produced at slightly lower yield than those expressing cytochrome *c* fusion proteins without a his-tag (Table 3.). Neither the amount of holo-cytochrome (Figure 6 and not shown) nor the cytochrome properties (Figure 7 and not shown) were affected by the his-tag. In essence, the his-tagging did not seem to impede production of proteins or insertion of heme to any great extent.

2.4.6 *Purification of the polypeptides using the his-tag*

Membranes containing his-tagged NuoLcyt, NuoMcyt or NuoNcyt were solubilized and purified using a HisTrap nickel column (see section 4.7). The eluted and pooled peak fractions were loaded on two SDS-PAGE gels run in parallel. One gel was stained with coomasie to visualize the total protein content, and the other gel was subjected to heme staining (Figure 6). Clear and thick bands of coomassie-stained protein of the same sizes as the heme-stained ones, i.e. bands exhibiting peroxidase activity, were seen, whereas only small amounts of other protein bands were apparent. This shows that the fusion proteins were more than 90% pure after one purification step. The estimated protein sizes were in agreement with those predicted from the primary sequences, given that membrane proteins often migrate atypically compared to the soluble standard proteins (compare Figure 4). The heme-staining method is much less sensitive than western blot (Figure 4) or coomassie-staining (Figure 6), but the relative size of the bands indicates that the his-tagged fusion proteins comprises mainly holo-cytochrome *c*. The purified samples showed no sign of other

optically detectable prosthetic groups than cytochrome c_{550} (Figure7 and not shown). The optical spectra of his-tagged cytochrome c fusion proteins where identical to those of cytochrome c fusion proteins without the his-tag (Figure 7 and not shown), demonstrating that introduction of the his-tag did not change spectral properties of the fusion proteins, which corroborates the finding that the heme insertion was not impeded by the his-tag.

3. Discussion

In this work we have developed a cloning vector, pTRC19, that enables tagging of membrane-spanning proteins with a redox-active cytochrome c domain. This tag makes inherently colorless proteins visible and easy to quantify, using the known extinction coefficient for cytochrome c. The expression level of the cytochrome-containing protein is easily assessed, and the amount of protein can likewise be monitored during solubilisation and purification. The cytochrome domain is relatively small and very robust. Even under denaturing conditions, the covalently bound heme will remain attached to the protein. *E. coli* is the most commonly used expression system for producing recombinant proteins in bacteria. *E. coli* does not produce any c-type cytochromes under aerobic growth conditions, making it easy to distinguish between the cytochrome c fusion protein and other endogenous cytochromes.

We have demonstrated that the complex I protein subunits NuoH, NuoL, NuoM and NuoN can be produced as cytochrome c fusion proteins in *E. coli*, with the cytochrome c domain retaining its native redox properties (Figure 3 and 7). The cytochrome-tagged real antiporters MrpA and MrpD could also be expressed in *B. subtilis*, and restored the wild type growth properties of their respective antiporter deletion strain (Figure 5), demonstrating that the cytochrome domain did not interfere with antiporter function. Although this may not necessarily be true for all putative cytochrome c fusion proteins, in the protein constructs examined at this point, the two domains of the fusion proteins seemed to be structurally and functionally independent.

The growth conditions optimal for production of the fusion proteins in *E. coli* were different than for the native cytochrome c_{550}, most likely reflecting the longer time needed for membrane insertion of the large membrane-spanning proteins that were tagged with the cytochrome (Figure 1). Expression of NuoHcyt consistently resulted in lower cytochrome c production than NuoNcyt or intact cytochrome c_{550}. This could have been due to more cumbersome protein membrane insertion or greater protease susceptibility of the NuoHcyt fusion-protein construct. However, in the western blot (Figure 4), the NuoHcyt and NuoNcyt gave rise to bands of similar intensity, indicating that it is rather the heme insertion that is less effective in NuoHcyt, resulting in a mixture of apo-NuoHcyt and holo-NuoHcyt. For NuoLcyt, NuoMcyt, NuoNcyt, MrpAcyt and MrpDcyt, the amounts of holo-cytochrome produced are even higher than what could be accomplished for intact cytochrome c_{550}, indicating that heme insertion in these fusion proteins is unimpeded. This is particularly gratifying since the high efficiency of NuoL, M and N production was rather unexpected. Expression of antiporter-like proteins of this family in *E. coli* has previously been difficult [15], and the high expression levels obtained in this work will facilitate comprehensive investigations of these key complex I subunits. Since it was possible to attach a C-terminal his-tag to the cytochrome c domain, without any detrimental effect to the cytochrome c properties, and allowing the fusion proteins to be purified with ease, a plethora of novel experiments can be conducted.

The only limitation for cytochrome *c* tagging of membrane proteins is that they must have their C-termini on the periplasmic side of the membrane, where the necessary thioether bonds can form. Therefore, in theory, the cytochrome c_{550} tag could also be used to address the transmembrane orientation of a membrane protein. Certainly, no heme insertion will ever occur if a C-teminal fusion is located on the inside of the *E. coli* inner membrane. However, since heme insertion efficiency can be different in different fusion proteins (Figure 4) and the optimal expression conditions also vary for different fusion proteins (Table 2) this application of the cytochrome-tag will require some careful optimization for each protein to be examined.

There is currently a large number of commercially available tagging systems for production of fusion proteins, adding different functionalities to proteins, such as the histidine tag, the green fluorescent protein (GFP) tag and the glutathione S-transferase (GST) tag. The heme tag presented here is a powerful addition to this set of tools, providing a robust, optically quantitative tag and, in applicable cases, an aid in effective membrane-protein production. It remains to be investigated if the cytochrome c domain might also facilitate crystallization of the fusion proteins, by adding a compact, soluble domain to the hydrophobic membrane proteins.

4. Materials and methods

4.1 *Growth of bacteria*
Bacterial strains and plasmids used are listed in Table 1. *E. coli* were grown in Luria Bertoni (LB) medium containing 2% tryptone, 1% yeast extract and 1% KCl, either under microaerophile growth conditions at 30°C (800 ml LB in 2 l baffled E-flasks and 200 rpm shaking) or under aerobic growth conditions at 37°C (400 ml LB in 2 l baffled E-flasks and 200 rpm shaking). For solid cultures 1.5% agar was added to the same medium. When indicated, 100 μg/ml ampicillin and/or 12,5 μg/ml chloramphenicol were included in the medium. The NaCl tolerance was tested under microaerophilic conditions at 30°C, 200 rpm omitting KCl and instead including different amounts of NaCl in the LB medium. Optical density was measured every hour to obtain growth curves. *B. subtilis* cells were kept on TBAB plates, containing 5 μg/ml chloramphenicol when appropriate. Growth studies of the antiporter-deletion strains were done using 35 ml cultures in 250 ml E-flasks with an attached sidearm consisting 16mm glass tube, allowing convenient monitoring of optical density without disturbing the growth. The aerobic growth was done in a shaker incubator kept at 37°C and 200rpm. The growth medium was nutrient broth 8 g/L (NB, Difco), 100mM Tris-HCl pH 7.4, 1μM $FeCl_3$, 5ml/L, 200mM NaCl and 5μg/ml chloramphenicol. The expression of MrpAcyt and MrpDcyt from plasmids was induced at the onset with 1mM IPTG. The optical density of the bacterial culture was measured at 600nM hourly using biowave cell density meter C08000, which is having error rate of <+/-0.05A. After the growth experiment the pH of the media was checked and the bacteria were streaked on plates to verify that the culture was pure.

4.2 *Molecular-biology techniques.*
Restriction enzymes, polymerase, ligase and related products were from Fermentas Life Science and used according to the manufacturer's recommendations. The PCR reactions were performed in a Peltier thermal cycler (PTC-200) with an initial denaturing step of 96°C for 3 min followed by 26 cycles consisting of denaturation at 96°C for 45 s, annealing at 52-55°C (depending on the primer pair) for 45 s, and elongation at 72°C for 2 min/kbp. Proofreading *Pfu* DNA polymerase, that

creates blunt-end PCR products, was used unless otherwise mentioned. The primers used were purchased from Invitrogen and are listed in Table 1.

4.2.1 *Construction of the pTRC19 plasmid.*
The *cccA* gene was amplified by PCR using pLUW1900 [17] as a template. The upstream primer (Table 1) omits the first 78 bases of *cccA*, encoding the transmembrane anchor helix. The revere primer is positioned such that the termination sequence downstream of the stop codon is kept and is included in the construct. This PCR product was digested with SacI and ligated into the pUC19 vector previously digested with SmaI and SacI, producing the plasmid pTRC19. The cccA up primer was constructed in such a way that the SmaI site will be recreated in pTRC19, allowing blunt-end cloning into the correct reading frame to produce a C-terminal cytochrome tag. The final construct was sequenced using pUC19 universal primers.

4.2.2 *Construction of the pHC1, pLC1, pMC1 and pNC1 plasmids.*
Chromosomal DNA was extracted from *E. coli* strain JM109 according to Wilson[30], and was subsequently used as a template for PCR. The *nuo* genes were amplified using the primers listed in Table 1. In the upstream end, a unique restriction-enzyme recognition site was included in the primer sequence; for *nuoH, nuoL and nuoM* a HindIII site was used, and for *nuoN* an XbaI site was introduced. The *nuoH* PCR product was digested with HindIII and ligated into previously SmaI and HindIII digested pTRC19. The resulting construct was transformed into *E. coli* JM109 by electroporation. This was repeated for *nuoL* and *nuoM*. The same procedure was also used for the construction of the cytochrome-tagged NuoN with the exception that the PCR product and vector pTRC19 was digested with XbaI instead of HindIII. The plasmids containing the fusion *nuo* gene and the cytochrome domain of *cccA* were named pHC1, pLC1, pMC1 and pNC1 (Table 1). The constructs were sequenced by the Sanger method and analysed at the Biomolecular Recourse Facility, Lund University, using Big Dye[TM].

4.2.2 *Construction of the pVM2, pVM4, pVM6 and pVM11 plasmids.*
Chromosomal DNA from *B. subtilis* 168A was prepared as descibed by Marmur[31], and was used as a template for amplification of the *mrpA* and *mrpD* genes using the primers listed in Table 1. In the upstream primer, a unique restriction-enzyme recognition site was created, for *mrpA* a SalI site was used and for *mrpD* a HindIII site was introduced. In the downstream primer sequence the stop codon was omitted from the respective gene sequences, to produce fusion proteins. The PCR product was digested with SalI or HindIII and ligated into previously SalI/HindIII and SmaI digested pTRC19. The resulting constructs were transformed into *E. coli* JM109 by electroporation. The plasmids were sequenced as before, and were named pVM4 and pVM2 respectively.

The pVM4 and pVM2 plasmids were subsequently used as templates for the amplification of the genes encoding MrpAcytc and MrpDcytc for subcloning into the *E. coli/B. subtilis* shuttle vector pCW6, using the primers listed in Table 1. In the upstream primers, a unique PstI site was introduced, and in the downstream primers, a site for XbaI was created. The PCR reaction was run as before, except that lower annealing temperatures (42ºC for the pVM4 template and 47ºC for the pVM2 template), and Dream Taq DNA polymerase was used.
The PCR products were digested with PstI and XbaI and ligated into pCW6. The resulting constructs were transformed into *E. coli* JM109 and confirmed by DNA sequencing as before. The new plasmids, named pVM11 and pVM6 respectively, were subsequently transformed into *B.*

subtilis 168A, *B. subtilis* ΔMrpA and *B. subtilis* ΔMrpD, that were grown to competence using the method of Arwert and Venema[32].

4.2.3 *Adding a his-tag to the plasmid constructs*

To attach a his-tag to the c-terminal end of the cytochrome the Phusion site-directed mutagenesis method (Finnzymes) was employed. Proofreading Phusion DNA polymerase, that creates blunt end PCR products, was purchased from Finnzymes, 5' phosphorylated primes were synthesized by Invitrogen (Table 1). The whole plasmids containing fusion genes of *nuoL, nuoM, nuoN, mrpA, mrpD* and the cytochrome domain were amplified by PCR using the same primer pair (Table 1) and the the following conditions: 1 min initial denaturation at 98°C, followed by 30 cycles of 20 s denaturation at 98°C, 20 s annealing at 59°C, 1 min 25s/1kbp elongation at 72°C and a final 5 min elongation at 72°C. The PCR products were subsequently ligated with T4 DNA ligase to obtain the plasmids encoding each of the fusion proteins with a his-tag at the C-terminal part of cytochrome domain. The resulting plasmid constructs were confirmed by DNA sequencing as before and were named pLch, pMch, pNch, pAch and pDch respectively (Table 1). The plasmids were subsequently transformed into *E. coli* JM109, also harboring plasmid pEC86 [27].

4.3 *Protein production*.

Cells were grown either microaerophilically at 30°C or aerobically at 37°C, as described in section 2.1. When indicated, Isopropyl β-D-1-thiogalactopyranoside (IPTG) was added to a final concentration of 10 - 50 μM when the cells had reached an OD of 0.5 at 600 nm. All protein expression experiments were made using *E. coli* JM109 cells harbouring the plasmid pEC86 [27] that express the *ccm* operon constitutively. The culture media was inoculated from cells grown confluently on LB agar plates. After growth, the cells were harvested by centrifugation at 9000g for 8 min, washed in 50 mM KPO_4 pH 8.0 and stored frozen at -20°C. The cell pellets were thawed and resuspended in 10 mM Tris-HCl, 30 mM KCl, 1mM phenylmethanesulphonylfluoride (PMSF), 5 μg DNase/ml pH 7.0 and passed twice through a French pressure cell at 6.9×10^6 Pa. Cell debris was removed by centrifugation at 9000g for 15 min and the membranes were subsequently collected after centrifugation at 120000g for 90 min. The membranes were homogenised in 20 mM bistrispropane-HCl (BTP) pH 7.0 using a handheld potter, and were frozen in liquid N_2 and stored at -80°C.

4.4 *Western blot and heme staining*.

SDS-PAGE was done as described by Neville using 10% acrylamide gels [33]. Membranes were thawed and solubilized in 4% SDS at room temperature for 30 min, then incubated with loading buffer at 37°C for 45 min, and were subsequently loaded on the gel. Electrophoresis was run at 100 V for 2 h. Transfer to polyvinylidene fluoride membrane (PVDF, Millipore) was done according to the manufacturer's instructions. The PVDF membrane was soaked in methanol for 15 s, then in Milli-Q water for 2 min and finally equilibrated in anode buffer II for at least 5 min. Anode buffer II contained 25 mM Tris, pH 10.4 and 10% (v/v) methanol. After electrophoresis the gel was immersed in 200 ml cathode buffer for 15 min. The cathode buffer contained 25 mM Tris, 40 mM Glycine, pH 9.4, 10% (v/v) methanol. For transfer of the proteins from the gel to the PVDF membrane, two pieces of filter paper soaked in anode buffer I were placed on the anode electrode plate. Anode buffer I contained 0.3 M Tris, pH 10.4 and 10% (v/v) methanol. This was followed by placing another filter paper soaked in anode buffer II on top of the first, then placing the membrane

on the stack of filter papers. Finally the gel was placed on the PVDF membrane and three pieces of filter paper soaked in cathode buffer were placed on top of the gel. The blot was run at 0.4 mA/cm^2 for 17 h. Immunodetection was done as recommended by Millipore. The blot was blocked in 1% (w/v) BSA and 0.05% Tween-20 (blocking solution) for 1 h at room temperature with agitation. The primary antibody, anti-cytc$_{550}$ (kindly provided by Lars Hederstedt), was diluted 1:5000 in blocking solution and incubated as above. The PVDF membrane was washed 3 times for 10 min in phosphate-buffered saline (PBST: 10 mM sodium phosphate, pH 7.2, 0.9% (w/v) NaCl, up to 0.1% Tween-20 detergent). Bound antibodies were detected using alkaline phosphatase-linked goat anti-rabbit antibodies diluted 1:20000 in blocking solution. Finally the PVDF membrane was washed 3 times for 10 min in PBST, and was subsequently developed with ECF substrate (GE Healthcare). Activities were monitored using a STORM 860 fluorimeter (Molecular dynamics, Amersham Biosciences) at 650 nm. The polyacrylamide gel was stained with colloidal Coomassie after blotting to confirm the efficiency of protein transfer.

For heme-staining an SDS-PAGE was run in the same fashion as before, but after electrophoresis the peroxidase activity in the gel was visualized by the method of Kashino et al.,[34] using 3,3-diaminobenzidine tetrahydrochloride as substrate.

4.5 *Optical spectroscopy*

Membrane proteins were solubilised from the membrane with Thesit in 5:1 w/w ratio. 200 μl of each membrane preparation (Table 2) was diluted six times in the solubilisation buffer containing 20 mM BTP pH 7.0 and a final Thesit concentration of 2%. The solubilisation was performed at room temperature for 45 min, and the samples were subsequently centrifuged at 20000g for 5-30 min. The supernatant was diluted in an equal volume of BTP buffer without detergent and optical spectra of the samples were recorded using a Shimadzu UVPC 2100 spectrophotometer. Purified proteins were used as is or diluted in BTP buffer. The samples were analysed as FeCN-oxidized (0.5 mM), ascorbate-reduced (10 mM) and dithionite-reduced (a few grains of solid reductant).

4.6 *Redox titration*

Membranes containing NuoHcyt or NuoNcyt were thawed and diluted to 10-15 mg membrane protein/ml in solubilisation buffer. Control membranes, either without plasmid encoded c-type cytochromes or containing native cytochrome c_{550}, were treated the same way. The detergent Thesit was used in 5:1 w/w ratio. The solubilisation buffer contained 20 mM BTP, pH 7.0, and 12% (w/v) Thesit. The solubilisation was performed while stirring at 4°C for 60 minutes followed by centrifugation at 120000g for 30 minutes to remove unsolubilised material.

Redox titrations of the solubilised material were made using an in-house constructed titration cell equipped with magnetic stirring and kept under an argon atmosphere. The redox potential was set via computer-controlled syringe pumps administering precise volumes of sodium dithionite for reduction and potassium ferricyanide for oxidation. The redox potential was monitored with an ORP-electrode from Microelectrodes Inc. Bedford, NH USA. Spectra were recorded at predetermined redox potentials with an integrated spectrometer consisting of a fiberoptic tungsten light source and a fiberoptic CCD detector. Absorbance at the redox-sensitive wavelength was subsequently plotted against potential and fitted to the Henderson-Hasselbalch equation to determine the midpoint redox potential. In all measurements, redox mediators were included to equilibrate the solution. The following compounds were present at 25 μM each: quinhydrone, 2,5-dimethyl benzoquinone, phenazine methosulfate, duroquinone, 2,5-dihydroxy-1,4-benzoquinone, 2-hydroxy-1,4-naphtoquinone and anthraquinon-2-sulphonic acid.

4.7 *Purification using the his-tag*

Each membrane preparation was diluted to about 10 mg/ml with 20 mM BTP pH 6.8 containing 10% dodecylmaltoside (DDM) to a final concentration of 5% detergent. The solubilisation was performed at 4°C with stirring for at least one hour, followed by centrifugation at 120 000 g for 30 min to remove unsolubilized material. 1 M imidazole and 5 M NaCl were added to the supernatant to achieve final concentrations of 40 mM and 500 mM, respectively. The supernatant was then loaded onto a hisTrap 1 ml column and washed with 20 ml binding buffer (20 mM BTP-HCl, pH 6.8; 0.1 % DDM, 40 mM imidazole, 500 mM NaCl). The protein was eluted with an imidazole gradient up to 1 M and fractions of 1 ml were collected. The cytochrome *c* fusion proteins eluted at about 300 mM imidazole. The fractions that had a clear red color were pooled and washed several times with sample buffer (20 mM BTP-HCl, pH 7.4; 0.1 % DDM, 50 mM NH_4Cl) to remove the imidazole and to lower sodium concentration to below 2 mM using Millipore spin columns.

4.8 *Protein quantification*

The total protein concentrations were measured by bicinchroninic acid method (BCA, Pierce) using bovine serum albumin (BSA) as standard. If membranes were analysed, 1% SDS was included both in the samples and in the BSA standard samples.

Cyt c_{550} tagged protein concentration was determined using the redox properties of the Q band of cyt c_{550}:

$$[\text{cyt}c_{550}] = [(A_{550}^{rd} - A_{550}^{ox}) - (A_{535}^{rd} - A_{535}^{ox})] / \varepsilon$$

where $\varepsilon = 24$ mM^{-1} cm^{-1}, [18] or, for a less accurate concentration estimate, the extinction coefficient of the Soret band at $\varepsilon_{410\ nm} = 106.1$ mM^{-1}cm^{-1}, was used.

References:

1. Wang DN, Safferling M, Lemieux MJ, Griffith H, Chen Y, Li XD. (2003) Practical aspects of overexpressing bacterial secondary membrane transporters for structural studies. Biochim Biophys Acta-Biomembr 1610: 23-36.
2. Manting EH, Driessen AJM. (2000) *Escherichia coli* translocase: the unravelling of a molecular machine. Mol Microbiol 37: 226-238.
3. Froderberg L, Houben ENG, Baars L, Luirink J, de Gier JW. (2004) Targeting and translocation of two lipoproteins in *Escherichia coli* via the SRP/Sec/YidC pathway. J Biol Chem 279:31026-31032.
4. Sazanov LA, Hinchliffe P. (2006) Structure of the hydrophilic domain of respiratory complex I from *Thermus thermophilus*. Science 311:1430-1436.
5. Sazanov LA. (2007) Respiratory complex I: Mechanistic and structural insights provided by the crystal structure of the hydrophilic domain. Biochemistry 46:2275-2288.

6. Baranova EA, Holt PJ, Sazanov LA. (2007) Projection structure of the membrane domain of *Escherichia coli* respiratory complex I at 8 angstrom resolution. J Mol Biol 366:140-154.

7. Roth R, Hägerhäll C. (2001) Transmembrane orientation and topology of the NADH : quinone oxidoreductase putative quinone binding subunit NuoH. Biochim Biophys Acta-Bioenerg 1504: 352-362.

8. Mathiesen C, Hägerhäll C. (2002) Transmembrane topology of the NuoL, M and N subunits of NADH : quinone oxidoreductase and their homologues among membrane-bound hydrogenases and *bona fide* antiporters. Biochim Biophys Acta-Bioenerg 1556: 121-132.

9. Kao MC, Di Bernardo S, Matsuno-Yagi A, Yagi T. (2002) Characterization of the membrane domain Nqo11 subunit of the proton-translocating NADH-quinone oxidoreductase of *Paracoccus denitrificans*. Biochemistry 41: 4377-4384.

10. Kao MC, Di Bernardo S, Matsuno-Yagi A, Yagi T. (2003) Characterization and topology of the membrane domain Nqo10 subunit of the proton-translocating NADH-quinone oxidoreductase of *Paracoccus denitrificans*. Biochemistry 42: 4534-4543.

11. Mamedova AA, Holt PJ, Carroll J, Sazanov LA. (2004) Substrate-induced conformational change in bacterial complex I. J Biol Chem 279: 23830-23836.

12. Holt PJ, Morgan DJ, Sazanov LA. (2003) The location of NuoL and NuoM subunits in the membrane domain of the *Escherichia coli* complex I - Implications for the mechanism of proton pumping. J Biol Chem 278: 43114-43120.

13. Baranova EA, Morgan DJ, Sazanov LA. (2007) Single particle analysis confirms distal location of subunits NuoL and NuoM in *Escherichia coli* complex I. J Struct Biol 159: 238-242.

14. Morino M, Natsui S, Swartz TH, Krulwich TA, Ito M. (2008) Single gene deletions of mrpA to mrpG and mrpE point mutations affect activity of the Mrp Na^+/H^+ antiporter of alkaliphilic Bacillus and formation of hetero-monieric Mrp complexes. J Bacteriol 190: 4162-4172.

15. Steuber J. (2003) The C-terminally truncated NuoL subunit (ND5 homologue) of the Na^+-dependent complex I from *Escherichia coli* transports Na^+. J Biol Chem 278: 26817-26822.

16. Gemperli AC, Schaffitzel C, Jakob C, Steuber J. (2007) Transport of Na^+ and K^+ by an antiporter-related subunit from the *Escherichia coli* NADH dehydrogenase I produced in Saccharomyces cerevisiae. Arch Microbiol 188: 509-521.

17. von Wachenfeldt C, Hederstedt L. (1990) *Bacillus subtilis* 13-kilodalton cytochrome c_{550} encoded by cccA consists of a membrane-anchor and a heme domain. J Biol Chem 265: 13939-13948.

18. von Wachenfeldt C, Hederstedt L. (1993) Physico-chemical characterisation of membrane-bound and water-soluble forms of *Bacillus subtilis* cytochrome c_{550}. Eur J Biochem 212: 499-509.

19. von Wachenfeldt C, Hederstedt L. (1990) *Bacillus subtilis* holo-cytochrome c_{550} can be synthesised in aerobic *Escherichia coli*. FEBS Lett 270: 147-151.

20. Earley FG, Patel SD, Ragan CI, Attardi G. (1987) Photolabelling of a mitochondrially encoded subunit of NADH dehydrogenase with [3-H]-dehydrorotenone. FEBS Lett 219: 108-113.

21. Wallace DC, Brown MD, Lott MT. (1999) Mitochondrial DNA variation in human evolution and disease. Gene 238: 211-230.

22. Kurki S, Zickermann V, Kervinen M, Hassinen I, Finel M. (2000) Mutagenesis of three conserved Glu residues in a bacterial homologue of the ND1 subunit of complex I affects

ubiquinone reduction kinetics but not inhibition by dicyclohexylcarbodiimide. Biochemistry 39: 13496-13502.

23.   Galkin A, Grivennikova VG., Vinogradov AD. (1999) H^+/e^- stoichiometry in NADH-quinone reductase reactions catalyzed by bovine heart submitochondrial particles. FEBS lett 451: 157-161.

24.   Gemperli AC, Dimroth P, Steuber J. (2002) The respiratory complex I (NDH I) from *Klebsiella pneumoniae*, a sodium pump. J Biol Chem 277: 33811-33817.

25.   Steuber J, Schmid C, Rufibach M, Dimroth P. (2000) Na^+ translocation by complex I (NADH : quinone oxidoreductase) of *Escherichia coli*. Mol Microbiol 35: 428-434.

26.   Yanisch-Perron C, Vieira J, Messing J. (1985) Improved M13 phage cloning vectors and host strains: nucleotide sequences of the M13mp18 and pUC19 vectors. Gene 33: 103-119.

27.   Arslan E, Schulz H, Zufferey R, Kunzler P, Thöny-Meyer L. (1998) Overproduction of the *Bradyrhizobium japonicum* c-type cytochrome subunits of the cbb(3) oxidase in *Escherichia coli*. Biochem Biophys Res Co 251: 744-747.

28.   Bolgiano B, Salmon I, Ingledew WJ, Poole RK. (1991) Redox analysis of the cytochrome o-type quinol oxidase complex of *Escherichia coli* reveals 3 redox components. Biochem J 274: 723-730.

29.   Kita K, Vibat CR, Meinhardt S, Guest JR, Gennis RB. (1989) One-step purification from *Escherichia coli* of complex II (succinate: ubiquinone oxidoreductase) associated with succinate-reducible cytochrome b_{556}. J Biol Chem 264: 2672-2677.

30.   Wilson K. Preparations of Genomic DNA from Bacteria. In: Moore DD, ed. (1994) Current Protocols in Molecular Biology, Preparation and Analysis of DNA. Volume 1: Wiley Interscience; p 2.4.1-2.4.5.

31.   Marmur J. (1961) A procedure for the isolation of deoxyribonucleic acid from bacteria. J. Mol. Biol.;3: 208-218.

32.   Arwert F, Venema G. (1973) Transformation in Bacillus subtilis - Fate of Newly Introduced Transforming DNA. Mol Gen Genet;123:185-198.

33.   Neville DM. (1971) Molecular weight determination of protein-dodecyl sulfate complexes by gel electrophoresis in a discontinuous buffer system. J Biol Chem 246: 6328.

34.   Kashino Y, Lauber WM, Carroll JA, Wang QJ, Whitmarsh J, Satoh K, Pakrasi HB. (2002) Proteomic analysis of a highly active photosystem II preparation from the cyanobacterium Synechocystis sp PCC 6803 reveals the presence of novel polypeptides. Biochemistry 41: 8004-8012.

35.   Kajiyama, Y., Otagiri, M., Sekiguchi, J., Kosono, S., and Kudo, T. 2007. Complex formation by the mrpABCDEFG gene products, which constitute a principal Na^+/H^+ antiporter in *Bacillus subtilis*. *J Bacteriol* **189:** 7511-7514.

36.   Mathiesen C. (2003) On the antiporter-like subunits of respiratory chain complex I; Ph.D. Thesis, Lund University, Sweden, ISBN 91-7422-020-9
37.   Ito, M., Guffanti, A.A., and Krulwich, T.A. 2001. Mrp-dependent Na(+)/H(+) antiporters of Bacillus exhibit characteristics that are unanticipated for completely secondary active transporters. FEBS Lett 496: 117-120.

38.   Ito, M., Guffanti, A.A., Oudega, B., and Krulwich, T.A. 1999. mrp, a multigene, multifunctional locus in Bacillus subtilis with roles in resistance to cholate and to Na+ and in pH homeostasis. J Bacteriol 181: 2394-2402.

Figure legends:

Figure 1. Schematic drawing of the fusion proteins presented in this paper, where the last transmembrane helix of the Nuo protein replaces the natural membrane-anchor helix in *B. subtilis* cytochrome c_{550}. A model of the cytochrome c_{550} is shown in A. The topology of the NuoH protein, shown in B, is based on Roth and Hägerhäll[7], and the topology of the antiporter-like proteins NuoL (shown in C) and NuoM/NuoN/MrpD (shown in D) are adapted from Mathiesen and Hägerhäll[8]. NuoM, NuoN and MrpD have the same transmembrane topology and number of transmembrane helices, thus only one model protein is shown representing all three proteins. MrpA is similar to NuoL, but contains an additional C-terminal extension (not shown)

Figure 2. Difference spectra (reduced minus oxidized) of solubilized *E. coli* membranes from microaerophilic growth at 30°C (see Table 2c) reduced with ascorbate (lower trace) or dithionite (upper trace). 0.5 mM ferricyanide was first added to fully oxidize the sample. A: membranes from wild-type cell harboring only the empty vector. B: membranes from cells expressing the native, full length cytochrome c_{550}. C: membranes from cells expressing the NuoHcyt fusion protein., D: membranes from cells expressing the NuoNcyt fusion protein. In aerobically grown samples (Table 2, a and b) the ascorbate-reduced and dithionite-reduced spectra are virtually identical (not shown).

Figure 3. Redox titrations of detergent-solubilized *E. coli* membranes, grown as in Figure 2. A: titration of the NuoHcyt-containing membranes monitoring the spectral feature at 550 nm. B: the same titration recorded at 559 nm. C and D: titration of the NuoNcyt-containing membranes monitred at 550 nm and 559, respectively. The membranes containing intact cytochrome c_{550} showed the same behavior as those containing NuoNcyt, both at 550 nm and at 559 nm (not shown). In wild-type membranes, only the peak at 559 nm, similar to that in B and D, could be titrated, whereas absorbance at 550 nm was absent (not shown).

Figure 4. Visualisation of cytochrome *c* fusion proteins in *E. coli* membranes by immunodetection (Panel A) and heme staining (Panel B). The membranes were from growth condition b (Table 2). The NuoNcyt polypeptide has a calculated mass of 62 kDa whereas the size of the NuoHcyt polypeptide is 46 kDa. As often with membrane proteins, the apparent mass on the gel is somewhat lower. **Panel A;** Western blot of *E. coli* membranes using antibodies against cytochrome c_{550}. 20 µg membrane protein from *E. coli* cells expressing the fusion protein constructs was loaded into each lane. Lane 1 contains membranes harboring the NuoNcyt fusion protein and lane 2 the NuoHcyt fusion protein. **Panel B;** SDS-PAGE gel stained for covalently bound heme by the method of Kashino et al. [34], where peroxidase activity is detected with 3,3-diaminobenzidine tetrahydrochloride. 200 µg of membrane protein from *E. coli* expressing the fusion-protein constructs were loaded on the gel. Lane 1 contains membranes harboring the NuoNcyt fusion protein and lane 2 membranes from cells containing the NuoHcyt fusion protein.

Figure 5. Growth curves of *B. subtilis* wild type and antiporter-deletion strains (Table 1) grown under aerobic conditions at 37^{0}C, in a rich media with 200mM NaCl and pH 7.4. In Panel A the *B. subtilis* ΔMrpA strain hosting only the pCW6 vector is shown with open circles and *B. subtilis* ΔMrpA expressing MrpAcyt from plasmid pVK11 is shown with filled triangles. The growth of wild type *B. subtilis* (open squares) is shown for comparison. In panel B, the growth of the *B.*

subtilis ΔMrpD strain containing the vector only is shown with filled circles and *B. subtilis* ΔMrpD expressing MrpDcyt from plasmid pVK6 is shown with open triangles. Wild type *B. subtilis* cells are represented by filled squares. The generation time for wild type *B. subtilis*, and the deletion strains expressing the respective cytochrome-tagged antiporter *in trans* was 62 minutes, 63 minutes and 86 minutes respectively. The lag phase observed in the *B. subtilis* ΔMrpD expressing MrpDcyt is also seen when expressing MrpD without cytochrome tag from a plasmid (not shown) and probably reflects that the Mrp proteins are part of an antiporter complex [35].

Figure 6. The NuoLcyt, NuoMcyt and NuoNcyt fusion proteins after a one step purification. The samples, purified from nickel column using the his-tag, were analyzed by SDS-PAGE. The left side gel is stained with Coomassie to visualize all proteins. Lanes 1, 2 and 3 contain 20 µg of protein from samples containing NuoLcyt, NuoMcyt and NuoNcyt respectively. The right side gel is stained for covalently bound heme i.e. peroxidase activity. Lanes 4, 5 and 6 contain 40 µg of protein from the same samples, loaded in the same order as previously. NuoLcyt has a calculated mass of 76 kDa , NuoMcyt is expected to be 66 kDa and has a size of NuoNcyt 62 kDa. As mentioned before (see Figure 4) the apparent mass on the gel is somewhat lower.

Figure 7. Spectra of a purified sample of his-tagged NuoMcyt (1.1 mg protein /ml). The solid lines represent the ascorbate reduced sample; dashed lines are ferricyanide oxidized sample; and dotted lines denote dithionite reduced sample. All the purified fusion protein have identical cytochrome *c* spectra. We could also not detect any spectral differences between the cytochrome-tagged fusion proteins with and without his-tag (not shown) .A sample of the purified protein in a 2 ml test tube on ice is shown as an inset. The clear red color originates from the cytochrome *c* fusion domain.

Table 1. Biological material.

Bacterial strains	Genotype	source/reference
E coli JM109	*endA1, glnV44, thi-1, relA1 gyrA96 recA1 mcrB*[+] Δ(*lac-proAB*) e14- [F' *tra*D36 *pro*AB[+] *lac*I[q] *lac*ZΔM15] *hsd*R17(r$_K^-$m$_K^+$)	[26]
E. coli XL1-blue	*recA1, endA1, gyrA96, thi-1, hsdR17, supE44, relA1, (lac)*	Promega
B. subtilis 168A	wild type (type strain) *trpC2*	*Bacillus* genetic stock center
B. subtilis ΔMrpA	*trpC2*, Δ*mrpA*, Ble[r]	[36]
B. subtilis ΔMrpD	*trpC2*, Δ*mrpD*, Ble[r]	[36]
Plasmids	**Relevant properties**	
pUC19	Amp[r]	[26]
pLUW1900	*cccA*, Amp[r]	[17]
pCW6	shuttle vector, Cm[r]	Claes von Wachenfeldt
pEC86	contains the *ccm* operon, Cm[r]	[27]
pTRC19	truncated *cccA* in pUC19, Amp[r]	This work
pHC1	*nuoH* fused with truncated *cccA*, Amp[r]	This work
pLC1	*nuoL* fused with truncated *cccA*, Amp[r]	This work
pMC1	*nuoM* fused with truncated *cccA*, Amp[r]	This work
pNC1	*nuoN* fused with truncated *cccA*, Amp[r]	This work
pVM4	*mrpA* fused with truncated *cccA*, Amp[r]	This work
pVM2	*mrpD* fused with truncated *cccA*, Amp[r]	This work
pVM11	*mrpA* fused with truncated *cccA*, Cm[r]	This work
pVM6	*mrpD* fused with truncated *cccA*, Cm[r]	This work
pLch	as pLC1, with his-tag added	This work
pMch	as pMC1, with his-tag added	This work
pNch	as pNC1, with his-tag added	This work
pAch	as pVM4, with his-tag added	This work
pDch	as pVM2, with his-tag added	This work
Primers	**DNA sequence**	
cccA up	5´-GGGCTTGATGACTCTCGGGAG-3´	This work
cccA down	5´-GTAT**GAGCTC**CGCTACTGTTTGC-3´	This work
nuoH up	5´-CGCG**AAGCTT**GAGGATCTCAAGG-3´	This work
nuoH down	5´-TTGCGCCTGCCAGAGAATGACAG-3´	This work
nuoL up	5´-CCAGAACCTG**AAGCTT**GATTC-3´	This work
nuoL down	5´-ACGCAGTACCATCAACAGTGC-3´	This work
nuoM up	5´-CCTGACG**AAGCTT**TTACAAGGAA-3´	This work
nuoM down	5´-CGGCCTTGTAGTAGTAACGGAAT-3´	This work
nuoN up	5´-TCCGCGATTGGCAATA**TCTAGA**AGTGG-3´	This work
nuoN down	5´-CATCAGCGGCATTGCCAAACGCACA-3´	This work
mrpA_vk_Up	5`-GCAGCTCTTAC**GTCGAC**CTATTTTATCGC-3´	This work
mrpA_vk_Dwn	5´-GCTTTTCCCCTCCTCTTTTACTTTTG-3´	This work

mrpD_vk_Up	5´-CAGGAATTGG**AAGCTTA**CGATATGG 3´	This work
mrpD_vk_Dwn	5´-CAGAACAGCTTCGATATATTTTTCC-3´	This work
mrpA_For_pCW6	5´-CCGCTACTGT**CTGCAG**TCGTTTA-3´	This work
mrpA_Rev_pCW6	5´-CGCCTTT**TCTAGA**TGCTTTTATC-3´	This work
mrpD_For_pCW6	5´-CCGCTACTGT**CTGCAG**TCGTTTA-3´	This work
mrpD_Rev_pCW6	5´-CGCCAAGC**TCTAGA**TATGGGTC-3´	This work
His-t Forward	5' **P**-AAGAACTATTTTTCTCTTTATACATTC-3'	This work
His-r Reverse	5' **P**-TTAATGATGATGATGATGATGTTTAATTTT TGACACCCACTC-3'	This work

Table 2: Cytochrome c_{550} content in *E. coli* membranes from different growth conditions.

Bacteria with plasmid / Conditions	pHC19 (encoding NuoHcyt) nmol cyt c_{550} /mg membrane protein	pLC19 (encoding NuoLcyt) nmol cyt c_{550} /mg membrane protein	pMC19 (encoding NuoMcyt) nmol cyt c_{550} /mg membrane protein	pNC19 (encoding NuoNcyt) nmol cyt c_{550} /mg membrane protein	pLUW1900 (encoding intact cytochrome c_{550}) nmol cyt c_{550} /mg membrane protein	pUC19 (vector only) nmol cyt c_{550} /mg membrane protein
a) 8h, 37°C, 10μM IPTG	0.05	nd	nd	0.14	0.22	<0.001
b) 16h, 37°C without induction	0.03	nd	nd	0.08	0.22	<0.001
c) 17h, 30°C, 10μM IPTG	0.04	nd	nd	0.23	0.08	<0.001
d) 42h, 30°C, 50μM IPTG	0.04	0.55	0.50	0.46	0.10	<0.001

All plasmids were hosted in *E. coli* JM109 that also contained the plasmid pEC86[27], constitutively expressing the cytochrome *c* maturation (ccm) proteins. In a) and b) the cells were grown under aerobic conditions whereas c) and d) were microaerophilic cultures. In a) and c) the expression was induced with 10 μM IPTG at OD_{600}=0.5, and in d) 50μM IPTG is included from the beginning. The amount of cytochrome c_{550} was determined from spectra using $\varepsilon_{550-535} = 24$ mM^{-1}cm^{-1} [18]. nd = not determined. The growth conditions were optimized for NuoNcyt and subsequently implemented for the homologous NuoLcyt and NuoMcyt proteins.

Table 3. Comparison of cytochrome yield in membranes expressing fusion proteins with and without his-tag

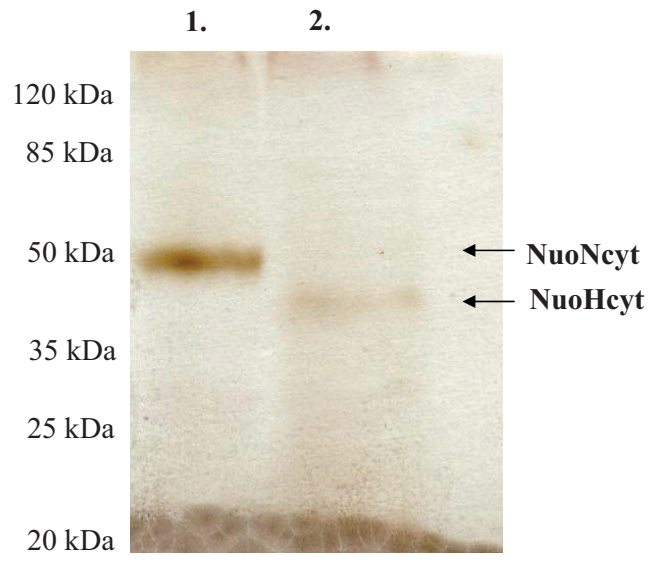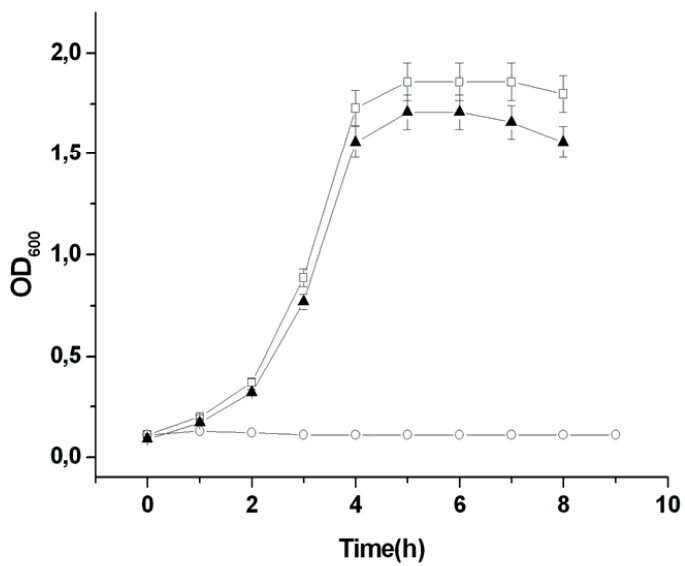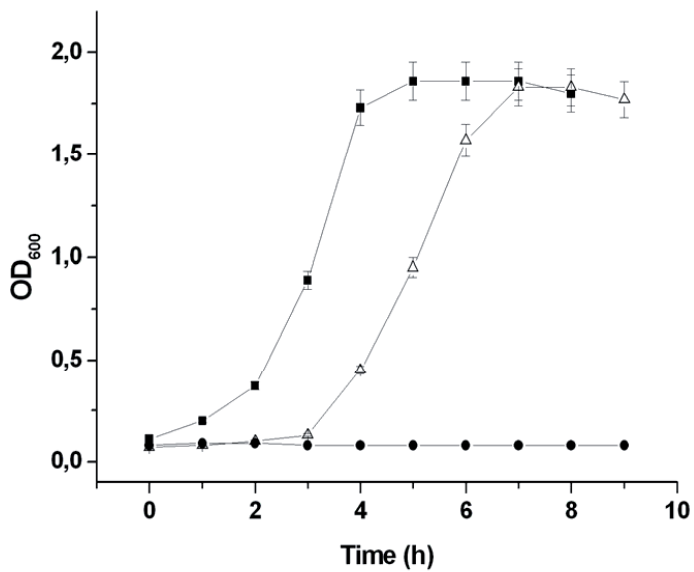| Protein	nmol cytochrome c_{550}/mg total membrane protein	Fusion protein per liter culture (mg/L)
NuoLcyt	0.55	2.10
NuoLcH6	0.29	0.88
NuoMcyt	0.50	1.66
NuoMcH6	0.43	0.63
NuoNcyt	0.46	1.14
NuoNcH6	0.41	0.66
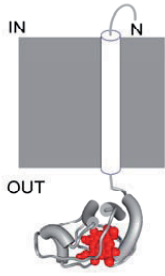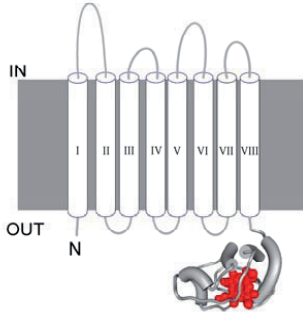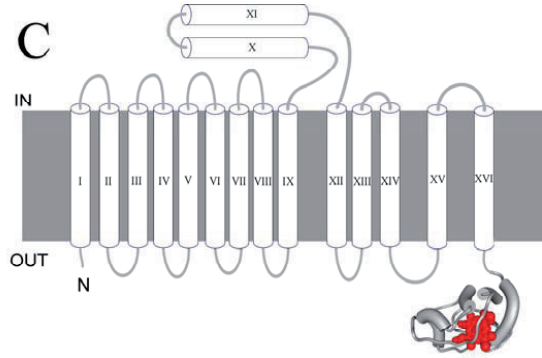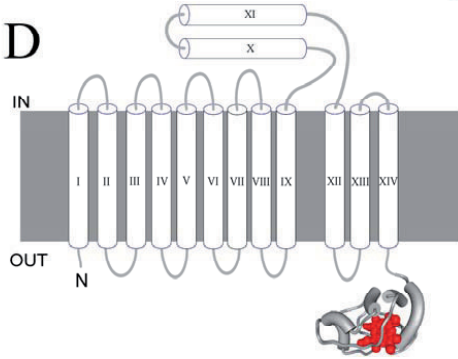
Figure 1

A

B

C

D
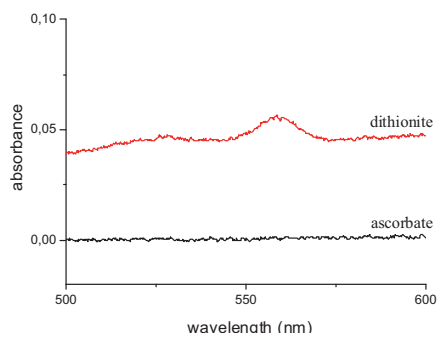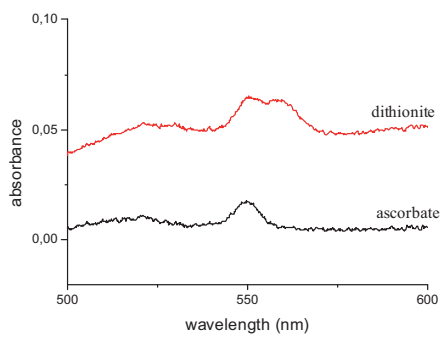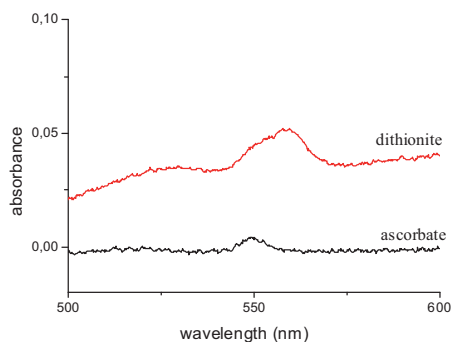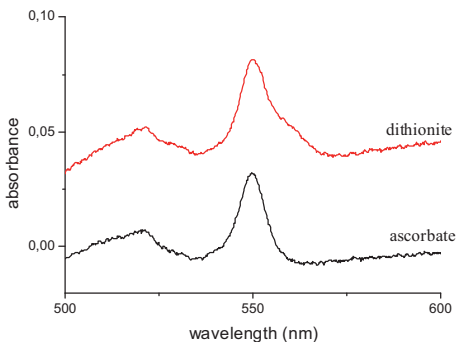
Figure 2
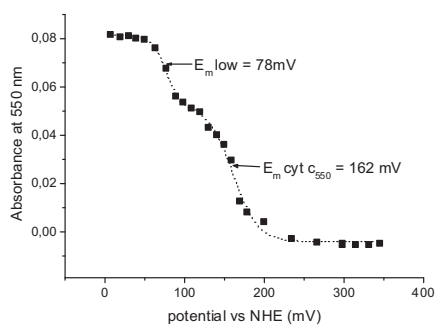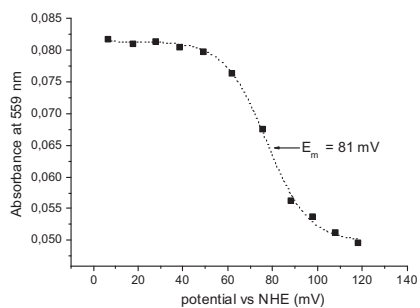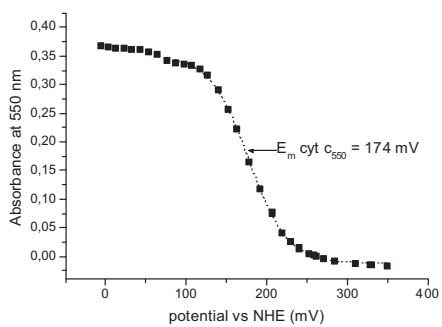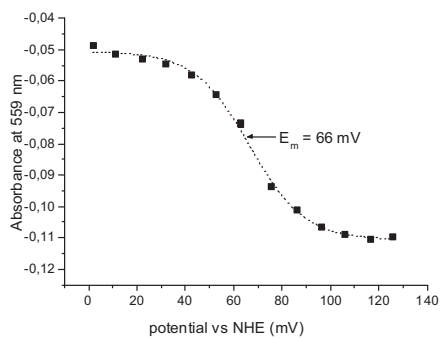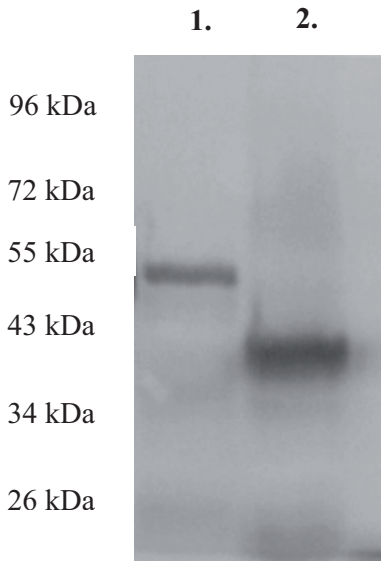
Figure 3

Figure 4

A

B

Figure 5

Figure 6

Figure 7